MAYNOOTH UNIVERSITY

DOCTORAL THESIS

NUI MAYNOOTH
Ollscoil na hÉireann Má Nuad

A MUSE Exploration of Edge Cases in Jet Launching

Author:
Andrew K. KIRWAN

Supervisor:
Dr. Emma T. WHELAN

A thesis submitted in fulfillment of the requirements
for the degree of Doctor of Philosophy

in the

Star and Planet Formation Group
Department of Experimental Physics
Faculty of Science and Engineering

February, 2023

Declaration of Authorship

I, Andrew K. Kirwan, declare that this thesis titled, “A MUSE Exploration of Edge Cases in Jet Launching” and the work presented in it are my own. I confirm that:

- This work was done wholly or mainly while in candidature for a research degree at this University.
- Where any part of this thesis has previously been submitted for a degree or any other qualification at this University or any other institution, this has been clearly stated.
- Where I have consulted the published work of others, this is always clearly attributed.
- Where I have quoted from the work of others, the source is always given. With the exception of such quotations, this thesis is entirely my own work.
- I have acknowledged all main sources of help.
- Where the thesis is based on work done by myself jointly with others, I have made clear exactly what was done by others and what I have contributed myself.

Signed:

Date:

"*How strange it is that the sky, which by day is a stationary ground on which the clouds are seen to move, by night becomes the backdrop for Urth's own motion, so that we feel her rolling beneath us as a sailor feels the running of the tide.*"

Severian, *Book of the Lictor* (Gene Wolfe, 1982)

MAYNOOTH UNIVERSITY

Abstract

Faculty of Science and Engineering
Department of Experimental Physics

Doctor of Philosophy

A MUSE Exploration of Edge Cases in Jet Launching

by Andrew K. KIRWAN

The evolution of stellar objects and the potential planetary systems that form around them are core preoccupations for astronomers. Common to many sun-like stars in their formative years is the presence of astrophysical jets. They are tightly linked to accretion processes and are believed to play a crucial role in stellar evolution by carrying away mass and angular momentum, but the process by which they are launched is not yet determined. The majority of our knowledge comes from the study of low-mass Classical T-Tauri stars, and advances in instrumentation – particularly in ground-based astronomy – have made it possible to observe jets closer to their region of launch. The goal of this thesis is to utilize high angular resolution integral field spectroscopy to explore less common jet launching sources in an effort to better understand jet behavior and its impact on stellar evolution. We present MUSE observations of the intermediate-mass Herbig Ae star HD 163296, the giant Orion proplyd 244-440, and the proto-brown dwarf candidate Mayrit 1082188, each of which features a unique outflow system and together constitute a rich data set spanning a range of age, mass, and environment. In our study of HD 163296 we observe a complex outflow system that is still active despite its age. We analyze the morphology of the proplyd jet system and find it is possibly driven by a smaller companion hidden within the photoevaporating disk. In our final study we discover a large cavity associated with Mayrit 1082188, which suggests a wind-driven process similar to standard outflow models. A key finding of this work is the evidence of commonality, and our results indicate that the outflow mechanism is efficient in its utilization of material, durable in its ability to launch under harsh conditions, and scalable in power to the mass of the driving source.

Acknowledgements

I would like to acknowledge all those in the Experimental Physics Department who aided my transition into Irish life. I especially thank my supervisor, Dr Emma Whelan, for her tireless support and encouragement throughout all stages of this foray into the unknown, and for making sure I have not allowed myself to be needlessly distracted by smaller things. My gratitude extends to all the staff who have made these last four years an adventure well worth the undertaking.

I acknowledge the priceless help and contributions of my collaborators, most especially Christian Schneider, Carlo Manara, Jochen Eislöffel, Catherine Dougados, and Aisling Murphy. Among them I have yet to find a question unanswered, and their patience and passion have both humbled and emboldened me.

I am extremely grateful to my fellow postgraduates for their inclusiveness and good humor. Not only have they offered help throughout my studies, but they have also been willing to spend time with me and offer friendship, teaching me the ways of mad craic.

I would also like to thank my family and friends back across the pond, who at every step along the way encouraged me to pursue my passion, no matter how late in life I might have started. Without their support it is unlikely I would have began my academic journey in the first place.

My greatest thanks extend to my wife, Dee Kirwan, for her support and the sacrifices she has made for me during my studies.

Finally, I wish to thank Steve Gunn and Sunil Patel for providing this thesis template.

Contents

List of Figures

List of Tables

Dedicated to the Wanderer within the Labyrinth of every Possibility...

Chapter 1

Introduction

> Probably the most ancient form of legitimation is the conception of the institutional order as directly reflecting or manifesting the divine structure of the cosmos, that is, the conception of the relationship as one between microcosm and macrocosm. Everything "here below" has its analogue "up above".
>
> — Peter Berger (1929-2017)

Throughout the ages we have concerned ourselves with deciphering the heavens: in dark caves, we sketched our observations in the light of the Pleistocene fires; in fields, we built monoliths to mark the passing of seasons; on hills and mountains, we built temples to embody on earth the precepts of the divine order. Wise-men of old propped up kings with their astrology, and the alchemists mapped the virtues of things to the stars in search of the waters of life. The apparent constancy of the cosmos has stood in stark contrast to the fleeting nature of our lives, and we have ever sought to alleviate an existential quandary through the permanence of societal structure. For the astronomer, we inherit this seemingly innate instinct, sublimating the urge to fixate structure into a burning curiosity for our universe, our sun and our solar system, and it is on this that we focus our attention. We seek not only to find an answer to the ancient question, "Where do we come from?", but to extend this outward and ponder, "Are we alone?" This latter question is undoubtedly beyond the scope of this work, but we can reasonably explore the former by observing young stellar objects (YSOs) similar to our sun in various stages of their development and thus begin to piece together a picture of our own star's evolution and the formation of the solar system around it. In this study I am focusing instead on a relatively small period of time in the life-cycles of stars, during which they often are seen to drive outflows of matter into the natal envelope around them. My primary goal is to contribute to the wealth of knowledge currently available with new observations in a further attempt to explain their mechanics and provide constraints on their model parameters, in particular by utilizing data from state-of-the-art instrumentation to peer deeper into those regions close to the star from which the outflows are emitted.

This chapter is organized as follows. In Section 1.1 I will provide a brief overview of the formation and life-cycle of stars comparable to our sun from their birth up to the pre-main-sequence (PMS). I will also discuss a few types of young stars which are especially relevant to jet studies, as they are the most commonly observed sources of outflows. In Section 1.2 I will examine the connection between accretion and outflow in YSOs and the importance of circumstellar disks in the role of both stellar and planetary evolution. This will all provide a foundation for the core concern of this research, which is to investigate the phenomenon of astrophysical jets, their relation to star formation, and the mystery of their launching. Section 1.3 will introduce the analysis of spectroscopic emission lines and shock waves and outline their importance in jet studies. Finally, Section 1.4 will motivate the desire to study the titular "edge cases" among known jet-driving sources, introducing the objects to which this focus of this thesis is devoted.

1.1 Star Formation and Evolution

1.1.1 Birth in the Gaseous Medium

It is widely accepted that stars have their origins in the collapsed cores of nebular clouds formed out of the gaseous remnants from the birth of the universe. This interstellar medium (ISM) which allows for their birth is quite diverse, and while there is no discrete delineation between the types of molecular clouds that exist within it, we can rely on some broad classifications of their general environmental characteristics. The most important type of cloud to our studies is the class considered *Giant Molecular Clouds* (GMCs), which are observationally defined as "over-densities" in the ISM and present as bright features arrayed with filaments of gas and dust across various distances (Chevance et al., 2022). These are always identified relative to their surroundings and as such they cannot truly be characterized as well-defined discrete objects, although across observations they tend to share some common features. For example, they are generally massive (M $\sim 10^5 - 10^6\ M_\odot$) structures spanning $d \sim 10 - 100$ pc across, with internal velocity structures typically characterized by power-law behavior expected of turbulent motion (Dobbs et al., 2014; Carroll and Ostlie, 2017; Chevance et al., 2022). However, key parameters such as the surface mass density, the relationship between cloud size and line width, and density distributions vary across galaxies, highlighting the importance of interpreting cloud properties in the appropriate contexts.

There are many processes which may lead to the formation of GMCs (see Dobbs et al., 2014). Whether by cloud collisions, gravitational compression, turbulence in ISM filament flows, or shock-compression due to supernovae, GMCs ultimately accrete out of the ISM and become storehouses of large amounts of H_2, which is readily photodissociated by far-ultraviolet (FUV) radiation. A combination of dust attenuation and molecular shielding protects some H_2 molecules from this fate, and allows for the conversion of atomic H to H_2 and the eventual formation of CO and other molecules. The efficiency of these conversions plays an important role in determining the density of GMCs, and constraining the chemistry of CO and H_2 formation in GMC models can reveal important information about the role of background photoionization and cosmic ray ionization, and ultimately shed light on the hydrodynamics of the cloud.

The virial parameter $\alpha_{\rm vir}$ is a simplistic manner in which to express the energy balance in GMCs, such that $\alpha_{\rm vir} = 2E_k/U_g$, where E_k and U_g are the kinetic and gravitational potential energies of the cloud. Values of $\alpha_{\rm vir} \leq 2$ suggest self-gravitation, though this value can be smaller for more massive systems and much larger for less massive clouds, with observational evidence suggesting a general $\alpha_{\text{vir}} \sim M^{-0.5}$ trend in CO-derived cloud masses (see Figure 2 in Chevance et al., 2022). This α_{vir} parameter is limited however in that it does not take into account other energetics in the clouds, for example magnetic fields or large velocity gradients, with simulations suggesting that perhaps <10% of the total cloud mass in GMCs is gravitationally bound (Mao, Ostriker, and Kim, 2020). This has led to arguments over cloud collapse theories, with the two dominant scenarios being hierarchical collapse (i.e., small fractions of the cloud collapse locally) and global collapse. Across observations, evidence strongly suggests an efficiency rate of $\sim 1\%$, which poses a challenge for both local and global collapse models. Clarke et al. (2017) argue that accreting filaments embedded in turbulent media, such as the Orion Integral Shaped Filament (see Figure 1.1), undergo “fragmentation” and ultimately collapse into localized densities that can give rise to star formation. Contrary to this, Vázquez-Semadeni et al. (2019) present the idea that a “global hierarchical collapse” occurs in which the entire GMC experiences gravitational contractions while smaller-scale structures collapse within it, with all localized collapses accreting from the larger GMC and flowing towards the overall system center. Both of these models present solutions to the problem of low star formation efficiency and explain the formation of stars within clusters, although current observational evidence ultimately appears to oppose global collapse (Chevance et al., 2022).

Once a core is formed, its evolution is determined by gravitational potential energy density, P_{grav}, expressed by

$$P_{\text{grav}} = -\frac{(4\pi)^{1/3} G (3M)^{2/3}}{5} \rho^{4/3}, \tag{1.1}$$

a self-gravitation which is opposed by the internal pressure P_{ig} of the core such that

$$P_{\text{ig}} = \frac{\rho k_{\text{B}} T}{\bar{m}}. \tag{1.2}$$

This internal resistance can also be supported by pressure from (non-relativistic) electron degeneracy, P_{ed}, which is given by

$$P_{\text{ed}} = \frac{\pi h^2}{60 m_e} \left(\frac{3}{\pi \bar{m}_e} \right)^{5/3} \rho^{5/3}, \tag{1.3}$$

with m_e being the electron mass, $\bar{m}$ being the mean gas-particle mass ($\sim 10^{-24}$ g), and h and k_{B} the Planck and Boltzmann constants, respectively (Bradt, 2014; Whitworth, 2018). The effective pressure of the core $P_{\text{eff}} = P_{\text{grav}} + 3P_{\text{ig}} + 3P_{\text{ed}}$ determines whether the core contracts (< 0), remains in hydrostatic equilibrium ($= 0$), or expands (> 0).

Star formation can only occur in a pre-stellar core if its mass M exceeds the Jean’s Mass, at which point gravitational pressure overcomes internal pressure and the core contracts. In low interstellar densities, electron degeneracy can be ignored and Equations 1.1 and 1.2 combined into the expression $P_{\text{grav}} + 3P_{\text{ig}} < 0$ to determine the density threshold (or Jean’s density) above which the core collapses, i.e. $\rho \geq \rho_{\text{Jeans}}$. Letting $a = \sqrt{k_{\text{B}} T / \bar{m}}$ be the isothermal sound speed, this becomes

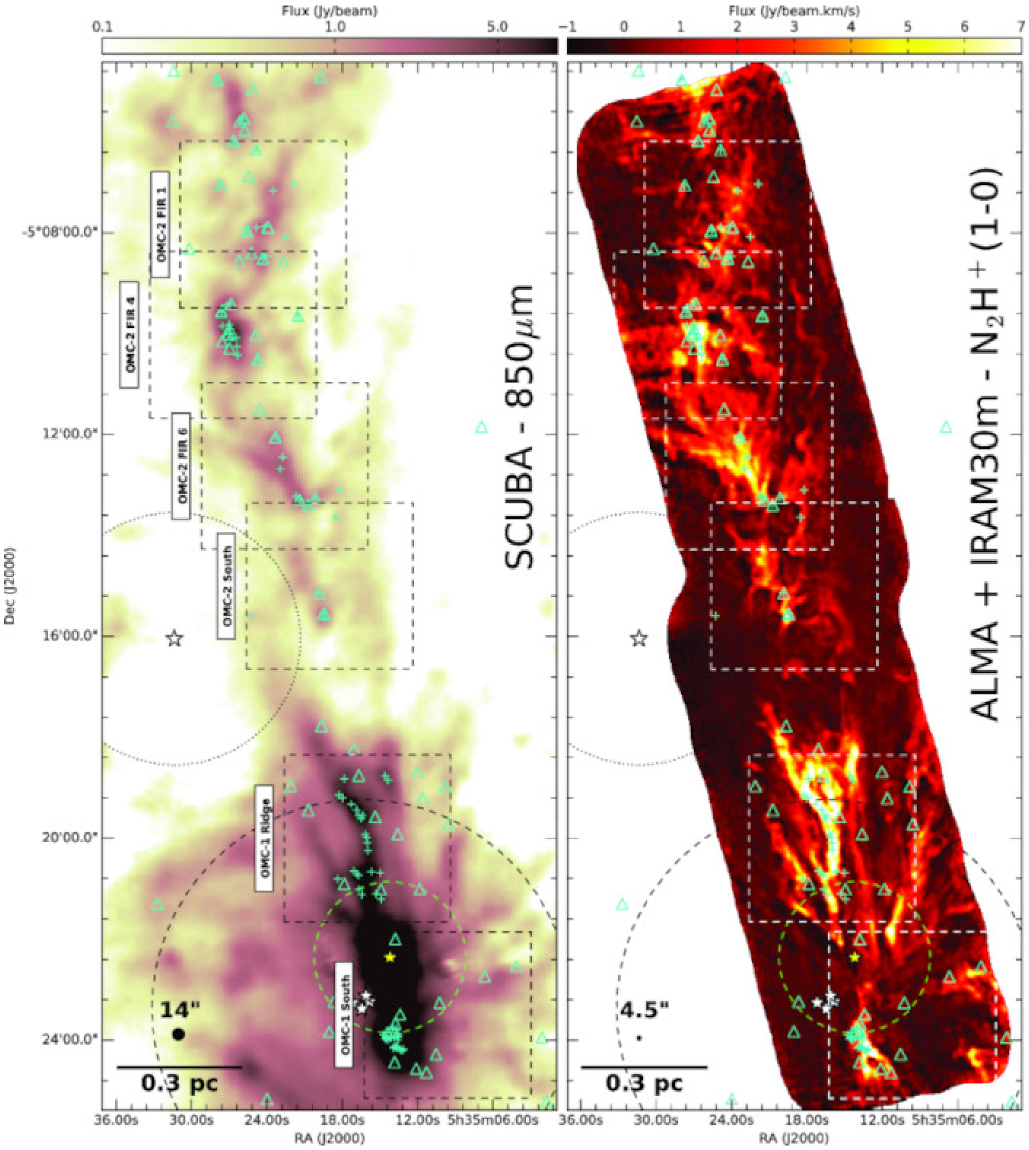

FIGURE 1.1: The Orion Integral Shaped Filament shown in SCUBA-850 μm continuum emission (left) and integrated N_2H^+ emission (right) obtained from ALMA and IRAM observations. The white stars show the positions of the Trapezium stars, the yellow star shows the Orion Becklin-Neugebauer source (a deeply embedded "run-away" protostar; see Bally et al., 2011), and the light green triangles show the protostars identified by Spitzer. Image from Hacar et al. (2018).

$$\rho \geq \frac{30a^6}{G^3M^2}. \tag{1.4}$$

Because these conditions are temperature-dependent, the Jean's density for low-mass star forming regions will be different than those in intermediate- or high-mass regions. Additionally this sets constraints on the radius of the region (Bradt, 2014; Whitworth, 2018; Chevance et al., 2022). Some interesting implications of this will be further discussed in Section 1.1.2. During collapse, asymmetric formations (i.e. "clumpiness") within the cloud become prominent as the mass requirement in Equation 1.4 decreases. In such a case, fragmentation can occur and lead to the formation of multiple stars in a collapsed region (Carroll and Ostlie, 2017; Whitworth, 2018; Chevance et al., 2022).

1.1.2 Pre-Main Sequence Stars

Our current understanding is that the coming-of-age of a young star may be split into three stages before its main sequence: the pre-stellar phase, the protostellar phase, and the pre-main-sequence (PMS) stage (Andre, Ward-Thompson, and Barsony, 2000; Li et al., 2014; Dunham et al., 2014; Chevance et al., 2022). When a gravitationally-bound "core" has formed within a collapsing region of a GMC as discussed above, it can continue to condensate and begin the pre-stellar phase of evolution. Typically these are observed by a combination of techniques, for example by mapping NH_3 transitions, and when used in conjunction with wide infrared (IR) surveys such as Herschel, Spitzer, and IRAS, this can aid in identifying which cores possess embedded objects (protostellar phase) and which cores are still in the pre-stellar phase (Andre, Ward-Thompson, and Barsony, 2000; Dunham et al., 2014). Over time, the condensation of the core can form a hydrostatic protostellar object and begin its next phase of evolution. In the discussion below, I will primarily consider low-mass Classical T-Tauri Stars (CTTSs) and the intermediate-mass Herbig Ae/Be stars (HAeBes) due to the large sample of outflows catalogued from them. Since, in recent years, outflows have been observed down into the very low-mass regime (Whelan et al., 2005), I will additionally discuss a class of sub-stellar objects known as brown dwarfs (BDs).

Low-mass regime

In the low-mass regime, the protostellar phase has historically been divided into three classes based on the infrared (IR) spectral index of the star, which is defined as

$$\alpha = \frac{\mathrm{d}\log(\lambda \mathrm{S}_\lambda)}{\mathrm{d}\log\lambda}, \tag{1.5}$$

where S_λ is the flux density at some wavelength λ (Dunham et al., 2014). This characterizes low-mass protostellar objects by separate classes: Class I ($\alpha \geq 0.3$), Class I Flat ($-0.3 \leq \alpha < 0.3$) Class II ($1.6 \leq \alpha < -0.3$), and Class III ($\alpha < -1.6$) types, with Class 0 objects later being added to account for objects so deeply embedded that their presence is inferred through e.g. outflows rather than near-infrared (NIR) observations (Andre, Ward-Thompson, and Barsony, 1993).

Class 0 types are very low-mass, and typically persist for around 30,000 years, accreting matter from the parent cloud all the while. Class I types begin around 200,000 years, where the object is now an evolved accreting protostar with a mass greater than the environment surrounding it. The spectral energy distribution (SED) of this object now exhibits a black-body curve with a very high IR excess, indicating the presence of an accretion disk (André, 2002; Kogure and Leung, 2010). Class 0 and Class I protostars are also often distinguished by jet-like molecular CO outflows, suggesting a decrease in the mass accretion rate over time. The flat-spectrum class exhibits SED curves different from both Class I and Class II, and as such is thought to be a transition between the two classes (Andre, Ward-Thompson, and Barsony, 2000; André et al., 2004). During the Class I stage, it is common for these accreting objects to launch large-scale jets of matter, which is discussed in Section 1.2.

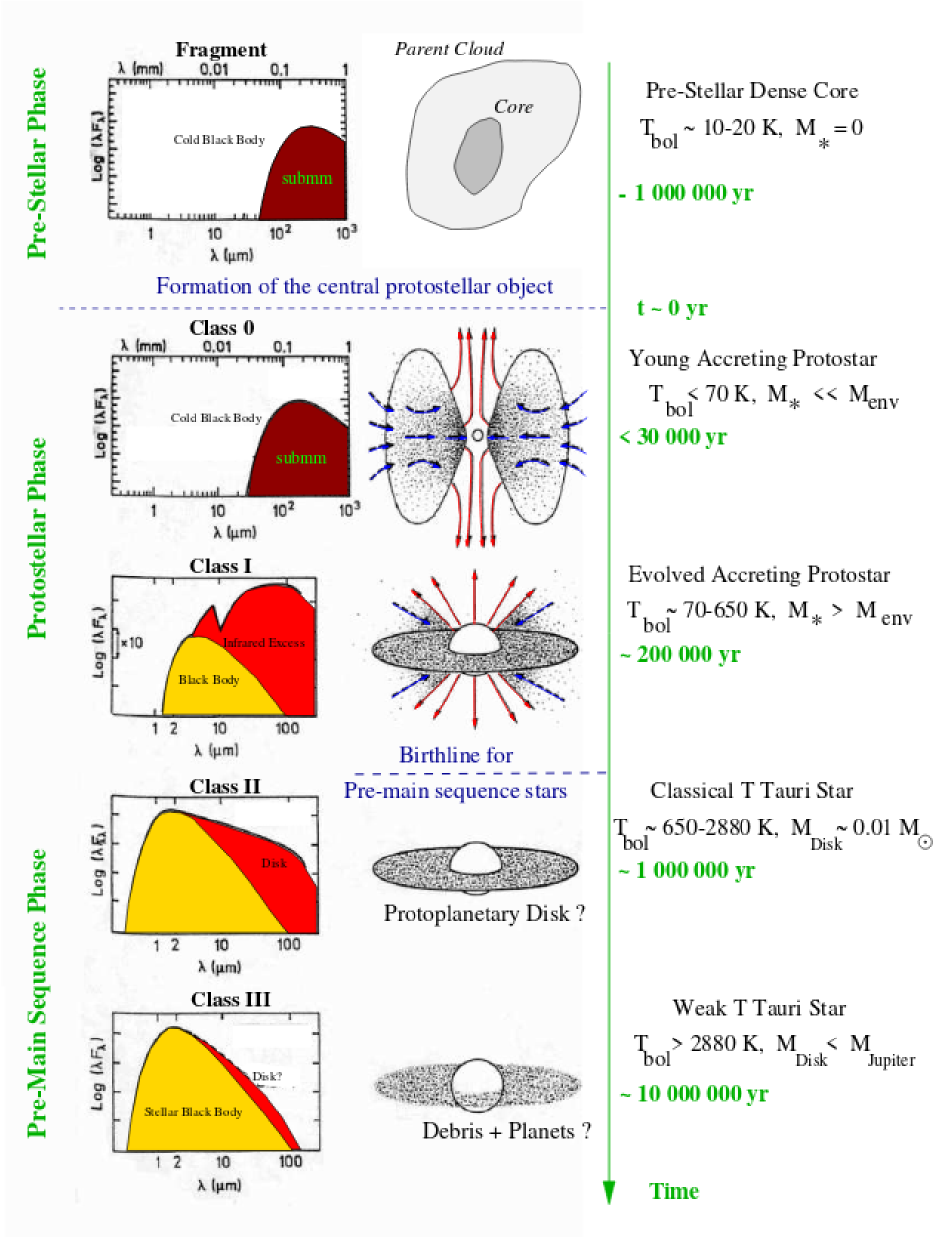

FIGURE 1.2: A diagram showing the phases of stellar evolution to the PMS. Image credit: André (2002).

The PMS stage (1-10 Myr) consists of Class II and Class III type stars. Class II types begin around 1 Myr and feature a protoplanetary disk with a disk mass around 0.01 $M_\odot$. They exhibit a bolometric temperature (T_{bol}) generally between 650-2880K, and the SED again features a large black body curve and an infrared excess. Smaller jets are typically associated with this class of objects (see Section 1.2). Class III types begin around 10 Myr and have a disk mass below a Jupiter mass, with $T_{bol} > 2880$K. They exhibit a stellar black body curve with a small infrared excess André, 2002. Characteristic SEDs of and cartoons representing these separate classes are shown in Figure 1.2. Additionally, some CTTSs feature "transitional disks" (TDs), where much of the optically thick material in the inner disk has disappeared as evidenced by small NIR excess, with mid-IR and far-IR excess dominating the SED. How the dust is cleared is hotly debated, with planet formation often being proposed (Andrews et al., 2018; Maucó et al., 2018) as a possible mechanism. Examples of TD/pre-TD SEDs for a sample of CTTSs in the Orion OB1 complex are shown in Figure 1.3.

T-Tauri stars are a prime example of low-mass PMS stars, and are generally classified as "classical" or "weak-line" T-Tauri stars. CTTSs still have disks and are still accreting, as evidenced by the IR and UV excess, placing them in the Class I/II region; in contrast, these excesses are not observed in weak-line TTS (WTTS) indicating that the disk is nearly or completely dispersed (Class III). CTTSs also typically host magnetic fields on the order of kG, and these are believed to play a role in disk dynamics and accretion processes, which is further discussed in Section 1.2.1. As outflows are ubiquitous to this class of star, CTTSs are a powerful laboratory for the study and understanding of jets, and as such much of our understanding of the outflow mechanism comes from these objects (Reipurth and Bally, 2001a; Ray and Ferreira, 2021; Frank et al., 2014; Whelan, 2014).

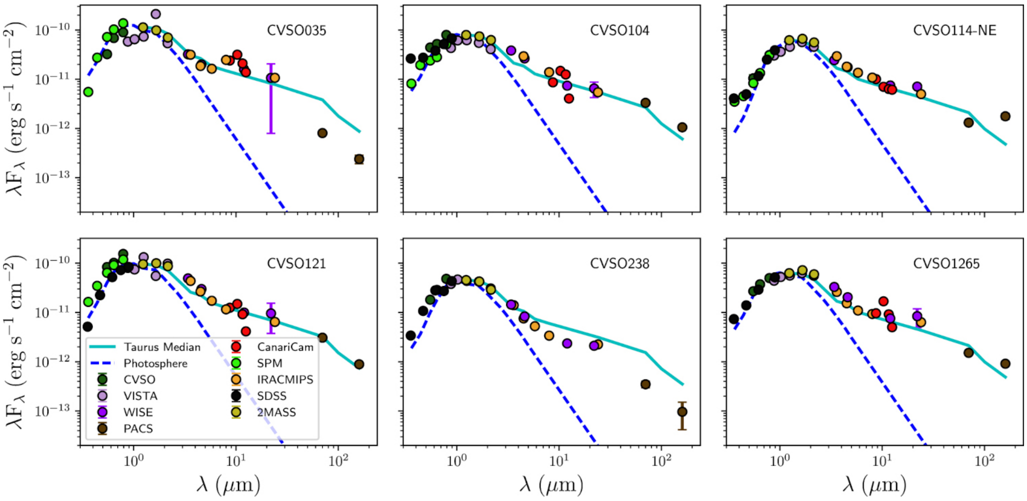

Figure 1.3: SEDs of a sample of CTTSs from Maucó et al. (2018), which they construct from a variety of literature sources. The dashed blue lines show stellar photospheric model fits. The IR "bump" in each object can be seen, indicating the presence of a disk. The red dots interesting display a bump at 10 μm which is a silicate emission feature that the authors interpret as the presence of submicron grains in the disk.

Intermediate-mass regime

In 1960, George Herbig classified Herbig Ae/Be stars (HAeBes, $\sim 2 - 10\ M_{\odot}$) as an intermediate-mass PMS counterpart to CTTSs (Herbig, 1960). Like CTTSs, these emission line stars display strong Balmer lines, often with P Cygni profiles (indicative of energetic outflows; see Figure 1.4) or double-peaked Hα lines (indicative of a rotating accretion disk; see Figure 1.5). They are generally found in obscured regions associated with star formation, and exhibit a strong infrared excess in their SEDs congruent with the presence of an optically thick accretion disk. These stars are often optically bright with a luminosity class between III and V (which distinguishes them from B[e] supergiants), and illuminate nebulous regions in their immediate vicinity, sometimes obscuring the stars themselves (Hillenbrand et al., 1992; Ray, 1994; Waters and Waelkens, 1998). These reflection nebulae can sometimes hide binary companions, and spectro-astrometric techniques have shown that up to $\sim 70\%$ of HAeBes exhibit binarity (Baines et al., 2006).

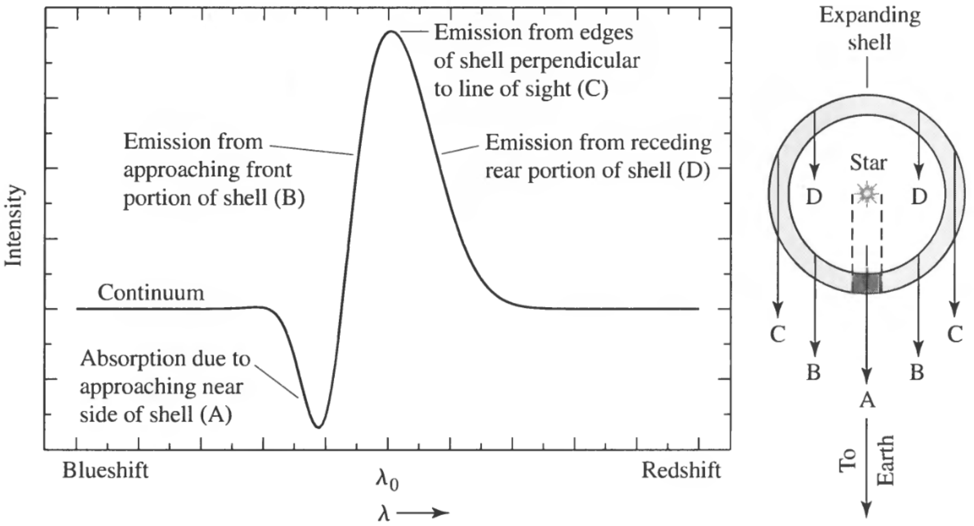

Figure 1.4: Example of a typical P Cygni spectral profile on the left, with the components A, B, C, and D illustrated in terms of the expanding shell of dust and gas coupled to the star/disk system on the right. Approaching matter is blue-shifted, and presents as an absorption feature due to the shell intercepting stellar photons. The emission peaks show both blue- and red-shifted components of the expanding shell. Image from Carroll and Ostlie (Figure 12.17 in 2017).

Because HAeBes are expected to follow a different evolutionary track than CTTSs, they cannot be classified in terms of Figure 1.2. Hillenbrand et al. (1992) analyzed the IR excess of over 40 HAeBes and proposed a classification system splitting them into Group I, Group II, and Group III objects. In this system, Group I objects were characterized by flat, optically thick disks, and Group II SEDS were interpreted as a disk+envelope system due to the rise in far-IR emission indicating cooler material. Waters and Waelkens (1998) revised this division in terms of Group I and Group II, with Group I being described by a power-law+black-body model, and Group II being being described only by a power-law. Later, it was found that Group II sources display a smaller FIR/NIR ratio than Group

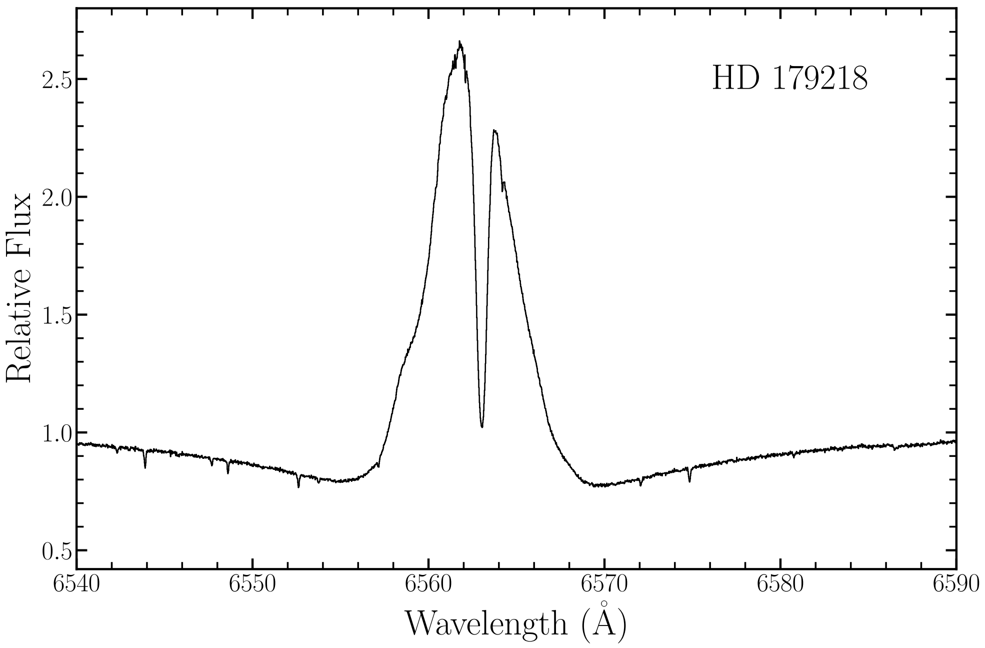

Figure 1.5: Example of a double-peaked emission profile seen in the UVES spectrum from the Herbig Ae star HD 179218 The spectrum was obtained from the ESO archive under program ID 077.C-0521 (PI. D. Fedele).

I, indicating Group I sources have a "flared" disk structure as opposed to the "flat" disk structure of Group II objects (Muro-Arena et al., 2018), although counterexamples have been observed which challenge this assertion (Pascual et al., 2016). Further differences in the evolution of these two groups were highlighted with the discovery that Group I sources tended to have larger gaps or cavities in the disk (> 20 au) than seen in Group II objects (< 1 au), the latter of which were observed near the dust sublimation radius of the disks, and a silicate feature at 10 µm was observed ubiquitously in Group II objects but not Group I (Pascual et al., 2016; Rubinstein et al., 2018; Muro-Arena et al., 2018). This feature can be very prominent, as shown in Figure 1.6. Similar to the Class Flat SEDs in the low-mass regime, it is possible that some HAeBes may also represent a transitional phase between Group I and Group II objects, which may be the case for the star HD 163296 (Grady et al., 2000; Isella et al., 2016; Muro-Arena et al., 2018, also see Chapter 3).

In contrast to CTTSs, HAeBes generally do not appear to host such large magnetic fields, and due to the large proportion of these objects exhibiting binarity it is difficult to separate the magnetic field contribution of the HAeBe from that of its companion. As will be discussed below, this raises questions and difficulties regarding the outflow mechanism in these intermediate-mass objects.

Sub-Stellar Objects

Another class of objects relevant to jet launching studies are brown dwarfs (BD). These sub-stellar objects are "failed stars" in that they are too small to support hydrogen burning (though they can burn deuterium) but too large to truly be planets, limiting their mass

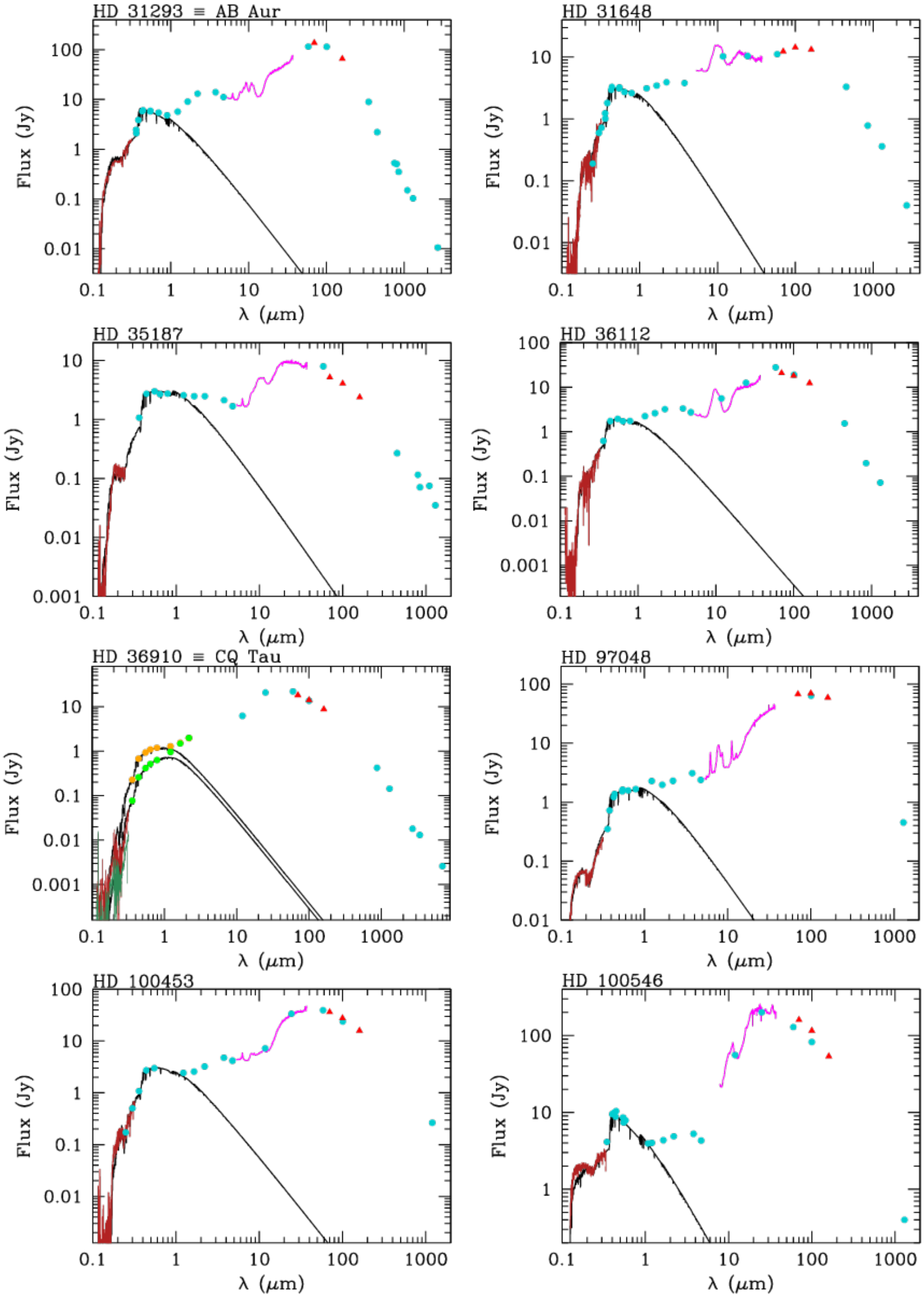

FIGURE 1.6: SEDs of a sample of Group I and Group II HAeBes from Pascual et al. (2016), which they construct from a combination of literature sources (blue circles) and their own measurements (red triangles). The red and black lines show stellar photospheric model fits, while the purple lines show the IR excess. The 10 μm silicon feature is seen in the purple lines for most of these objects.

range between $\sim 13-80\ M_{\text{Jup}}$ (Whelan, 2014; Schlaufman, 2018; Whitworth, 2018; Grieves et al., 2021). These objects are of a low enough mass that they can only be supported against collapse by electron degeneracy pressure (see Eq. 1.3), and are believed to have formed out of gravitational instabilities on timescales $\leq 10^5$ yr, formally distinguishing them from planets which form through core accretion on the scale of $\geq 10^6$ yr (Pollack et al., 1996; Grieves et al., 2021).

Numerous theories exist regarding the birth of these objects. One possibility is that they form within the filaments that feed larger stellar clusters, in which case they pass through a more mature star forming region and potentially get ejected at high velocities, and are therefore unable to accrete enough mass to sustain hydrogen burning (Clarke, Whitworth, and Hubber, 2016; Whitworth, 2018). It may also be that pre-stellar cores are dynamically ejected from the larger cluster (see e.g. Reipurth and Clarke, 2001). Additionally, because many brown dwarfs are observed as companions to larger stars, it is possible that they form out of the disk fragmentation of the primary, although Whitworth (2018) argues that due to the dynamics of this fragmentation this is only likely to occur in outer regions of the disk. If BDs do indeed form in filaments or are ejected from larger clusters, this would imply that their formation track is similar to that of proper stars; conversely, if they are formed out of a primary circumstellar disk, then this suggests that they follow a more planetary formation track.

While these objects appear to be at a boundary between stellar evolution and planetary evolution, in literature they are often referred to in the same class system as seen in Figure 1.2 (see e.g. Doppmann et al., 2005; Riaz et al., 2015; Riaz and Whelan, 2015; Schutte et al., 2020). Similarly, the SEDs of these objects show IR-excess consistent with the presence of disks and envelopes (Joergens et al., 2012; Schutte et al., 2020), as seen in Figure 1.7. Since the first positive detection of an outflow by Whelan et al. (2005), several BDs have been observed to drive powerful jets (see e.g. Whelan, 2014; Joergens et al., 2012; Riaz et al., 2015), providing us with a fascinating laboratory to test the robustness of current jet-launching models and better understand whether the same or a similar mechanism observed in CTTSs is also responsible for BD outflows as a “scaled down” version.

1.2 The Accretion-Outflow Connection

1.2.1 Hungry Like the Wolf

After the formation of a protostellar object (see Sec. 1.1.1), the protostar gains mass by accreting material from the collapsed cloud. Due to rotational dynamics, the material spreads out around the central rotating source in the form of a circumstellar disk. The accretion rate of the star is measured via its accretion luminosity, which is determined from analysis of various line profiles (Hartmann, Herczeg, and Calvet, 2016). How material is funnelled into the star is typically described in terms of magnetospheric accretion (MA) or boundary layer (BL) accretion, which I briefly describe below.

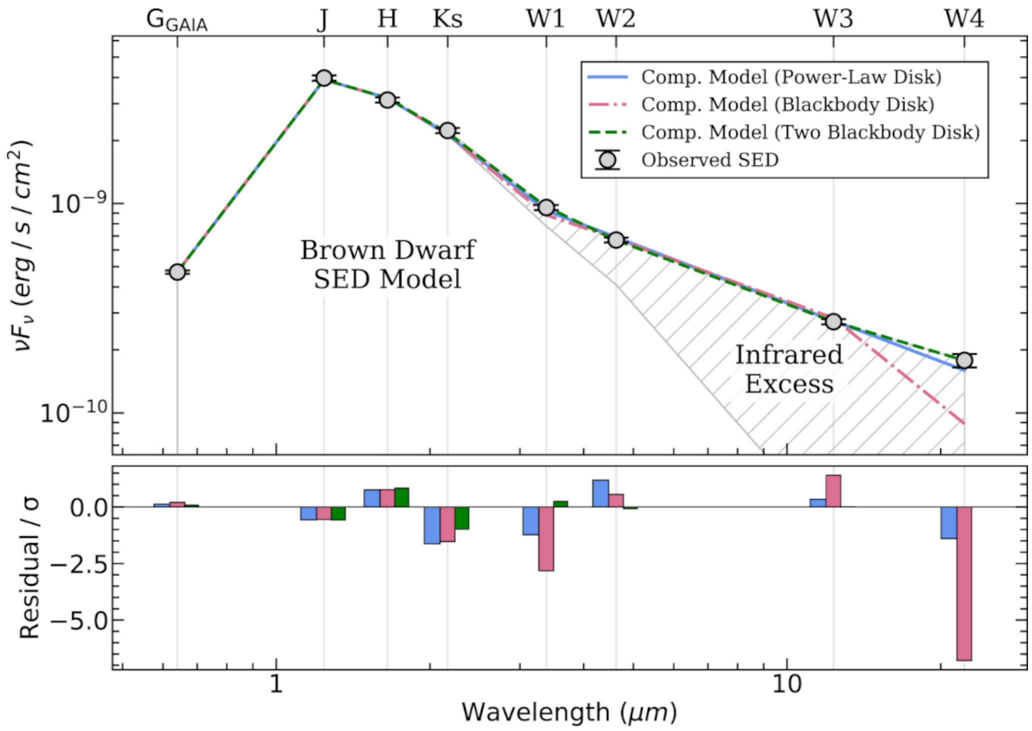

FIGURE 1.7: The SED of the BD W1200−7845, as shown in Schutte et al. (2020, their Figure 4). This demonstrates the presence of a warm ($\sim$ 600 K), dusty disk.

In the MA model, magnetic field lines anchored in this disk funnel dust and gas onto the surface of the star, during which course it reaches free-fall velocities and produces accretion shocks on the stellar photosphere. These processes are evidenced by observed NIR excesses (the inner disk heating and radiating its absorbed energy), broad line profiles (high-temperature gas columns in the funneled flow), and X-ray and strong UV excesses (accretion shocks; see Figure 1.8, and Shu et al., 1994b; Mendigutía, 2020; Hartmann, Herczeg, and Calvet, 2016). The accretion column has three regions: the pre-shock region, the post-shock cooling region, and the photosphere heated by the shock below the column. As the material is shocked, X-rays propagate up into the pre-shock region and downward towards the photosphere, and the heated photosphere emits energy back upwards into the post-shock region. The post-shock region is typically cooler and more dense than the pre-shocked or shocked regions, cooling by X-ray and UV emission at a rate determined by initial temperature and post-shock electron density. Computational modeling of the physics behind this found that flux excesses were reproduced for most stars from T-Tauri to low-mass brown dwarfs, and further that this treatment was even applicable to some HAeBes, although Hartmann, Herczeg, and Calvet (2016) caution that accretion columns are far more complex than idealized treatment.

While magnetically controlled accretion processes dominate in low-mass stars (e.g. CTTSs) due to their large magnetic fields, it is uncertain whether this applies for higher mass stars as well. The low magnetic fields observed in HAeBes (see Section 1.1.2) suggests that there may be a different process at work (Nisini et al., 2018; Garufi et al., 2019; Mendigutía, 2020). Although many accretion measurement methods can potentially be

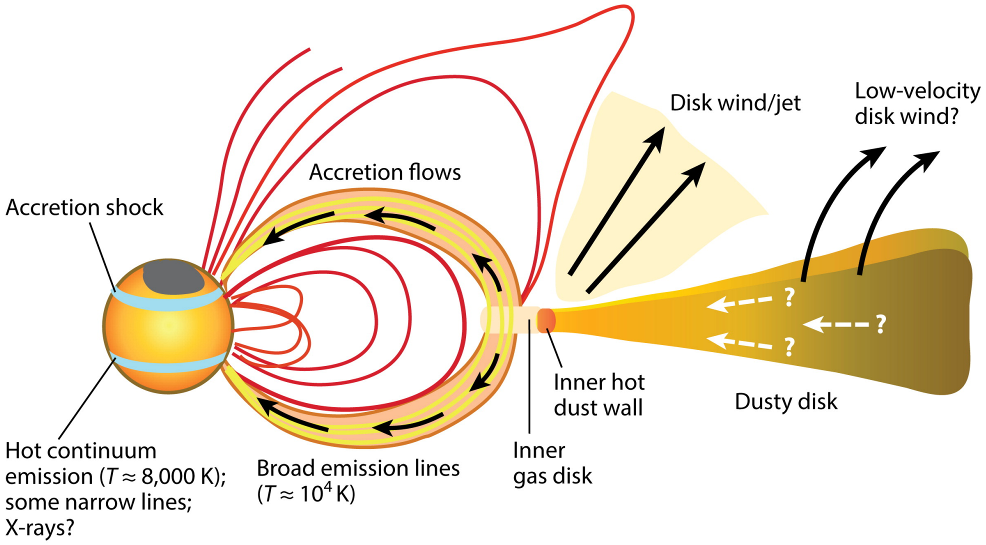

FIGURE 1.8: A cartoon demonstrating various aspects of accretion from the disk onto the star. Material flows along magnetic field lines onto the star, and if the lines are twisted due to differential star-disk rotation, matter can be ejected outward as a jet. Figure from Hartmann, Herczeg, and Calvet (2016).

applied to HAeBes, whether or not the MA model is valid is currently debated due to the fact that large magnetic fields are required to sustain the MA model, and to date the majority of HAeBes have measured magnetic fields on the order of a few hundred G, which is often well below the minimum limit for MA, and generally around 25% of the values measured for CTTSs (Johns-Krull, Valenti, and Koresko, 1999; Hubrig et al., 2014; Cauley and Johns-Krull, 2014; Mendigutía, 2020). Wichittanakom et al. (2020) argue that the MA shock model is likely valid at least at the lower-mass end of the Herbig spectrum and find a distinct break in accretion rates between HAe and HBe objects, indicating a "transition" from MA to another model beginning around 4 $M_\odot$.

One such proposed model is the BL model, where the disk deposits material directly onto the star through a hot, viscous region in which the gravitational and centrifugal forces are no longer balanced (Wichittanakom et al., 2020). In contrast to MA in which magnetic fields result in accretion regions at high latitudes on the star, a consequence of the BL model is an equatorial accretion region whose brightness thus depends on the inclination angle of the star. In a broad review of accretion measurements in HAeBes Mendigutía (2020) found that, in agreement with Wichittanakom et al. (2020), the MA model is unlikely to consistently extend to HBe objects; they caution however that the BL model may not be the most accurate for these stars either, particularly as it suggests accretion rates that are far larger than expected based on the age of HBe sources. They suggest that photoevaporation may have a non-negligible role in HBe stars, and conclude that more in-depth studies of Balmer and UV excesses could help in discriminating between models and quantify the effects of photoevaporative flows.

Whatever model is assumed, a critical issue is raised with respect to stellar evolution. Accretion from the disk transports both mass and angular momentum onto the star, therefore the final star should be spinning far more quickly than what is observed in most main-sequence stars (Hartmann, Herczeg, and Calvet, 2016). The energy released in the accretion process alone is not sufficient to explain the observed rotation rates, and thus how angular momentum is removed from the system remains an open question. Disk winds and outflows arising from magnetohydrodynamic (MHD) processes and/or magnetorotational instabilities (MRI) have been invoked as explanatory mechanisms, and as such much attention is devoted to constraining the mass-loading and outflow rates of these two phenomena. As will be discussed below, these outflows appear intrinsically linked to disk processes.

1.2.2 The Role of Outflows

Ubiquitous to all accreting YSOs is the observed presence of outflows of collimated matter, indicating that these astrophysical jets play a crucial role in star formation and have a close connection with the circumstellar disk (Hillenbrand et al., 1992; Cabrit, Ferreira, and Dougados, 2011; Beall, 2015; Ray and Ferreira, 2021). These outflows manifest as spectacular jets of ionized matter, emitting radiation at wavelengths ranging from the radio to X-ray regimes as molecular outflows (CO, SiO, H_2) and atomic jets ([S II], [O I], Hα), and spatially extending from the source as far out as several parsecs (Reipurth and Bally, 2001a; Woitke et al., 2018; Lee et al., 2022). It is typical to see complex structures within these outflows such as nebular Herbig-Haro (HH) objects, chains of linearly spaced or “wiggling” knots, and bow shocks; and spectroscopic data indicates a range of ionization and excitation, as seen for example in Figure 1.9 (Brugel, Olmsted, and Boehm, 1983; Hartigan, Morse, and Raymond, 1994; Maurri et al., 2014; Hartigan, Holcomb, and Frank, 2019). In general, the jet length-to-width ratios are ≈ 10, and there further exists a tendency for jets and counterjets to possess asymmetries. There are also varying degrees of collimation close to the source, demonstrating a range of “opening angles” or apertures from which the jet is launched.

As discussed in Section 1.1.2, CTTSs are typically considered the “touchstones” of jet dynamics. Using the low-mass model in Figure 1.2, Class 0 sources have the highest accretion rate, and in these objects we typically observe slow, wide bipolar CO outflows nested around fast, collimated outflows in SiO and H_2. Class I sources are more evolved and so accretion has slowed significantly. In these we typically observe jets in forbidden optical lines such as [S II] and [O I], as well as recombination lines (e.g. the Balmer series of hydrogen). Finally, in Class II objects the envelope is depleted but the disk may remain, and jet emission is typically fainter and further out from the source. Importantly, Hartigan, Edwards, and Ghandour (1995) demonstrate that jets are not observed where accretion is absent, indicating that there is a fundamental connection between accretion and outflow processes. While outflows from low-mass objects have typically been the launching template, in recent years we have observed that the launching mechanism extends down to the sub-stellar BD regime (see e.g. Whelan et al., 2009) as well as to the range of massive YSOs (Marti, Rodriguez, and Reipurth, 1993; McLeod et al., 2018). Relativistic jets from

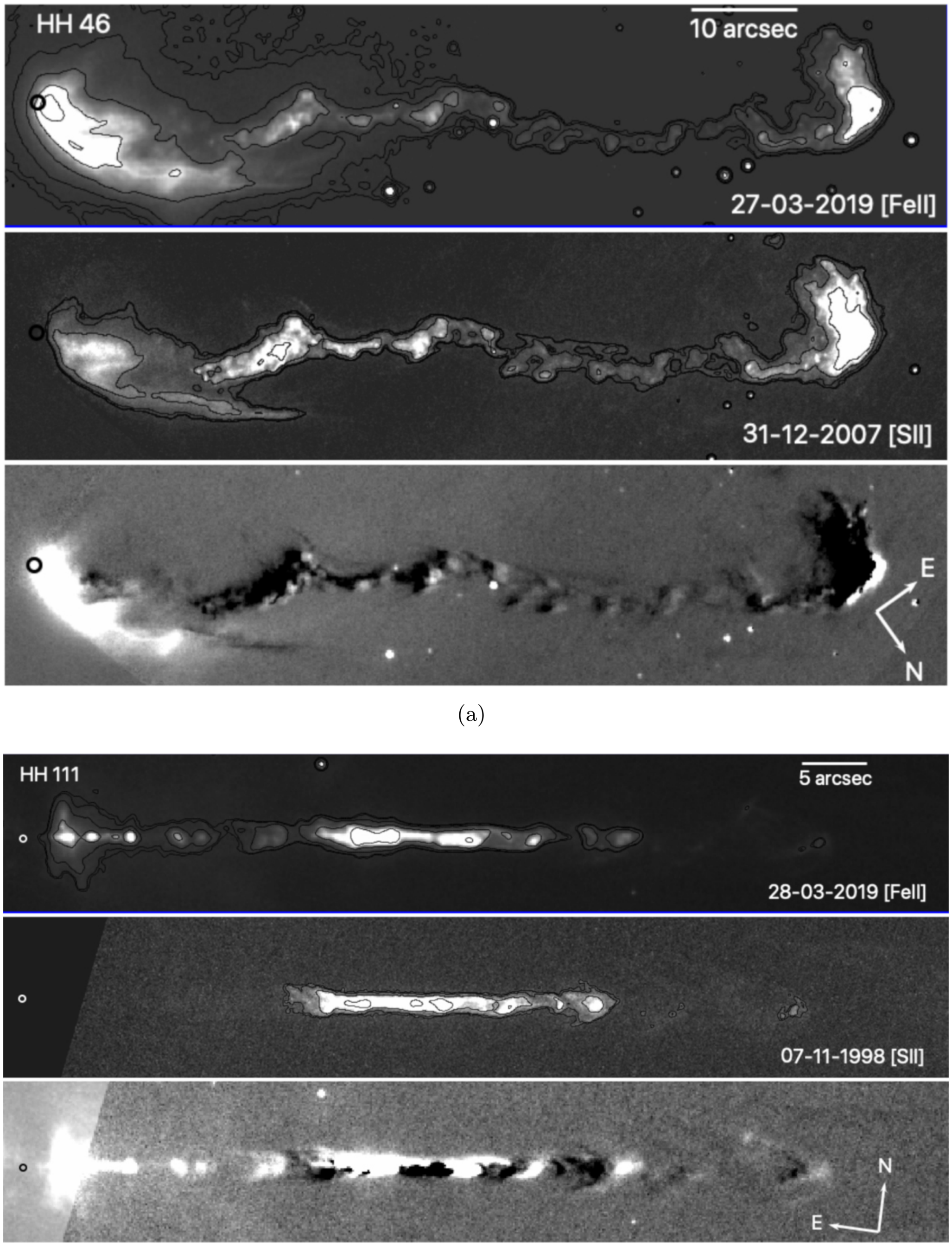

(a)

(b)

FIGURE 1.9: HST WFC3 images of the (a) HH 46 and (b) HH 111 outflows. The top panel in each figure shows the IR [Fe II]$\lambda(1.25+1.64)$ μm emission, and the middle panels show the optical [S II]$\lambda\lambda$6716,6731 doublet, with baselines of 11 yr (a) and 21 yr (b) to display the morphological changes over time. The bottom panels show the [Fe II]−[S II] difference images. In each panel, a black circle denotes the driving source. Of note in HH 46 is the sinusoidal-like morphology and asymmetry shocks. Images from Erkal et al. (2021b)

black holes and active galactic nuclei appear to be linked with accretion processes as well, suggesting they could be a “scaled-up” version of stellar jets (Blandford, Meier, and Readhead, 2019). These observational facts indicate that there may be a universal mechanism behind jet-launching and that it is intimately linked with accretion.

In a stellar context, the exact mechanism behind the launching of these jets is thus far unknown, but it is generally agreed that a magneto-centrifugal process is at work (Whelan, 2014; Ray and Ferreira, 2021). Within this there are two competing models which seek to explain the phenomenon: the X-Wind model (see Shu et al., 1994a; Shu et al., 2000) and the Disk-Wind or D-Wind Model (see Königl and Pudritz, 2000; Pudritz et al., 2007). Additionally, it is not clear whether these models extend to the extreme low-mass or higher-mass regimes. Nevertheless, both models argue that the magnetic fields which shape the accretion disk of the star play some role in driving the observed outflows via magneto-centrifugally driven winds, and both seek to account for how angular momentum is lost from the system – a critical parameter in the evolution of a YSO.

The X-Wind Model

Shu et al. (1994a) initially put forth the idea that a spinning, magnetized YSO accreting from a circumstellar disk will truncate the disk at some inner radius R_x where the disk co-rotates with the stellar magnetosphere, and argued that the magnetic field lines anchored in the star and disk will begin to “twist” due to rotational differentials (see Section 1.2.1). The accretion funnel formed at this interface carries material from the disk to the star. Beyond this co-rotation radius, some of the $\bar{B}$-field lines become diffuse, resulting in a magnetized “X”-wind that transports angular momentum and a portion of material away from the disk and star, some of which is collimated into a jet. A schematic of this is shown in Figure 1.10, where it is seen that the X-wind launches outwards along the open field lines. In this model, the expected jet ejection radius will then be on the order of $\simeq 0.5$ au (Bjerkeli et al., 2016).

The D-Wind Model

Conversely, the D-wind model (Figure 1.11) holds that a centrifugally-driven wind originating in a magnetized disk lifts material from the surface and ejects it outwards. As this material is accelerated away from the disk, hoop stress in the toroidal component of the magnetic field forces the inertia of the infalling gas to corotate with this outflow. If the field lines exceed some critical angle, it produces a rotational differential (similar to the X-wind model) resulting in a self-collimation of the jet (Königl and Pudritz, 2000). An important consequence of this is that the outflow is not launched from a singular footpoint; rather, it is launched over a range of disk radii ($\sim 0.3 - 4$ au) with a range of velocities (Königl and Pudritz, 2000; Pudritz et al., 2007). Recent works have provided favorable evidence of this model. For example, de Valon et al. (2020) presented ALMA observations of the DG Tau B system and found that not only were the outflows rotating, but that they were “nested”

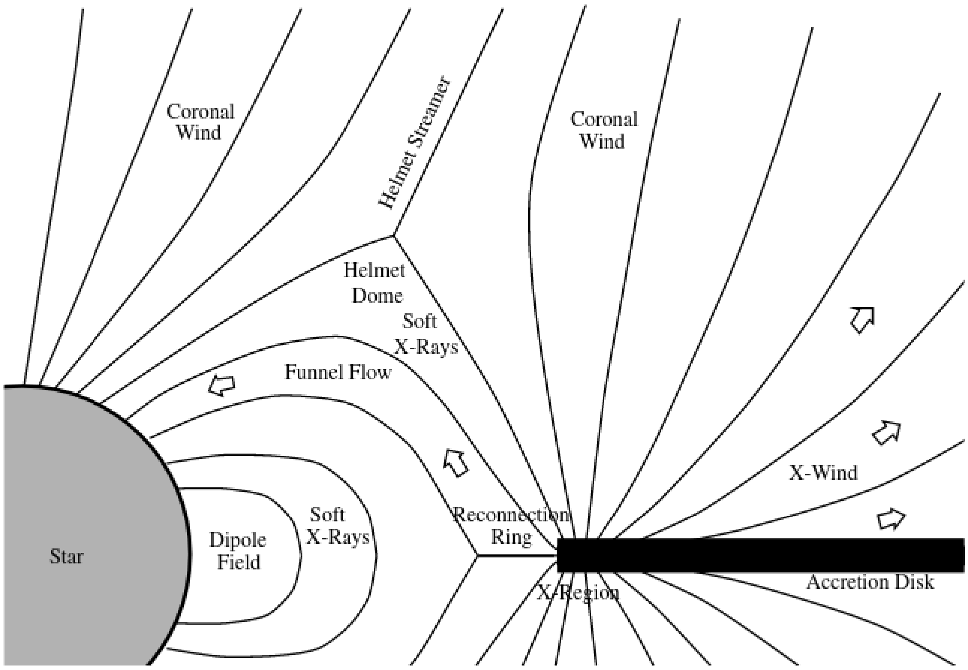

FIGURE 1.10: A diagram demonstrating the X-wind launching model, where the field lines from the star truncate the inner disk at an "X-point" that launches the jet outward. Image from Shu et al. (2000).

as well: a high-velocity, collimated outflow was embedded within a slower, wide-angled molecular component.

Jet Rotation Signature

In a pioneering work utilizing the HST/STIS spectrograph, Bacciotti et al. (2000) placed several slit positions along the outflow axis of DG Tau to determine if there were Doppler gradients across the jet. They found distinct differences between high-velocity components (HVC) and low-velocity components (LVC), particularly at the base of the jet. This demonstrated the first evidence of the existence of nested layers in the jet which increased in velocity towards the jet axis, providing one of the first confirmations of the MHD model of magneto-centrifugally driven outflows. A consequence of this model is that as the jet carries angular momentum away from the disk, the jet should be observed to rotate. Later, Bacciotti et al. (2002) interpreted small velocity shifts across the jet as a signature of of this predicted rotation. A similar technique was applied by Coffey et al. (2004) to other CTTSs, instead placing the slit perpendicular to the base of the jet but offset from the star. In two sources, they found the blue and red jet lobes were rotating in the same direction, providing evidence of the angular momentum transport predicted by MHD and D-wind models (see also Coffey et al., 2007; Coffey et al., 2012). Similar rotation structures were observed by Lee et al. (2022) who argued their observations provided evidence of either an X-wind or inner D-wind, demonstrating the complexity of the outflow mechanism may not lend itself to a single explanatory model, but rather a combination of them.

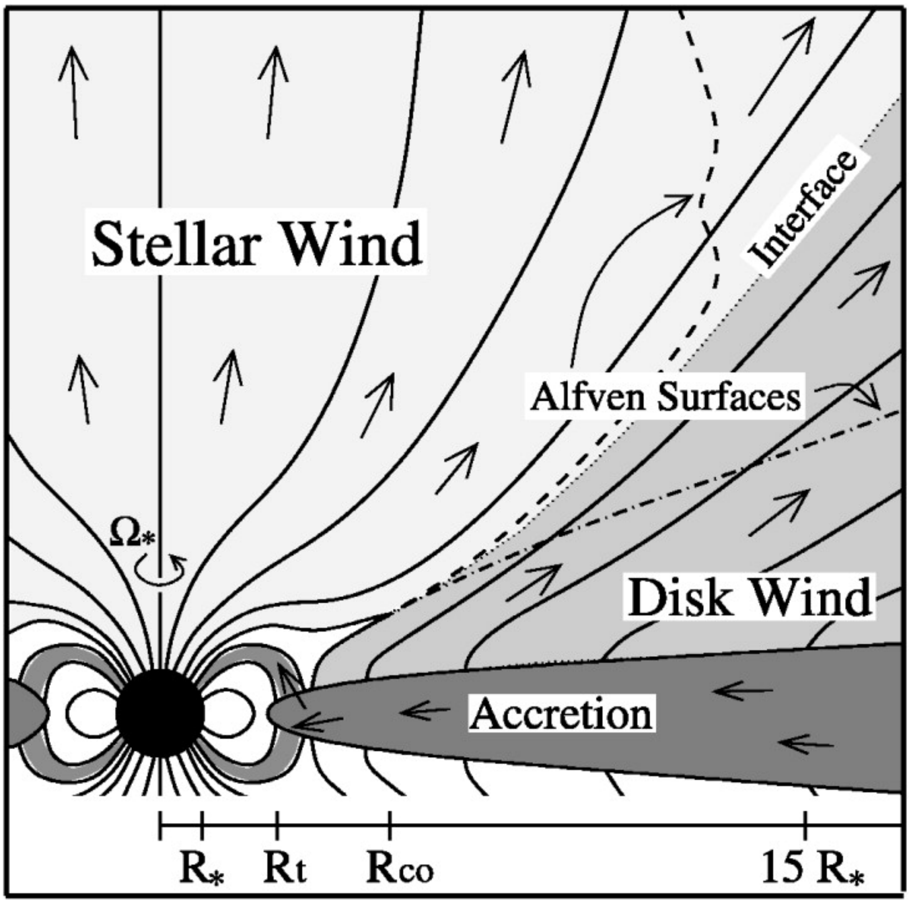

FIGURE 1.11: A diagram demonstrating the D-wind launching model. Similar to the X-wind model, magnetic fields truncate the inner accretion disk which co-rotates with the star, but the outflow is launched over a range of disk radii. Image from Ray and Ferreira, 2021.

1.2.3 Discerning the Engine

The above examples highlight the importance of resolving the innermost regions of the jet to determine the model at work. This launching engine is made all the more difficult to resolve as the small scales involved in the mechanism are not yet reachable with current instrumentation (Frank et al., 2014). As astronomical instrumentation advances, we are able to peer deeper into the region where jets are launched using more precise imaging and spectroscopic techniques. For example, the advent of adaptive optics (AO) on ground based telescopes has allowed for sub-arcsecond spatial resolution, permitting the probing of jets within 10s of au from the source; and emission lines such as Lyα have been used to trace the jets to $\sim$ 7.3 au of the core (Devine et al., 2000). Large baseline interferometers such as ALMA and the VLA have likewise proven powerful tools for resolving molecular flows close to the base with high velocity resolution.

Resolving this inner engine is particularly critical as it allows the robustness of our current understanding to be tested. As discussed in Sections 1.2.1 and 1.1.2, the centrality of magnetic fields in jet models and the relatively weak field strengths observed in HAeBes (noted in Section 1.1.2) raises some difficulties. Curiously, while one might assume that the weak $\vec{B}$-fields in HAeBes would preclude the X-Wind model, recent work by Rodríguez-Kamenetzky et al. (2022) explored the outflow from a deeply embedded $\sim 3\ M_{\odot}$ triple radio source in Serpens using high resolution ($\sim$ 15 au) observations from the VLA and e-MERLIN (operated from Jodrell Bank, UK). They found evidence of collimation as close as 60 au from the source, as well as a $\sim$ 28 au wide cavity consistent with material excited by either wide-angled X-Wind or a tight D-wind, and ultimately interpreted the results as being some combination of the two.

Other useful tools can be applied in untangling the accretion-outflow connection, particularly determinations of the mass-flux (or mass-loss rate) $\dot{M}_{\rm jet}$ and angular momentum-flux $\dot{J}_{\rm jet}$ of the jet. In general, the mass-loss rate of the jet can be expressed as

$$\dot{M}_{\rm jet} = \mu m_{\rm H} \langle N \rangle v_{\rm jet} A \tag{1.6}$$

where μ is the mean molecular weight ($\sim$ 1.4 assuming a gas with cosmic abundances), $\langle N \rangle$ is the geometric mean of pre- and post-shock densities in the jet, $v_{\rm jet}$ is the gas velocity relative to the star, and A is the cross-sectional area of the jet (Hartigan, Morse, and Raymond, 1994; Podio et al., 2006). While the jet velocity and cross-sectional area are easy enough to measure from images and spectroscopy, the density $\langle N \rangle$ is slightly more difficult to constrain. This requires a combination of techniques. Forbidden emission lines (FEL, see Section 1.3) present a powerful diagnostic tool for probing temperature, density, and ionization within jets (T_e, N_e, and $\langle I \rangle$, respectively) and when combined with shock models (Section 1.3.3) they can provide an estimate of the shock compression $\langle C \rangle$ of the gas, such that

$$\langle N \rangle = \sqrt{\frac{\langle C \rangle}{\langle I \rangle}} n_e. \tag{1.7}$$

n_e here is the electronic density, which is found through the ratio of the [S II]$\lambda\lambda$6716, 6731 doublet (Hartigan, Morse, and Raymond, 1994). Close to the star however, this method can be difficult to apply due to the high densities involved, and Hartigan, Edwards, and Ghandour (1995) propose the use of the [O I]λ6300 line instead. In this manner, they compute the mass-loss rate according to the equation $\dot{M} = M v_{\rm tan}/\ell_{\rm tan}$, where $v_{\rm tan}$ and $\ell_{\rm tan}$ are the velocity and aperture width measured in the plane of the sky. Using atomic data from literature (see Hartigan, Edwards, and Ghandour, 1995, Appendix A), the mass-loss can be found by

$$\begin{aligned} \dot{M}_{\rm jet} = 2.27 \times 10^{-10} \left(1 + \frac{n_c}{n_e}\right) \left(\frac{L_{6300}}{10^{-4}\ L_\odot}\right) \\ \times \left(\frac{v_{\rm tan}}{150\ {\rm km\ s^{-1}}}\right) \left(\frac{\ell_{\rm tan}}{2 \times 10^{15}\ {\rm cm}}\right)^{-1} M_\odot\ {\rm yr}^{-1} \end{aligned} \tag{1.8}$$

where L_{6300} is the [O I] luminosity (in units of L$_\odot$) and N_c is the critical density of the [O I] emission.

To determine if jets do indeed remove excess angular momentum from the disk, it is necessary to compare the momentum flux in the jet or wind, $\dot{J}_{\rm out} \simeq \dot{M}_{\rm out} \Omega r_A^2$, to that of the accreting flow, $\dot{J}_{\rm acc} \simeq \Omega r_l^2 \dot{M}_{\rm acc}$. Here, Ω is the angular velocity, r_l the launch radius, and r_A is the Alfvén radius, which is the point where the magnetic field density is roughly equivalent to the kinetic energy (Bacciotti et al., 2002). That is, the total angular momentum which must be removed from the disk is given by the ratio (Frank et al., 2014; Bacciotti and Eislöffel, 1999):

$$\frac{\dot{M}_{\rm out}}{\dot{M}_{\rm acc}} = \frac{1}{2} \left(\frac{r_l}{r_A}\right)^2 \tag{1.9}$$

where the ratio $\lambda \simeq (r_A/r_l)^2$ is considered the magnetic lever arm, and from numerical and theoretical work is estimated to have a value of ~ 3 (see e.g. Bacciotti et al., 2002; Lee et al., 2021).

A review by Pudritz et al. (2007) discusses the consequences of this further, and using studies such as those done of DG Tau (e.g. Bacciotti et al., 2002) suggest momentum extraction upwards of 60%. The importance of this measurement is most clearly seen in the comparison of X- and D-wind models. As the footpoint of launching is fixed in the X-wind model, the momentum removed by the jet will have a fairly uniform value. On the other hand, if the launching points occur across a range of disk radii with a range of values, then we would observe a gradient of momenta across the base of the flow to support a D-wind model.

The ratio $\dot{M}_{\rm jet}/\dot{M}_{\rm acc}$ provides a parameterization of the jet launching efficiency of the source as well. Multiple observational studies have shown that the efficiency of jet launching in CTTSs is on the order of $\sim$ 10% (Hartigan, Morse, and Raymond, 1994; Königl and Pudritz, 2000), and exploring this efficiency in higher or lower-mass stellar regimes can provide clues as to the robustness of the model (Whelan, 2014). In the sub-stellar regime, observations suggest substantially higher efficiencies and in this regard may help explain why e.g. brown dwarfs are unable to accrete enough mass to fuse hydrogen (Whelan et al., 2009; Whelan, 2014).

Recent studies have highlighted the importance of the consideration of MHD winds in angular momentum extraction as well. As discussed in Section 1.2.1 models have traditionally relied upon MHD disk winds and MRI-induced turbulence to explain viscous transport, and while MHD winds were originally favored (see Königl and Pudritz, 2000) the role of MRI soon became the prevailing model. This has been challenged by recent computer modeling, however, with results suggesting that MRI is largely suppressed within ∼30 au by non-ideal MHD processes, ultimately bringing MHD disk winds back to the fore as the principal means of momentum extraction (Whelan et al., 2021).

1.3 Emission Line Analysis

Analysis of spectral emission lines is central to all of astrophysics. A comprehensive treatment of the physics behind atomic transitions for permitted emission lines (PEL) and FELs will not be discussed here (see Hartigan, 2008, for a detailed review). Instead, this section will focus on the importance and applications of emission line analysis in outflow phenomena with respect to FELs, photoionization, and shock physics.

1.3.1 Forbidden Transitions

Examination of FELs is at the heart of emission outflow and accretion studies. Contrary to the name, these are not strictly "forbidden" emissions but rather atomic transitions that have a very low probability of occurring. They are very often seen in low-density environments like those found in jets and plasmas where collisional excitation is most common, as these regions are generally too cool to produce strong PELs due to the inability to populate their upper states (Hartigan, 2008). Some of the most commonly seen FELs in the optical are the doublets in [O I]$\lambda\lambda6300, 6363$ Å, [N II]$\lambda\lambda6548, 6583$ Å, and [S II]$\lambda\lambda$6716,6731 Å; higher-ionization lines such as [O II] and [O III] are also seen in some jets, as well as refractory species like [Fe II] and [Ni II].

Because of the quantum mechanical nature of collisional excitation, some FEL ratios will be temperature-dependent or density-dependent. For example, $2p^3$ and $3p^3$ atomic configurations such as the [S II]$\lambda\lambda$6716,6731 Å and [O II]$\lambda\lambda3726, 3729$ Å doublets have one $^4S_{3/2}$ ground state with slightly different upper levels at $^2D_{5/2}$ and $^2D_{3/2}$. Because these only slightly differ in excitation energies (on the order of a few thousands of an eV), the intensity ratio of these lines will depend only on the density. On the other hand, transitions that arise from the same upper level have a fixed emission ratio governed by the ratio of their spontaneous transition probabilities. Where atomic transitions arise from levels of considerably different energies, the relative populations of the levels will have a strong dependence on the kinetic energy of the colliding particles, and so will be regulated by temperature. Common tracers of this are the [O III] and [N II] ions. Because of the variance in these excitation energies, the excitation rates are strongly dependent on temperature, making them useful for this diagnostic.

For the [S II] ion, the low-density limit ($n_e \to 0$) reduces the relative level populations ratio to the ratio of the statistical weights of the levels, i.e. $j_{\lambda 6716}/j_{\lambda 6731} = N_2/N_1 = g_2/g_1 = 1.5$. In the high-density limit ($n_e \to \infty$) a Boltzmann distribution is observed, such that

$$\begin{aligned} \frac{j_{\lambda 6716}}{j_{\lambda 6731}} &= \frac{N_{^2D_{5/2}} A_{\lambda 6716}}{N_{^2D_{3/2}} A_{\lambda 6731}} \\ &= \frac{6}{4} \times \frac{2.8 \times 10^{-3}}{9.4 \times 10^{-3}} \\ &= 0.45 \end{aligned} \tag{1.10}$$

where N is the level population and A is the transition probability for that line. It is worth noting that

The ratio [N II]λ(6548+6584)/5755 is similarly treated for temperature, and is expressed as a function of collision strengths and transition probabilities for the lines (Osterbrock and Ferland, 2006):

$$\frac{j_{\lambda 6548} + j_{\lambda 6584}}{j_{\lambda 5755}} = \frac{7.53 \exp\left(2.5 \times 10^4/T\right)}{1 + 2.7 \times 10^{-3}\left(N_e/T^{1/2}\right)}. \tag{1.11}$$

Additionally, Bacciotti and Eislöffel (1999) showed that the large charge-exchange cross sections of O and N ions effectively ties their ionization fraction to H, allowing determination of T_e, n_e, and $\langle I \rangle$ (also denoted x_e) from only four emission line fluxes.

It is important to note however that the above analysis assumes *collisional* excitation. In the optical, the ratio [S II]$\lambda(6716 + 6731)$/Hα is a common measure for determining the excitation parameter of the outflow (i.e., high-, intermediate-, or low-excitation), with typical HH objects having fairly large observed [S II]-to-Hα flux ratios. If this value is very low ($\lesssim 0.1$) then this indicates that irradiation of the jet is non-negligible (Reipurth and Bally, 2001b), and so purely collisional treatment will not provide accurate estimations of the physical parameters.

1.3.2 Photoionization & Photoexcitation

For CTTSs and HAeBes the stellar photospheres typically do not emit enough extreme UV (EUV) radiation to photoionize the jets. However, in dense star-forming regions such as the Carina nebula and Orion nebula jets can become irradiated by Lyman continuum photons from the more massive O- and B-type stars present (Bally et al., 1998; Bally and Reipurth, 2001; Mesa-Delgado et al., 2012). Because the observed emission lines of interest occur because of shocks within the jets any quiescent material surrounding the shocked material will be unseen, but if the jet is externally irradiated the unshocked material will be brightly illuminated and ionized.

This can have effects on the mass-loss rate in the jet, as the outflow experiences photoablation from the Lyα radiation. Additionally any neutral core shielded by a high-density jet, which may initially emit in FELs, will eventually become complete ionized and present as an H II spectrum over time. Bally and Reipurth (2001) demonstrated that the density in photoionized flows can be estimated from the Hα emission measure:

$$\mathrm{EM} = \frac{\mathrm{L(Lyc)}}{4\pi a \alpha_B D^2} \tag{1.12}$$

where L(Lyc) is the luminosity of the Lyman continuum at some distance D, $a \simeq 1$, and α_B is the hydrogen recombination coefficient under Case B assumptions (see Hummer and Storey, 1987). From this the density is found simply by $n_e = \sqrt{\mathrm{EM}/\ell}$ cm^{-3}, where ℓ is the width of the emission feature.

Related to this is process is that of photoexcitation and fluorescent pumping, where faint UV presence can enhance emission and produce anomalously bright lines or ratios of lines that diverge from predictions of collisional excitation. Lucy (1995) and Bautista, Peng, and Pradhan (1996) examined this in relation to [Fe II] and [Ni II] emission, and demonstrated that the [Fe II]λ7155/8617 Å and [Ni II]λ7411/7479 Å are particularly well-suited to determining fluorescent contribution (see e.g. Table 2 in Giannini et al., 2015).

1.3.3 A Shocking State

The presence of HH objects prompts the study of shock physics to better understand the total outflow, their visibility is made possible by shock-heated gas in the flow. This occurs as the jet interacts either with itself or the ambient medium around it, forming a so-called "working surface" which traces the collisions in the gas. As launching events can occur periodically, hot, fast gas can catch up with the slower, older gas from prior events and form internal working surfaces, which often present as knotted structures along the outflow (see Figure 1.9). As in the accretion model presented above, the hot ($\geq 10^5$ K) pre-shocked material in the jet approaches a "shock transition" where it is compressed and dissipates some of its kinetic energy into heat. The cooling of this gas occurs downstream to the front in the post-shock region where the extra energy of the free electrons excite upper atomic levels, which subsequently decay radiatively and give rise to the observed emission. Radiation from the post-shock region can radiate back into the pre-shock region as it approaches the shock front, resulting in a "radiative precursor" as seen in Figure 1.12 (Draine and McKee, 1993). The shocks are treated in the context of fluid dynamics, where the gas is modeled as a "bullet" that collides with a stationary material where the shock velocity is taken as the speed in the post-shock region.

Line intensities in each of these regions are affected by ionization, compression, and electron density, which can vary over the range of the emission region. In a seminal paper, Hartigan, Morse, and Raymond (1994) produce various shock models to calculate numerous emission line ratios over a variety of species for a range of shock velocities and pre-shock densities. They additionally include magnetic fields in these models, providing a powerful template for interpreting observed flux ratios in stellar jets. These utilize [S II],

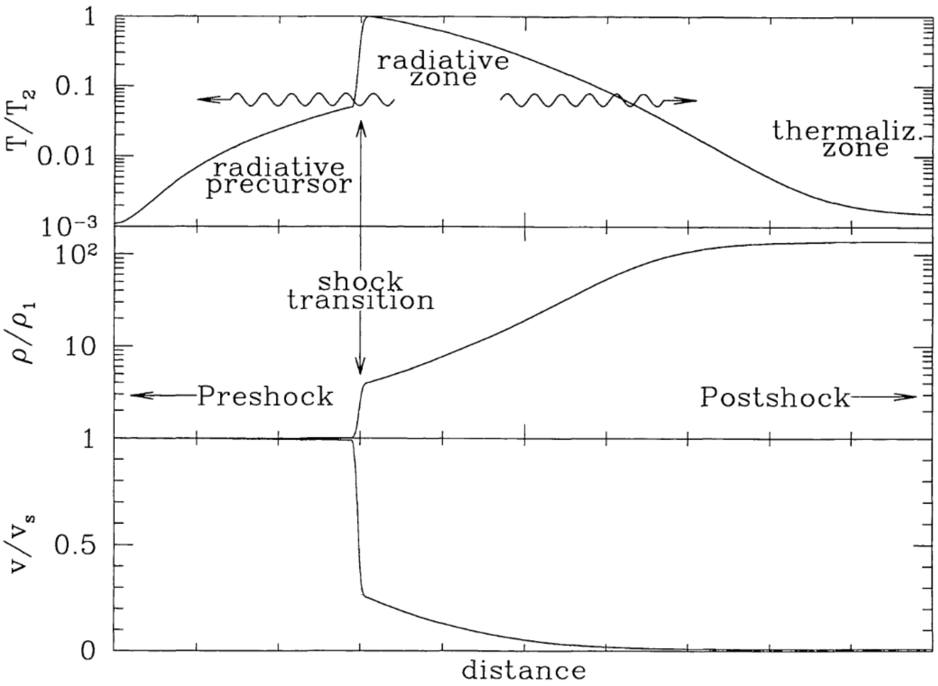

FIGURE 1.12: A diagram of a shock wave of temperature T, density ρ, and velocity v. In the pre-shock region, the gas has density v_1 and temperature T_2. Figure from Draine and McKee (1993).

Hα [N II], and [O I] ions, making them especially applicable to high angular-resolution optical telescopes, which are capable of resolving jets on sub-arcsecond scales.

The cooling regions are easily identified in images by examining key ratios and so-called "difference images". For example, the Hα line is a tracer of shocked material, while [S II] and [O I] trace the cooling region behind the shocks. Subtracting the [S II] + [O I] image from the Hα image can reveal the Mach disk in the shock in resolved images, as well (Hartigan, Holcomb, and Frank, 2019). Differentiating between pre- and post-shock regions is critical to understanding the physical conditions inferred from the emission line ratios, and for making comparisons to shock models in literature.

1.4 Edge-Cases in Jet Launching

The above discussion strives to convey the criticality of jet launching and motivate the focus of this current work on the phenomenon. Not only do outflows function as a sort of "archaeological" site to explore part of the mass-loss history of the star, but its connection to accretion processes and disk winds further suggests a role in regulating the angular momentum of the driving source. These two points alone reveal the importance of jets in the overall evolution of the protostar. Furthermore, the energy injected by outflows and bow shocks into the surrounding medium contribute directly to the turbulence of the natal cloud, potentially impacting the overall star formation rate of the region.

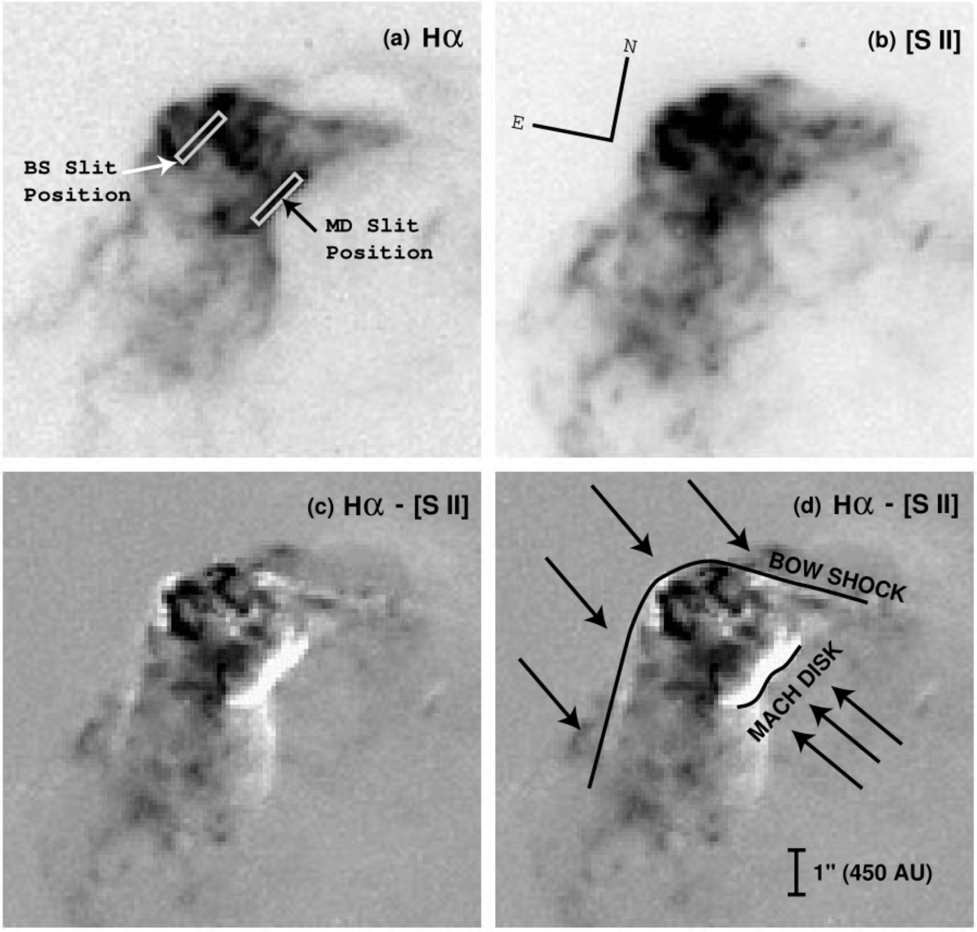

Figure 1.13: The HH object 47A as observed with the HST. Figure from Hartigan et al. (1999).

While this certainly justifies the study of stellar jets in the current work, my gaze is nonetheless cast a bit further afield: CTTSs are the touchstones; but what other tools may we apply to assay the launching mechanism? It is here that we turn our focus to edge case objects, investigating the behavior of jets in less well-constrained scenarios. In Chapter 3, I will examine the Herbig Ae star HD 163296, an intermediate-mass star approaching the end of its accretion phase yet still driving an active jet. Chapter 4 will explore the Orion Proplyd 244-440, an externally irradiated object with a curious jet being launched despite the photoevaporation of system. Finally, in Chapter 5 we will turn to the sub-stellar regime and analyze the irradiated outflow of the lowest-luminosity BD yet observed. Each of these cases is unique and each provides a critical data point in the overall sample of jet-driving sources, allowing us to more closely examine the robustness of current launching models.

Chapter 2

Data Reduction & Analysis

These studies rely almost exclusively on Integral Field Spectrograph (IFS) observations. Due to some significant differences between IFS and traditional imaging and spectroscopy, the development of new data reduction and analysis tools is important. Additionally, the immensity of IFS data presents unique challenges in the data reduction process. In this chapter I will introduce the European Southern Observatory's (ESO) Multi-Unit Spectroscopic Explorer, or MUSE instrument, on board the Very Large Telescope (VLT) in Cerro Paranal, Chile. I will discuss the MUSE data reduction pipeline, as well as some of the tools I have developed to aid in analysis the science cubes the pipeline produces.

2.1 The MUSE Spectrograph

The MUSE instrument is an IFS which allows for a spatial image to be captured as a function of wavelength and recorded into a data cube. The result of this is a 3D file where every spatial pixel has a corresponding spectra over the wavelength range of the instrument, which spans the optical range from $4800 - 9300$ Å (see Figure 2.1.) At the lower wavelength range, it has a resolving power $R \sim 1770$, which increases to $R \sim 3590$ at its upper spectral limit, corresponding to a velocity resolution of $90 - 170$ km s^{-1}. It operates in two modes: narrow-field mode (NFM), with a spatial extent of $7\overset{\prime\prime}{.}5 \times 7\overset{\prime\prime}{.}5$ at $0\overset{\prime\prime}{.}025$ pixel^{-1}; and wide-field mode (WFM), with a spatial extent of $60'' \times 60''$ at $0\overset{\prime\prime}{.}2$ pixel^{-1}. MUSE also boasts an adaptive optics instrument (AO) which, at the time of the first observations (see Chapter 3), was offered only in NFM, but is now available in both WFM and NFM operations.

This instrument was chosen due to its high resolution spatial sampling and large spectral range. It is important to note that the spatial sampling in AO-assisted mode results in an effective resolution (given in terms of the FWHM of the PSF) of approximately a factor of two greater than the sampling. In WFM this corresponds to a resolution of $\sim 0\overset{\prime\prime}{.}4$, and $\sim 0\overset{\prime\prime}{.}05$ in NFM. Without AO the resolution is dominated by the atmospheric seeing. Some jets may extend out to parsec-scales from the source resulting in a large angular size in the plane of the sky, so an extended field of view (FOV) is preferable for their studies (Riaz et al., 2017). Furthermore, the jet launching region is within a few au of the star, requiring resolution on the sub-arcsecond scale and thus demanding high spatial resolution (Frank et al., 2014). The large wavelength range of MUSE also makes it a powerful instrument,

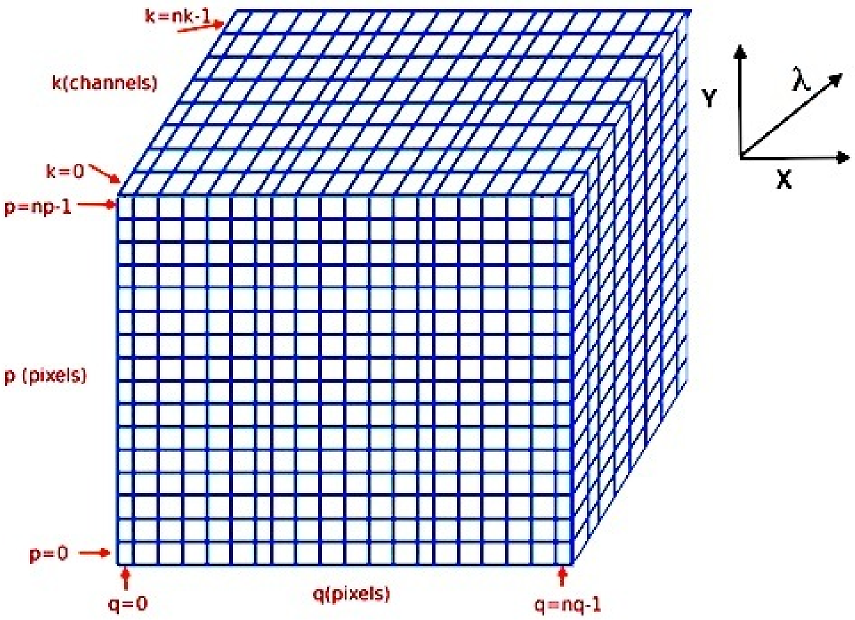

Figure 2.1: A visualization of the Python convention for handling the indices of a data cube. Image from the `mpdaf` online documentation.

as high resolution spatial images of jets can be produced in many key diagnostic emission lines, allowing for simultaneous examination of spatial and spectral structures in the outflows. As such it is well-suited to studying jets on a large scale in WFM, as well as probing the inner regions of launching with NFM.

Light entering the instrument passes through several systems before being recorded into a dataset. A series of lamps, motors, and mirrors vary illumination fields and act as a calibration unit before passing the light to the fore-optics subsystem, which simply reshapes the image to pass to the splitting and relay optics system. This system slices the MUSE FOV into 24 sub-fields. This is accomplished by a set of 24 mirrors placed at various angles which act to separate and split the field into horizontal beams of light, passing the signals onto a set of relay optics to correct for optical path discrepancies. Finally, each beam is fed to an integral field unit (IFU) on the instrument for the next stage of processing. IFUs on the instrument are composed of a slicer, spectrograph, and detector. For each incoming 2D FOV sub-field, the slicer splits the signal into a 1D "slit" with a $0\farcs2$ width. The image is continually sliced into 48 of these slits, and then rearranged into a single slit to pass to the spectrograph. The slicer also handles masks to reduce scattering and ghost images. A diagram showing the splitting and slicing of the incident field is shown in Figure 2.2.

The spectrograph is more familiar, being composed of a collimator, a grating, and a CCD (charge couple device) camera. As each channel is fed to a spectrograph, there are necessarily 24 identical spectrographs on the instrument. The light from each spectrograph is passed to a 4k × 4k 15 μm pixel CCD which operates at 163 K. The detector is further divided into four quadrants of 2048×2056 pixels which are separated by pre- and over-scan regions. Each pixel is a light-sensitive cell that exploits the photoelectric effect to produce free electrons from incident photons. The pixel cells are contained within non-conductive

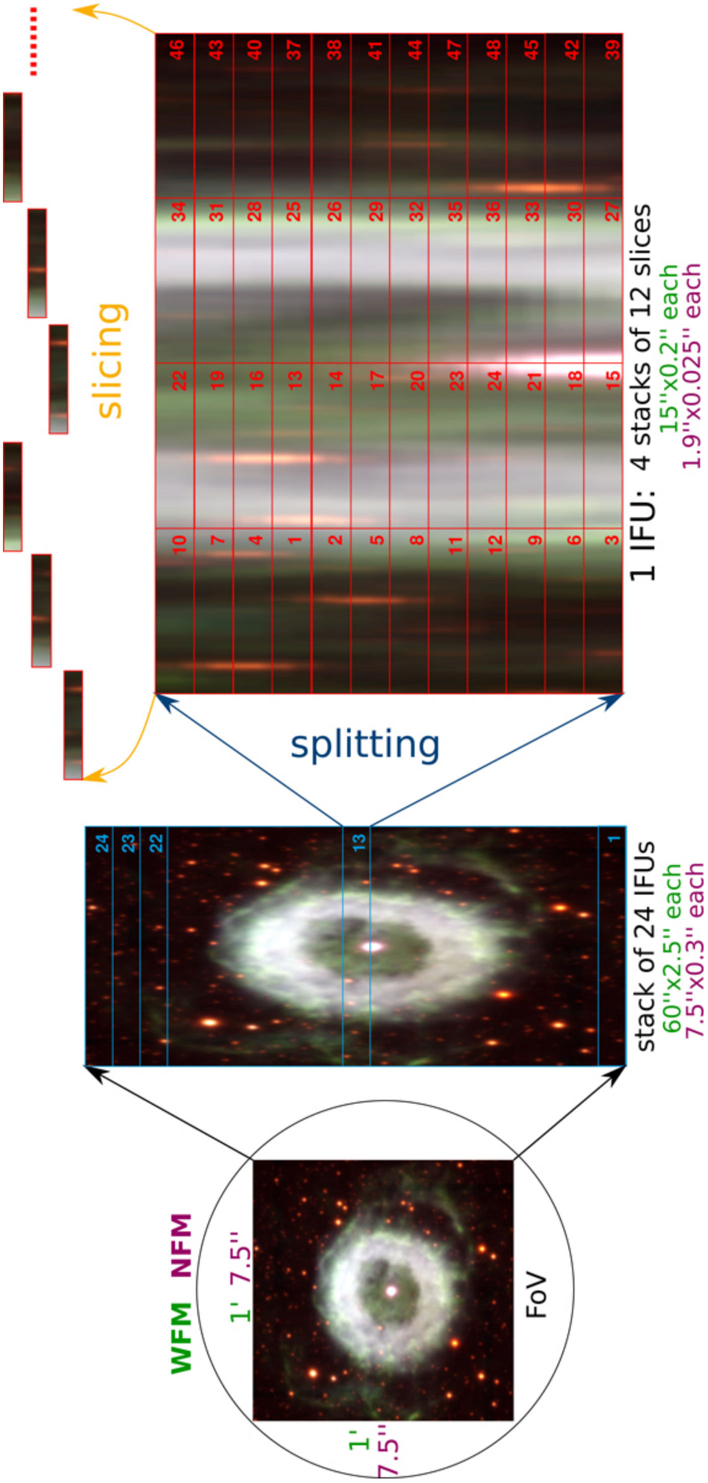

Figure 2.2: Splitting and slicing of the MUSE FOV. The image is split into a stack of IFUs, each of which is stacked into slices. Image from Weilbacher et al. (2020).

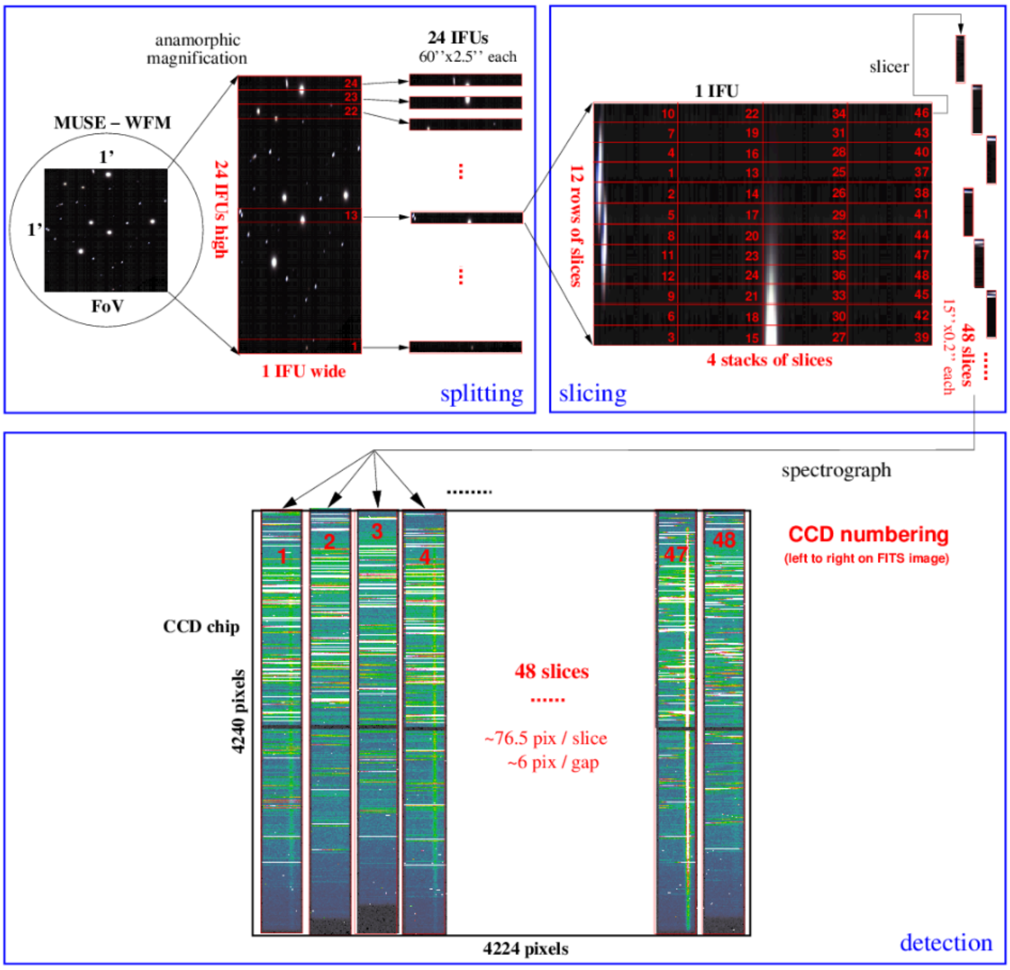

FIGURE 2.3: A schematic similar to Figure 2.2, but demonstrating how each IFU slice is mapped to the CCD chip. Image from the MUSE User Manual, published by ESO and available at: https://www.eso.org/sci/software/pipelines/muse/.

boundaries to ensure the electrons remain where the photon has struck. As light continues to impinge upon the cell, electrons accumulate to produce an image on the CCD (see Figures 2.4 and 2.3).

2.2 Data Reduction Pipeline

A series of calibration files are produced for each observation to allow for correction of the output image. These include pixel tables, bias frames, dark frames, flat-field frames, wavelength calibration tables, and astrometric corrections, all of which are processed by the MUSE data reduction pipeline (DRP). The basic schematic for the reduction pipeline is shown in Figure 2.5. Below I will discuss some of the basic “recipes” or scripts in the DRP (see Weilbacher et al., 2020, for a rigorous presentation of the entire pipeline process). If the user operates from the command line it is possible to run each recipe for each IFU individually, or write a simple script to automate the procedure for all IFUs. In most cases it is simpler to use the Graphical User Interface (GUI) provided with the pipeline and

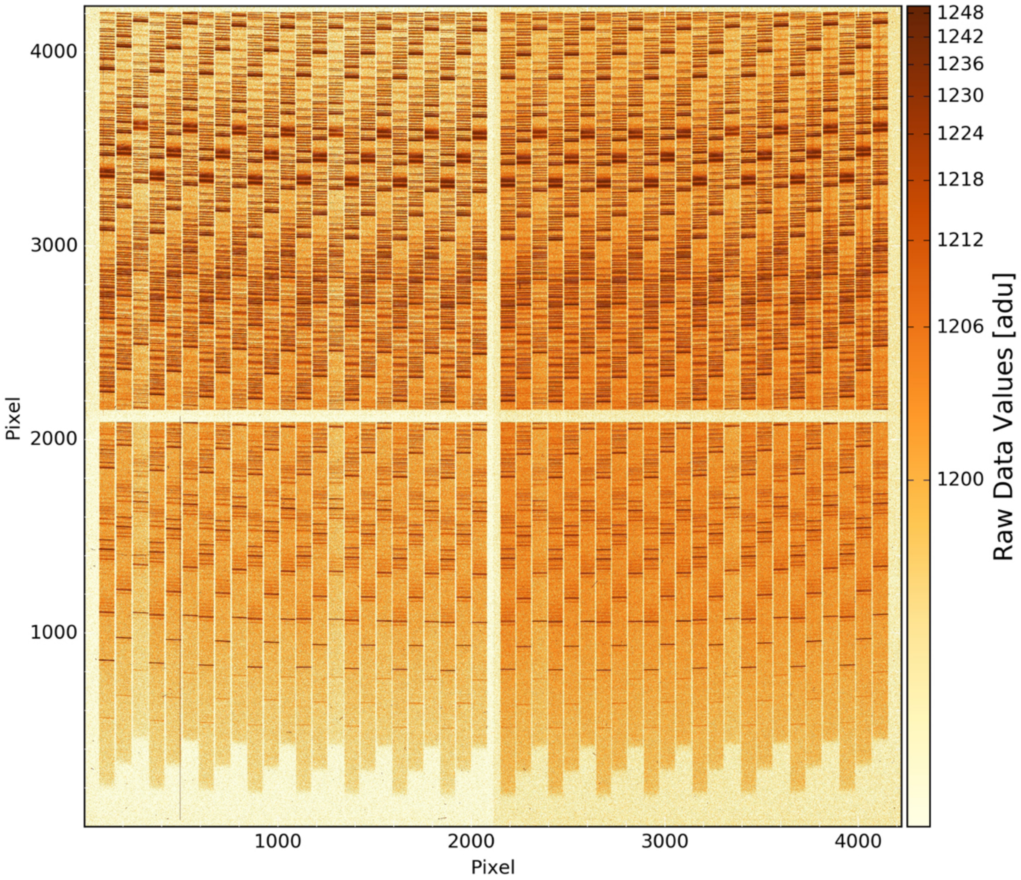

Figure 2.4: Raw CCD data from a MUSE IFU. The slices of the IFU are shown as strips, with blue and red ends of the MUSE wavelength range shown at the bottom and top, respectively. Image from Weilbacher et al. (2020).

automate the procedure by that method. For the data used in this thesis, the GUI was utilized with primarily default recipe parameters. Exceptions to this will be discussed in later chapters where applicable.

2.2.1 Calibration Files & Recipes

The MUSE DRP consists of two phases: pre-processing and post-processing. Each of these utilizes recipes which are scripts that define the parameters used by the algorithms of the pipeline to perform operations on the raw science exposures and the corresponding calibration files in order to produce the final science cubes. While it is possible to provide specifications for custom calibration files in observing proposals, it is easiest to use the standard files provided by the pipeline. Generally 11 bias frames are produced daily, five 30-minute dark frames are produced each month, and flat field illumination frames are taken at least once per hour. Bias frames are mandatory in the pipeline, but darks and flats are optional. Each step in the reduction process is repeated for each CCD and outputs reduced pixel tables. These reduced pixel tables are corrected using on-sky calibrations and used to construct the final data cube.

Pre-Processing

Initially, the raw science data is processed to produce an intermediate pixel table to send to the post-processing algorithm, which is most simply done with the `muse_scibasic` recipe. Bias frames – or zero-time, non-illuminated exposures – allow the pipeline to compute read-out noise for each CCD and isolate any CCD defects using statistical algorithms. In conjunction with overscan regions, these bias frames can be corrected for any gradients across the images. The CCD gain is converted to units of electrons in this step. Optionally, dark frames can be specified, which are non-illuminated exposures with integration times comparable to the science exposure times, to characterize thermal effects or "dark current" in the CCDs.[1] Master bias, dark, and flat-field images are produced by the `muse_bias`, `muse_dark`, and `muse_flat` recipes, respectively. If the dark field parameter is specified, the master dark is subtracted from the master bias. The master bias is then subtracted from the science image, and the residual image is finally divided by the master flat.

In the next pre-processing step, the pipeline generates a trace table, wavelength calibration file, and geometry table. This latter table is typically provided with the MUSE pipeline, and does not need to be produced by the user. These allow each CCD pixel to be assigned spatial and spectral coordinates, and this produces a pixel table for each exposure. The trace table determines the edges of the 48 slices for each IFU by examining how much of the CCD is illuminated by light from the slices. This step is part of the `muse_flat` routine, and only executed if the `trace` parameter is toggled to `true`.

The wavelength calibration routine is called by `muse_wavecal` and uses the three arc lamps onboard MUSE (HgCd, Ne, and Xe) to compute the wavelength solution for the

---

[1] Generally, the cooling system in the spectrograph makes dark frames unnecessary as it minimizes these thermal effects.

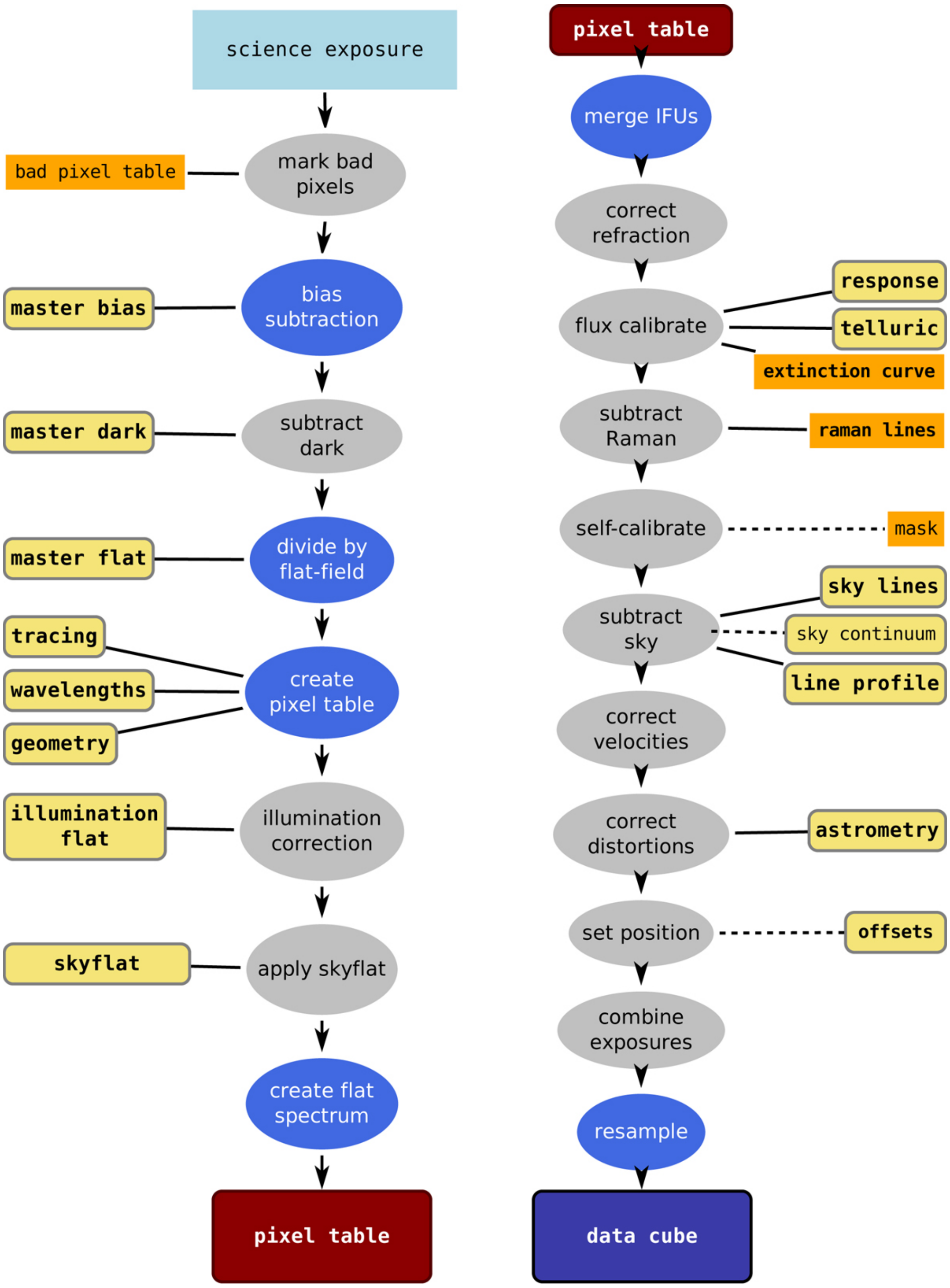

FIGURE 2.5: A diagram of the MUSE pipeline processing steps. The left shows the pre-processing phase, and the right shows the post-processing phase. Optional steps are gray, mandatory steps are blue. Yellow and orange boxes indicate calibrations and manually-constructed inputs, respectively. Image from Weilbacher et al. (2020).

cube. These lamps cover most of the spectral range of MUSE, and five exposures for each lamp is sufficient to ensure a strong S/N for the faintest lines. Each image is bias subtracted, but instead of combining the exposures they are organized by lamp to minimize emission line blending and aid in identification. Emission lines are identified with Gaussian fitting and comparison to an arc line reference list, and a 2D polynomial is fit to all the measured line centers to produce the wavelength solution. A table is produced containing the polynomial coefficients. Sky emission lines are then used to correct the wavelength zero-point, an important step if night-time observations use day-time calibration files.

Related to the wavelength calibration is the computation of the line-spread function (LSF; the spectral response of the instrument to the point-spread function [PSF]), called with the `muse_lsf` recipe. The LSF allows the pipeline to perform a reliable sky subtraction and correct for the Raman lines induced by the laser guidance system (LGS). This uses the same inputs as `muse_wavecal` and additionally requires the derived wavelength solution. The arc exposure images are used to produce a table populated only by data around the brightest lines in the list, where the arc lines are along the $x-$axis and the central wavelengths of the arc lines are along the $y-$axis. 2D polynomials are fit at each step along the LSF direction, and these polynomials are evaluated to produce a 2D image for each slice of the IFU, resulting in an LSF data cube.

Post-Processing

The pixel tables produced by the pre-processing routines are then passed to post-processing to produce the final data cube. If sky twilight exposures are present, they are used to compute the relative efficiency of each IFU, and the tables are combined into a common pixel table for each exposure. Atmospheric correction is also applied to account for Raman scattering due to the LGS, as well as extinction in the upper atmosphere. These Raman lines can be handled with a self-calibration routine for each slice, which simply ensures the background across the FOV is uniform. The common pixel table is used for all of the routines and finally combined over all exposures and resampled into the science data cube.

Flux-calibration and sky-line handling are an important and non-trivial part of the reduction process, and the sky modeling method can change depending on whether the field is sparse or filled. A standard star is used to compute both the response curve of the instrument and the model template for telluric corrections. Telluric emission lines are identified using a list of thousands of lines originating from OH molecules, O_2 molecules, [O I] lines, Balmer lines, and other known double groups. This produces a sky spectrum and an LSF for that spectrum which can be used to model its contribution to the flux in each IFU. The response curve, telluric model, and extinction model are all used to correct the calibrate the flux at each pixel in units of 10^{-20} erg cm^{-2} s^{-1} Å^{-1}. Additionally, a sky cube can be subtracted using the exposures themselves or sky off-set fields with short exposures, with the latter being most applicable to filled field cases. Regardless of the case, the user specifies to the pipeline which regions are sky-dominated so the pipeline can construct the model. These steps are all accomplished using the `muse_scipost` routine.

Radial velocity corrections and spatial coordinate corrections are the final step before the exposures are resampled into the final output data cube. Velocity corrections are by default applied with respect to the solar system barycenter, using the longitude and latitude of the telescope to compute the correction factor. Spatial coordinates are calibrated first by projection of the pixel table coordinates into a spherical system, and then projecting these into celestial coordinates using the field center in the exposures. Coordinate offsets can be supplied by the user in order to fine-tune this calibration, or they can be calculated by the pipeline using object detections in the exposures.

In the final step, the `muse_scipost` recipe is called to combine the pixel tables using any weighting scheme that might be specified, and the exposures are resampled into a data cube using a drizzling algorithm. This propagates the variance from the raw data as well, allowing for the highest data quality. The pipeline by default will reduce each science exposure to its own data cube. If multiple exposures are provided, such as in the case of a mosaic, these must all first be aligned to common coordinates using `muse_exp_align`. The user has the option to save these to individual cubes, or combine them with the `muse_exp_combine` recipe to produce a cube spanning the entire spatial range of all of the exposures.

2.3 Science Product Analysis Tools

Once the final reduced cubes are produced, other processing is necessary to ensure accurate analysis of the data. In this section, I discuss some of the further corrections applied to the data, as well as the analysis tools used throughout the body of this work. All of these methods are accomplished with Python, using a combination of standard libraries, custom libraries, and specialized community-developed astronomical libraries. The development of these routines constituted a significant portion of my early research work and provided a groundwork for the analysis in this thesis.

2.3.1 Background & Continuum Subtraction

Before reducing the processed science cubes into position-velocity diagrams (PVD) or spectro-images, it is necessary to perform background subtraction. This subtraction is intended to remove both general background contributions and source/continuum emission. It is important to remove these as the signals from jet emissions may become "buried" in certain emission lines, particularly Hα and [O I]. A few methods were explored in reducing data in this manner, which are outlined below. As there is no single method for data reduction, knowledge of each of the techniques combined with empirical testing was necessary to obtain the most satisfactory results. In this section I discuss the methods utilized in the Python scripts for the data reduction process.

Baseline Method

The first method is a simple baseline subtraction. This removes the baseline from a spectrum, correcting for contributions from overall continuum emission, and is best suited to embedded and unresolved sources. For each spatial pixel in the cube, a spectrum is extracted and a sigma clip is applied to suppress large fluctuations in the data. This spectral baseline is not assumed to be linear, and so a polynomial function is used. A baseline is fit to this sigma-clipped spectrum and simply subtracted from the raw spectrum, and the difference and background curves are stored in new cubes. Because of the large size of the data cubes, it is computationally less expensive to select an emission line of interest, for example [O I], [S II], or [N II], and extract a sub-cube centered on this emission line prior to performing the baseline subtraction. An example of this method is shown in Figure 2.8.

The baseline fit is performed using a Vandermonde method (Bretscher, 1997). Since it is assumed that the baseline may be modeled by a polynomial with the coefficients α_0, α_1, …, α_n, one defines

$$P_n(x) = \alpha_0 + \alpha_1 x + \alpha_2 x^2 + \cdots + \alpha_n x^n \tag{2.1}$$

If this polynomial interpolates some number of points, a system of linear equations may be constructed and solved. For many points it is easiest to construct an nxm matrix of the form:

$$\underbrace{\begin{bmatrix} 1 & x_0 & x_0^2 & \dots & x_0^n \\ 1 & x_1 & x_1^2 & \dots & x_1^n \\ 1 & x_2 & x_2^2 & \dots & x_2^n \\ \vdots & \vdots & \vdots & \ddots & \vdots \\ 1 & x_m & x_m^2 & \dots & x_m^n \end{bmatrix}}_{\text{V}} \underbrace{\begin{bmatrix} \alpha_0 \\ \alpha_1 \\ \alpha_2 \\ \vdots \\ \alpha_n \end{bmatrix}}_{\vec{a}} = \underbrace{\begin{bmatrix} y_0 \\ y_1 \\ y_2 \\ \vdots \\ y_n \end{bmatrix}}_{\vec{b}} \tag{2.2}$$

The solution to the matrix is easily found using singular-value decomposition and pseudoinverse matrices. In Python, this is achieved with routines from the `numpy.linalg` package.

In practice, a Vandermonde matrix is constructed from the normalized, sigma-clipped spectrum. The coefficients are calculated by minimizing the difference between the new and initial estimations to within a specified tolerance, and the dot product of the matrix and coefficients yields the baseline fit. A "noise test" routine examines the reliability of the subtraction by plotting the standard deviations of the pixels in the subtracted cube against the mean values in the continuum cube, as shown in Figure 2.7.

Scaled Reference Method

The second method is more useful for strong emission lines, particularly Hα. In this method, an iteration over the spatial pixels in the cube is done, but here some reference spectrum is selected and modified by a scaling factor. This reference spectrum is chosen

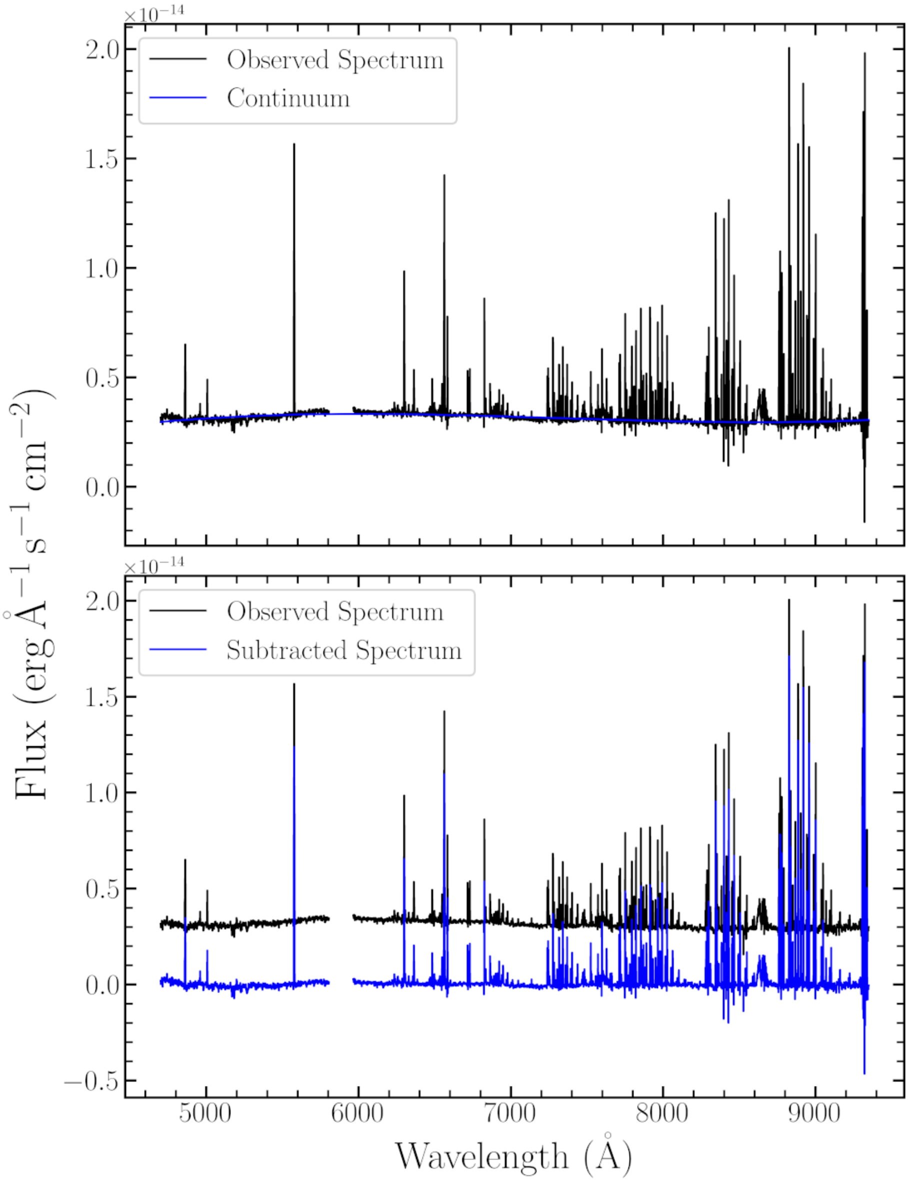

FIGURE 2.6: An example of the baseline subtraction method applied to the ESO-HA 1674 dataset. A spectrum is extracted at some (x, y) pixel coordinate, a polynomial is fit to the baseline of the spectrum, and the baseline is subtracted from the spectrum and stored in a new cube.

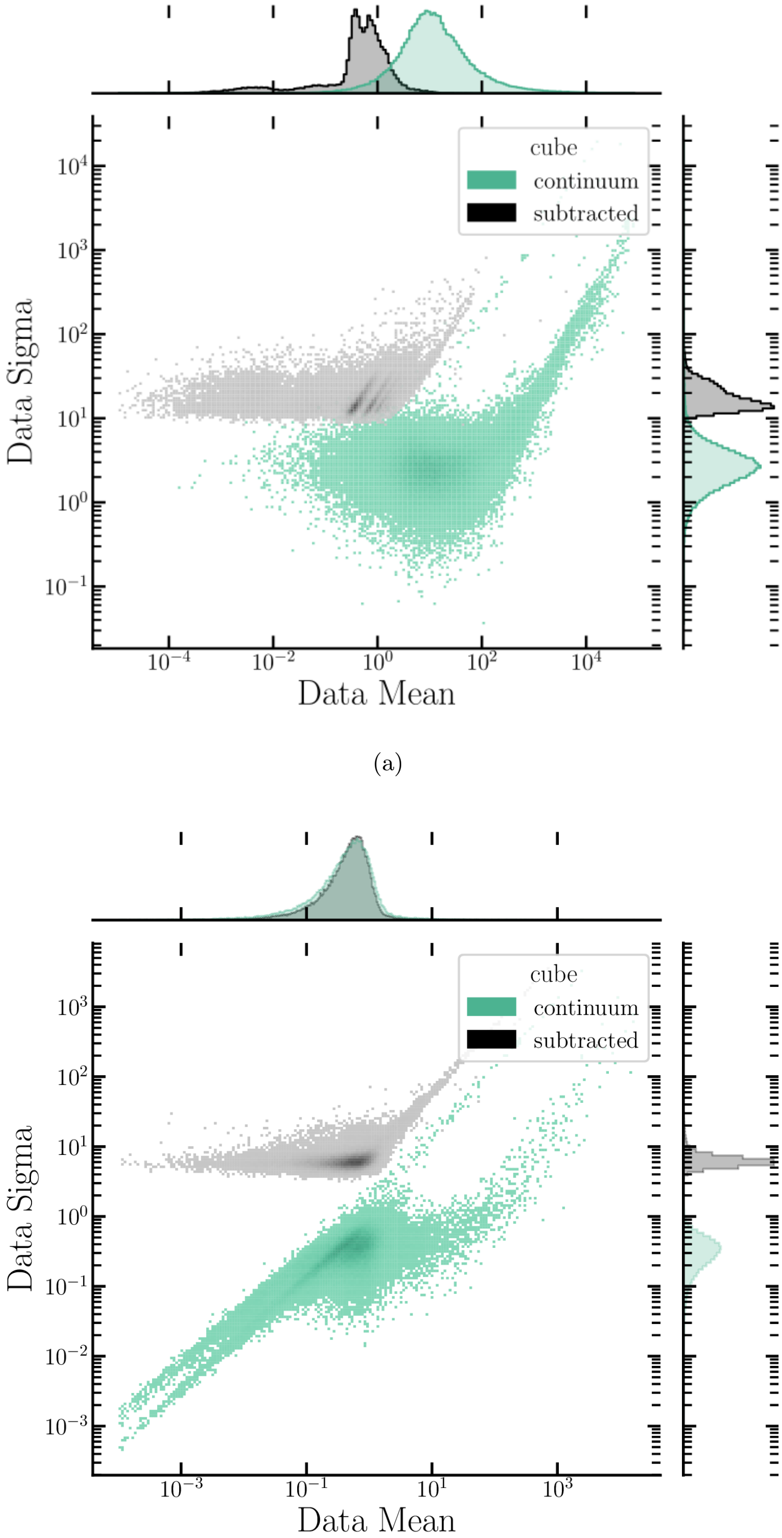

(a)

(b)

FIGURE 2.7: An example of the noise test of a cube subtractions centered on the [S II]λ6716 lines for the a) HD 163296 and b) ESO-HA 1674 data sets. The graphs show the 1σ standard deviation versus the data mean for the continuum cubes (green) and background subtracted cubes (black).

such that it best represents pure stellar emission in a region unaffected by the outflows. As before, for each spatial pixel a spectrum is extracted and a background fit is performed. This fit is converted to a scaling factor by dividing by the reference background, and then multiplying by the reference spectrum. This new scaled spectrum is subtracted from the pixel spectrum and assigned to a new cube. An example of this method is shown in Figure 2.8.

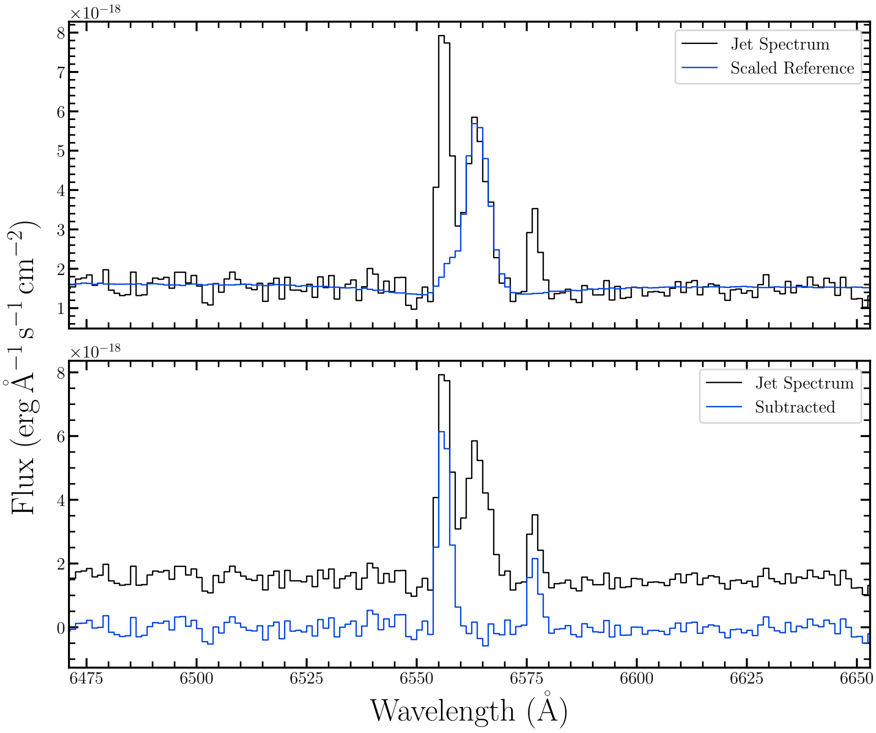

FIGURE 2.8: An example of the scaled reference subtraction method applied to the HD 163296 dataset. A reference spectrum is chosen close to the source and scaled to the spectrum at a point in the blue-shifted jet. When the scaled spectrum is subtracted from the raw jet spectrum, the stellar contribution is minimized and the jet emission is clearly visible.

It is important to note that the FWHM of the PSF in all MUSE cubes is known to vary such that the total signal in any given pixel is wavelength-dependent. If caution is not taken, the subtracted spectrum can be biased such that it presents more red or blue than the true spectrum. To mitigate this issue, it is necessary to perform this scaled subtraction very locally. An optimal locality was found by examining the PSF in regions red- or blue-shifted from a target emission line. This was best accomplished in the HD 163296 cubes due to the large number of background stars visible in the FOV. The positions of approximately 20 field stars were measured, and subcubes were extracted and truncated to a $7'' \times 7''$ FOV centered on the stars. For each field star subcube, a 2D Moffat profile was fit at each wavelength step and the FWHM extracted in the x$-$ and y$-$directions. A distribution of these values is shown in Figure 2.9. As a secondary check, a spectro-image was extracted over a 20 Å bin to either side of the Hα line with the lower limit of the blue emission and the upper limit of the red emission spanning a line width of 100 Å (see

Figure 2.10). By these two examinations it was found that for small line widths (∼ 100 Å) the FWHM varies by approximately 1%, indicating a small variance over this wavelength range. Thus this method is strictly limited to 100 Å-wide subcubes to minimize biasing the spectrum.

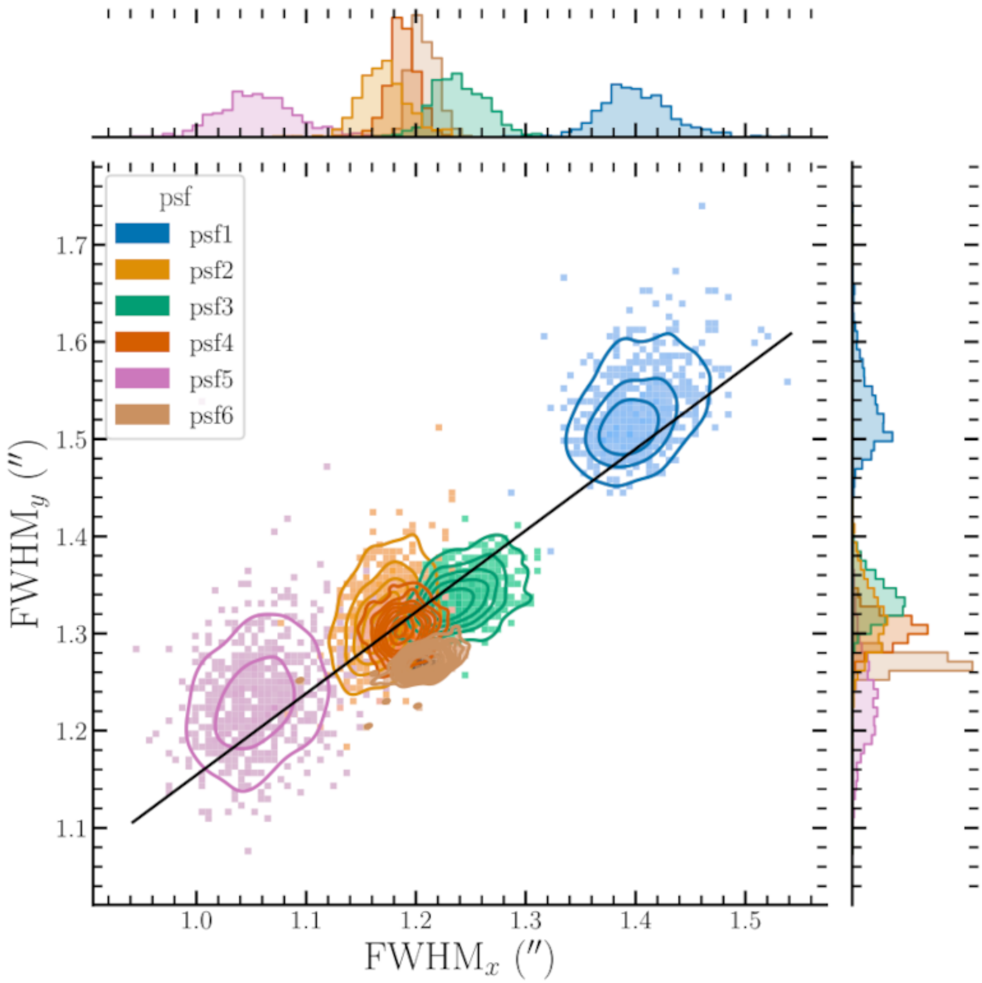

FIGURE 2.9: A scatter-distribution of the PSF FWHM along each axis, extracted from field stars in the HD 163296 cube. Each $x, y-$pair is extracted from a wavelength slice from the cube, spanning a $6000 - 6800$ Å range. The kernel densities (contoured lines) show that for each PSF, the ratio of FWHM values is nearly unity.

The greatest difficulty with this method is the proper selection of the reference spectrum, and even with a potentially suitable reference the removal of stellar contamination is not trivial. This is particularly true in datasets with over-saturation centered on the source, or data where the source is occluded by the circumstellar disk or nebular emission. In the latter case, this method is not applicable and a baseline subtraction must be performed. Nebular emission in the proplyd data presented unique difficulties, which I discuss in the next section.

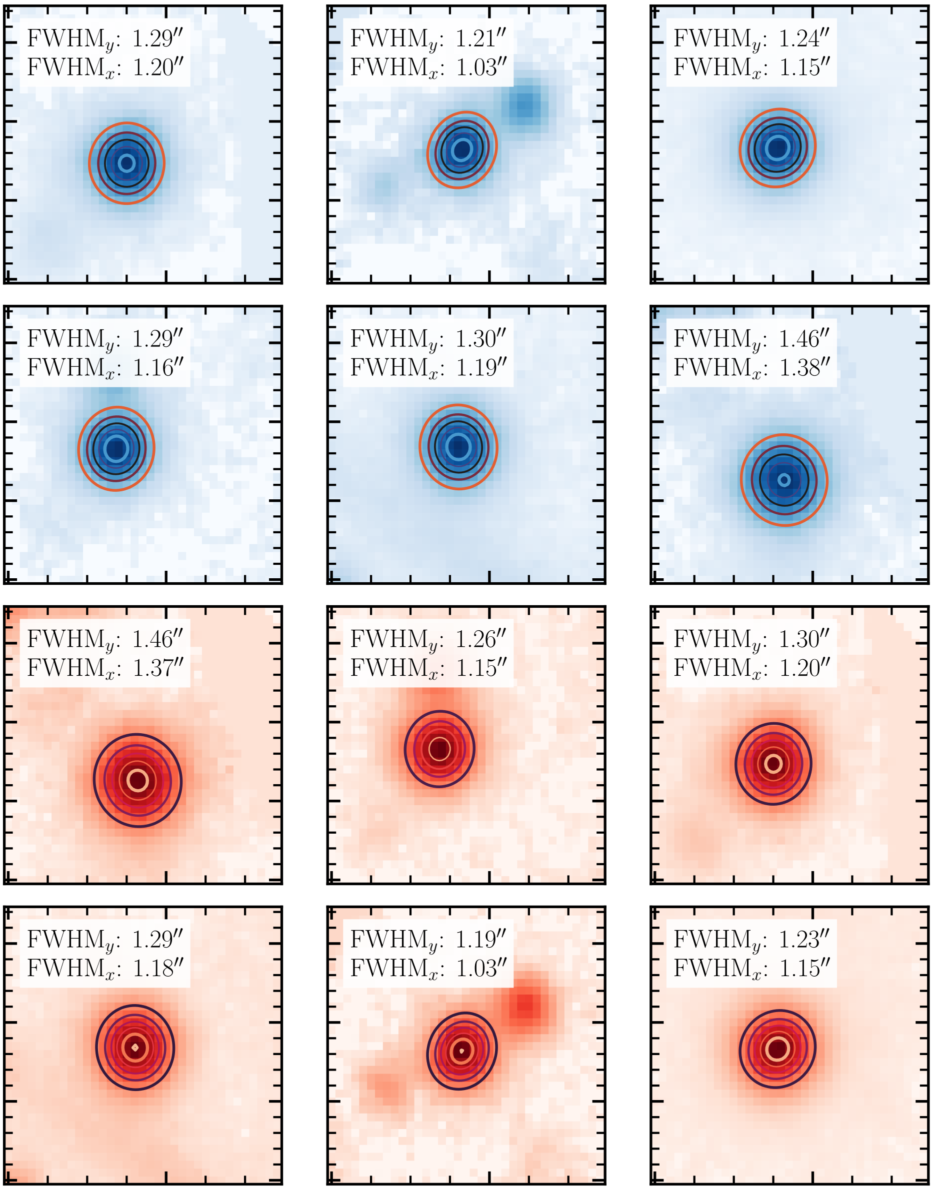

FIGURE 2.10: A sample of source stars used to estimate the PSF in the HD 163296 cube. Blue continuum images are shown in blue, and red continuum images are shown in red, and are taken with respect to the Hα line. Each image is integrated over a 20 Å bin. With these fits, a ratio is seen $\mathrm{FWHM}_y/\mathrm{FWHM}_x = 1.09 \pm 0.03$, demonstrating that the scaled subtraction routine is suitable for very local (~ 100 Å) windows.

Nebular Subtraction

As stated above, the proplyds presented unique, non-trivial problems in the data reduction process. Particularly, the velocity resolution of the MUSE spectrograph is not fine enough to distinguish between nebular and jet velocities, so the line shapes have similar widths. In order to carry out proper diagnostics of the jets it is important to minimize the nebular contribution to the fluxes measured in the jets, most especially in the [O I], [S II], and [N II] lines where the nebular emissions are the strongest. To address this issue, three methods were explored.

The first method examined the spectro-images. As the [Fe II] lines trace the pure jet, an aggregate image of various [Fe II] emissions was created to estimate the spatial extent of the jet. This image was used to create a pixel mask which was applied to images with prominent nebular emissions, and a Gaussian kernel was used to interpolate over the masked pixels. The interpolated image was subtracted from the raw image, resulting in a new image where only the jet is visible. A limitation of this method is that the nebular emission is neither uniform nor well-modeled, and the larger the pixel mask the less accurate the interpolation over the masked regions will be. Additionally, different lines may have different emission regions, and interpolation can thus result in the loss of data. This method was ultimately eschewed in later analysis as being too uncertain.

The second method is applied to PVDs, which is significantly more simple than the spectro-image method due to the reduced dimensionality of the data (i.e., examining 1D lines instead of a 2D image). This method treats the complicated structure of the spatial profile as a series of piece-wise polynomials which can be approximately represented by spline curves. Control points t_i are selected around the profile which are used to generate a set of basis functions such that

$$\begin{aligned} B_{i,0}(t) &= \begin{cases} 1, & \text{if } t_i \leq t < t_{i+1} \\ 0, & \text{otherwise,} \end{cases} \\ B_{i,j}(t) &= \frac{t - t_i}{t_{i+j} - t_i} B_{i,j-1} + \frac{t_{i+j+1} - t}{t_{i+j+1} - t_{i+1}} B_{i+1,j-1}(t) \end{aligned} \tag{2.3}$$

where $j = 1, 2, \ldots, k$ with k being the degree of the spline. A linear combination of the control points c_i and the B-spline basis functions in Equation 2.3 expresses the curve:

$$C(t) = \sum_{i=0}^{n} c_i B_{i,k}(t), \qquad n \geq k - 1. \tag{2.4}$$

For each pixel of interest along the dispersion axis, a curve $C(t)$ is evaluated using a selected list of control points and subtracted from the observed line, resulting in an "envelope subtracted" spatial profile. Examples of this subtraction are shown in Figures 2.11 and 2.12. In these figures the control points were placed in positions where there was no expected jet emission to minimize removal of potentially critical features.

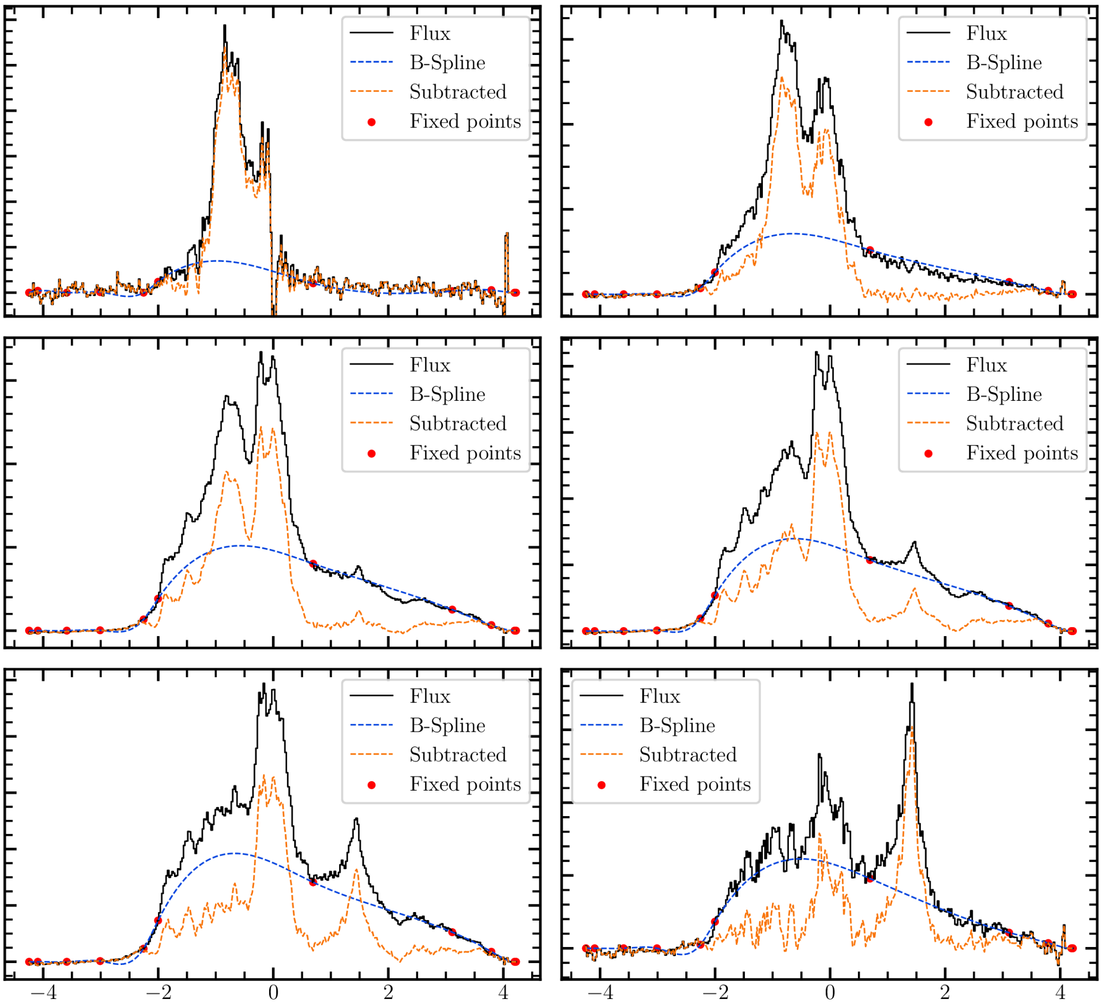

FIGURE 2.11: A spline interpolation of the envelope emission in the proplyd 244-440. Each panel shows the spatial profile at a chosen velocity in the [O I] line (see Figure 2.12). Control points are selected (red dots) as a spline basis and the interpolated line is subtracted from the spatial profile.

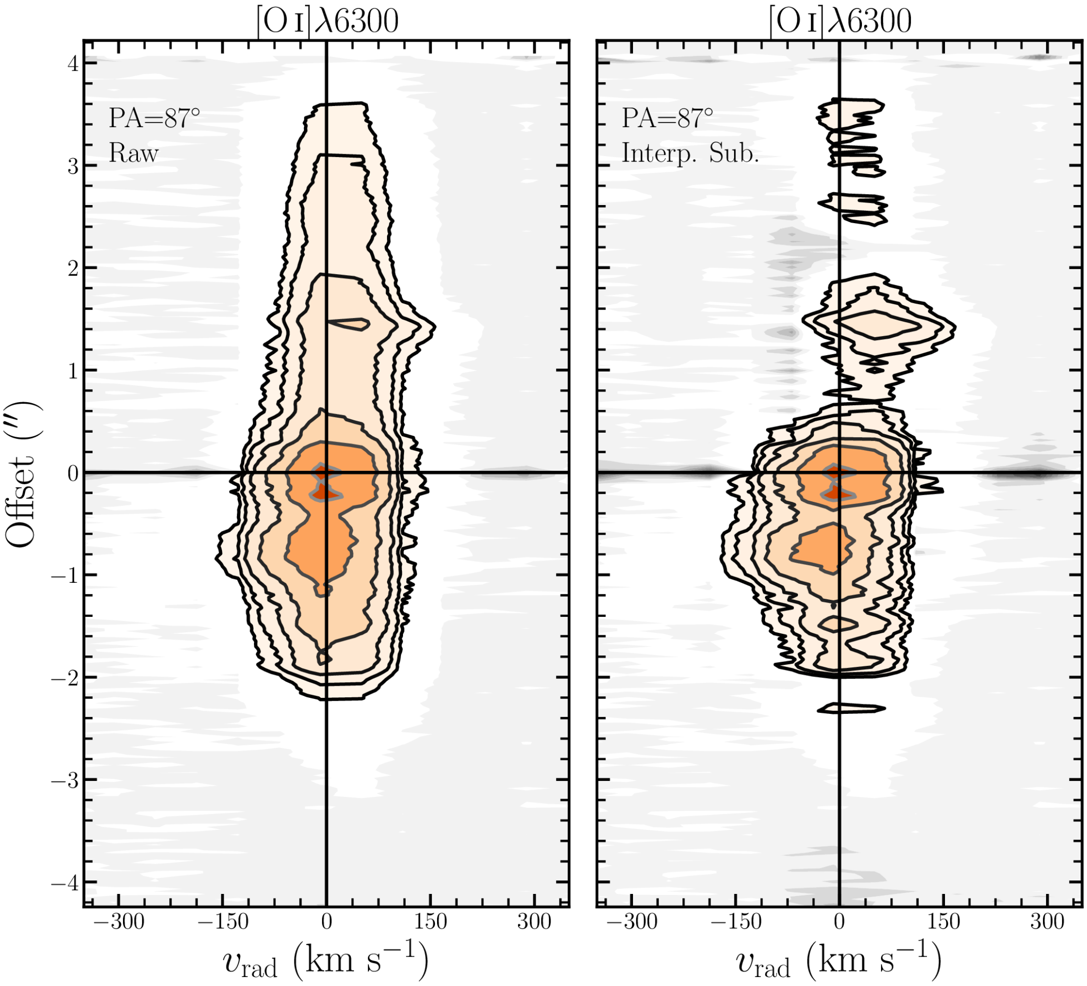

FIGURE 2.12: A spline nebular subtraction method applied to a PVD. A significant portion of the envelope is removed, though this introduced significant uncertainties to the jet.

The third and simplest method is useful for flux measurements in lines where the observed flux is a combination of the knot and envelope emission. In this method, one aperture is centered on the knot emission, and another aperture of the same size is offset from this position to estimate the envelope contribution. The envelope flux is subtracted from the jet+envelope flux, and the residual is taken as the intrinsic knot flux. In all proplyd analysis, this final method was used exclusively for lines contaminated by envelope emission due to its simplicity.

Skyline Removal

While the MUSE DRP can correct for sky emissions as a basic level, some skylines are still prominent in the processed science cubes, particularly the [O I] line. The effects can be mitigated in spectro-images, as integration over a wavelength bin can minimize the sky contributions, but when producing 2D position-velocity (PV) arrays the skylines are far more prominent.

A basic 2D PV array is shown in Figure 2.13. It is seen that despite being continuum-subtracted there are still stellar contributions and sky-line emissions in the dataset. As these skylines originate in the upper atmosphere, they can be useful for wavelength calibration; but they are otherwise contaminations in the dataset. For ground-based instruments like MUSE this led to the task of identifying the skylines and assembling them into a list with the emission line name and minimum and maximum wavelengths at which the line is visible. In the `telassar` package (discussed further below) this list is easy registered for that `telassar.PVSlice` instance, and convenience functions allow for the removal of the skylines.

The removal itself interpolates the data utilizing a Chebyshev polynomial of the form,

$$p(x) = c_0 + c_1 T_1(x) + \cdots + c_n T_n(x) \tag{2.5}$$

where n is the degree of the polynomial. For Chebyshev polynomials of the first kind, the $T_n(x)$ functions may be defined as

$$T_n(x) = \cos(n\theta) \tag{2.6}$$

with $\theta = \arccos(x)$. This polynomial family chosen here on the justification that if the background flux can be modeled as some function $F(\lambda)$ defined on a set interval, then there exist a solution such that

$$f(\lambda) \approx \sum_i c_i T_i(x) \tag{2.7}$$

and the Chebyshev polynomials are convenient basis functions because convergence is guaranteed on finite intervals; while defined on the $[-1, 1]$ interval they can be mapped to other coordinates while preserving their convergent properties.

Once the minimum and maximum wavelength values of a skyline are registered, a sigma clipping is performed on the entire array to suppress large gradients. This clipped mask is

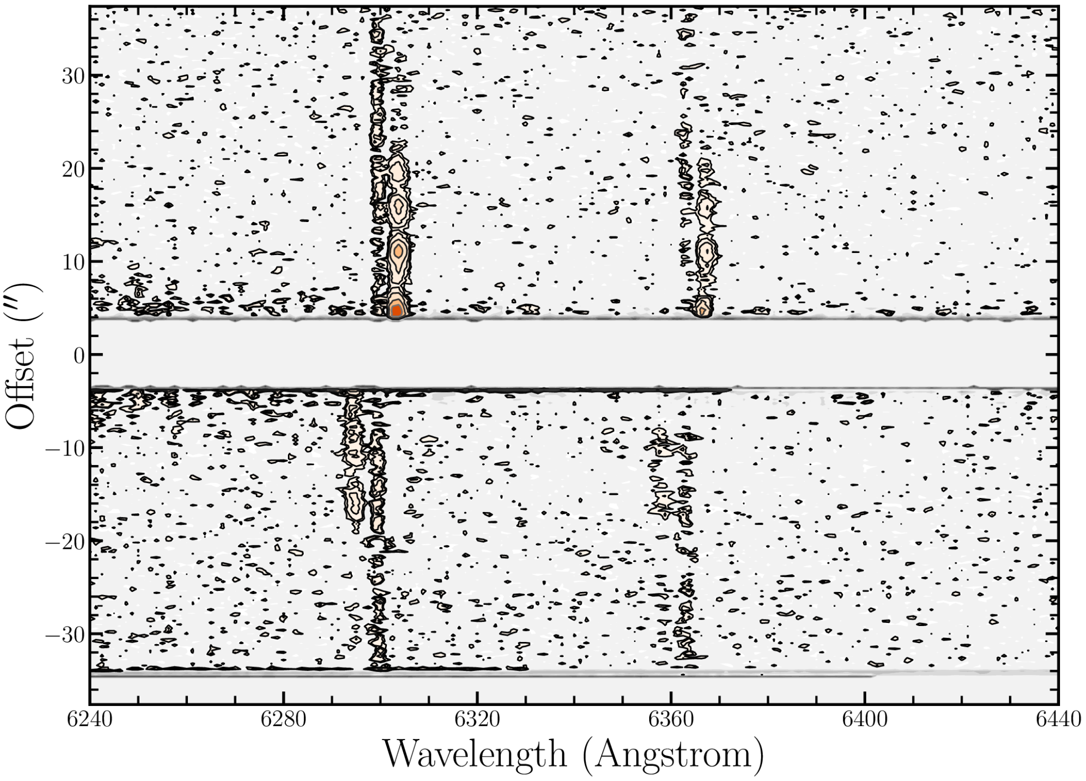

FIGURE 2.13: An example of a PVD extracted from MUSE. This features the [O I] doublet in the HD 163296 dataset prior to any skyline removal.

next applied to the data and passed to the `chebfit` function in the `chebyshev` package in `numpy`, which parses the non-masked data and evaluates the coefficients of the polynomial of a given degree (by default, it is 3). The window bounded by the min/max wavelength values is masked and the Chebyshev coefficients evaluated over this masked region with the `chebval` function (from the same `numpy` package). The interpolated values then replace the original data in the PV array, resulting in a skyline-free region. An example of this is shown in Figure 2.14.

2.3.2 Kinematic features in the jets

The analysis of 2D spectroscopic data was primarily done with the `telassar`[2] package. The proper motion study for HD 163296 and knot identification for Mayrit 1082188 (Chapters 3 and 5 respectively) utilized `lmfit`[3] routines in conjunction with custom scripts for the fitting of knots and calculating the radial velocities. This carries out a least-squares fit to the data and finds a solution such that the χ^2 value is minimized. Because of the closeness of some of the knots and the sensitivity of the multiple-peak fitting routine it was necessary to experiment with parameters to provide the best fit. Some knots could not be resolved and so they could not be reliably fit. Features which fall below a 3σ rms value (see Section 2.3.6) are excluded from fitting routines.

---

[2] https://github.com/akirwan361/telassar

[3] https://lmfit.github.io/lmfit-py/index.html

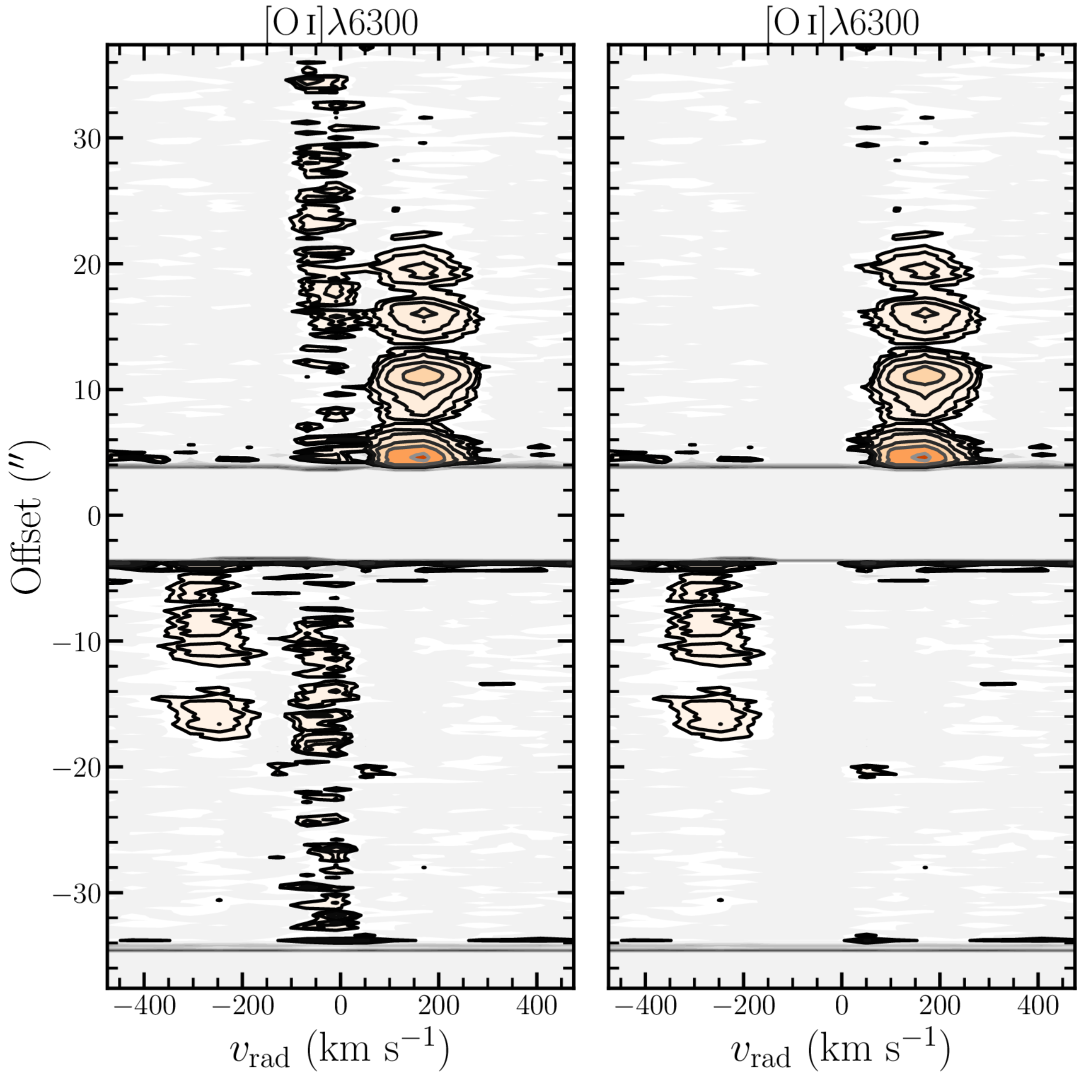

FIGURE 2.14: A PVD of the HD 163296 [O I]λ6300 emission line, showing pre- and post-skyline removal using a third-degree Chebyshev interpolation. The skyline is useful for wavelength calibration, but can contaminate the data.

Additionally, it was necessary to apply combinations of different models to account for different physical processes in the knots themselves, briefly described here.

Gaussian Profiles

The velocities of molecules in motion can often experience Doppler shifting, where the observed and emitted wavelengths are related by the equation

$$v = \left(\frac{\lambda_{\rm obs} - \lambda_{\rm ref}}{\lambda_{\rm ref}} \right) c \tag{2.8}$$

The general form of the Gaussian profile is well known, and here I have used the form:

$$G(x) = c + \frac{A}{\sigma\sqrt{2\pi}} \exp\left(-\frac{(x-x_0)^2}{2\sigma^2}\right) \tag{2.9}$$

Where c is some continuum value estimated by linear interpolation, and x_0 and σ are standard Gaussian parameters.

In general, Gaussian profiles are a standard approach for line fitting as they are versatile and effective. Given that we are dealing with optical lines, Doppler broadening can be prevalent and so this is a preferred model to use in fitting procedures. For estimating radial velocities and knot offsets as a function of distance from the star, I have generally used a Gaussian model.

Lorentzian Profiles

Lorentzian profiles are considered here as emission lines are observed due to electronic transitions. While the lines are treated as being optically thin and thus lower gaseous densities are common, there are still collisional effects to consider in the shape of the lines. This Lorentzian lineshape follows from a Cauchy distribution and can generally be expressed as

$$L(x) = \frac{\gamma/\pi}{x^2+\gamma^2} \tag{2.10}$$

where γ is a scale parameter representing the HWHM. In this case, it is assumed that atomic collisions decrease the lifetime of the upper energy state, and the broadening generally results in extended wings in the profile.

Voigt Profiles

Mathematically speaking, the Voigt profile is simply a convolution of the Gaussian and Lorentzian profiles. This convolution is of the form

$$\begin{aligned} V(x) &= \int_{-\infty}^{+\infty} L(x-\xi)G(\xi)d\xi \\ &= \frac{\omega_L/\omega_G}{\pi^{3/2}} \int_{-\infty}^{+\infty} \frac{\exp^{-(\xi/\omega_G)^2}}{(x-\xi)^2+\omega_L^2} d\xi \end{aligned} \tag{2.11}$$

where ω_G and ω_L are the widths of the Gaussian and Lorentzian functions respectively. Much recent work has been done in deriving various representations of this core function, not only due to its usefulness in modeling procedures but also because it cannot be expressed in terms of elementary functions. It can, however, be related to the real part of the Faddeeva function, $w(z)$, by

$$V(x) = \frac{\mathrm{Re}\left[w(z)\right]}{\sigma\sqrt{2\pi}}, \text{where} z = \frac{x+i\gamma}{\sigma\sqrt{2}} \tag{2.12}$$

This particular profile emerges in such areas as molecular spectroscopy and radiative transfer, and it is strongly related to the plasma dispersion function (Pagnini and Saxena, 2008). Being a convolution of the Gaussian and Lorentzian functions, it is thus a physical descriptor of Doppler broadening and pressure broadening, which can be useful in modeling knots whose shape might be affected by pressure gradients, such as bow shocks.

2.3.3 Spatial features in the jets

Measurements of the jet axis position, intrinsic jet width, and jet position angle were obtained from spectro-images, which are simply created by integrating over a spectral bin that encompasses the desired features of the jet. These three quantities can all be obtained simultaneously in the following manner. For each pixel along the axis of the jet (the spectro-images are rotated via affine transformation if necessary), the corresponding row or column of pixels orthogonal to it are extracted, resulting in a series of 1D cuts across the width of the jet. A Gauss-like profile is fit to each cut and the peak, center, and FWHM are recorded. The measured width is broadened by instrumental and seeing effects, such that

$$\sigma_{meas} = \sqrt{\sigma^2_{intrinsic} + \sigma^2_{seeing} + \sigma^2_{instrum}}, \tag{2.13}$$

where σ is related to the width by FWHM = 2.335 σ. The instrumental and seeing effects can be effectively combined as a single term by fitting Gauss-like profiles to multiple stars in the FOV of the processed science cube prior to background or continuum removal and computing an average FWHM. This estimation is only applied to the case of HD 163296 as the observations were obtained without AO-correction. An example of the seeing estimation is shown in Figure 2.10.

2.3.4 Extinction Correction

Extinction due to interstellar dust is a phenomenon that must be accounted for in astronomical data. As light passes through dense regions, it can be scattered, absorbed, or polarized by the particles in those regions. This extinction is dependent on wavelength: blue light is more heavily attenuated than red, resulting in objects appearing more red than they truly are. It is also dependent on distance, as the column depth of the material will affect the magnitude by which the light is extincted (McCall, 2004). The wavelength-dependent extinction is expressed in a function of the fractional change in the flux due to occultation:

$$A_\lambda = -2.5 \log \left(\frac{F_{\lambda,\mathrm{obs}}}{F_{\lambda,\mathrm{emit}}} \right), \tag{2.14}$$

We can further parameterize extinction by several terms: R_V, the relative visibility; A_V, the total extinction; A_λ, the extinction at a measured wavelength; $E(B-V)$, the color excess, related to the $B-V$ color; and $c(\mathrm{H}\beta)$, the extinction coefficient. R_V is simply the ratio of total extinction to reddening $A_\mathrm{V}/E(B-V)$ and characterizes the steepness of the reddening curve. $c(\mathrm{H}\beta)$ is a special logarithmic coefficient related to the color excess by

$c(\mathrm{H}\beta)$= 0.4 $E(B-V)$ $f(\lambda)$, where $f(\lambda)$ is a normalized value chosen such that the flux of Hβ is 1.

Additionally, a variety of extinction laws are available, with some better suited to different wavelength regimes (see Fitzpatrick (1999) and Draine (2003) for greater discussion of the differences in various laws). A plot of the extinction curves produced by a several laws (all available in the Python package `PyNeb`[4]) is shown in Figure 2.15.

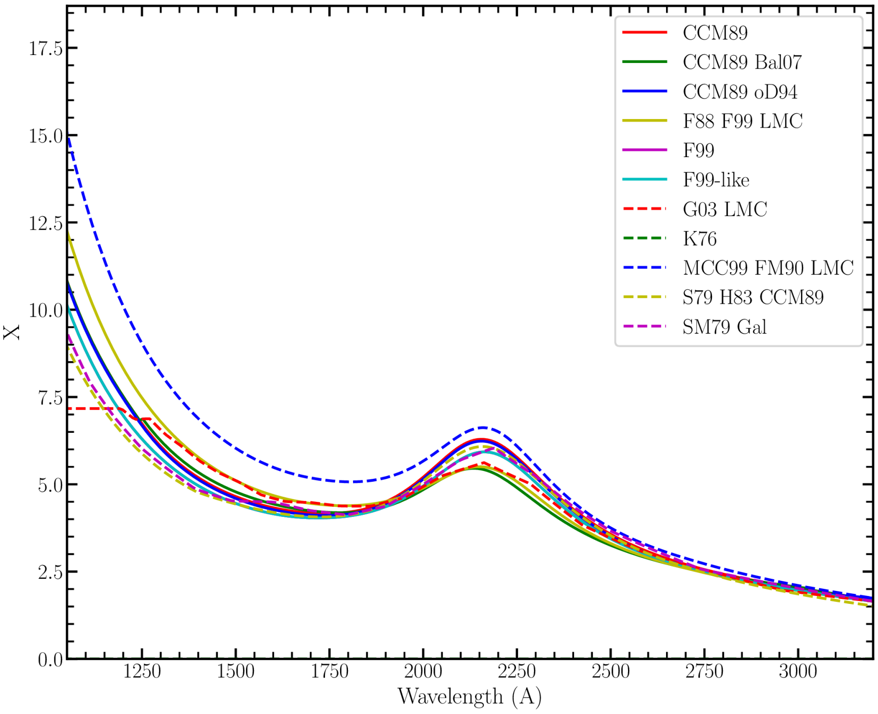

FIGURE 2.15: Extinction curves for different laws available in the `PyNeb` library, shown over a small wavelength range.

Generally, $c(\mathrm{H}\beta)$ along the line of sight is found by comparing the observed Balmer ratio $F(H\alpha)/F(H\beta)$ to the theoretical ratios predicted by quantum mechanical calculations. This is taken to be 2.86 throughout this work, under the Case B assumption of optically thin emission (see Hummer and Storey, 1987). The Balmer ratios are utilized because they are weakly dependent on density in Case B calculations, with variations in the theoretical ratios over broad density and temperature regimes being on the order of 2% (Mesa-Delgado et al., 2012). However, any two lines from the same species can be utilized if they are significantly far apart in wavelengths, for example the [Fe II]1.64 µm/1.32 µm ratio. These are outside the spectral range of MUSE, so they are not utilized here.

For any data set, a relative visibility R_V is assumed (3.1 in general cases, or 5.5 in the ONC; see Weilbacher et al., 2015), as well as O'Donnell's modification of the Cardelli, Clayton, and Mathis extinction formulation (O'Donnell, 1994; Cardelli, Clayton, and Mathis, 1989), given as "CCM89 oD94" in `PyNeb`. This law was chosen because it is valid for wavelengths between 3300 – 9100Å, making it well-suited to the analysis of MUSE data. The

---

[4] https://github.com/Morisset/PyNeb_devel/tree/master/docs

Balmer ratio allows for the creation of an “extinction map” for each $c(\mathrm{H}\beta)_{i,j}$, found by the equation (Robberto et al., 1993):

$$c(H\beta)_{i,j} = \frac{\log \frac{F^{emit}_{i,j}(H\alpha)}{F^{emit}_{i,j}(H\beta)} - \log \frac{F^{obs}_{i,j}(H\alpha)}{F^{obs}_{i,j}(H\beta)}}{f(\lambda)} \tag{2.15}$$

where the ratio $F_{emit}(H\alpha)/F_{emit}(H\beta)$ is the intrinsic flux assumed above. The correction for the observed flux is applied by

$$\begin{aligned} F_{\lambda,\mathrm{corr}} &= F_{\lambda,\mathrm{obs}} \times 10^{(0.4\ E(B-V)\ f(\lambda))} \\ &= F_{\lambda,\mathrm{obs}} \times 10^{A_\lambda/2.5} \end{aligned} \tag{2.16}$$

with the wavelength-dependent extinction defined by $A(\lambda) = 2.5 \times c(\mathrm{H}\beta) \times f(\lambda)$.

These computations are easily done with `PyNeb`, a Python tool developed for the computation of emissivities for forbidden (i.e. collisionally excited) and recombination lines, as well as for the determination of ionic abundances and reddening correction.[5] First, flux integrated images are created for the two Balmer lines and the ratio of the images is taken. If only the object features are of interest, a sigma-clipping routine can be performed to apply a mask to the data prior to input to the function. This ratio map is iterated over pixel-by-pixel in `PyNeb` assuming the “CCM89 oD94” reddening law with some specified R_V value and $F(H\alpha)/F(H\beta) = 2.86$. `PyNeb` stores the calculated $c(\mathrm{H}\beta)$ and A_V values as arrays in the `RedCorr` object, which are easily converted to 2D images representing the respective maps. `PyNeb` computes the extinction correction factor for some given wavelength with the `RedCorr.getCorr()` function, allowing the user to apply a wavelength-based flux correction pixel by pixel across the whole cube, if desired. If there is substantial variance in the extinction across the FOV, the maps allow for estimation of a representative $c(\mathrm{H}\beta)$ value to use for corrections instead. An example of this is shown for the proplyd in Figure 2.16.

For close, relatively isolated stars like HD 163296 (see Sec. 3) which are not embedded in a cloud, there is very little reddening due to extinction; but in these cases it can still be useful to examine extinction in the outflow itself. For objects in dense star-forming regions or young, embedded sources still obscured by their natal cloud, extinction effects are far more prominent, and can sometimes affect the fluxes by factors of ~ 5 or more. In the case of the Orion proplyd (Chapter 4), it is expected that the flux is significantly suppressed due to extinction from neutral material between us and the ONC (Blagrave et al., 2007), in addition to the attenuation from the photoevaporated envelope surrounding the proplyd (Mesa-Delgado et al., 2012, Kirwan et al., 2022, submitted). A similar assumption is made for the brown dwarf(s), which are embedded sources and are thus expected to suffer from non-negligible extinction.

---

[5] https://github.com/Morisset/PyNeb_devel

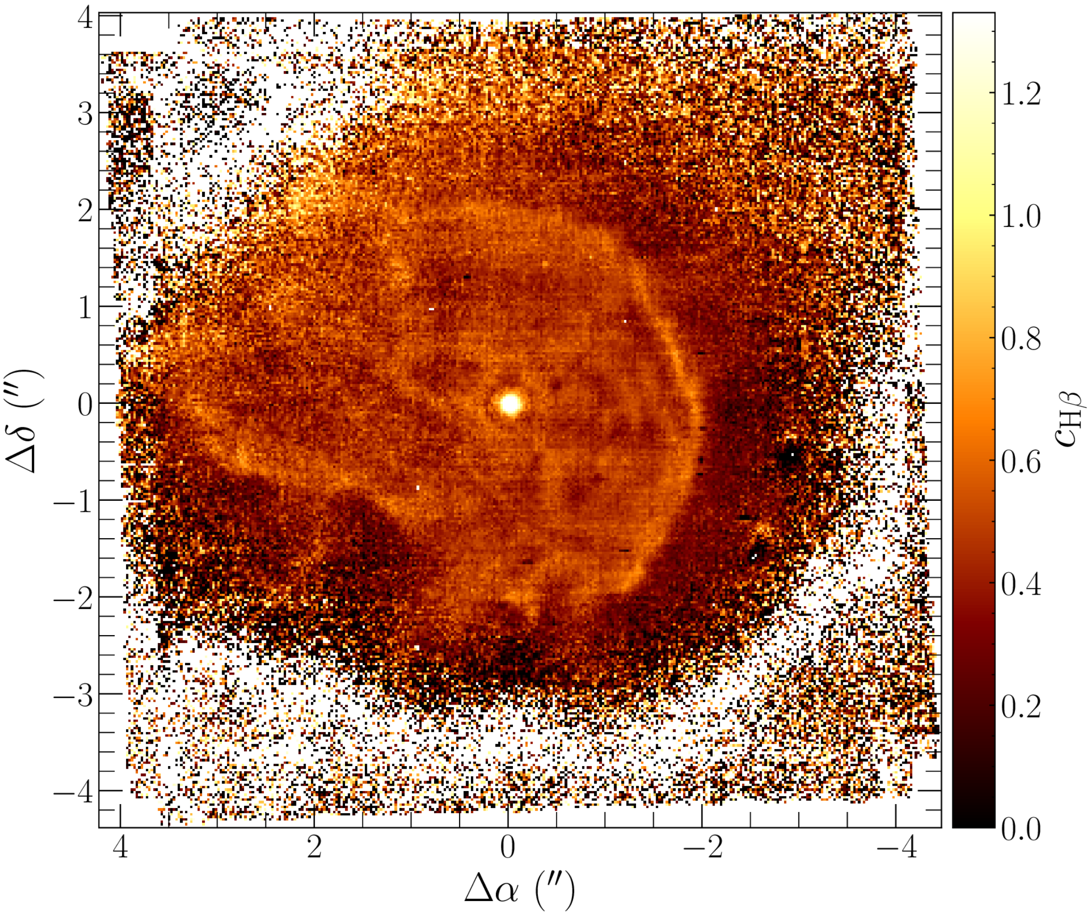

FIGURE 2.16: An example of an extinction coefficient map computed with `PyNeb`. For this object, a general trend of approximately $0.1 - 0.2$ dex difference is observed between the background and the proplyd envelope.

2.3.5 Physical conditions in the jet

There are several key parameters crucial to understanding jet outflow behavior and characterizing the physical conditions in the jet. These are the electron density, n_e (in units of cm^{-3}); the electron temperature, T_e; the ionization fraction with respect to hydrogen, $x_e = n_e/n_{\mathrm{H}}$; and the hydrogen density n_{H} (in units of cm^{-3}). The simultaneous spatial and spectral imaging of the MUSE instrument allows for these parameters to be computed for every spatial pixel, making this a powerful instrument for physical diagnostics. As discussed in Section 1.3, these calculations are performed using ratios of specific FELs.

In Section 1.3.1, the utility of specific FELs in the determination of basic physical conditions was discussed, particularly in relation to the [S II] and [N II] ions. Many HH objects emit in these lines, and as MUSE operates in the optical the considerations discussed in that section allow for fairly reliable determinations of two basic physical conditions in the outflows. It is easy to compute either quantities using the Python package `PyNeb`. This package allows the user to choose from a number of available atomic data sets, as well as to use a custom data set if desired.

To obtain either temperature or density the user provides the observed intensity ratio of two suitable lines to the `getTemDen()` routine, with the assumption of one constant condition, i.e. if computing density, assume a constant temperature. Alternatively, if ratios of suitable temperature- and density-dependent lines are known, the `getCrossTemDen()` task can use these find the (n_e, T_e) convergence.

2.3.6 Error estimation

For the methods discussed in Sec. 2.3.2 and Sec. 2.3.3, the uncertainty in the Gauss-like fitting is related to the signal-to-noise ratio (S/N) in the line. Porter, Oudmaijer, and Baines (2004) showed that for IFU observations the error on centroid position measured by a Gauss-like profile can be expressed in terms of the FWHM and S/N by:

$$rms = \frac{FWHM}{2\sqrt{2\ln 2} \times \mathrm{SNR}} \tag{2.17}$$

The noise of the channel is estimated by the median absolute difference (MAD):

$$\sigma = 1.482602 \ \mathrm{median}(|m - x(i)|) \tag{2.18}$$

where m is the median over pixels i. As this is not a fixed value, we can use higher orders of the MAD (following Stoehr et al., 2008). The third order approximation can be expressed:

$$\sigma = f_3 \ \mathrm{median}(| - x(i-2) + 2x(i) - x(i+2)|) \tag{2.19}$$

where

$$f_n = 1.482692 \frac{1}{\sqrt{\sum_{k=1}^{n-1} \binom{n}{k}^2}} \tag{2.20}$$

arises from error propagation. Prior to utilizing these methods, a sigma-clipping routine is applied to the data to minimize the effects of large peaks and better sample the noise in the line, allowing the S/N to be found easily.

Note that this applies exclusively to errors on the centroids in Gaussian fitting. Additionally, as MUSE has only moderate spectral resolution, this treatment is used solely for the spatial centroid measurements. Where Gaussian fitting is applied along a spectral line as in velocity measurements, the error is considered as the Gaussian sigma of the fit.

Chapter 3

HD 163296

3.1 Introduction

The primary interest of this thesis is the exploration of outflows in "edge-case" targets. As discussed in Chapter 1, much of our understanding of the launching mechanism is inferred from low-mass stars, and it is unclear whether the model appropriately scales to other mass regimes. Additionally, stars typically drive jets in the prime of their youth; once the accretion disk has dissipated we would expect outflows to cease (see Section 1.2). Thus we may be justifiably curious about outflows from intermediate mass stars approaching the transition disk phase and seek to understand the behavior of the system near the end of the star's adolescence.

In this chapter I will explore the jet system of HD 163296, a Herbig Ae star with a large circumstellar disk of diameter $d \sim 1000$ au, which is inclined at an angle of 45° ± 0.3° with respect to the plane of the sky with a position angle (PA) of 132.3° ± 0.5° (Rich et al., 2019). It is an intermediate mass star ($M \sim 2\ M_{\odot}$, Xie et al., 2020) located approximately 100 pc from our sun (Flaherty et al., 2015; Pinte et al., 2018). At $\sim 5 - 7$ Myr old (Xie et al., 2020) it is relatively mature, and the rings within its disk were observed by the Disk Substructures at High Angular Resolution Project (DSHARP; Andrews et al., 2018), which may indicate it is approaching the transition disk phase of its evolution (Isella et al., 2018). This makes it a particularly interesting source, as it may be in a transitional state between Group I and Group II intermediate-mass YSOs (see Section 1.1.2). Such gaps in circumstellar disks have often been thought to be carved out by planets, and for this object in particular, a curious crescent-shaped structure in the inner disk revealed by DSHARP has sparked extensive research which has lent credence to arguments for the existence of a planetary system (Teague et al., 2018; Pinte et al., 2018; Guidi et al., 2018; Zhang et al., 2018; Huang et al., 2018; Rodenkirch et al., 2021). A focus of many recent studies has been constraining the parameters of potential companions, with masses generally $< 9\ M_{\mathrm{Jup}}$ at separations between $\sim 50 - 260$ au (Teague et al., 2018; Rich et al., 2019; Pinte et al., 2020).

The discovery of an extended bipolar jet was first reported by Grady et al. (2000) using HST observations, and subsequent studies have placed the length of the jet at ~ 3000 au to either side of the source (Devine et al., 2000). The jet is made up of a series of at least ten knots with radial velocities of $100 - 300$ km s^{-1} (Wassell et al., 2006; Ellerbroek

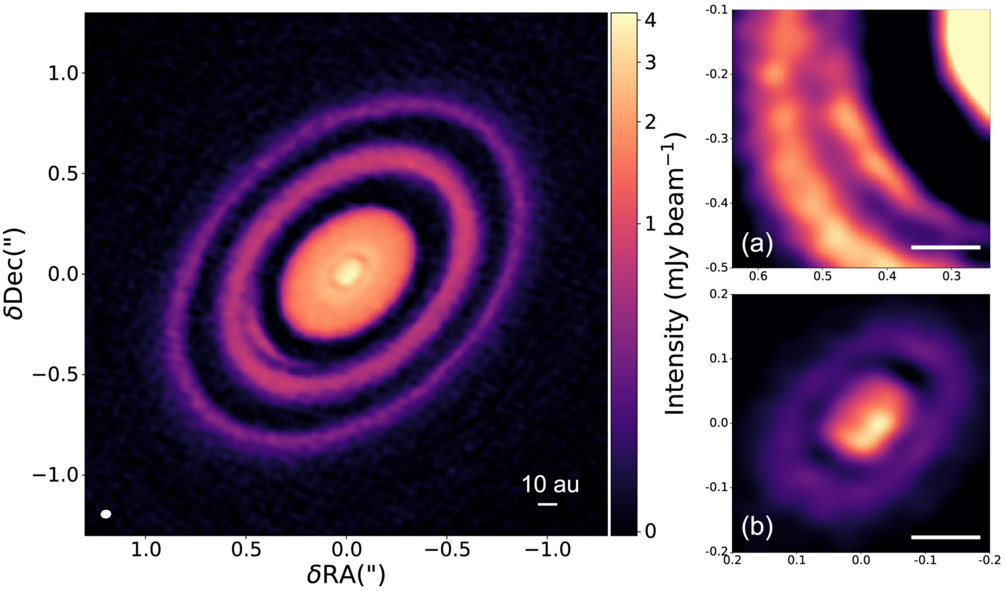

FIGURE 3.1: 1.25 mm continuum images of the HD 163296 inner disk as observed with by ALMA under the DSHARP project. Inset (a) reveals an asymmetric "crescent" feature in the disk at about 55 au, and inset (b) features a second crescent at about 4 au. The feature in inset (b) could be present due an optically thick and warped inner disk misaligned with the outer disk. Figure from Isella et al. (2018).

et al., 2014). Ellerbroek et al. (2014) found what appeared to be a 16-yr periodicity in the ejection events of the jets, which they note corresponds to a Keplerian orbit at 6 au. Ellerbroek et al. also examined the photometric variability of the source and discovered that NIR brightening and optical fading events weakly correlated with jet ejection events. In such a scenario, a high velocity wind lifts dust clouds from the disk and the jet forms shock fronts in the cloud during ejection events. Not only was this the first study to propose a planet so close to the star, but it also argues a direct link between jet launching and disk dynamics. They note however that not all ejection events corresponded with NIR brightening.

Additionally, the periodicity proposed by Ellerbroek et al. predicts that a new launching event should have been observed in 2018. HST Observations by Rich et al. (2020) report that not only did they not observe any new knots, but also that they did not observe any of the knots reported in literature. While they note a $\sim$ 32% chance of a launch occurring prior to their observations, they also report that they did not observe any NIR excess between 2016-2018, which was proposed as a signature for jet launching events by Ellerbroek et al. (2014). This periodicity is further challenged by Xie et al. (2021), who detect a knot at $\sim 2\farcs5$ in their MUSE NFM observations, which should be located much closer to the source at the time of their observations. While the proximity of the detected knot to the edge of the disk could mean that disk obscuration only makes it appear distinct as a knot, if the NIR excess events observed in 2011 and 2012 (Ellerbroek et al., 2014; Rich et al., 2020) are indicative of outflow events, then coupled with the proper motions determined by Ellerbroek et al. (2014) these would indicate that this was indeed a positive detection.

Due to the uniqueness of this object I will pay particular attention to the morphology of the jet, focusing on the optical regime covered by the MUSE instrument. Analysis will be structured in light of the above arguments for planets within the circumstellar disk, with further emphasis being placed on the dynamical nature of the outflow. As will be seen below, HD 163296 is still an active source with a complex outflow system, making it an ideal object of study to ascertain the durability of the outflow mechanism.

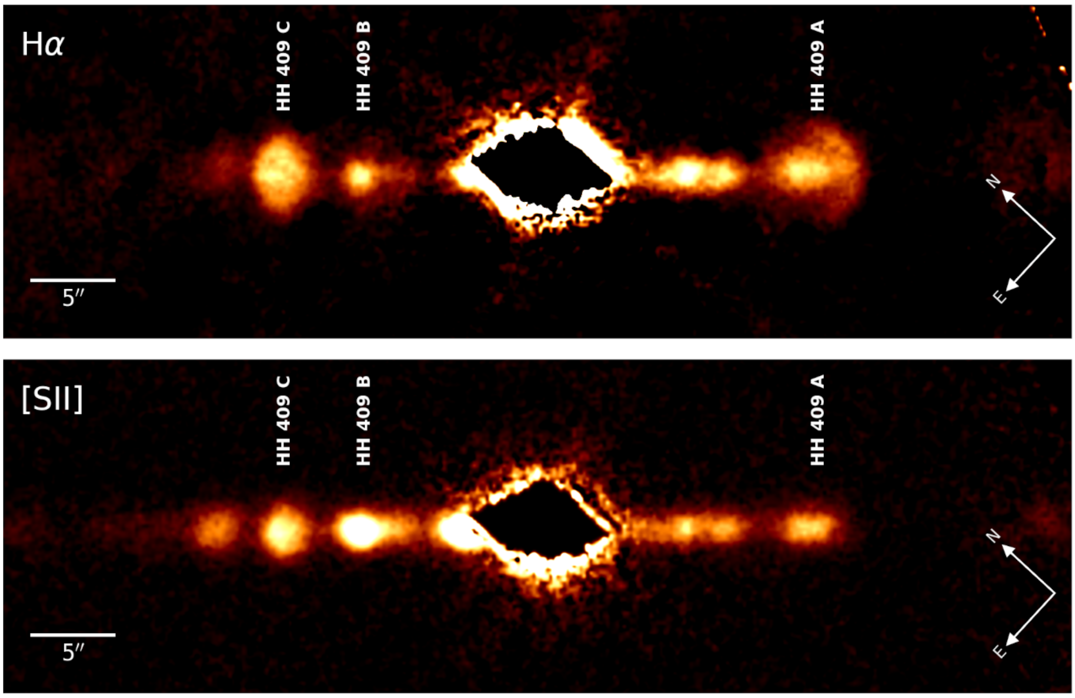

FIGURE 3.2: Images of the jet in Hα and [S II]λ6731, with the prominent HH objects labeled. The image corresponds to a ~12.5Å wide bin centered on the peak of the emissions and rotated by an angle of 47.3° with respect to the plane of the sky. Note the lack of emission in the first few arcseconds due to the saturation effects discussed in Section 3.2.

3.2 Observations

Observations of HD 163296 were done on 2 October 2017 under Program ID 099.C-0214(A) (PI: C. Schneider). These were taken in WFM without adaptive optics correction, with an airmass between 1.3 and 1.5 and a seeing varying between $0\overset{''}{.}8$–$1\overset{''}{.}2$. The position angle (PA) of the IFU was rotated between the exposures to improve image sampling, and we have primarily concentrated on the exposures with $t_{exp} = 100\,\mathrm{s}$, which comprise 75% of the on-target time. Observations were also obtained with $t_{exp} = 10\,\mathrm{s}$, and while the jet is not as visible in these cubes, we nonetheless detect some important diagnostic stellar emissions which can be used to analyze the accretion of the star.

The ESO MUSE pipeline (version 2.6) was used to reduce the data. For this, the standard calibration files provided by the pipeline were used with standard recipe parameters described in Section 2.2. However, the optical brightness of the star (V= 6.8 mag) resulted in saturation effects in the immediate region around its core, making it impossible to recover jet signatures within the inner $4'' - 5''$. Scattering within the detector also added excess noise in parts of the IFU which were discarded during the data reduction, as the utilization of multiple PAs resulted in full spatial coverage in the outer jet regions. The final cube was created by combining the individual exposures into combined cubes stretching fixed wavelength ranges, which in total covered the entire wavelength range of MUSE ($4800 - 9300$ Å) with an average spectral resolution of ~ 3700 in our primary region of interest. Due to the rotation of the exposures in the reduction process, the final cube has an approximately circular sky coverage with a diameter of $\sim 84''$.

These cubes were further reduced using methods for removing background and continuum contributions discussed in Chapter 2.3.1. Prior studies (see Ellerbroek et al., 2014; Xie et al., 2020) determined that extinction in the jet is minimal, so the cubes were not corrected for reddening. For each detected emission line, a subcube ranging ~ 100 Å was extracted centered around the emission line and continuum-subtracted. Flux-integrated spectro-images and pseudo-long-slit spectra were also extracted from each subcube.

In addition to using data obtained from MUSE, I have relied on some archival data for comparative studies. Specifically I have used the X-Shooter instrument at ESO and the Space Telescope Imaging Spectrograph (STIS) onboard the Hubble Space Telescope (HST). X-Shooter operates over the $300-2490$ nm range, splitting the optical to NIR range into three arms: UVB, VIS, and NIR. The STIS operates within a broad range, covering a spectral window from the UV to the NIR. In addition to high-resolution spectroscopy, it features a coronograph to allow for high spatial resolution imaging. The X-Shooter observations were taken in July, 2012 by Ellerbroek et al. (2014) under Program ID 089.C-0874. These were reduced through the X-Shooter pipeline and kindly provided to us by L. Ellerbroek. Data from the STIS/HST were obtained early September 1998 by Grady et al. (2000) under Program ID 7565.

3.3 Results

The full, known extent of the HD 163296 bipolar jet was covered by the MUSE FOV. Figure 3.2 presents wavelength-integrated images (spectro-images) in Hα and [S II]λ6731 with the brightest knots labelled. The convention adopted by Ellerbroek et al. (2014) for the labelling of the knots has been followed in this analysis. The blue-shifted jet extends in the south-west direction and boasts at least three well-defined knots within the first $20''$ (~ 2000 au) with a prominent bow shock at $\sim 15''$ (HH 409 A), and another blob-like feature is seen at a low S/N at $\sim 30''$ (HH 409 H). In the red-shifted arm (extending north-east) we observe four well-defined knots with a bow shock labeled HH 409 C located at $\sim 18''$ from the source. We further detect knots E, F, and G in the red lobe at a low S/N. We note as well the lack of emission in the central $\sim 4''$ of the source, which is missing due to the saturation effects discussed previously. While the jet is observed in over 20 lines in numerous species, my primary focus for this object is on the common FEL doublets at [O I]λλ6300,6363 Å, [N II]λ6583 Å, and [S II]λλ6716,6731 Å as well as the Hα recombination line at λ6562.8 Å and the [Ca II]λλ7291, 7323 Å doublet.

3.3.1 Morphological Changes & Proper Motions

PV diagrams of the jets in [O I]λ6300 Å, Hα, [S II]λ6731 Å, and [Ca II]λ7291 Å are presented in Figure 3.3. The radial velocities of the knots were measured from the PV diagrams by Gaussian fitting of the line emission profile at each knot position. For the Hα and [S II]λ6731 lines, spatial profiles were extracted along the jet axis and the knot positions estimated from Gaussian fits to the profiles. These fits are presented in Figure 3.4, and the radial velocity measurements and knot positions are given in Table 3.1. A direct comparison between MUSE and X-Shooter suggests important changes in the outflow, and the morphological changes are clearly shown in Figure 3.5. In the blue jet, knot H (HH 409 H) is outside the X-Shooter FOV so it is not considered in this analysis. In the red jet, only the first 20″ are considered due to the low S/N of knots E, F, and G. It was not possible to resolve knots A and A2 in the MUSE data, but three previously unreported knots – labelled B2a, A3a, and A4 – are observed, indicating stark changes in the jet between the two epochs.

To investigate these differences between X-Shooter and MUSE data further, a spatial profile was extracted from the X-Shooter data in the same manner as done for MUSE, and fits were made to the knot positions. The results for Hα and [S II]λ6731 are shown in Figure 3.4. Emission associated with B2a and A3a is identified in the X-Shooter data, but it is not as prominent as in the MUSE data. A4 would not have been within the range of the X-Shooter observation as it lies within 5″ of the driving source. Ellerbroek et al. (2014) acquired the X-Shooter data by offsetting the slit with respect to the source, and thus the inner 5″ are not covered in their data. The previously observed knots A and A2 are not resolved in the MUSE data, which may indicate a collision in the knots where knot A slowed post-shock and A2 collided into it. The knot profiles in Figure 3.4 provide evidence of this blending/collision.

Proper motions were measured and are included in Table 3.1, and in this are also shown the two epochs reported by Ellerbroek et al. (2014). In their analysis of the proper motions, Ellerbroek et al. (2014) applied a global fit to archival data dating back to 1998 (see Figure 3.9) and report average values for the red and blue arms of the jet to be $v_{t,\mathrm{red}} = 0.28 \pm 0.01$ ″ yr^{-1} and $v_{t,\mathrm{blue}} = 0.49 \pm 0.01$ ″ yr^{-1} respectively. Comparatively, our measurements yield average values of $v_{t,\mathrm{red}} = 0.38 \pm 0.04$ ″ yr^{-1} and $v_{t,\mathrm{blue}} = 0.34 \pm 0.01$ ″ yr^{-1}, with an average jet inclination angle $i_{\mathrm{jet}} = \arctan \langle v_{\mathrm{rad}} \rangle / \langle v_{\tan} \rangle = 47° \pm 10°$. This angle is in agreement with the findings of Rich et al. (2019). The uncertainties in the angles are given as the standard deviations of the values in Tables 3.1 and 3.2. The large differences between X-Shooter and MUSE proper motions will be discussed in Section 3.4.1.

Knots	x_t MUSE 2017 ($''$)	x_t XSh 2013 ($''$)	x_t XSh 2012 ($''$)	Proper motion ($''$ yr^{-1})	V$_{rad}$ MUSE 2017 (km s^{-1})	V$_{rad}$ XSh 2012 (km s^{-1})
Blue Arm						
A	15.67 ± 0.05	-	13.85 ± 0.03	0.35 ± 0.01	255 ± 20	260 ± 20
A2	-	-	12.12 ± 0.02	-	-	-
A3a	10.91 ± 0.05	-	9.18 ± 0.13	0.33 ± 0.01	270 ± 17	-
A3	8.34 ± 0.05	-	6.53 ± 0.02	0.35 ± 0.01	280 ± 11	260 ± 20
A4	4.61 ± 0.05	-	-	-	280 ± 30	-
Red Arm						
B2	4.77 ± 0.05	3.2 ± 0.03	-	0.37 ± 0.02	125 ± 20	-
B2a	8.83 ± 0.87	-	6.4 ± 0.14	0.46 ± 0.05	150 ± 18	-
B	11.11 ± 0.13	9.6 ± 0.03	9.18 ± 0.03	0.36 ± 0.01	160 ± 15	170 ± 15
C	15.80 ± 0.23	-	13.89 ± 0.06	0.36 ± 0.01	160 ± 15	160 ± 15
D	19.68 ± 0.68	-	17.9 ± 0.64	0.34 ± 0.01	145 ± 25	145 ± 25

TABLE 3.1: Proper motion measurements calculated from the MUSE data and the two X-Shooter epochs. The radial velocities and knot offsets here are calculated from the co-added measurements of the Hα and [S II]λ6731 lines. We do not include some knots previously reported due the inability to resolve their features in the MUSE data.

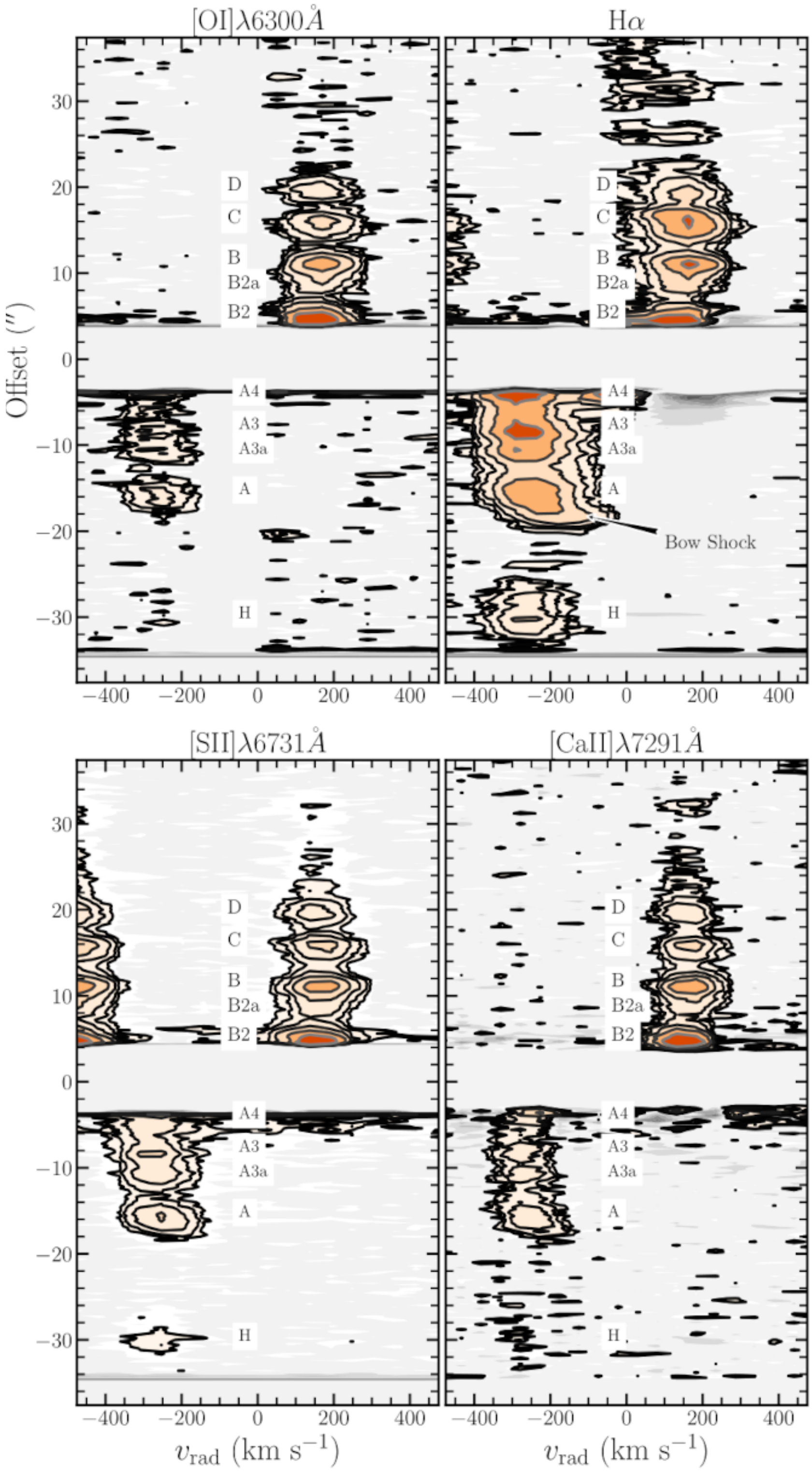

FIGURE 3.3: Position-velocity diagrams of the [O I]λ6300 (top left), Hα (top right), [S II]λ6731 (bottom left), and [Ca II]λ7291 (bottom right) emissions of the HD 163296 outflow, corrected for the local standard of rest. The colour contours represent a 3σ detection, and the background contours are on a log scale up to 2σ. The bow shock in knot A is visible in Hα, [S II]λ6731, and [Ca II]λ7291 (see Table 3.1).

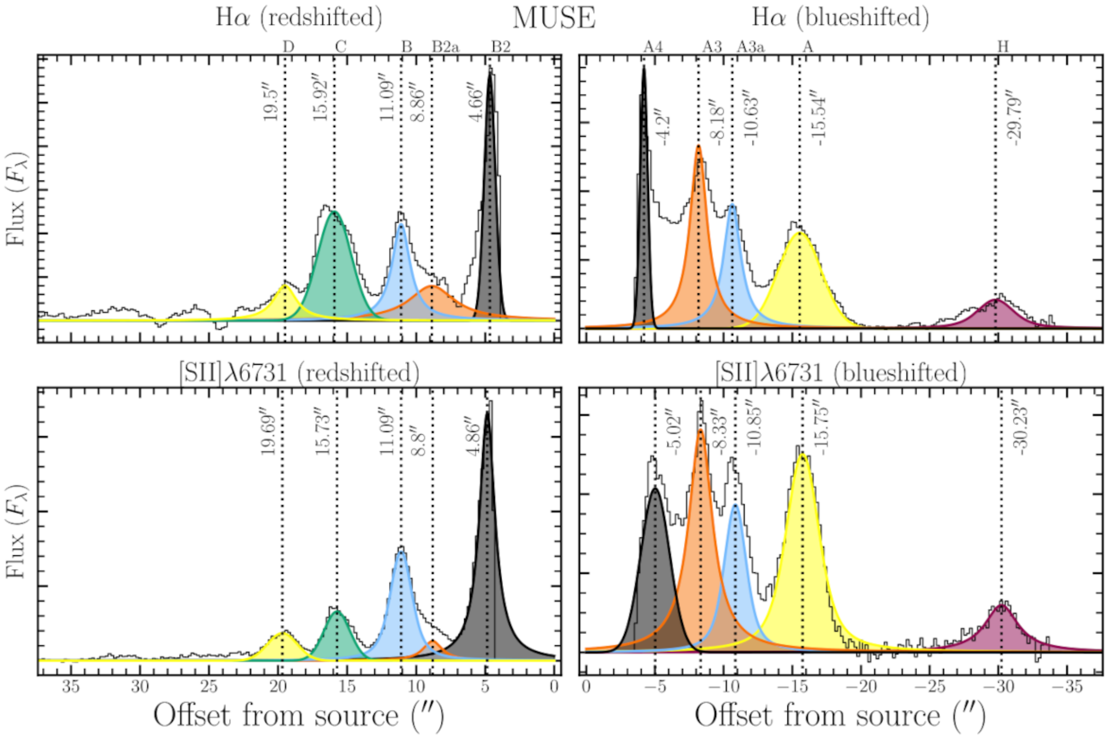

(a)

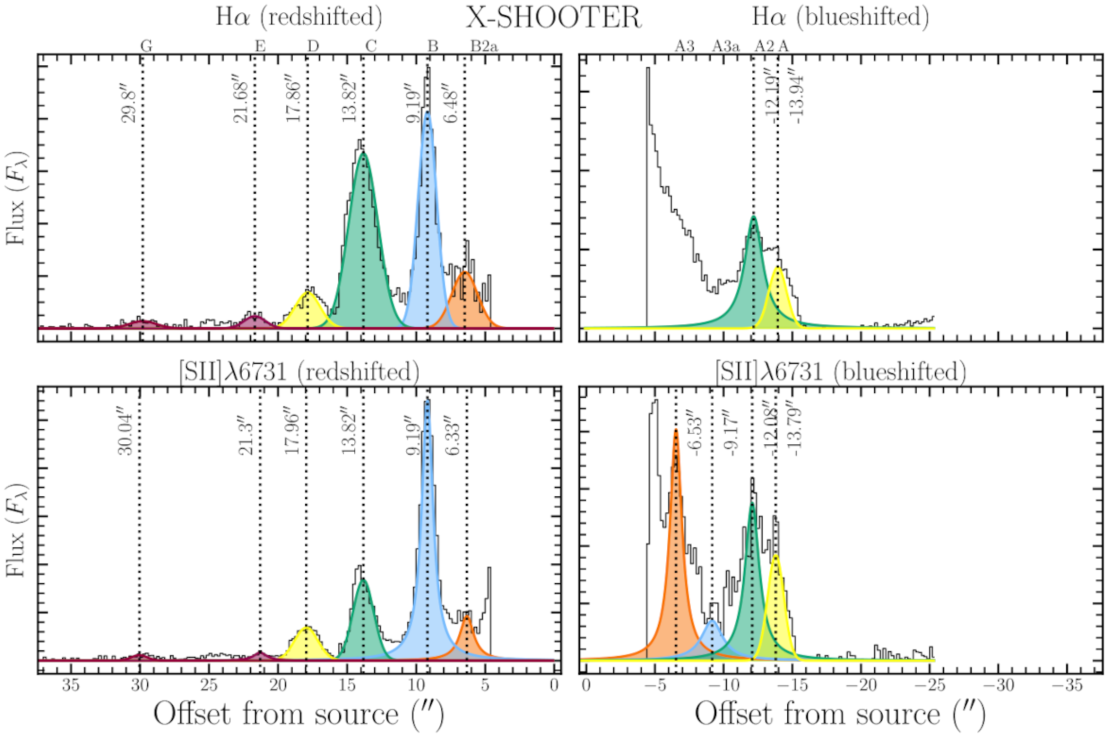

(b)

FIGURE 3.4: Spatial profiles of the Hα and[S II]λ6731 lines extracted from the PVDs.

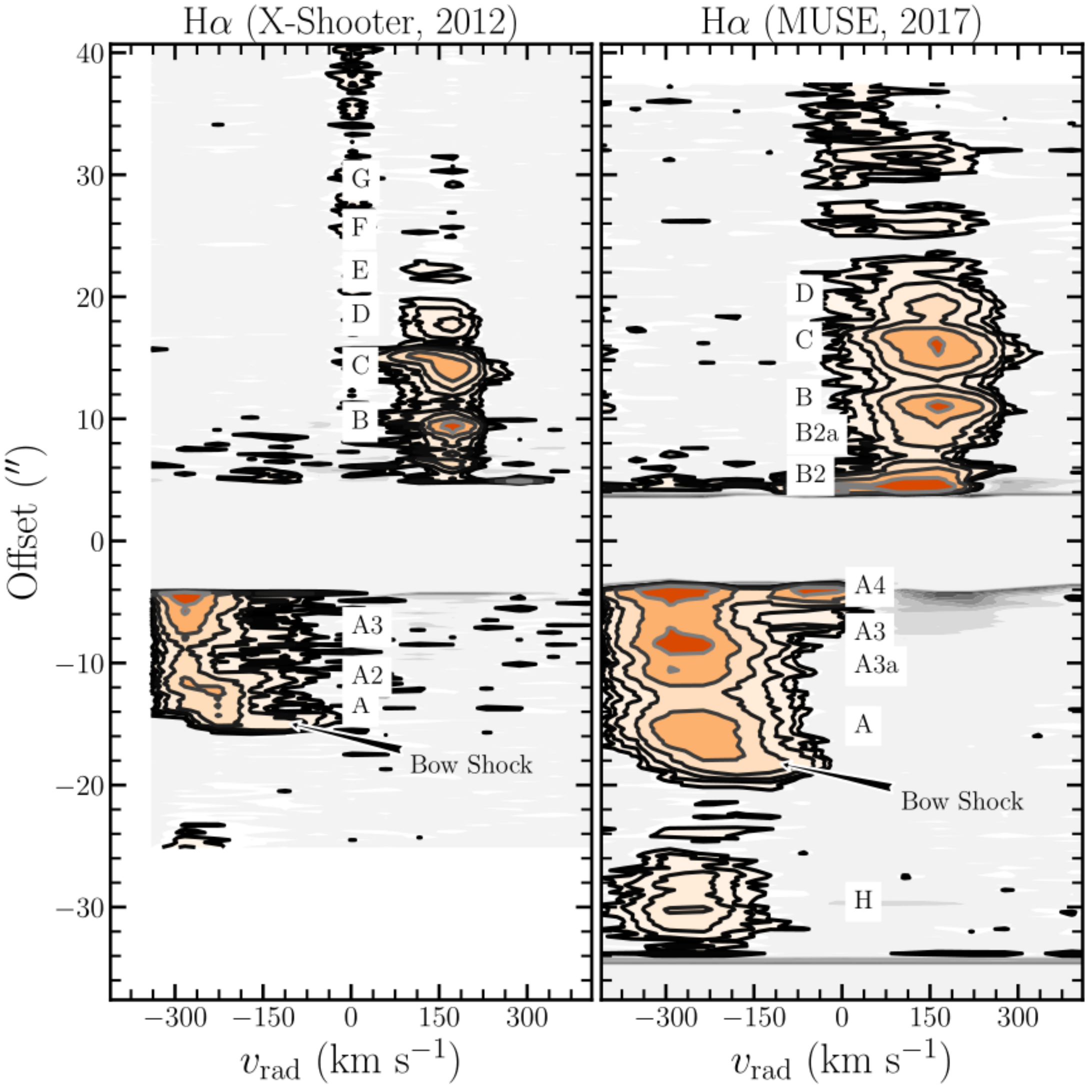

FIGURE 3.5: Comparison of X-Shooter data with MUSE for the Hα line. The X-Shooter spectrum has been degraded to match the spectral resolution of MUSE. Black contours correspond to $\log F_\lambda = [-17.2, -17.0, -16.7, -16.3, -16.0, -15.8, -15.5]$ for the X-Shooter data and $\log F_\lambda = [-18.8, -18.5, -18.2, -17.9, -17.6, -17.3, -17.0]$ for the MUSE data.

Table 3.2: Proper Motion Estimates & Jet Inclination

Knots	v_t ($''$yr^{-1})	v_t (km s^{-1})	v_{space} (km s^{-1})	i_{inc} (°)
A	0.35 ± 0.01	167 ± 5	305 ± 10	57 ± 2
A3a	0.33 ± 0.01	160 ± 5	315 ± 10	60 ± 2
A3	0.35 ± 0.01	165 ± 6	325 ± 10	60 ± 2
B2	0.37 ± 0.02	180 ± 10	220 ± 20	35 ± 3
B2a	0.46 ± 0.05	220 ± 25	270 ± 20	35 ± 4
B	0.36 ± 0.01	175 ± 5	235 ± 10	43 ± 2
C	0.36 ± 0.01	175 ± 5	235 ± 10	42 ± 2
D	0.34 ± 0.01	165 ± 6	220 ± 20	42 ± 4

3.3.2 Exploring the Axis Asymmetry

As discussed above, the spectro-images hinted at an axis asymmetry, prompting investigation of the evolution of the jet morphology with respect to distance from the driving source. A method adapted from the "jet fitting" process described in Raga, Mundt, and Ray (1991) is used to measure the both the jet axis position and width. At each pixel along the jet, a spatial profile is extracted perpendicular to the axis and fit with a Gaussian function, which provides the axis centroid position and the jet FWHM. The measured width is the quantity 2.335 σ, which is related to the intrinsic width, seeing width, and instrumental width as shown in Equation 2.13. Following the method discussed in Section 2.3.3, an average seeing of $1''\!.1$ was computed and used to correct for the intrinsic jet width. The FWHM can further be used to constrain the opening angle of the jet, which I discuss below.

As the jet is most collimated at the highest velocities, I focus on these components of the jet by integrating the spectro-images from -300 km s^{-1} to -200 km s^{-1} for the blue lobe and $+150$ km s^{-1} to $+250$ km s^{-1}for the red lobe. The brightest emissions are seen in Hα, [N II]λ6583, and the [S II] doublet, so these are used for this analysis. The FWHM and opening angle of the fits are shown in Figure 3.6, and the jet centroid positions and position angles are shown in Figure 3.7. The uncertainty in the pixel positions are computed as discussed in Sect. 2.3.6. Fits with a low (< 5) S/N were rejected, which excludes some inter-knot regions of the jet.

The jet opening angle is computed using a linear regression on the intrinsic FWHM assuming a non-zero jet width at the source. It is seen in Figure 3.6 that the FWHM has a minimum corresponding to the maximum jet intensity, a phenomenon observed by Raga, Mundt, and Ray (1991) that arises due to observing under non-Gaussian PSF conditions. They therefore recommend limiting any measurements of the jet width the intensity maxima, i.e. the knot peaks. Similar fluctuations are seen in the HD 163296 jets, particularly in the red lobe. Hence, in Figure 3.6 two fits are shown: one which incorporates all the data points (black line); and one which uses only the widths measured at the intensity peaks (red line). The difference between the angles estimated from the two fits is not significant. It is observed that the red lobe has a greater opening angle than the blue, which measure 4°$-$6° and $< 2.5°$ respectively, which are in broad agreement with the values reported by Wassell et al. (2006) and confirm the asymmetric nature of the jet. As the jet is most likely collimated within the first 100 au ($\sim 1''$ for this object), it is reasonable to expect such angles (Frank et al., 2014; Eislöffel, Smith, and Davis, 2000).

The axis along the direction of the outflow is also measured where the Gaussian centroid of the fit is taken as the jet axis position (Murphy et al., 2021). These results are shown in Figure 3.7. Similar methods applied to other jet sources Masciadri and Raga, 2002; Erkal et al., 2021a; Murphy et al., 2021 have measured deviation of the centroid positions from the jet axis, presenting a picture of a "wiggle" in the jet that has been argued to be due to the effect of a companion to the source. While the results here do not indicate a clear wiggling pattern, a deviation along the axis is noted as well as an asymmetry in the PAs of the lobes. Examining the FELs, an average PA$= 0.84°$ is measured in the blue lobe and $-0.37°$ in the red lobe. The Hα emission is excluded here as it traces the bow shocks and not the core of the jet, but a similar asymmetry is nonetheless observed.

The agreement in the pattern of the centroid positions with distance for the FELs could lead us to conclude that we are detecting a jet axis wiggling. To probe this further, we directly compare the Gaussian centroid measurements against the jet width measurements shown in Figure 3.8, where the three FELs are combined and smoothed with a 3-pixel running average. This allows the full inter-knot regions to be included. This comparison again reveals a change in the centroid of the jet emission, but we further observe a correlation between the centroid deviation, FWHM, and knot position. Notably, larger displacements and FWHM are seen in the inter-knot regions. This points to a different origin for the pattern observed in the FEL centroids, possibly due to shock dynamics within the jets.

3.4 Discussion

Similar to many other young stars, the detection of rings in the disk of HD 163296 first uncovered the possibility that its disk could host planets (Grady et al., 2000; Isella et al., 2018; Zhang et al., 2018). HD 163296 is an interesting case as the presence of more than one planet has frequently been proposed (see Section 3.1, meaning that with HD 163296 we can talk of a planetary system being present. Teague et al. (2018) studied the rotation curves of CO isotopologue emission relative to the Keplerian rotation. Deviations in the rotation curves were postulated to be a result of gaps carved in the gas surface density by Jupiter-mass planets. Comparison with hydrodynamic simulations suggested two Jupiter-mass planets orbiting at radii of 83 au and 137 au. Pinte et al. (2018) used CO channel maps to study the Keplerian velocity of the HD 163296 disk. They find an asymmetry between the southeast and north-west sides of the disk which they argue matches a localised deviation from Keplerian velocity. Modelling shows that this could be caused by a $\approx 2\ M_{\mathrm{Jup}}$ planet orbiting at a distance of 260 au. Similarly, Guidi et al. (2018) present KECK/NIRC2 L$'$ band imaging of HD 163296 with the aim of seeking planetary mass companions and identified a point-like source at a deprojected distance of ~ 67 au. Planetary isochrones suggest that the emission could be explained by the intrinsic luminosity of a 6-7 M_{Jup} planet. However, the work of Rich et al. (2019) argues against the companion proposed

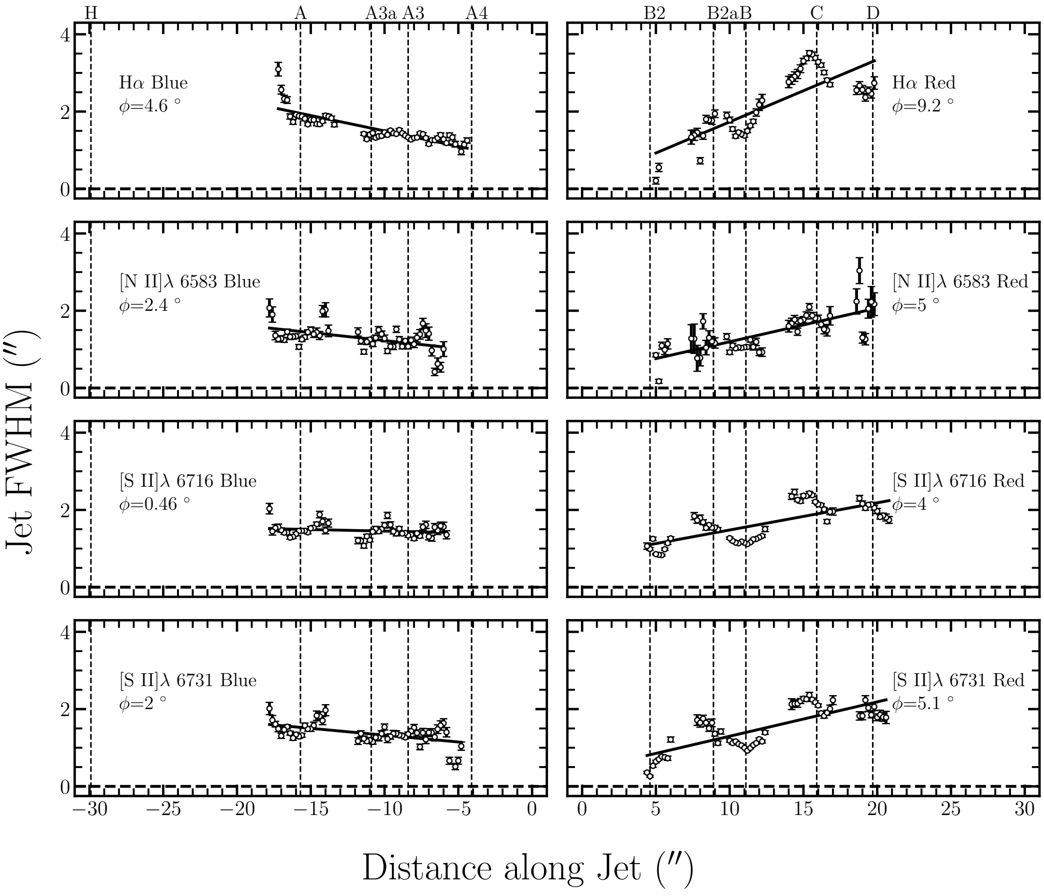

FIGURE 3.6: Intrinsic jet width and opening angle measurements for both red- and blue-shifted lobes of the outflow.

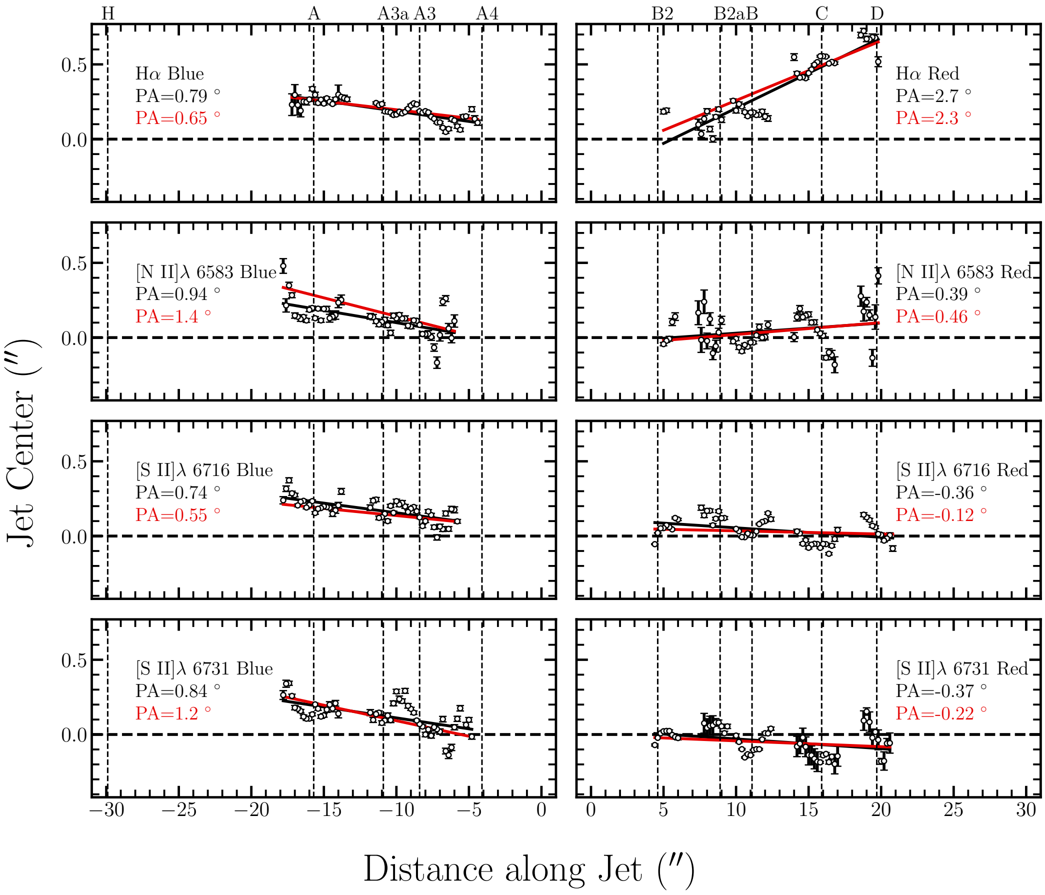

FIGURE 3.7: Gaussian centroids fit along the jet axis for the aforementioned emission lines.

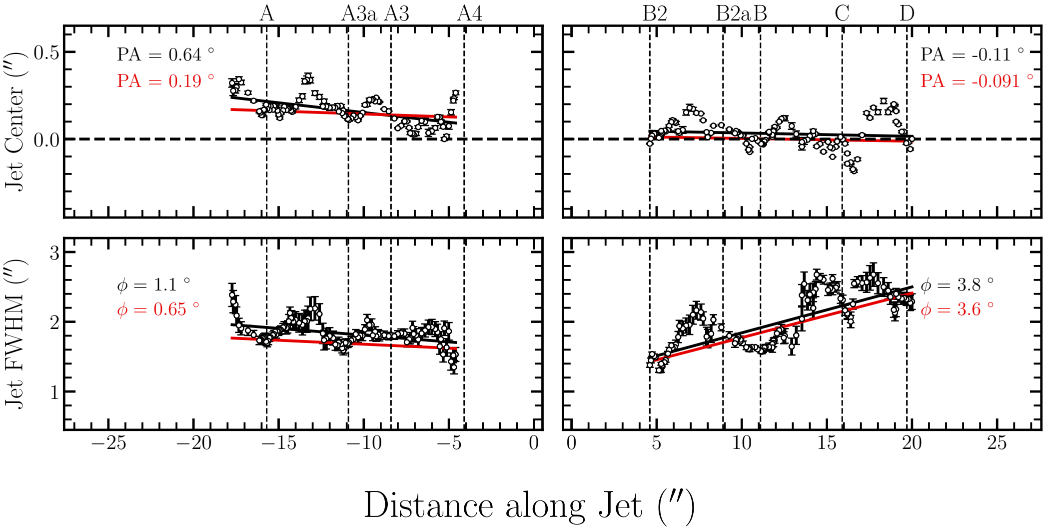

FIGURE 3.8: Top: average centroid positions of the three FELS in Fig. 3.7. Bottom: average FWHM measurements of the same three FELs. The data is smoothed with a 3-pixel running average. Black lines are linear fits to the entire data, while red lines are fit only to the peaks.

by Guidi et al. (2018) while placing much more stringent mass limits ($< 9\ M_{\rm Jup}$) on the planets proposed by Teague et al. (2018). More recently, Rodenkirch et al. (2021) modelled the origin of the crescent shape asymmetry detected by Huang et al. (2018) within the inner gap of the HD 163296 disk. They find that their models show that its origin could be a Jupiter-mass planet orbiting at a radial distance of about 48 au.

All of the studies described above examined the planet hosting disk to look for evidence of a planetary system. Ellerbroek et al. (2014) focused on the HD 163296 jet and discussed whether the 16 yr period in the emission of knots in the jet could point to the presence of a companion. They note that the periodicity of 16 yr corresponds to a Keplerian orbit at 6 au and a radial velocity signal of a few km s^{-1}. This is the first suggestion of a possible planetary companion orbiting close to the star. Below is a discussion of what this MUSE study tells us about the HD 163296 planetary system.

3.4.1 Knot So Simple: Time-Evolution of the Outflow

As stated in Section 3.3.1, we observe the presence of new knots in the MUSE data as well as evidence of collisions between knots. In comparing our results with those previously reported, we find a large discrepancy between proper motion estimates which warrants closer investigation. Our average proper motions are $0.34{\pm}0.01''$ yr^{-1} and $0.38{\pm}0.01''$ yr^{-1} for the blue and red lobes, respectively, while Ellerbroek et al. (2014) report averages of $0.28{\pm}0.01''$ yr^{-1} and $0.49{\pm}0.01''$ yr^{-1} for the same lobes. The values reported by Ellerbroek et al. (2014) combined multiple epochs of knot observations beginning with HST data from 1998 (see Section 3.3.1). While there appears to be a discrepancy between reported proper motions, it can be seen in Figure 3.9 that the slopes for the individual knots in the red lobe reported by Ellerbroek et al. are larger than their reported $0.28 \pm 0.01''$ yr^{-1} and appear to be consistent with the values we report. Additionally, the global fit calculated by Ellerbroek et al. uses only 4 knots from the blue lobe, compared to the 7 knots from the red lobe. Further complicating the estimates of the proper motions for the MUSE data is the blending of knots A and A2, and the less-resolved presence of knots A3a and A3 in the X-Shooter data contributes a higher degree of uncertainty.

Interestingly, the observation of the knot A4 in our MUSE data raises questions about the assumed 16 yr periodicity of jet launching events proposed in Ellerbroek et al. (2014), as the presence of this knot appears to violate this periodicity. This periodicity predicts that a new launching event should have been observed in 2018. In addition to not observing any new knots, Rich et al. (2020) curiously report that they do not observe any of the previously reported knots in their 2018 HST data, but note a $\sim 32\%$ chance of a launch occurring prior to their observations. Rich et al. also note that they did not observe any near-infrared excess between 2016-2018, which was proposed as a signature for jet launching events (Ellerbroek et al., 2014).

In a study by Xie et al. (2021), they report the detection of a knot B3 at $\sim 2.5''$ in their MUSE NFM observations, which should be located much closer to the source at the time of their observations if the periodicity was correct. If we assume the jet launching time frame for all of the knots, then separations of $\sim 7''$ and $\sim 4''$ should be observed

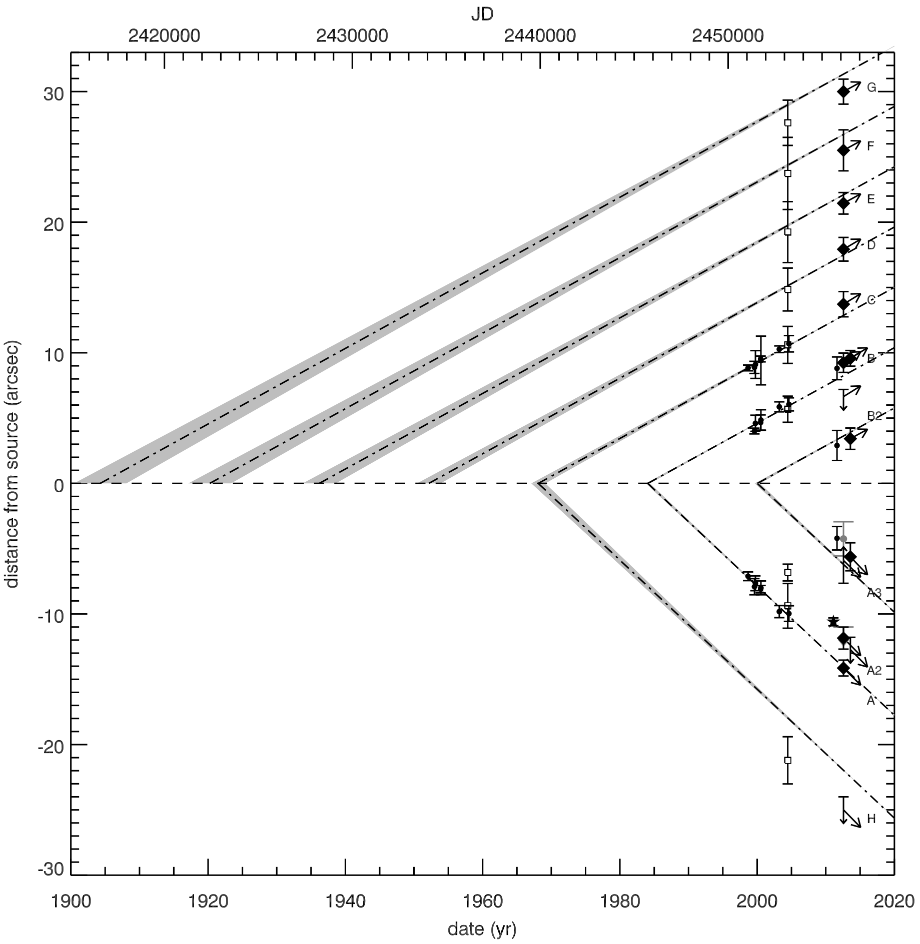

Figure 3.9: A global fit of the knot positions to estimate the average proper motions of the HH 409 jet. Image credit: Ellerbroek et al. (2014).

between the blue knots and red knots, respectively. Instead, we observe a separation of $< 4''$ between knots A3 and A4, but we caution that due to the closeness of knots B2 and A4 to the region of oversaturation, it may be that we simply are not seeing the full knot in our observations and are thus underestimating the separations. This violation of the periodicity is still observed, however, if we accept that A3a and B2a are true knot detections.

A possible alternative explanation for this is that of disk obscuration. Xie et al. (2021) noted that the presence of knot B3 in the NFM data is close to the edge of the disk, and suggest that if we assume the previous periodicity then this knot B3 could be interpreted as being a part of the knot B2. However, our WFM observations are unable to see this region, and Xie et al. further caution that instrumental issues resulted in contamination in the Hα line and they were thus unable to characterize the extinction. Additionally, near-infrared excess was observed in 2011 and 2012 Ellerbroek et al., 2014; Rich et al., 2020, strengthening the claim that B3 is a positive knot detection.

This interpretation of results appears to challenge the underlying assumptions of Ellerbroek et al. of periodic, simultaneously ejected, and uniformly propagating knots. The results present instead a picture of a complicated, complex jet system that defies generalization.

3.4.2 Origins of the Apparent Wiggling

The observed correlation between the centroid of the jet emission perpendicular to the jet axis, the FWHM, and the knot/inter-knot regions suggests that the origin of this pattern is not jet axis wiggling. What, then, could be its origin?

One possibility is an intrinsic bias due to asymmetry in the PSF. An argument for this follows from the idea that if the PSF is asymmetric, then rotating the images may introduce a bias in the spread of the data which may be falsely interpreted as a jet axis wiggling. To examine this, two sets of continuum images were extracted in the manner discussed in Section 2.3.1 (see Figure 2.10) for both the rotated and non-rotated cubes. If the observed deviation is due to an asymmetric PSF, then a comparison of the PSF in the rotated and non-rotated cubes should reveal a discrepancy in the profile shapes. However, the same 1:1 ratio was observed between the FWHM_x and FWHM_y values, making it unlikely that what we are seeing is the result of a rotation artifact.

The next question was: are there any processes which could potentially affect the knot photocenters? The calculated i_{inc} values show a standard deviation of $\sim 10°$, and along with shock processes in the knots this may shift the emission peaks away from the jet axis. Evidence of these off-center shocks are most clearly seen in Hα, and less clearly in the [S II] lines. If we examine radial velocity maps of outflow, we do observe what appears to be a slight asymmetry in the line-of-sight velocities transverse to the knots, which is seen in Figure 3.10. This is primarily observed in knots A and C, where the lower velocity features form a "shell" around the higher velocity emission. This is anticipated in Hα as this line traces the bow-shocks, and as the faster material in the flow approaches this region the shocked material is compressed and slows down relative to the pre-shocked flow. If the

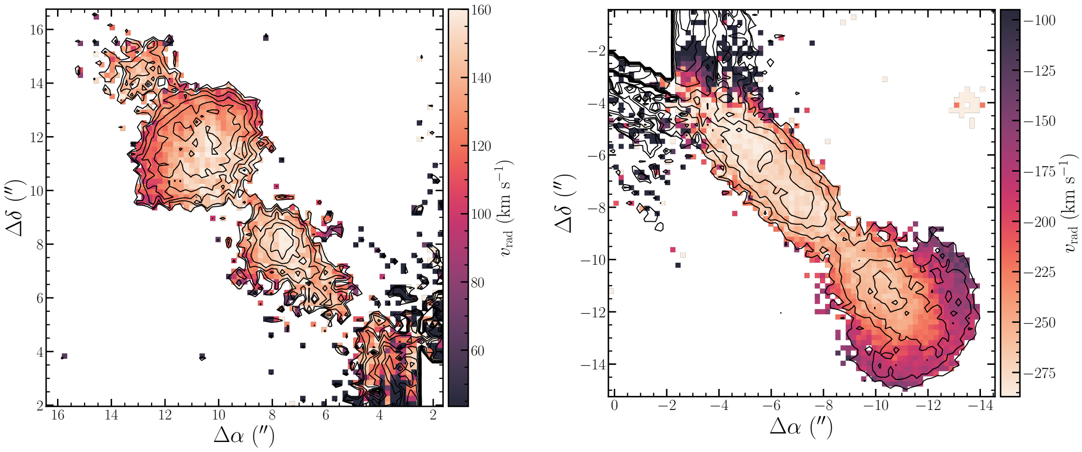

(a)

(b)

Figure 3.10: Radial velocity maps of the Hα line for the (a) red-shifted and (b) blue-shifted jet lobes.

inclination angle of the jet is varies with launch events and thus produce variable working surfaces within the flow, we might expect that the emission photocenters along the jet axis shift as well.

However, the proper motions study above focused primarily on comparisons with X-Shooter data, which provides only the magnitude of the motion and does not account for directionality beyond a general motion away from the source. Accounting for the proper motion vectors would require multi-epoch spatial imaging of the knots. Additionally, if we wished to explore the vectors and their relationship to the inclination angles of the knots, we would require each epoch of 2D images to be coupled with simultaneous spectral observations. While HST images do exist, the large gaps in time between observations would add a substantial degree of uncertainty to our calculations. While it may be that the analysis of the proper motion vectors could shed more light on the origins of the observed change in the centroids with distance along the jet, such a study is beyond the scope of this work. Instead, the focus is on the question of emission asymmetry within the knots themselves.

To determine whether the centroid pattern observed in Figures 3.7 and 3.8 is due to an intrinsic emission asymmetry in the knots, an effective PSF was constructed from the field stars discussed above. Next, we examined the spatial profiles transverse to each measured knot peak, focusing on knots A, A3, B, and D as these have the largest S/N. Then we extracted spatial profiles from inter-knot regions on either side of the knot, again choosing profiles with the strongest S/N. Finally, a spatial profile was extracted across the effect PSF in the same direction as the transverse knot cuts, and this profile was subtracted from the knot and inter-knot cuts in order to analyze the residuals. For this analysis all the profiles were normalized before subtraction, as the interest is in the relative size and direction of the residual peaks with respect to the center of the PSF.

From this it is seen that the residuals of the knot profiles exhibit strongly shifted peaks away from the jet axis, and that these peaks favor shifts in the negative direction with the exception of the Hα line, as this line primarily traces the bow shocks in the jet. In the cases of the knots, the residuals are primarily single-peaked, and where they are double-peaked it is found that one peaks is often significantly larger than the other. The residuals of the PSF-subtracted inter-knot profiles general exhibit shifted peaks as well, but these are far more noisy and in many cases peak opposite the knot residuals. As these profiles are generally wider than the knot profiles, particularly in the [S II]$\lambda\lambda$6716,6731 lines, we often find double-peaked residuals where on peak slightly dominates the other. The most representative knot and inter-knot residuals are shown in Figure 3.11. This behavior exists throughout the inter-knot regions with no clear systematic preference towards positively or negatively shifted peaks. We additionally observe a general trend toward more extended and asymmetric wings in the inter-knot regions, with the asymmetry of the profile generally favoring positive offsets from the jet axis.

This analysis leads us to conclude that the knots possess an intrinsic emission asymmetry that makes them present more brightly on one side of the axis than the other. This has been observed in other jets (see Hartigan, Holcomb, and Frank, 2019) and would cause changes in the Gaussian centroids between the knot and inter-knot regions, as seen in Figure 3.8. Curiously, we find that the red-shifted knots have a greater tendency towards asymmetry than those in the blue. This is seen in Figure 3.11 where the spatial profiles and PSF-subtracted residuals are compared for knots A and B. Perhaps most interesting is that knot A in the FELs is less pronounced in this asymmetry, while in Hα the asymmetry is quite stark. It could perhaps be that the age of the knot has an impact here, such as a decrease in brightness (Rich et al., 2020) or a more uniform distribution of the knot through time evolution. In the absence of a more detailed proper motion analysis, we conclude that an intrinsic emission asymmetry in the jet is believed to be the most reasonable explanation for our observations.

3.4.3 A Window into the Planetary System

In Section 3.3.2, we argue that the weak wiggling signature suggested by the data is unlikely to be real, and better explained by an asymmetry in either the PSF or the intrinsic emission of jet. To further confirm this, we explore this wiggle pattern using both orbital motion and precession models, following models set forth by Masciadri and Raga (2002), Anglada et al. (2007), and Murphy et al. (2021).

Wiggling in a ballistic jet has been suggested to arise due to the presence of a companion, where two models are generally posited. In an orbital model, a companion pulls the jet source away from the barycenter in the orbital plane, thereby inducing a deviation of the jet axis from the orbital axis. The precession model, on the other hand, suggests that the ejection axis of the jet precesses due to tidal interactions between the disk and a companion in a non-coplanar orbit.

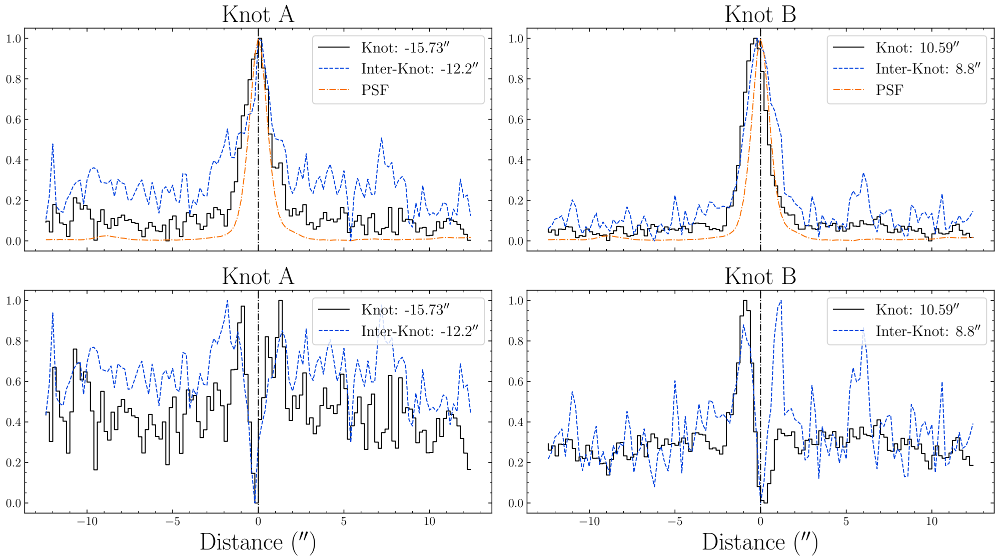

FIGURE 3.11: Representative spatial profiles (top) and PSF-subtracted residuals (bottom) for the [S II]λ6731 line. Transverse cuts each with a width of 1″ (5 pixels) are taken across the PSF and knot/inter-knot regions specified on the plots, and the profiles are normalized before subtraction. The center (in arcseconds) is taken to be the location of the peak of the PSF, as the primary concern is with the relative shifts in knot centroid positions. Note the differences in the knots B and C compared to A and A3, suggesting that the red-shifted jet is less symmetric than its blue-shifted counterpart.

Following Anglada et al. (2007), we express the shape of the jet (in its native coordinates) with the equation

$$\frac{x'}{r_o} = \kappa \frac{|y'|}{r_o} \sin\left(\kappa \frac{|y'|}{r_o} - \psi\right) + \cos\left(\kappa \frac{|y'|}{r_o} - \psi\right) \tag{3.1}$$

where $\kappa = v_o/v_j$ is the ratio of the orbital velocity to the jet ejection velocity, ψ is the phase angle, r_o is the orbital radius, and y' is the oriented along the orbital rotation axis. This primed coordinate system is related to coordinates in the plane of the sky by

$$x = \frac{x'}{D} \qquad\qquad y = \frac{y' \cos\phi - z' \sin\phi}{D} \tag{3.2}$$

where D is the distance (in parsec) to the source and ϕ is the inclination angle of the jet. As the inclination of the HD 163296 jet is not negligible, it is necessary to deproject the data by the above transformations before the application of any model.

If instead we explore the precession model, then the shape of the jet (following Murphy et al., 2021) is expressed by the equation

$$y = x \tan\beta \cos\left(\nu \left[t - \frac{x}{v_j \cos\beta}\right]\right) \tag{3.3}$$

where β is the half-opening angle of the precession cone, ν the precession frequency, v_j is the jet velocity, and t a phase parameter.

As each of these models assumes a companion, we express the binary separation between the source and the companion as a function of the orbital period:

$$a = (M_{\rm sys}\tau_o^2)^{1/3} \tag{3.4}$$

with $M_{\rm sys}$ being the total mass of the system and τ_o the orbital period. Boundaries on τ_o (and similarly, τ_p) are obtained through examination of the proper motion and spatial extent of the jet, setting upper and lower limits on the length scale and period it would be possible for us to detect. In the case of the orbital motion model, this can be used to set τ_o directly; for precession, this it taken simply as the precession period τ_p. Further, we can express the ratio of orbital and precession periods as a function of the mass fraction μ ($= M_{\rm comp}/M_{\rm sys}$) by

$$\frac{\tau_o}{\tau_p} = \frac{3}{8} \frac{\mu}{\sqrt{1-\mu}} \sigma^{3/2} \cos i_p \tag{3.5}$$

where the parameter $\sigma = R_d/R_p$ is the ratio of the radii of the companion and the disk, respectively, and i_p is the angle between the rotational axis of the disk and the planetary angular momentum vector (see Zhu, 2019). We assume $\sigma = 1$ and that $i_p < 1°$, which is similar to the precession angle. This relationship is chosen as the short precession periods in such a case imply a small companion orbiting at separations $\lesssim 1$ au.

In the case of HD 163296, the MUSE observations trace approximately $25''$ to either side of the source. We utilize the average jet velocity $v_j \simeq 0.4''$ yr^{-1} (see Section 3.3.1), and estimate that the maxmimum period which would show a clear deflection in the jet is approximately 150 yr, corresponding to a length scale $\lambda_{\mathrm{wiggle}} \simeq 60''$; similarly the minimum period is ~ 10 yr with a length scale $\lambda_{\mathrm{wiggle}} \sim 4''$. These provide upper and lower bounds of the parameter space excluded by our observations, as illustrated in Figure 3.12.

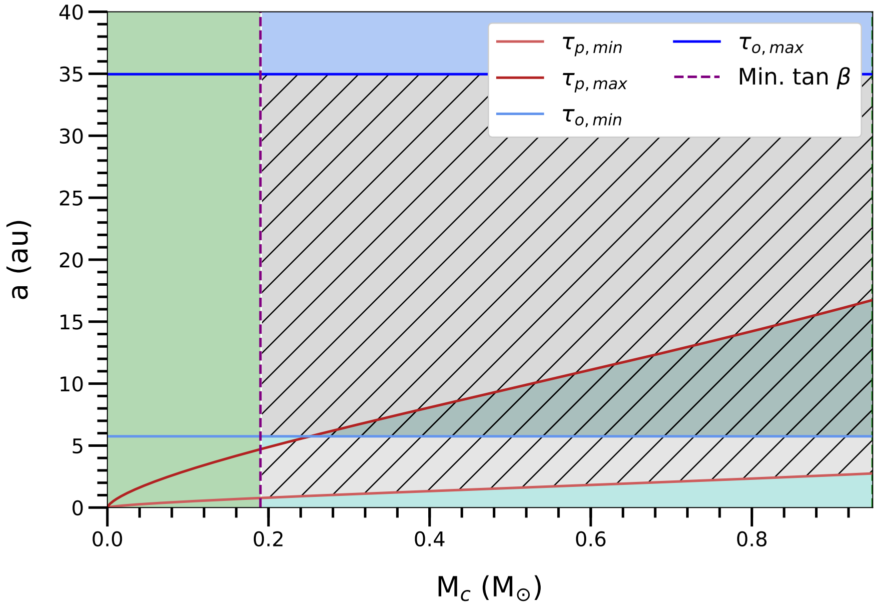

FIGURE 3.12: Parameter space of the possible companion ranges that are expected to produce a detectable jet axis wiggling in the HD 163296 outflow. The grey hatched regions indicate parameter regions excluded by our observations (where a companion would be likely to cause a wiggling due to either orbital motion or precession, corresponding to the upper and lower hatched regions, respectively). The region shaded in green (left) contains companion objects which would produce a wiggle opening angle too small to detect in our observations; the regions shaded in blue (top) and light blue (bottom) give companions with wiggling period too long or short, respectively, to be observed in these data.

We then consider the possibility of a wiggling in the jet on a length scale within our observable range, but with an amplitude too small to be detected. Fitting the apparent wiggle in the jet yields a half-opening angle $\beta = 0.2°$. Since any wiggle smaller than this is likely to go undetected, and since β is related to the maximum orbital velocity of a possible companion by $\kappa \leq \tan\beta$ (where $\kappa = v_o/v_j$), we can utilize this to set an upper limit on the maximum orbital velocity of a companion too small to produce a wiggling. This provides a lower mass limit from Figure 3.12. Finally, the maximum companion mass can be set from physical considerations, as it is unlikely for the companion to be more massive than the jet source (i.e. $M_c \leq 0.5\ M_{\mathrm{sys}}$). We can therefore construct bounds for the companion parameters excluded by the non-detection of a wiggling in this jet.

From Figure 3.12, the bounds set by these limits exclude jet wiggling due to the presence of objects greater than $\sim 0.1\ M_\odot$ with separations in the range $1-35$ au (the grey-shaded regions). A companion below $0.1\ M_\odot$ would not produce a wiggling amplitude large enough to be detected, while a companion of mass $> 0.1\ M_\odot$ at smaller or larger separations would produce a wiggling either too short or too long to be observed within the jet length we trace. We note that Figure 3.12 illustrates the two parameter regions which individually would be expected to produce a detectable wiggling motion, given the assumptions outlined above. This analysis shows that we would not expect to detect any of the planets inferred to be present from the studies of HD 163296 accretion disk using the jet wiggling method. It also tells us that if the periodicity of the jet holds and is caused by a companion at ~ 6 au, the companion must have a mass $< 0.1\ M_\odot$, i.e. a brown dwarf or planet, otherwise we would have expected to detect it.

Under what conditions would we expect to detect a planetary-mass companion from the HD 163296 jet? To explore this question we compute the anticipated jet shape for a $1.9\ M_\odot$ primary with a $10\ M_\mathrm{Jup}$ companion, which has a μ value of 0.005. A companion of such a low mass would most likely produce a jet axis deviation via precession in a close orbit. Assuming a precession period of 10 yr (that is, within the range observable from this jet), the precession model implies $v_o = 0.7$ km s^{-1} with $a = 0.09$ au from Equations 3.4 and 3.5. With a jet velocity of 235 km s^{-1} we can infer $\beta_\mathrm{min} \geq 0.17°$ due to the orbital motion. The observed β due to precession may be significantly larger as this is determined by the precession axis. Additionally, this minimum angle is inverse proportional to the jet velocity, so if $v_j \sim 100$ km s^{-1} then $\beta \geq 0.4°$.

Conversely, if we consider observing an orbital motion model, then $v_o = 0.1$ km s^{-1}, and the expected half-opening angle is $0.02° - 0.06°$, with larger values corresponding to lower v_j. Since the opening angle directly corresponds to the ratio v_o/v_j, this is not merely a lower limit. Considering a longer period of e.g. 100 yr we find even smaller β values; yet with a lower system mass $\sim 1\ M_\odot$ we derive larger β values.

From this it can be inferred that we are more likely to detect a small object through precession as opposed to orbital motion, as the corresponding precession angle will be larger in amplitude. Additionally, the jet axis deviation will be easier to detect for short precession periods (hence very short orbital periods), low-velocity jets, and lower-mass jet sources. This poses two limitations: first, that the precession wiggle will only give us an upper limit to the companion mass and is therefore unlikely to directly constrain this to a value of a few M_Jup or less; and second, that this method is most likely to detect planetary-mass objects as separations of < 1 au (Erkal et al., 2021a).

3.5 Conclusions & Future Work

In this chapter, a morphological study of the HD 163296 jet was presented, which included an examination of the jet width and axis position as observed in MUSE WFM. The main results indicate that the jet associated with this source is a rich and complex system. Importantly, we find that despite its maturity this is a relatively active source. We also explore the application of a "jet wiggling" model as a method for detecting the presence of close-in planetary mass companions. Additionally, future work is planned focusing on an in-depth study of the unique bow shocks HH 409 A and HH 409 C and the physical conditions within the jet. I briefly summarize the key conclusions with the following points.

1. The detection of three new knots – labeled B2a, A3a, and A4 – and a proper motions study challenge the 16 yr periodicity proposed by Ellerbroek et al. (2014), suggesting instead variable launching epochs. This is supported by the MUSE NFM observations of Xie et al. (2021), who additionally found a mass accretion rate of $\sim 10^{-10} - 10^{-9}\ M_{\odot}\ \mathrm{yr}^{-1}$, which is about two orders of magnitude lower than typical HAe accretion rates ($\sim 10^{-7}\ M_{\odot}\ \mathrm{yr}^{-1}$; see Mendigutía, 2020). This is noteworthy as it demonstrates that HD 163296 may be approaching the latter stages of the PMS phase, in which case we are fortunate to observe such activity in so mature a YSO.

2. We observe a regular deviation of the jet centroid emission from the jet axis, which has been observed in other jets and has been argued as a potential indication of a companion (Masciadri and Raga, 2002; Erkal et al., 2021a; Murphy et al., 2021). By directly comparing the emission centroids, jet FWHM, and knot position, we rule out the wiggling jet model as an explanation, and instead find evidence of an intrinsic emission asymmetry in the knots themselves which presents as a similar wiggling pattern. While unable to determine its exact nature, it seems reasonable that a combination of shocks in the jet and effects from the viewing angle may be contributors to this asymmetry.

3. Finally, the jet wiggling model is explored to determine whether this method can be useful for discovering planetary companions, and utilize the companion parameters present in recent literature (Teague et al., 2018; Pinte et al., 2018; Guidi et al., 2018; Rich et al., 2019; Rodenkirch et al., 2021). It is found that if we are to detect a planetary-mass companion with this method, it will be more likely to be inferred through precession of the jet rather than orbital motion. Importantly, we use the non-detection of a jet axis wiggling to rule out the presence of a companion greater than about $0.1\ M_{\odot}$ with separations between $1 - 35$ au.

Chapter 4

Proplyd 244-440

4.1 Introduction

In this Chapter I turn our attention to a member of a unique class of objects known as "proplyds" (**PRO**to-**PL**anetar**Y** **D**isk**S**) – YSOs which possess externally illuminated, photo-evaporating disks often surrounded by nebular structures and ionization fronts (IFs). With their discovery came the observations that many of them are associated with jets and HH objects (O'Dell et al., 1997; Bally and Reipurth, 2001; Ricci, Robberto, and Soderblom, 2008). In the Orion Nebular Cluster (ONC), the jets are typically one-sided and exhibit C-shaped curvature pointing away from the massive ionizing stars within the cluster. As such, these objects provide a fascinating glimpse into a more extreme end of the jet-launching phenomena, offering us a window into the durability of the launching mechanism.

Proplyds in the dense, inner regions of the ONC present us with a so-called "lifetime problem", as the measured mass-loss rates due to UV irradiation are too high and should evaporate the disk quickly (Clarke, 2007). However, NIR excess is still observed in $\sim 80\%$ of the ONC stars, implying their disks may survive longer than predicted. It further implies that either initial disk masses are large ($> 1\ M_\odot$) and therefore unstable, or that the massive O- and B-type stars have ages ≤ 0.1 Myr, which is short compared to the region average ($2 - 4$ Myr; see Beccari et al., 2017). Estimates of disk masses in the inner regions of the ONC have not generally been larger than $10^{-2}\ M_\odot$ (Henney and O'Dell, 1999), and more recent ALMA surveys have indicated a maximum dust mass of $\sim 80\ M_\oplus$ (Eisner et al., 2018). A combination of age spread and stellar dynamics, with the youngest stars migrating inward to the central regions, may help solve the lifetime discrepancy (Winter et al., 2019); however such a case is beyond the aim of this work. Nonetheless, this should have direct implications on the morphology of the jets and on the accretion/outflow connection in photoevaporated disks, granting deeper insights into the mechanics of jet launching and the impact of the environment.

The giant proplyd 244-440, known also as V* V2423 Ori and HH 524, is located at a distance of 400 ± 23 pc (Gaia Collaboration et al., 2021). With a width of $3''.5$ (~ 1400 AU), it is one of the largest proplyds in the ONC (Bally, O'Dell, and McCaughrean, 2000). It is not located in the inner core of the ONC, as its large IF of radius $\sim 2''$ (~ 800 AU) points towards θ^2 Orionis A (instead of the Trapezium cluster), located south-west of the proplyd and beyond the prominent photo-dissociation region (PDR) known as the "Orion Bar", as shown in Figure 4.1. Hubble Space Telescope (HST) images in Hα were interpreted by Bally and Reipurth (2001) as showing a nearly edge-on disk in silhouette with a size of approximately $0\farcs15 \times 0\farcs6$, and a tilted jet with a $\sim 15°$ difference between the jet axis and the disk minor axis. Bally, O'Dell, and McCaughrean (2000) further note that the star appears offset from the center of the disk by $\sim 0\farcs1$, and suggest a binary system where one star is hidden within the disk. Spectral observations of the source suggest that it is a low-mass star ($< 1\ M_{\odot}$; see Appendix B).

Henney and O'Dell (1999) initially proposed a total mass-loss rate for the proplyd of $\sim 1.5 \times 10^{-6}\ M_{\odot}\ \mathrm{yr}^{-1}$, although Winter et al. (2019) posit that this is an overestimation, suggesting instead a mass-loss rate on the order of $\sim 5 \times 10^{-8}\ M_{\odot}\ \mathrm{yr}^{-1}$. Direct estimates of the disk+envelope mass are difficult, but range from as high as $0.01\ M_{\odot}$ (Bally et al., 1998) based on millimeter measurements, to as low as $\sim 5 \times 10^{-3}\ M_{\odot}$ with the VLA (Sheehan et al., 2016).[1] While the values of Bally et al. (1998) suggest evaporation times $t_e \sim 10^4$ yr (see also Henney and O'Dell, 1999), those of Sheehan et al. (2016) and Winter et al. (2019) suggest $t_e \sim 0.1 - 0.2$ Myr, which ultimately set a lower limit on the age of the proplyd.

This Chapter presents the first detailed analysis of the bi-polar jet associated with this proplyd using the highest spatial and spectral resolution integral field observations to date. Particular focus will be placed on the unique morphology of the jet, with an aim to provide a possible explanation for its complex curvature.

4.2 Observations

Observations of the proplyd 244-440 were obtained on 23 October 2019 under program ID 104.C-096 (PI: C. F. Manara). The instrument was operated in adaptive optics (AO) assisted Narrow-Field Mode (NMF) under clear sky conditions, which allows sampling of the target with a pixel size of $0\farcs02\ \mathrm{pixel}^{-1}$. The image quality delivered by the AO was measured by fitting a Moffat function to the source (see e.g. the PSF-fitting in Chapter 3) at multiple wavelengths, resulting in an average seeing of $\sim 0\farcs14$. For at least 50% of the total observation, the coherence time of the laser (a measurement of the laser stability) was > 6 ms. The data was reduced using standard calibrations and recipes delivered with the MUSE pipeline (v2.8) through the ESO Reflex GUI tool (for a brief description of the MUSE data reduction pipeline, see Chapter 2; a more rigorous description is given in Weilbacher et al., 2020). A final cube was produced spanning the entire nominal wavelength range of the MUSE instrument ($\sim 4750 - 9350$ Å), with a field of view (FOV) of $8\farcs4 \times 8\farcs6$.

The final cube was further processed in Python to remove local continuum and nebular contributions, as discussed in Section 2.3.1. Additionally, to account for nebular background and foreground line emission a mean, local background spectrum was constructed for each sub-cube by sampling regions away from the proplyd envelope but close enough

---

[1] It is important to note that the VLA is free−free (FF) emission dominated, and while it is possible that the proplyds are FF dominated as well, this latter value is presented with caution.

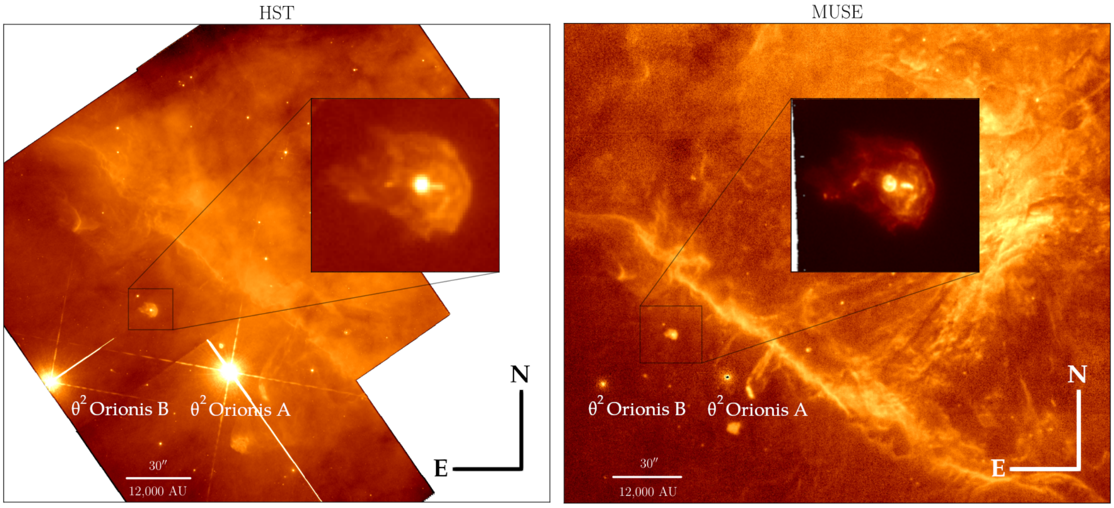

Figure 4.1: HST (left) and MUSE (right) field images of the region around 244-440. The fields and insets in both images are shown in the [O I] emission line. The stars θ^2 Orionis A and B are seen just below the proplyd to the southwest and southeast, respectively. The inset in the MUSE panel is a flux-integrated image from our current NFM observations discussed in Section 4.2.

to be representative of the background emission profile, and subtracted this from the subcube. The cubes were further corrected for extinction using the method in Section 2.3.4, with a modification that will be further explored below.

In addition to the MUSE NFM-AO data, two epochs of archival HST Wide-Field Planetary Camera (WFPC2) images were used to estimate the proper motions of the knots. The observations were obtained on 14 November 1995 and 17 September 1998 as part of the General Observer programs GO 5976 (PI: J. Bally) and GO 6603 (PI: C. O'Dell), respectively. I have focused on the F631N ([O I]λ6300, both epochs) filters in this study, which have total exposure times $t_{\rm exp}$ = 2100 s and $t_{\rm exp}$ = 1200 s respectively. Additionally, GO 5976 has observations in the F673N ($t_{\rm exp}$ = 2100 s) and F791W filters ($t_{\rm exp}$ = 200 s), and GO 6603 has observations in the F656N ($t_{\rm exp}$ = 600 s) and F814W filters ($t_{\rm exp}$ = 60 s). The jet is seen in the F631N and F673N filters, while only the envelope is seen in the F791W and F814W filters. A description of these observations can be found in O'Dell et al. (1997).[2] To increase the S/N, the images for each epoch were combined into two individual stacks. Each stack of images was then separately aligned to its own common reference frame in Python using the `mpdaf` function `align_with_image`, and median-combined the two epochs separately. The jet-free images for each epoch were finally subtracted from the [O I]λ6300 images to better isolate the jet emission, as shown in Figure 4.2.

---

[2] The science-ready data described here may be found on the MAST archive at `http://dx.doi.org/10.17909/y66h-8p10`.

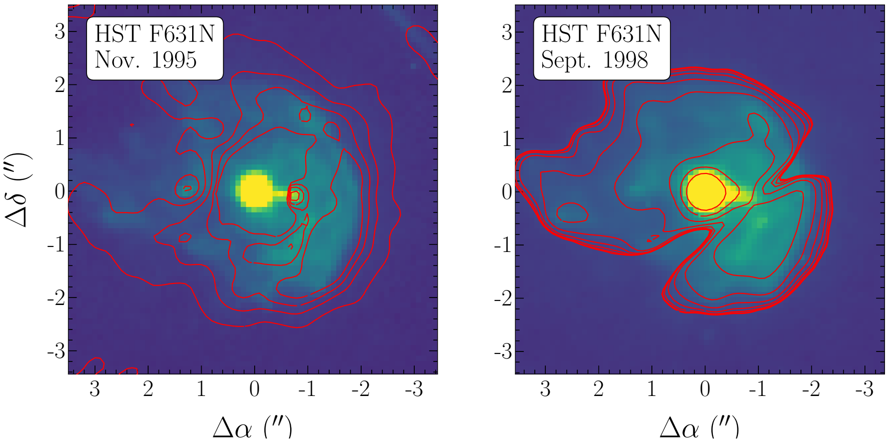

FIGURE 4.2: Median combined F631N images of the two HST epochs used in our proper motion study. The red contours are calculated from the residuals of the [O I]λ6300 − continuum images. The "indented" structure (right image) is due to the presence of a large diffraction spike in one of the stacked images.

4.3 Results

4.3.1 Morphology

Knot Identification in the MUSE Data

The angular size of the giant proplyd and the spatial sampling of MUSE NFM+AO allows for an unprecedentedly detailed view of the bipolar jet, which is detected in multiple emission lines as seen in Table B.1. In many cases, most notably the [O I] emission, one observes both the jet and the envelope. Lines such as [Fe II] and [Ni II] show pure jet emission, while others (e.g. [Ar III] or He I, which have higher ionization potentials) show the envelope and ionization front (IF). By comparing the different morphologies traced by different emission lines, it is possible to clearly identify the jet knots by removing the "contamination" by nebular and envelope emission. Figures B.2−B.4 show tri-color composites of the proplyd to demonstrate how the envelope and jet trace these different emission features.

Six distinct knots are identified with relatively strong S/N (> 10), which is computed by choosing an aperture focused on the knot emission and comparing the peak flux to a similarly sized aperture at a background position away from the source. Clumpy emission signatures at low S/N (< 5) are identified in at least two additional places. Not all knots are visible in the integrated channel maps due to integration over the entire emission range, while they are more clearly seen in smaller velocity channel maps. High velocity channels also show unresolved emission within $0\farcs3$ ($\sim$ 120 au) of the source. This is shown in Figures 4.3 and 4.4. A simple notation scheme is adopted where each knot is labelled according to its distance from the driving source, i.e. knot E1 is furthest from the source in the eastern direction while knot W3 is closest to the source in the western direction.

Knot	$\Delta\delta$ ($''$)	$\Delta\alpha$ ($''$)
E1	-0.4896	2.7336
E2	-0.5338	2.2182
E3	0.0070	1.4726
W3	-0.0793	-0.6504
W2	-0.1006	-0.8255
W1	-0.1177	-0.9649

TABLE 4.1: Offsets of the primary knots relative to the source in 244-440 measured in the MUSE data. The source position is taken to be $0''$. Knots labeled E_n correspond to eastern, red-shifted knots, while W_n refers to western, blue-shifted knots.

Eastern knots are red-shifted and western knots are blue-shifted, and these are labelled in Figure 4.5. The knot names and offsets relative to the source are given in Table 4.1.

Proper Motions

The current MUSE observations were compared with archival HST data to examine the time-evolution of the outflow. Blue-shifted emission is seen in the narrowband F631N and F673N filters, and red-shifted jet emission is faintly seen in the F631N filter. In both epochs of archival observations, the western jet appears as a continuous stream, making proper motions unreliable as the knots are unresolved. However, knots E1 and E3 are seen in the F631N images with the longer exposure times.

To estimate the positions of the red-shifted knots, a centroid fitting was performed on the knots E1 and E3 as well as the stellar profiles in both the median [O I]λ6300 and residual [O I]λ6300 images using 2D Gaussian functions. The relative offsets in the x- and y-directions are listed in Table 4.2. The largest uncertainty is in the 1998 observations due to the low exposure times. Additionally, knot E1 is very faint in both HST epochs, resulting in large uncertainties for its position. Figure 4.6 shows the relative knot offsets as a function of observation time and the best-fit line through the data, the slope of which provides a proper motion of 9.5 ± 1.1 mas yr^{-1}, corresponding to $\sim 15-19$ km s^{-1}. This is in agreement with typical tangential velocities of HH objects in the ONC (< 50 km s^{-1}; see Reiter, Smith, and Bally, 2016) and consistent with the values normally found in low-mass stars and sub-stellar objects (Whelan, 2014; Riaz et al., 2017).

The radial velocity can be calculated from centroid fits of the knots at each emission line with respect to the ONC flow velocity, resulting in an average value of $v_{\rm rad} = 56 \pm 10$ km s^{-1}, and thus an absolute jet velocity of the same order, about 60 km s^{-1}. The resulting jet inclination angle $i_{\rm inc} = \tan^{-1} v_{\rm rad}/v_{\rm tan} = 72.2° \pm 4.2°$ with respect to the plane of the sky is not consistent with the previous interpretations of a nearly edge-on disk, which would imply a much lower jet inclination. This is further discussed below.

These values additionally allow us to estimate a lower limit on the dynamical age $t_{\rm dyn}$ of the knots, as the jet must be at least as old as the time required for knot E1 to reach its present position. This knot is most distant with a deprojected angular separation of $\sim 2\farcs8$ (~ 1120 au) yielding $t_{\rm dyn} \sim 300$ yr.

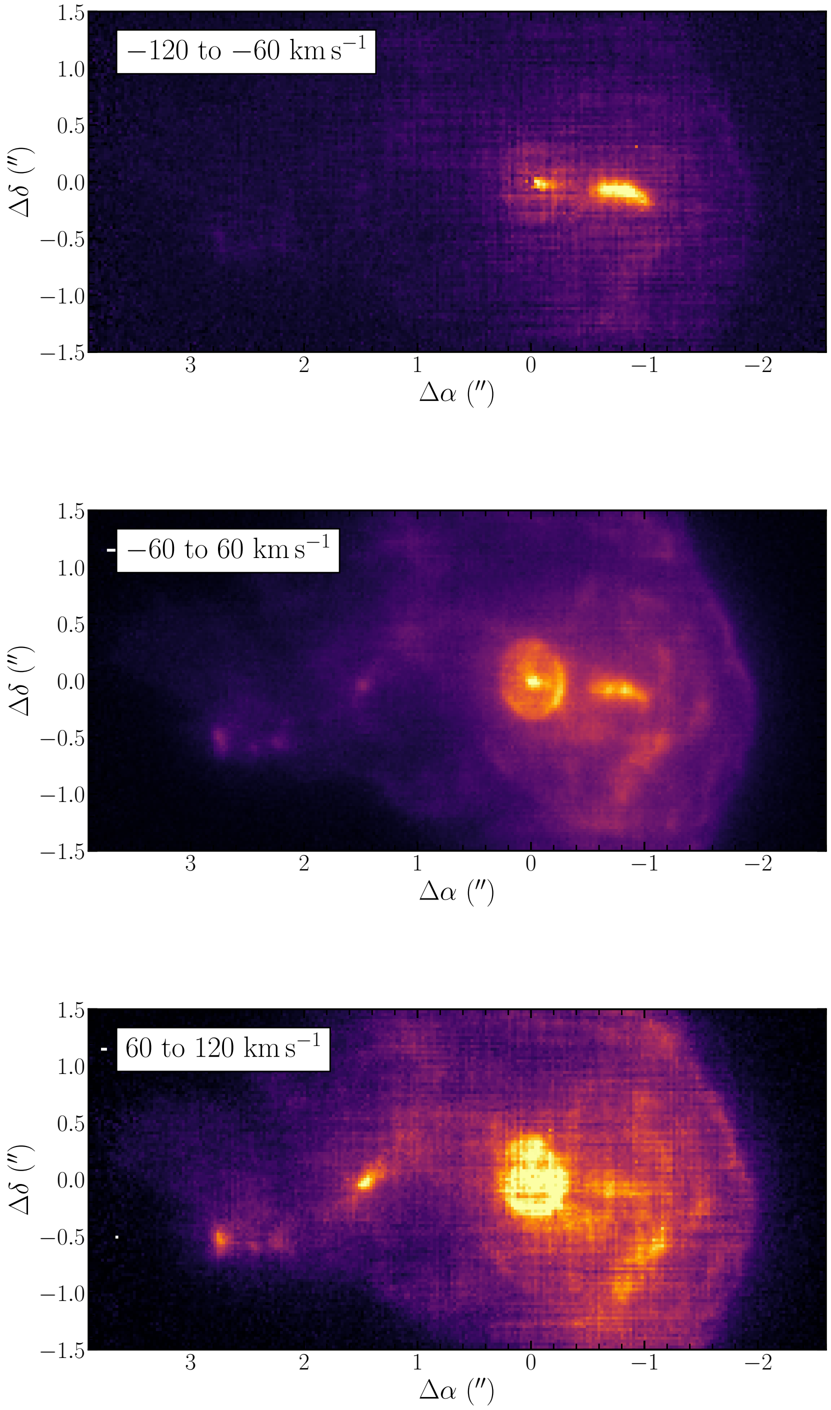

FIGURE 4.3: Velocity channel maps of the [O I]λ6300 line in the MUSE data.

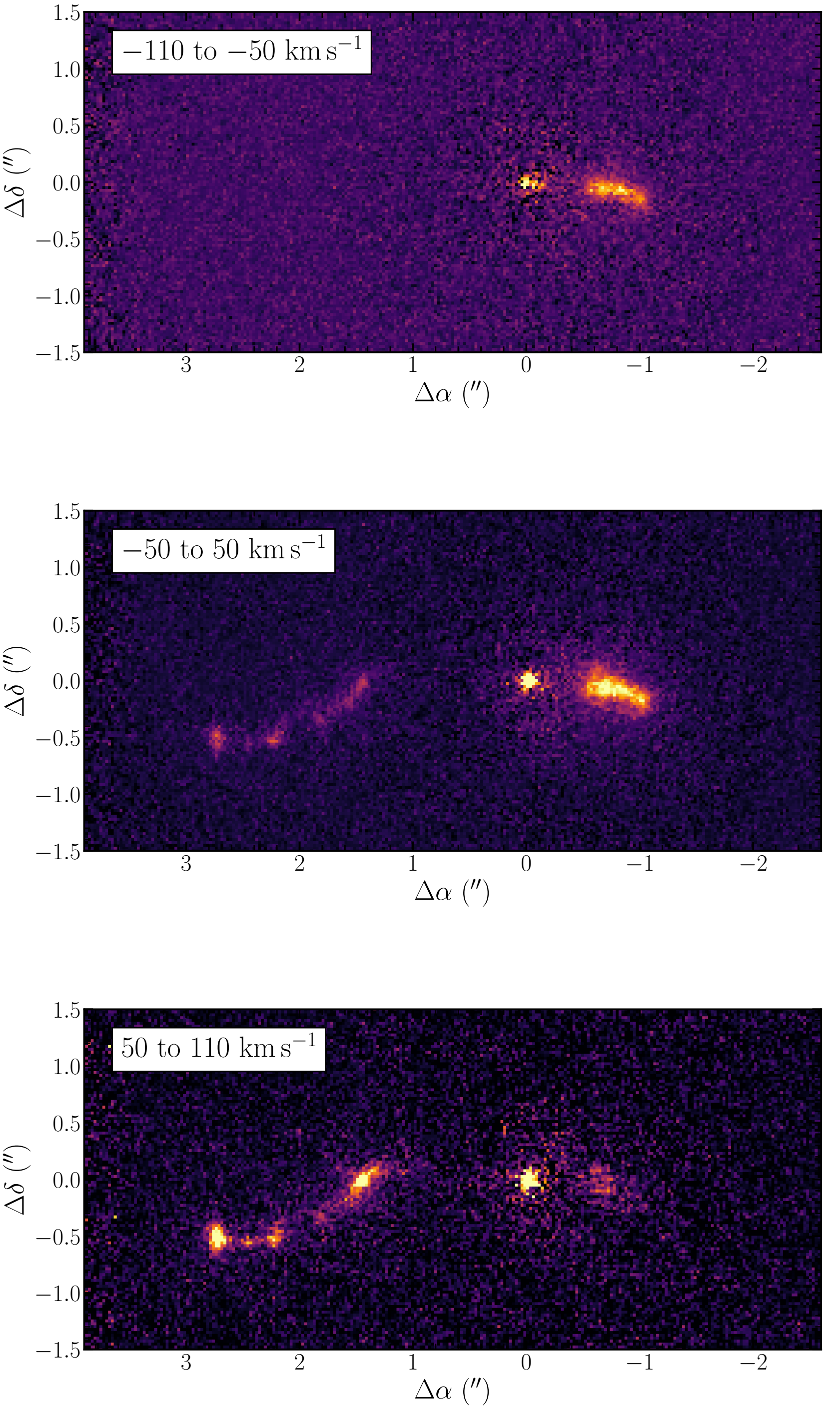

FIGURE 4.4: Same as Figure 4.3, but for the [Fe II]λ7155 line.

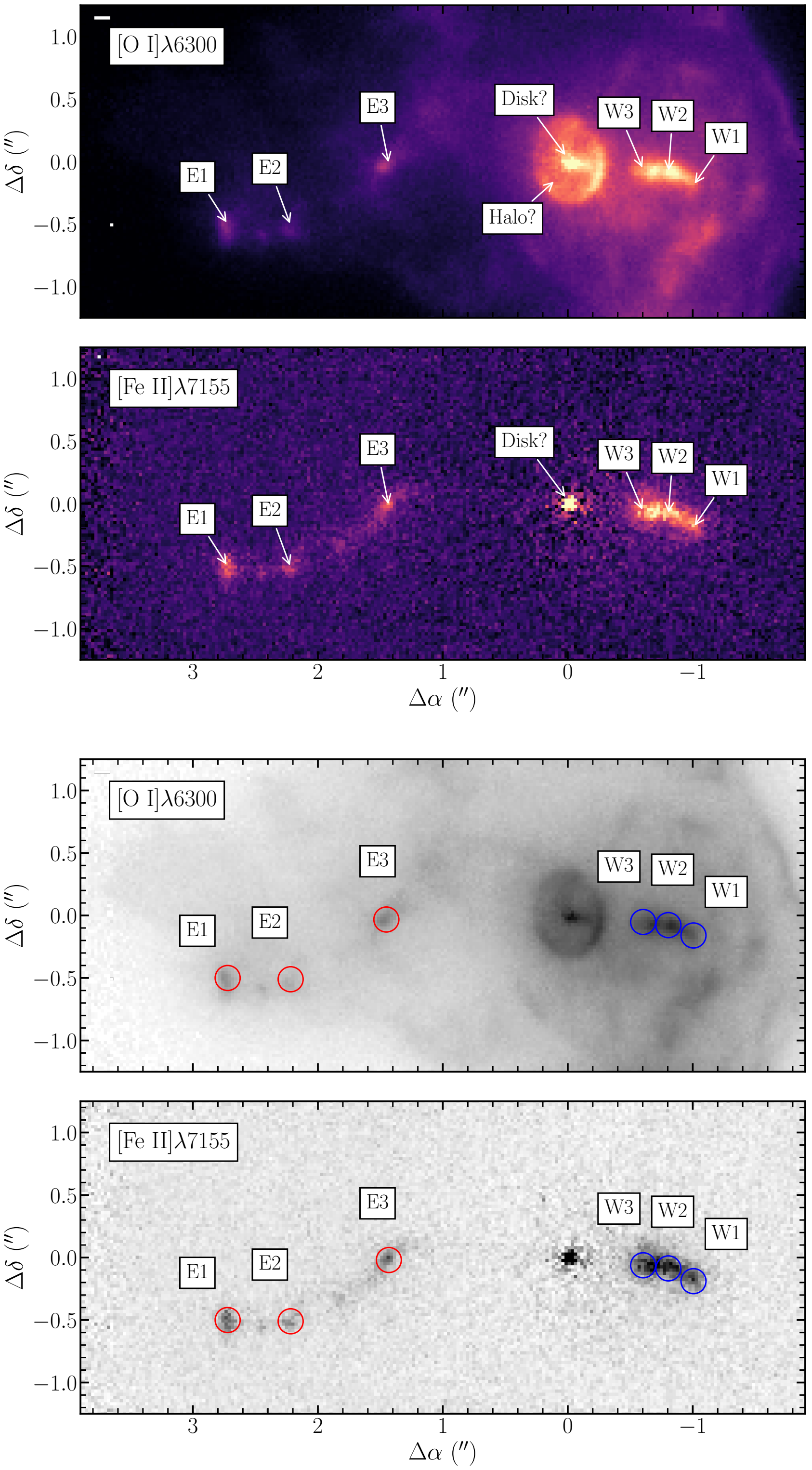

FIGURE 4.5: (a) MUSE images of 244-440 in [O I]λ6300 (top) and [Fe II]λ7155 (bottom) with the identified knots labeled. Emission is seen very close to the source, but whether this is the disk or the jet is undetermined. The tentative disk and halo have also been noted in the [O I] images at the top. (b) The same images in greyscale, with the red- and blue-shifted knots indicated by colored circles.

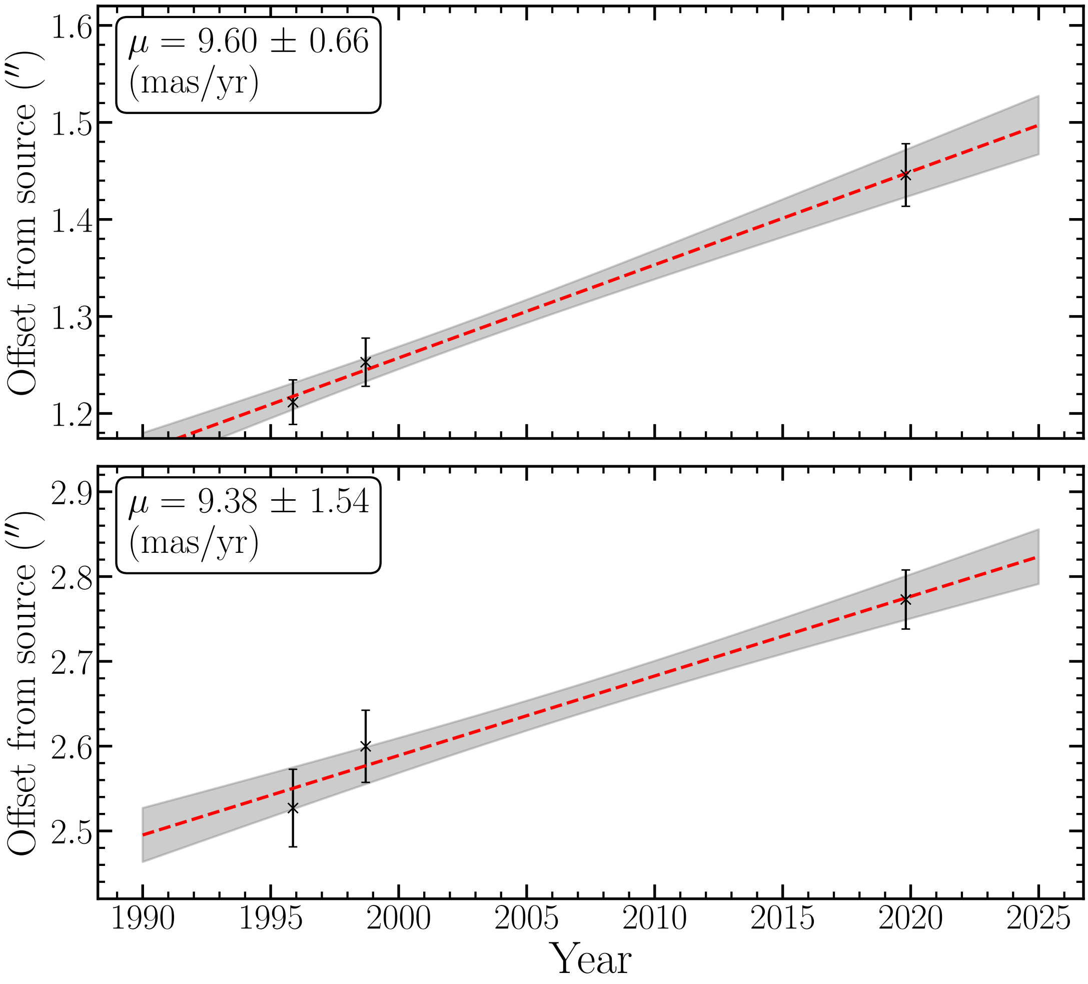

FIGURE 4.6: Relative knot offsets for the three epochs of observations. A weighted least-squares fit is plotted in red and indicates a proper motion of 9.60 ± 0.66 mas yr^{-1} for knot E3 (top) and 9.38 ± 1.54 mas yr^{-1} for knot E1 (bottom). The filled gray bars indicate the 1σ uncertainty of the fits.

Obs. Date	E1			E3		
	$\Delta\delta$ ($''$)	$\Delta\alpha$ ($''$)	P.A. (°)	$\Delta\delta$ ($''$)	$\Delta\alpha$ ($''$)	P.A. (°)
1995 Nov 14	−0.4358	2.4981	99.9	0.0497	1.2106	87.7
1998 Sep 17	−0.4266	2.5646	99.4	0.0808	1.2502	86.3
2019 Oct 23	−0.5018	2.7272	100.4	0.0145	1.4457	89.4

TABLE 4.2: Relative offsets and PAs for knots E1 and E3 calculated from the three epochs of observations.

Jet Curvature

The presented MUSE data allow us to observe, for the first time, the red-shifted jet and its strong curvature. The [O I]λ6300 line shows the morphology of the jet and the direction of the IF. As θ^2 Ori A is the dominant ionization source east of the Orion Bar (O'Dell, Kollatschny, and Ferland, 2017), one would expect it to contribute the greatest amount of radiation. The radiation contribution from θ^2 Ori B is not as powerful but is likely non negligible. Indeed, in Figure 4.5 we observe knot E3 in the red-shifted jet with what may be a bow shock pointing approximately 50° north through east, congruent with a wind for Ori B, and the curvature traced by knots E2 and E1 appears to be in agreement with a strong wind from θ^2 Ori A that is deflected in part by a lesser wind from θ^2 Ori B. Additionally, we see in Figure 4.5 a distinct asymmetry in the outflow scale, with the red-shifted jet having a larger angular displacement that its blue-shifted counterpart. As the eastern jet flows downstream with respect to θ^2 Ori B, it may be that crossing the photoionization front and associated shocks, or even puncturing through the envelope, highly disturbs the western jet such that it appears truncated.

4.3.2 Physical Properties of the Jet

The environment in the Orion region presents a unique opportunity to examine the physical conditions of outflows and compare what we can observe in irradiated proplyds with what is known about more isolated outflow conditions. The electron densities and electron temperatures in the proplyd structure are key elements for determining the mass-loss rates of proplyds (Reipurth and Bally, 2001b), and are integral in understanding the nature of stellar evolution on the whole (Ray and Ferreira, 2021). Accurate flux measurements are thus necessary to explore the physical conditions of the proplyd jets. In this section I will discuss some difficulties with traditional diagnostic determinations, the role of extinction, and finally I will examine emission line ratios to explore what diagnostic tools can be applied to this object.

In this analysis, knot fluxes are extracted using circular apertures ($r = 3$ pixels or 0.″075) centered at the positions given in Table 4.1. These fluxes were then corrected for extinction as discussed in Section 2.3.4, and shown in Table 4.3. In lines where the observed flux in a combination of the knot and envelope emission, apertures of the same size were used to extract fluxes nearly in the envelope to estimate the proplyd contribution and subtract these from the knots. Examples of this are shown in Figures 4.7 and 4.8.

Diagnostic Difficulties

As discussed above, the physical conditions in the jet are key to understanding the evolution of the star. The difficulty posed by proplyds, however, is that their densities often exceed the critical limits of traditional diagnostic ratios, such as [S II], [O I], and [N II] (see Bally et al., 1998; Henney and Arthur, 1998; Mesa-Delgado et al., 2012, for a deeper discussion).

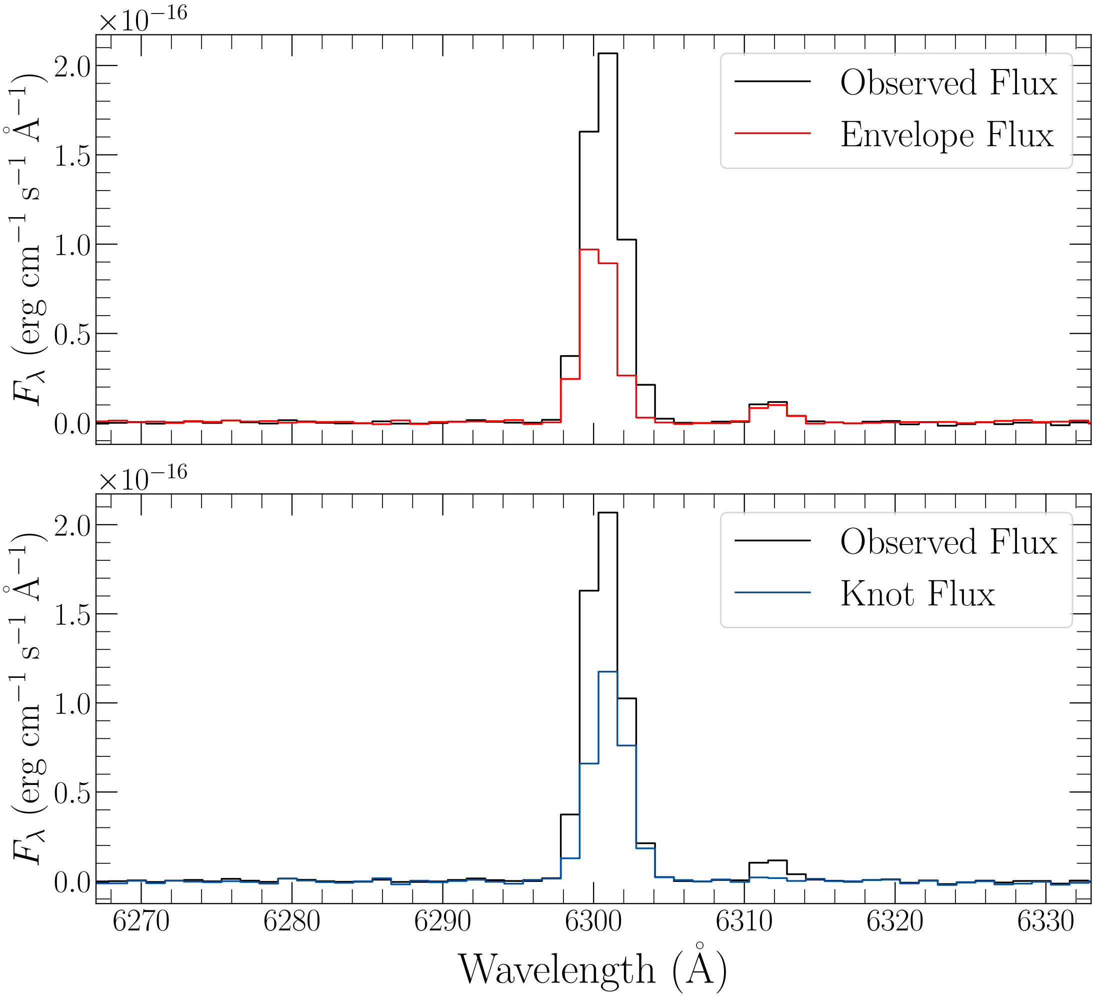

FIGURE 4.7: Spectral profiles of the observed flux, envelope flux, and intrinsic knot flux. The top panel compares the observed and envelope contributions, while the bottom shows the observed and intrinsic residual. The spectra are of knot E3 extracted from the [O I]λ6300 line.

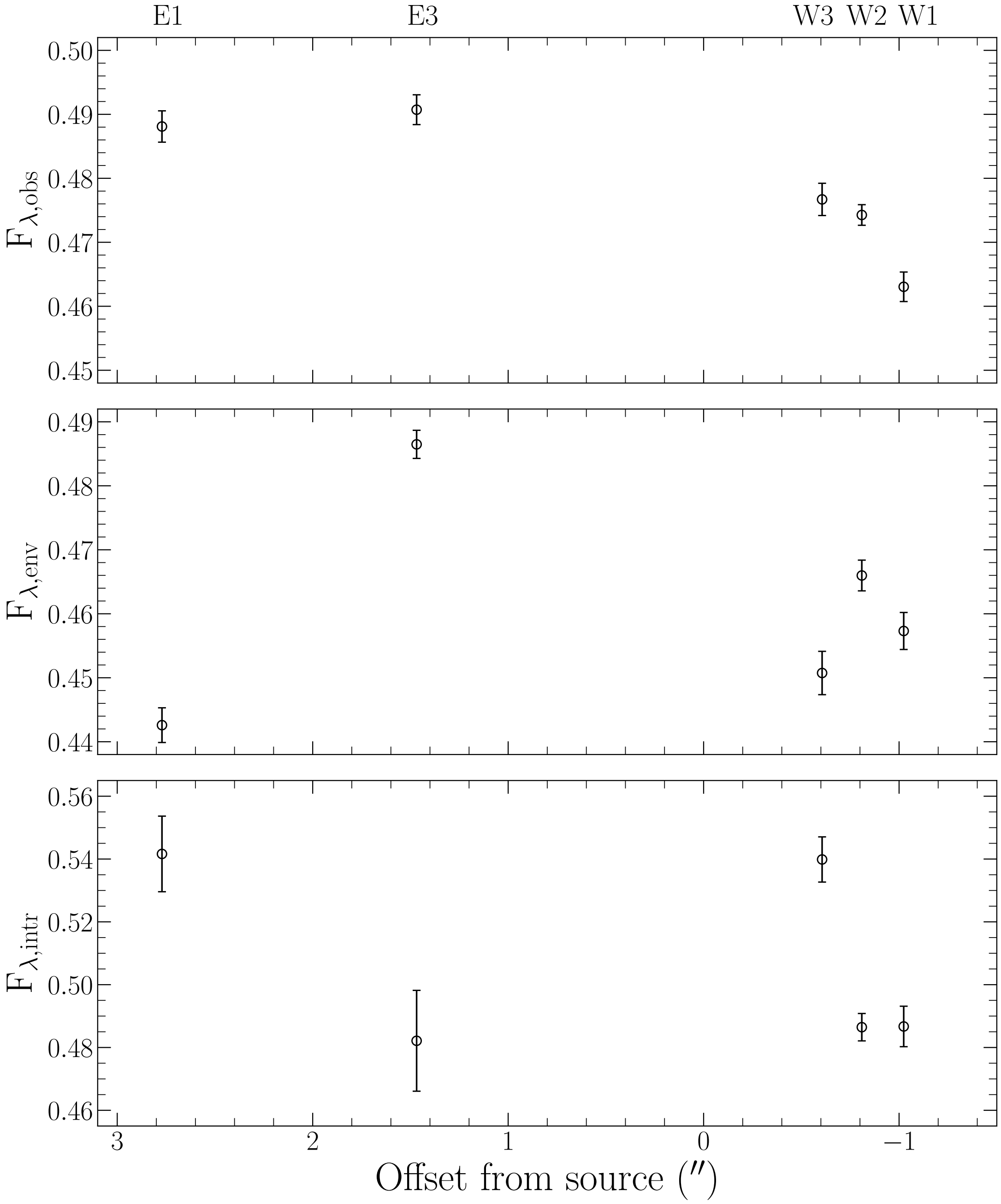

FIGURE 4.8: Ratios of the [S II] emission line for the total observed flux (top), envelope flux (center), and jet flux (bottom). The jet flux is estimated by subtracting nearby envelope flux from the total observed flux and correcting for the intrinsic proplyd extinction.

$\lambda_{\rm air}$ (Å)	Ion	F_{E1}	F_{E2}	F_{E3}	F_{W3}	F_{W2}	F_{W1}
5158.8	[Fe III]	...	...	...	...	14.87	13.23
6300.3	[O I]	70.15	26.98	73.41	160.32	183.44	99.47
6363.8	[O I]	23.47	7.47	25.75	53.78	60.33	39.66
6716.4	[S II]	15.48	...	15.95	52.92	71.16	49.25
6730.8	[S II]	28.59	...	33.08	98.02	146.27	101.20
7155.2	[Fe II]	11.88	8.38	11.03	20.39	19.78	17.19
7172.0	[Fe II]	2.71	2.47	2.99	6.45	5.72	4.80
7255.8	[Ni II]	...	...	...	...	7.89	4.27
7320.0	[O II]	71.86	31.25	46.76	...	...	...
7330.2	[O II]	54.27	23.45	36.61	...	...	...
7377.8	[Ni II]	8.11	4.82	5.72	12.36	12.77	12.22
7388.2	[Fe II]	2.10	...	...	3.35	3.20	2.80
7411.6	[Ni II]	1.29	...	...	...	1.68	2.04
7452.5	[Fe II]	2.83	2.23	...	5.78	5.81	5.65
8578.7	[Cl II]	2.64	...	...	3.74	2.36	5.51
8617.0	[Fe II]	13.64	9.27	12.27	23.93	23.47	20.48
9052.0	[Fe II]	...	...	...	6.44	5.54	4.46

TABLE 4.3: Dereddened mission line fluxes for the knots in the Proplyd 244-440 jet, in units of 10^{-17} erg/s/cm^2. Line fluxes were computed through the Gaussian fitting of spectral profiles extracted from the aperture sizes given in Section 4.3.2 The average uncertainty in the lines fluxes is ~5 × 10^{-18} erg/s/cm^2, which we calculate from the RMS noise in adjacent portions of the spectrum. Empty entries denote positions where either no knot emission is observed or the emission is below the detection threshold, or the knot emission could not be reliably disentangled from the proplyd envelope.

Additionally, such techniques as those proposed by Bacciotti and Eislöffel (1999) (the so-called "BE" technique) rely on ratios of O, S, and N. However, due to the lack of reliable flux measurements in [S II] and [N II], the BE technique cannot be used here.

To test if the above is the true for this object, flux integrated images were produced of the [S II] doublet and used to explore the brightness ratios of the two lines. For this the continuum-subtracted (but not nebula-subtracted) cubes were used in order to compare background emission with that of the proplyd. In Figure 4.9, two histograms of the [S II] emission lines are shown with the joint correlation in the corner in 200 pixel bins. The upper and lower red dotted lines correspond to the high- and low-density limits, with ratios of 1.45 and 0.45 corresponding to electron densities of $> 10^5$ cm^{-3} and < 100 cm^{-3} respectively. It is seen that much of the brightness is in the high-density limit, which is expected as the proplyd dominates the FOV in the MUSE NFM data.

A brightness partition of the full image was created to explore this further, which is shown in Figure 4.10 as a cumulative distribution of the ratios as a function of electron density. This segments the full image into four classes: very faint, faint, bright, and very bright. In the very faint partition the background dominates, producing a broad distribution with a median of ~ 0.6, which corresponds to $\sim 3 \times 10^3$ cm^{-3} and is in reasonable agreement with density measurements in this region (see Méndez-Delgado et

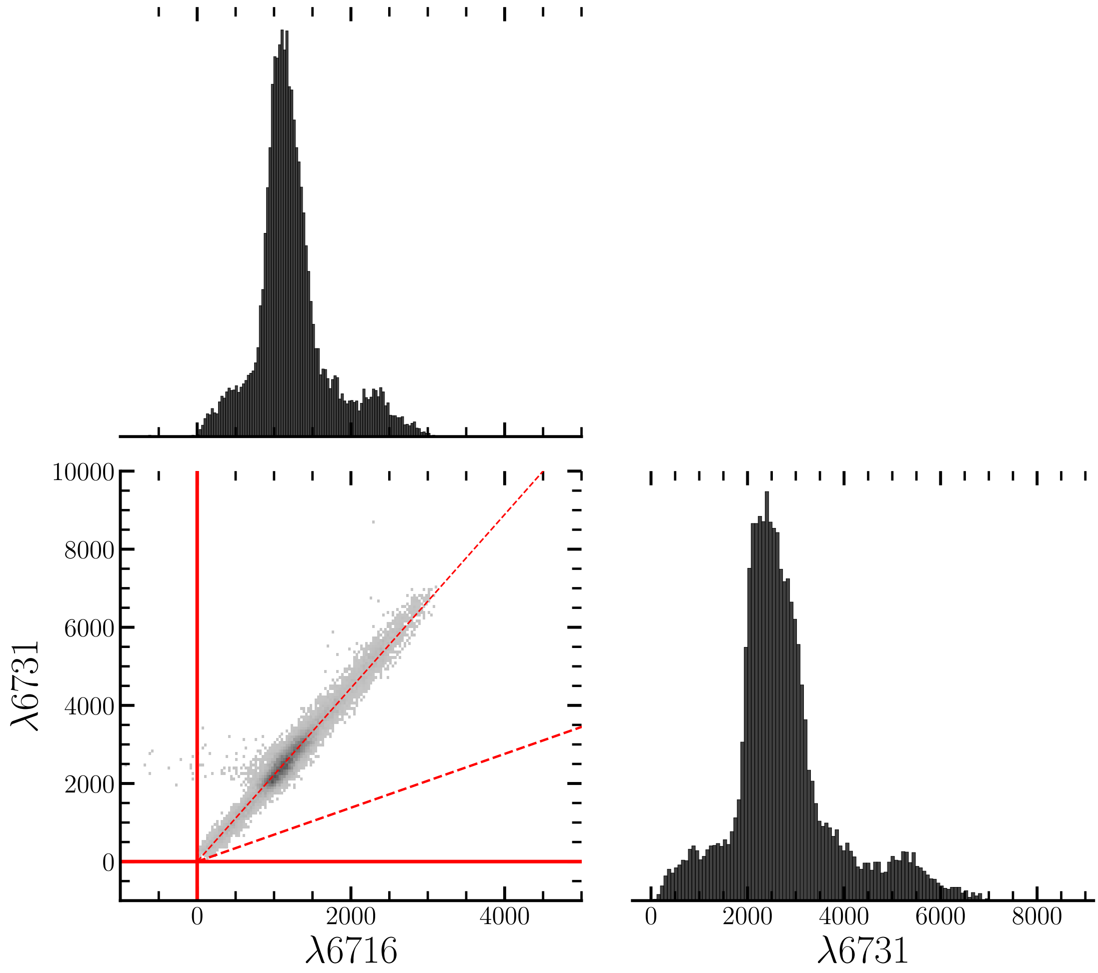

Figure 4.9: Brightness correlations for the [S ii] doublet across the entire MUSE NFM FOV. The side plots display the histogram distributions of each region for each emission line, while the central plot presents the ratio. The upper dotted line corresponds to the high-density limit, and the lower dashed line corresponds to the low-density limit. Brightness is given in units of 10^{-20} erg cm^{-2} s^{-1}.

al., 2021). The distribution for the other partitions trends linearly with brightness towards the high density limit on the left-hand side, implying n_e values approaching or exceeding 10^5 cm^{-3} in these regions. If the images are sub-sectioned into smaller boxes encompassing emission regions of interest, this trend is seen more clearly, with the background regions exhibiting a broad spread that generally falls within the permitted regions and the west and east regions of the proplyd falling along the high-density limit line (see Figure 4.9 as well as Figure B.4). This will be further discussed below in Section 4.4.

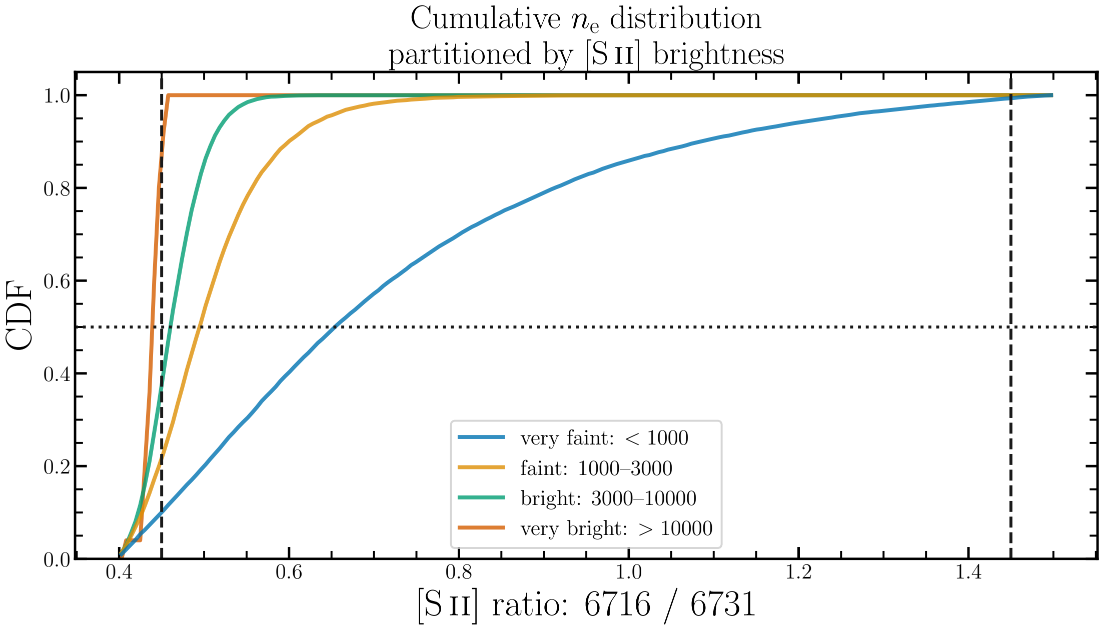

FIGURE 4.10: Cumulative distribution of the partitioned [S II] brightness as a function of electronic density n_e for the entire [S II] image. The high- and low-density limits are given by the vertical dashed lines to left (0.45) and right (1.45). The brightness limits (in units of 10^{-20} erg cm^{-2} s^{-1}) are given in the legend, with a trend towards the high-density limit corresponding with an increase in brightness.

Alternative density-sensitive lines are seen in our data, primarily the forbidden Fe lines, which can be a powerful diagnostic tool for tracing denser emission regions (Podio et al., 2006). Additionally we observe [Ni II] emissions, which can be used to probe the role of fluorescent excitation as well (Lucy, 1995; Giannini et al., 2015).

Extinction

Extinction plays a critical role in the analysis of the proplyd. Its quantification is further complicated by the role of extinction in the envelope of the proplyd as well as the photo-evaporated and photoionized flow itself (Henney and O'Dell, 1999; Mesa-Delgado et al., 2012), and the difficulty in determining what amount of nebular emission occurs in the forefront of or behind the proplyd envelope. Since the dust within the proplyd is not well known, these issues make disentangling the intrinsic proplyd emission from the nebular cloud – and by extension, the jet from the envelope – a difficult procedure.

Following the method discussed in Chapter 2.3.4, what we observe is that there is a clear morphological difference between background extinction and extinction due to dust in the proplyd envelope. The envelope displays a clumpy but still fairly uniform structure, with the IF having the highest extinction. Examining the extinction in adjacent regions and within the proplyd reveals a general trend towards higher extinction in the proplyd than in the nebular, as anticipated for a dusty envelope. This is shown in Figure 4.11.

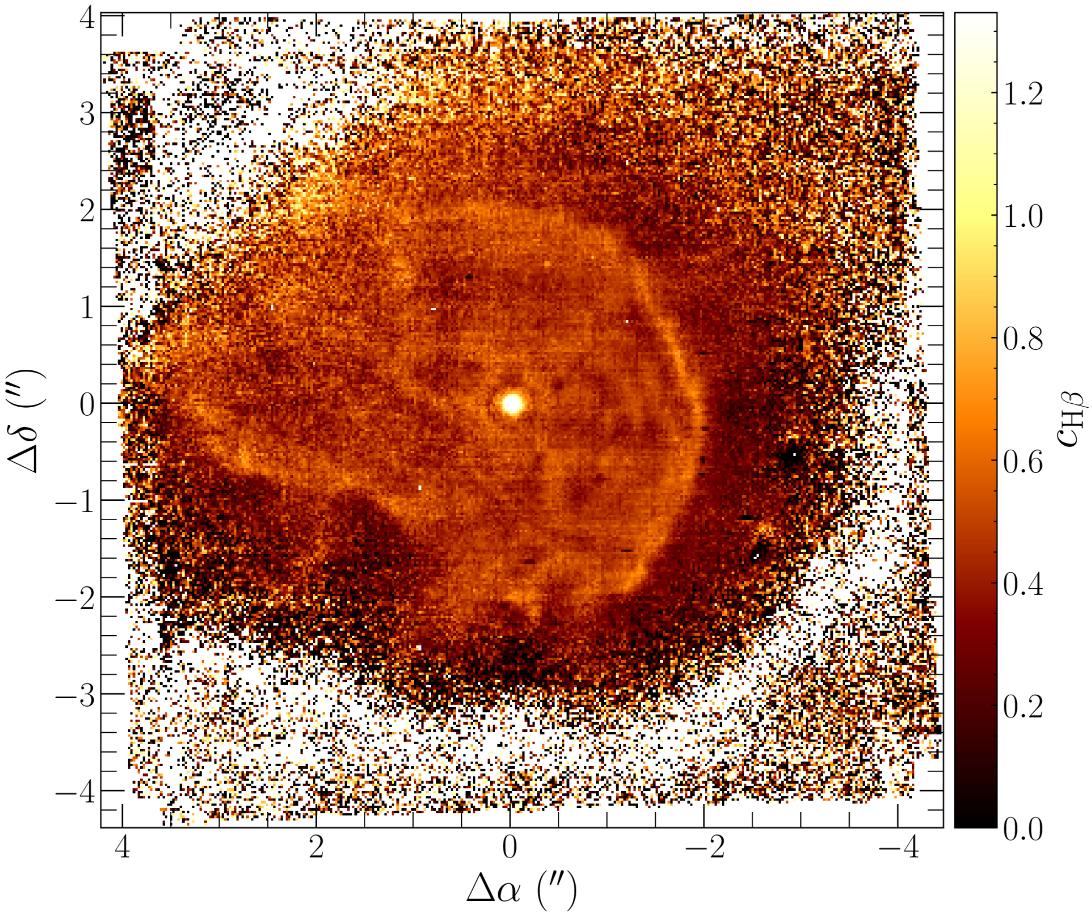

FIGURE 4.11: An example of an extinction coefficient map computed with `PyNeb`. For this object, a general trend of approximately $0.1 - 0.2$ dex difference is observed between the background and the proplyd envelope.

Using this map, regions are selected adjacent to and within the proplyd envelope to calculate a representative $c(\mathrm{H}\beta)$ value. Under the assumption that foreground and adjacent background extinction from the Orion nebula is relatively uniform in this FOV, an intrinsic proplyd extinction $c(\mathrm{H}\beta)_p$ is estimated as the difference between the nebular extinction ($c(\mathrm{H}\beta)= 0.44 - 0.45$) and that of the proplyd envelope ($c(\mathrm{H}\beta)\simeq 0.6$) such that $c(\mathrm{H}\beta)_p = 0.15$. This intrinsic reddening coefficient is similar to what is found by Mesa-Delgado et al.

(2012) for other proplyds closer to the Trapezium cluster. With this intrinsic reddening coefficient, the corrected flux can be expressed by

$$F_{\lambda,p} = F_{\lambda,t} - F_{\lambda,b} 10^{-c(\mathrm{H}\beta)_p \left(1+f(\lambda, R_{V,p})\right)}, \tag{4.1}$$

where subscripts p, t, and b denote the intrinsic, total, and background values respectively, and $f(\lambda, R_{V,p})$ is a standard reddening law (in this case that of Cardelli, Clayton, and Mathis (1989)).

Due to this small intrinsic extinction, the correction here is simplified by taking a constant $c(\mathrm{H}\beta)$ value of 0.45 for all calculations. To eliminate the nebular contribution, a sample of background regions is selected away from the proplyd envelope and utilized to construct a mean representative spectrum, which is subtracted from every pixel in the continuum-subtracted cubes. In order the check that this approximation is reasonable, flux correction was done according to Equation 4.1 as well as with a constant $c(\mathrm{H}\beta)$ value and the results compared. The fluxes were found to differ by negligible amounts, and thus the simplification was deemed appropriate.

Shock and Photoionization

The fluxes measured in Table 4.3 were used to estimate line ratios and compare with those given in Table 2 of Giannini et al. (2015) to test for fluorescent excitation. The predicted collisional+fluorescent excitation ratio for the [Ni II]λ7411/7378 line is given as 0.34, while the collisional case is given in the range $0.05 - 0.07$; in the MUSE data we observe ratios from $0.13 - 0.17$. The [Fe II]λ7155/8617 ratio is in the range $0.8 - 0.9$, which is higher than both collisional and collisional+fluorescence predictions.[3] These are shown in Figure 4.12. These results indicate that while fluorescent pumping does appear to enhance emission it is not the dominant process, which is expected as optical lines such as [Fe II] are more likely to arise from collisional excitation than photoexcitation (Bautista, Peng, and Pradhan, 1996).

Mass-Loss Rate in the Jet

In Section 4.3.2 I discussed the difficulty posed by the general densities of proplyd envelopes. Similarly, the lack of jet emission in temperature-sensitive lines further complicates traditional diagnostic techniques, introducing uncertainties to determination of the electron density. However, it is noted that the mass-loss rate is only weakly dependent on the electron temperature and so we can set reasonable bounds on some physical parameters. Estimations are made based on Figure 4.13 where the observed [Ni II] ratios imply electron densities 7×10^4 cm$^{-3} \leq n_e \leq 2 \times 10^5$ cm^{-3}. The [Fe II] ratios similarly imply electron densities $\sim 10^5$ cm^{-3}. As the [Fe II] and [Ni II] ratios for the observed knots exhibit relatively small scatter in their respective emission lines (see Figure 4.12), a mean density of $n_e = 1.3 \times 10^5$ cm^{-3} at $T_e = 8200$ K is assumed.

---

[3] The λ7453Å line is omitted here due to the low S/N.

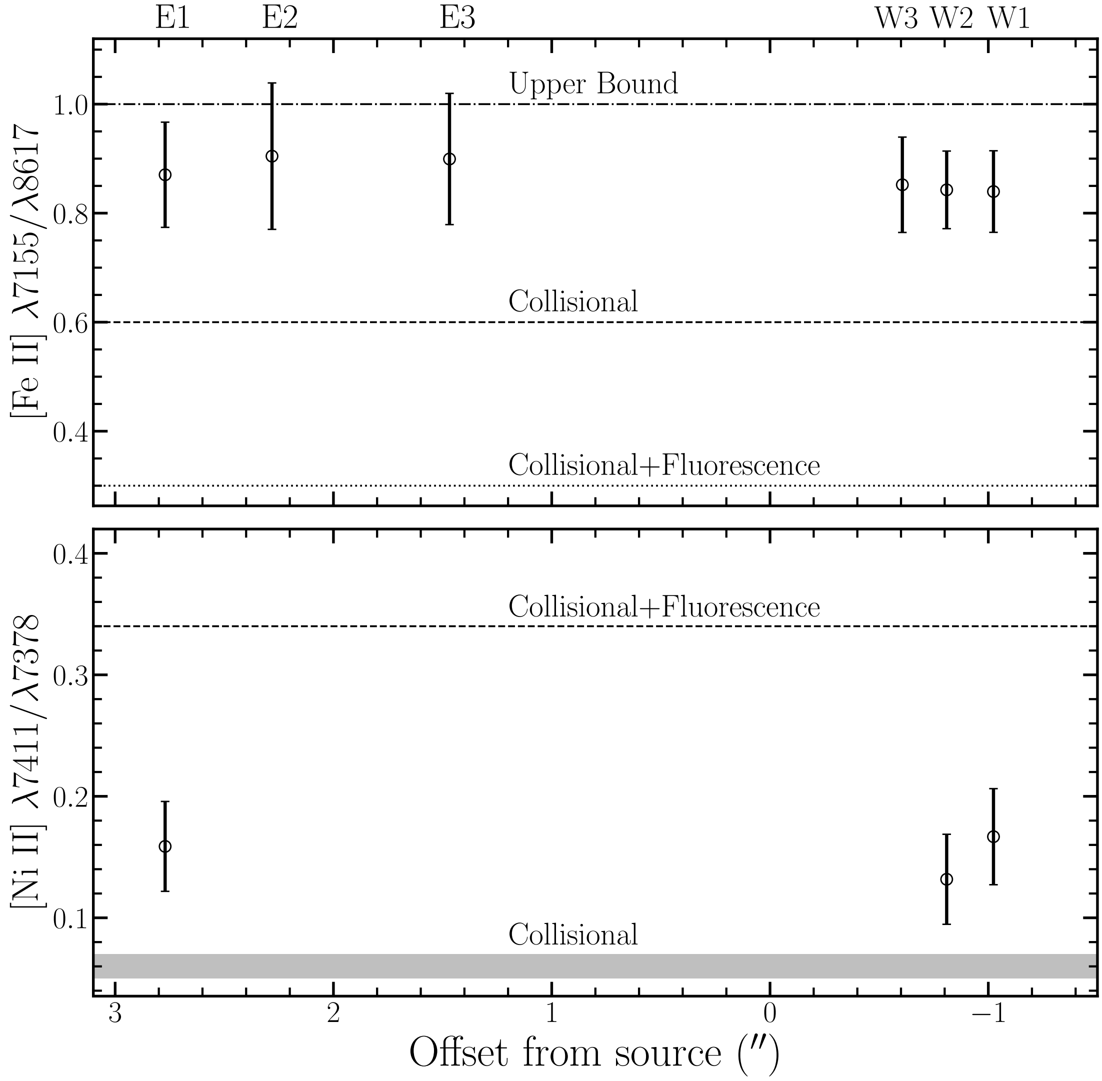

FIGURE 4.12: Emission line ratios of the [Fe II] and [Ni II] lines sensitive to fluorescent pumping. Horizontal lines indicate the predicted ratios for each case, taken from Giannini et al. (2015).

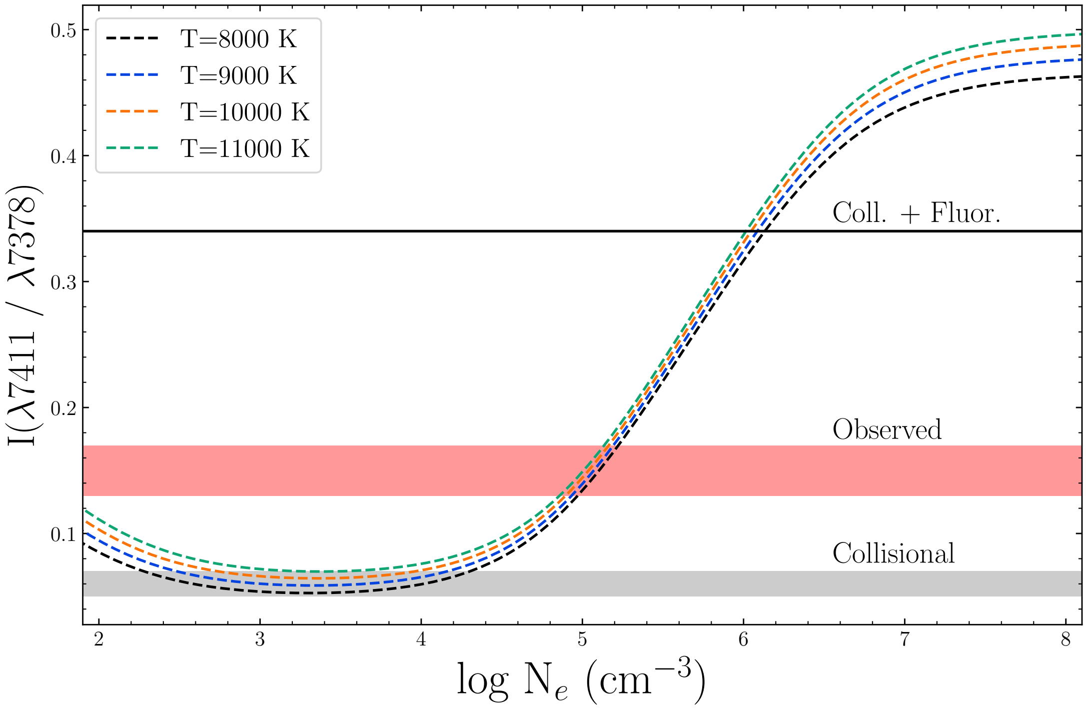

FIGURE 4.13: Emissivity ratio of the optically forbidden Ni emission line, calculated in `PyNeb`. The dashed curves are the emissivity ratios calculated for each given temperature. The gray region denotes the predicted range of ratios for collisional excitation. The red region denotes the range of values we observe in our data. The solid black line denotes the predicted ratio for collisional+fluorescent excitation. The predicted values are taken from Giannini et al. (2015) assuming $T_e = 10,000$ K and $n_e \sim 10^3 - 10^5$ cm^{-3}.

Knot	[O I]λ6300			[S II]λ6731		
	L	M	$\dot{M}_{out}$	L	M	$\dot{M}_{out}$
E1	−5.2	−9.0	−10.5			
E2	−5.6	−9.5	−10.9			
E3	−5.2	−9.0	−10.5	−5.7	−9.7	−9.9
W3	−4.8	−8.6	−10.1	−5.0	−9.0	−9.3
W2	−4.7	−8.6	−10.0	−4.9	−8.9	−9.2
W1	−5.0	−8.9	−10.3	−5.0	−9.0	−9.3

TABLE 4.4: Luminosity, mass, and outflow rates for the red-shifted knots in the [O I]λ6300 and [S II]λ6731 emission lines. Luminosity is given in units of log $L_\odot$, masses in units of log $M_\odot$, and mass-loss rates in units of log $M_\odot$ yr^{-1}.

Following Hartigan, Edwards, and Ghandour (1995), the intrinsic knot luminosity of the [O I]λ6300 Å and [S II]λ6731 Å lines is utilized to estimate the jet mass and outflow rate. The mass outflow (in units of $M_\odot$ yr^{-1}) is given by the equation

$$\begin{aligned}\dot{M}_{out} = 2.27\times10^{-10}\left(1+\frac{n_c}{n_e}\right)\left(\frac{L_{6300}}{10^{-4}\ L_\odot}\right)\\ \times\left(\frac{v_{\rm tan}}{150\ \rm km\ s^{-1}}\right)\left(\frac{\ell_{\rm tan}}{2\times10^{15}\ \rm cm}\right)^{-1} M_\odot\ \rm yr^{-1}\end{aligned} \tag{4.2}$$

for the [O I]λ6300 line, where n_c is the critical density, n_e the electron density, $v_{\rm tan}$ the proper motion (in km s^{-1}), and $\ell_{\rm tan}$ is the size of the aperture (in cm) in the plane of the sky. The expression is similar for the [S II]λ6731 line,

$$\begin{aligned}\dot{M}_{out} = 3.38\times10^{-8}\left(\frac{L_{6731}}{10^{-4}\ L_\odot}\right)\left(\frac{v_{\rm tan}}{150\rm km\ s^{-1}}\right)\\ \times\left(\frac{\ell_{\rm tan}}{2\times10^{15}\ \rm cm}\right)^{-1} M_\odot\ \rm yr^{-1}\end{aligned} \tag{4.3}$$

where it is assumed to be in the high-density limit so that the ratio $n_c/n_e \ll 1$. We note that we do not consider abundance ratios in these equations and as such they are estimations.

For these calculations, a tangential velocity $v_{\rm tan} = 17$ km s^{-1} and an aperture size $\ell_{\rm tan} = 9.0\times10^{14}$ cm is used. We find low luminosities and mass-loss rates for all of the knots, with the blue-shifted jet presenting higher values due to its exposure to the ionizing winds. For the [O I]λ6300 lines the mass-loss rate is on the order of 10^{-11} $M_\odot$ yr^{-1}, while in the [S II] line it is on the order of 10^{-10} $M_\odot$ yr^{-1} (see Table 4.4).

It is important to note however that these values do not account for any photoionization effects, and so represent a lower limit of the mass outflow rate. If instead we assume photoionization plays a large role in the jets, then we can calculate an upper limit of the mass-loss rate from

$$\begin{aligned}\dot{M}_j = 3.4 \times 10^{-9} \left(\frac{v_j}{100 \text{ km s}^{-1}}\right) \left(\frac{n_e}{10^3 \text{ cm}^{-3}}\right) \\ \times \left(\frac{r_j}{115 \text{ au}}\right)^3 M_\odot \text{ yr}^{-1}\end{aligned} \tag{4.4}$$

as given in Bally and Reipurth (2001). With this equation and our range of n_e values, it is estimated that $\dot{M}_j$ would have an upper limit of 10^{-9} $M_\odot$ yr^{-1}.

4.4 Discussion

4.4.1 Implications of the Proper Motions

Constraints on Disk Inclination

Throughout this study I have relied largely upon proper motion measurements to constrain the jet velocity. This parameter is important for both considerations of the wiggling jet model, and for calculations of the jet mass-loss rate. In Section 4.3.1 proper motions were computed < 20 km s^{-1}, with an estimated jet inclination angle i_{inc} of $72.2° \pm 4.2°$. While the low proper motion is not unusual for objects in the ONC, it is notable that i_{inc} is inconsistent with the observations of Bally, O'Dell, and McCaughrean (2000), which the authors interpret as a nearly edge-on disk. I examine a few possibilities for this below.

The assumption in the text is that the jet moves through the medium in a ballistic manner, i.e. with a constant velocity. If the jet encounters a dense material, it may be deflected and result in a change in its bulk flow velocity. A similar phenomenon was recorded by Hartigan, Holcomb, and Frank (2019) in the objects HH 8 and HH 10, where stationary "loop" structures occurred in the knots as they interacted with sheets of ambient material, resulting in no measurable proper motions. If there are dense, unseen obstacles within the proplyd envelope along the flow path of the jet, or if the jet is piercing through the envelope, it may be possible that the jet is significantly slowed or deflected as it encounters the material, or that the unshocked or weakly shocked material in the jet produces shocks in its vicinity that falsely present as knots. The latter case would raise the possibility that the locations of the knots observed in the HST data are not knots at all, but density enhancements in the surroundings. In such a scenario the proper motions reported here would not be reliable as a way to estimate the inclination angle of the jet, and we would require measurements closer to the driving source that are more likely to be unaffected by the above interactions. However, note in Figure 2.16 that the while there is obvious structure in the density distribution of the envelope, it does not appear sufficient to deflect the jet in this way. It is important to note nonetheless that the proximity of the blue-shifted jet to the IF may affect a change in the jet structure as it passes through the front. If this is the case, the ballistic assumption may not be appropriate for the blue-shifted jet.

In the HST images, particularly the Hα filter, Bally, O'Dell, and McCaughrean (2000) observed a silhouetted structure which they interpreted as an edge-on disk (see their Figure

7b) with a semi-major axis nearly aligned vertically in the image. In our MUSE observations we observe a bright "halo" structure around the source in Hα and [O I]λ6300 but at this point we are unable to determine its cause. If we look solely at the properties of the jet, we conclude that it does not support an edge-on disk scenario. Moreover, if the jet is close to the plane of the sky, the radial velocities would imply a driving source larger than the one supported by its spectral type (see Appendix B). Additionally, the large gap between the source and the nearest knot E3 in the red-shifted flow versus the smaller gap observed in the blue-shifted side suggests a system where the size and orientation of the disk effectively obscures the receding jet. Finally, the jet direction is not centered with the disk axis.

This thesis argues that all these discrepancies are reconcilable if one assumes that the disk observed in the HST images is not associated to the jet-driving source. Such a scenario would explain the position angle of the jet, its low proper motion, and our derived jet inclination angle. In our discussion on the jet curvature below, we see that this conclusion is also a possible outcome of our modeling and consistent with previous observations.

Dynamical Age of the Jet

In Section 4.3.1 a best-fit proper motion of the jet and the offset of knot E1 from the source was used to present a minimum age of the jet of at least 300 yr. This is a most interesting result, as it tells us not only that the jet is quite young and still active, but also that photoionization and photoevaporation of the proplyd do not seem to affect the ability of the star to launch a jet. The jet may have been launched within a "bubble" that shielded it from the majority of hard-UV radiation, which may also explain why collisional excitation appears to dominate in the jet.

Additionally, note above (Sec. 4.4.1) that the proximity of the blue-shifted jet to the IF may change the jet structure. Along with the age estimate, this raises questions about the length of the blue-shifted emission, which is substantially shorter than that of its red-shifted counterpart. The measured radial velocities of the knots are not too dissimilar between the red and blue lobes, suggesting similar launch velocities in the absence of any appreciable jet position angle asymmetries. If we further assume similar launch epochs, then we would expect the blue lobe to extend to at least the same length, yet we observe no emission beyond the envelope of the proplyd. Furthermore, YSOs typically begin driving outflows early in their life-cycles (as early as 10^4 yr; see Andre, Ward-Thompson, and Barsony, 2000), so it is expected that the true extent of the jet may be far greater than what is observed (Frank et al., 2014). This is not unreasonable, and two points are raised here to address this.

Firstly, visible knots are formed by shocks as the jet interacts with itself or the ambient medium (in isolated regions), or by illumination from an external source (in irradiated regions). The minimum age of the star suggests that the jet is far older than 300 yr, so the jet must have punctured through the envelope and passed into the larger region of the nebula, which in the neighborhood of our object of interest typically has a density on the order of 10^3 cm^{-3} (Méndez-Delgado et al., 2021). That other HH objects are seen in the ONC beyond the protective shells of the proplyds indicates that the ONC is either dense enough or irradiated enough to render these objects visible. It may be that the jet has lost so much of its density after passing beyond the envelope that it is simply not visible, which is reasonable as the luminosities of HH objects tend to decrease with separation from the driving source. Secondly, the environment surrounding a proplyd is not hospitable to transient objects. Given the low luminosity and radial velocities of the jets we do not anticipate a very strong driving force, so it is likely that the stronger stellar winds and radiation in the ONC have entirely dissipated the portions of the jet beyond the envelope.

4.4.2 Origin of the curvature

To explain the C-shaped symmetry common to irradiated jets in the Orion nebula (Bally and Reipurth, 2001, and references therein), a few models have been put forth involving ram pressure from stellar winds (Raga et al., 2009; Estalella et al., 2012). Additionally, sinusoidal jet morphologies may arise due to the presence of a binary companion which causes either orbital motion of the jet source (Masciadri and Raga, 2002; Lai, 2003; Murphy et al., 2021; Erkal et al., 2021a), or a precession of the jet ejection axis due to the inner disk not being coplanar with a companion's orbit (Zhu, 2019; Terquem et al., 1999). Bally, O'Dell, and McCaughrean (2000) initially proposed the idea of a hidden companion based on the offset of the photometric center from the geometric center of the disk as seen in their [O I] observations. Recent evidence put forth by Tobin et al. (2009) and Kounkel et al. (2019) also indicates that 244-440 is a spectroscopic binary. The possibility of 244-440 possessing a companion that may produce a "wiggling" in the jet axis, as well as the ram pressure from the stellar winds from the stars in the Trapezium cluster and θ^2 Ori A and B, may all act in conjunction to produce the complex morphology that we observe in this object.

In this section I explore whether the observed curvature in the jet can be explained by a wiggling jet model in the absence of an appreciable side-wind. The basic parameters of these models are the length scale of the wiggle λ and the half-opening angle of the jet cone β, an important parameter in the precession model. They can be inferred by visual inspection of the data and the proper motion estimates presented in Section 4.3.1. The knot centroid positions are measure by Gaussian fitting of the jet along the outflow axis as discussed in Chapter 2.3.3, and utilize the jet inclination angle estimated above to de-project these positions from the plane of the sky. The analysis below follows the method explored by Murphy et al. (2021) and discussed in Chapter 3.4.2.

Using the derived inclination angle, the de-projected length-scale of the jet is estimated as $\lambda \sim 8''$. The half-opening angle β is also observable from the data by fitting the slope of the peaks of the wiggle curve. Even if we do not observe as many peaks as some other wiggling jets, we can safely estimate $\beta = 3.4°$. One can further relate the precession model to the orbital model by means of β. In an orbital model, we define the ratio of the orbital velocity to the jet velocity as $\kappa = v_o/v_j$, and this is related to β by $\kappa \leq \tan\beta$.

Parameter	Orbital		Precession	
	$0.4\ M_\odot$	$0.8\ M_\odot$	$0.4\ M_\odot$	$0.8\ M_\odot$
μ	0.9	0.7	0.5	0.3
a (au)	30	40	10	5
τ_o (yr)	250	250	50	30
τ_p (yr)	220	220	230	240

TABLE 4.5: Derived parameters for orbital and precession models of the proplyd 244-440 for lower and upper system mass limits. μ is the mass-fraction $M_c/M_{\rm sys}$, a is the binary separation, τ_o is the orbital period, and τ_p is the precession period.

Using these parameters and the equations shown in Murphy et al. (2021) we explore both an orbital motion model and a precession model for the jet. We use the Python package `lmfit`[4] and rewrite the equations as functions of λ and β, allowing them to vary by about 15%. We use a fixed value of $v_j = 65$ km s^{-1} for the jet velocity and set an upper limit on r_o of $0\farcs1$ (see Section 4.1). The results of the fits are shown in Figure 4.14. The errors on the centroids were calculated according to Equation 2.17. Both models are weighted with the centroid errors computed by the above equation.

It is important to recognize that given the short length-scale of the blue-shifted jet and the inability to estimate a proper motion for that emission lobe, it is difficult to determine whether the wiggle is point-symmetric (precession) or mirror-symmetric (orbital motion) around the origin, though Figure 4.14 does appear to favor mirror-symmetry. Nevertheless we can make assumptions based on the values derived from these fitted models.

A primary driver of the values derived from the fitted curves is the total system mass. The spectral type of the visible central star implies a low-mass object (see Appendix A) and we therefore limit our considerations to $\mathrm{M_{sys}} \leq 0.8\ M_\odot$. For the orbital motion model, the results imply μ ($= M_c/M_{\rm sys}$) values ranging from 0.7 with $\mathrm{M_{sys}}= 0.8\ M_\odot$ to 0.9 with $\mathrm{M_{sys}}= 0.4\ M_\odot$. We can estimate the maximum binary separation a as the ratio of the orbital radius r_o of the source about the barycenter and the mass ratio μ, $a = r_o/\mu$, obtaining separation in the range $\sim 30-40$ au. The implied orbital period τ_o is found by

$$\frac{M_{\rm sys}}{M_\odot} = \mu^{-3}\left(\frac{r_o}{\rm au}\right)^3\left(\frac{\tau_o}{\rm yr}\right)^{-2} \tag{4.5}$$

which suggest an orbital period of ~ 220 yr.

A similar calculation for the precession model results in a precession period $\tau_p = 238$ yr with μ ranging from 0.3 ($\mathrm{M_{sys}}= 0.8\ M_\odot$) to 0.5 ($\mathrm{M_{sys}}= 0.4\ M_\odot$). These results imply orbital periods of $\sim 30-50$ yr and binary separations from $\sim 5-10$ au. This smaller value is not unreasonable as the precession model requires a warped inner disk, and if this is induced by a companion then the companion must be relatively close. The derived parameters for the orbital and precession models are shown in Table 4.5.

In the precession model, the inferred mass-ratio indicates an equal-mass binary at close separation. The length scale of the deprojected jet (~ 4000 au) and large fluctuation in the

---

[4] https://lmfit.github.io/lmfit-py/

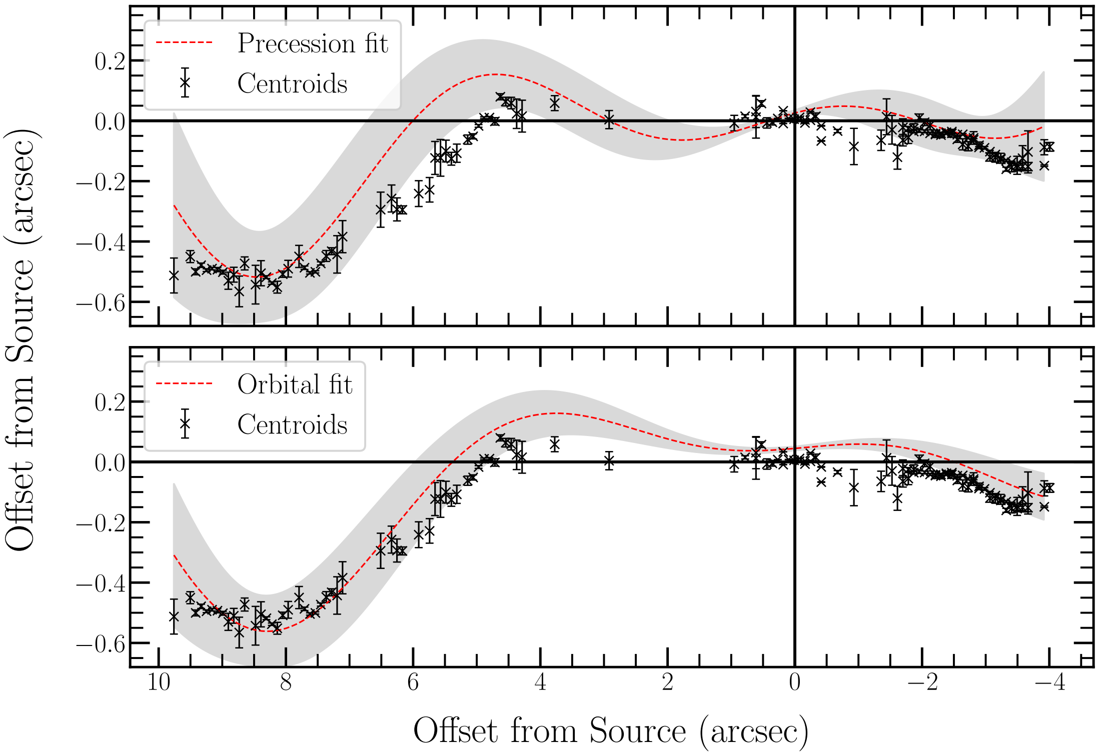

FIGURE 4.14: Best-fits for the precession (top) and orbital (bottom) models for the [Fe II]λ7155 Å jet. The relative offset along the jet axis is deprojected by $x' = x/\cos\theta$ for an angle of 73° assuming a distance d = 400 pc. The gray region indicates a 3σ uncertainty in the model.

red lobe are consistent with precession models, as fluctuations due to orbital motion are more likely to appear within 100s of au of the source (Masciadri and Raga, 2001). However, this model presents some difficulties. If the companion is close in mass to the primary, one should wonder whether or not this companion would truly be hidden in observations. Unfortunately, we cannot resolve the binary separations in our MUSE observations, nor is our spectral resolution high enough to perform accurate spectro-astrometry. If we consider larger system masses, i.e. $\mathrm{M_{sys}} \simeq 1\ M_{\odot}$, the derived μ values still imply an appreciably large companion. Another issue is the observed properties of the jet. The μ values obtained with the precession model suggest a jet driven by the primary, and this cannot be reconciled with the assumption that the disk seen in the HST images is associated with the primary in the system. Therefore it seems unlikely that a precession model is an appropriate explanation for the observed wiggle.

In the orbital model, we find a mass-ratio that implies the jet-driving source is not the primary in the system. As discussed in Section 4.4.1 this outcome is very reasonable and is supported by observational evidence. If this is an equal-mass binary, we would anticipate a different spectral type than what the observed stellar spectrum suggests. If one assumes that the primary conforms to an M0 or M1 spectral type ($M_p \simeq 0.5\ M_{\odot}$), we argue that this model gives good agreement for $\mathrm{M_{sys}} \sim 0.6 - 0.7\ M_{\odot}$. Additionally, the orbital model curve seen in Figure 4.14 best matches the morphology of the jet. All of these arguments provide compelling evidence that if the curvature can be explained by a wiggling jet model, the orbital motion model is a strong candidate, and that the jet is associated with the smaller, hidden star in the system.

We do not explore the impact of stellar winds here. Generally, side-wind deflection models imply a hyperbolic curvature as the jet is deflected away from the wind source (Raga et al., 2009), although more complicated morphologies in photoionized regions are possible (Masciadri and Raga, 2001). In our observations, the C-shaped morphology anticipated by a deflection model appears to be applicable primarily to the envelope but not the jet, indicating that the jet is either shielded to some degree from the winds or that multiple winds are influencing the system in a way that is beyond the scope of this paper. Furthermore, using the derived proper motions and overlaying their vectors on the data (see Figure 4.15), it is seen that the knots do point radially outward from the source with a slight difference (∼ 7°) in their directions. The decrease in angle exhibited by knot E1 could potentially indicate a jet/sidewind interaction; however with proper motions available for only two knots either conclusion is approached with caution. Nevertheless these models lay a positive groundwork, as future observations may help provide greater constraints on the parameters of a potential companion.

4.4.3 Diagnostics and mass-loss

In Section 4.3.2 it was seen that the proplyd is very close to or exceeding the high-density limit as inferred from the ratio of the [S II] doublet. Additionally, the lack of jet emission in temperature-dependent species hinders the reliable determination of the electronic temperature in the jet. While the correlations observed across the full images in Figures 4.9

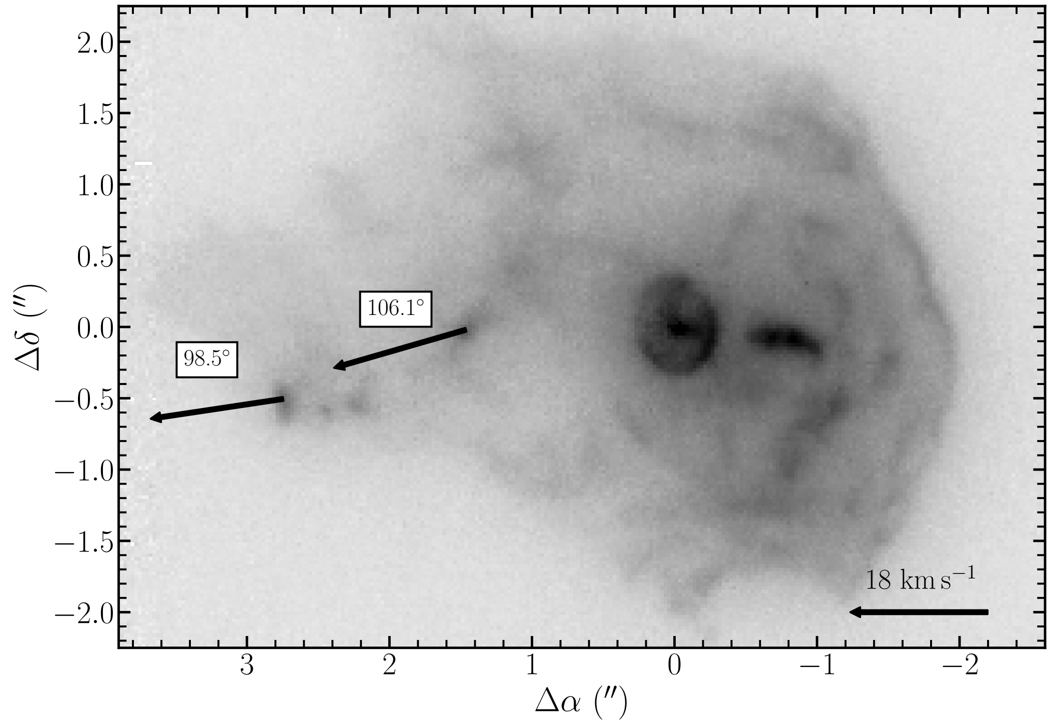

FIGURE 4.15: Proper motion vectors superimposed on the [O I]λ6300 emission line. A small difference is observed, pointing overall radially outwards though possibly pointing along the direction of the jet curvature. The angles are measured east of north in the plane of the sky.

and 4.10 are useful, a further check was made by sub-sectioning each image in smaller boxes encompassing regions of interest. This is shown in Figure 4.16. Again it is seen that the background emission falls largely within permitted regions, while the western and eastern regions of the proplyd trend towards the high-density limit.

It is further important to note that while Figure 4.8 and Table 4.3 appear to indicate that the envelope-subtraction technique discussed above places the [S II] knot fluxes within the permitted ratio limits, the uncertainty to their relative fluxes due to the homogeneous emission nature of the envelope is appreciable. Additionally, the [S II] flux is weakest (and thus most uncertain) in the red-shifted lobe of the outflow. With the given intrinsic emission ratios, the blue-shifted lobe still implies densities of $\sim 2 \times 10^5$ cm^{-3}. An effort is made to explore how reasonable this is below.

Even if we could not reliably determine the temperature of the jet in our data through traditional diagnostic diagrams, the presence of refractory species like [Fe II] and [Ni II] provides opportunity to explore ranges of density, as well as the potential role of fluorescent pumping of the jet. It is reasonable to assume that the presence of external ionizing sources may induce fluorescence in the jet, particularly given the presence of the [Ni II] lines and the observed line ratios in Figure 4.12. However, the density ranges estimated from the [Ni II] lines ($\sim 10^4 - 10^5$ cm^{-3}) are above the critical limit for fluorescent pumping, which suggests that shock processes play the larger role in producing the emission lines. This may be due to the envelope shielding the jet to some degree from incident radiation, making it

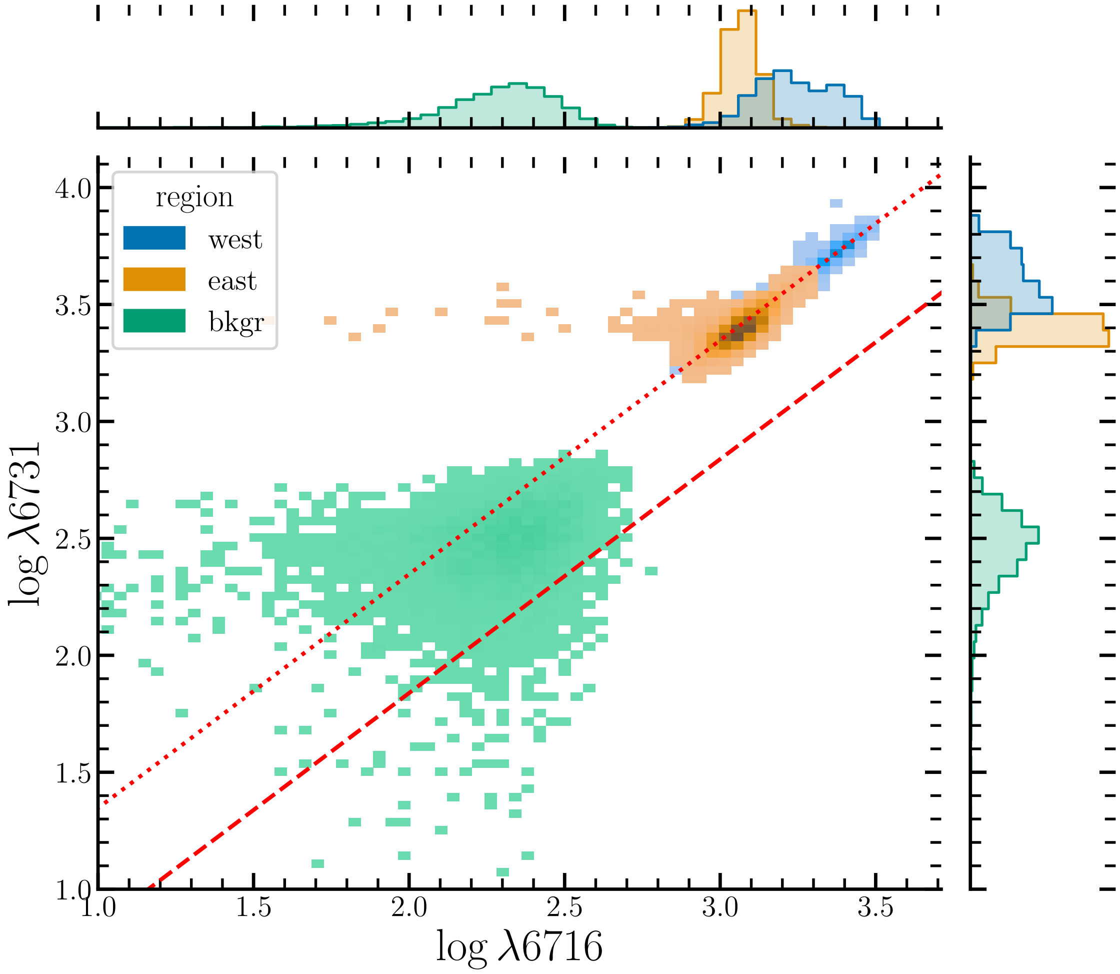

FIGURE 4.16: Same as Figure 4.9, but partitioned by region. Each region encompasses a $2'' \times 2''$ window, with the background being a combination of two regions adjacent to the proplyd. The side plots display the histogram distributions of each region for each emission line, while the central plot presents the ratio. The upper dotted line corresponds to the high-density limit, and the lower dashed line corresponds to the low-density limit. The background emission (green) is falls within these bounds, while the envelope+jet emission falls primarily along the high-density line. Brightness is given in units of $\log 10^{-20}$ erg cm^{-2} s^{-1}.

not as exposed as others to the external environment.

This result has interesting implications when considering the mass-loss rate. In Section 4.3.2 we present limits on $\dot{M}_j$ in the range $10^{-11} - 10^{-10}$ $M_\odot$ yr^{-1} and argue that even if photoionization plays a large role, we would not expect a mass-loss greater than 10^{-9} $M_\odot$ yr^{-1}. Additionally there is an asymmetry in the luminosities and mass-loss rates with the blue-shifted jet presenting generally higher values. While the jet may benefit from shielding by the envelope, the fact that the computed values are higher in the blue lobe than the red demonstrates that the jet may still be partially exposed to external radiation. These lower values are typically seen in very low-mass protostars and brown dwarfs (Whelan et al., 2009; Riaz et al., 2017), which is consistent with the spectral typing of the source (Figure B.1).

4.5 Conclusions

This Chapter presents the first analysis of the possible origins of the curvature and physical conditions of the proplyd 244-440 jet using high spatial resolution IFU observations with MUSE NFM+AO. The results all argue for a unique and complicated outflow system. Perhaps most striking is the indication the implication that photoionization and photoevaporation of the host disk do not appear to hinder the ability of the source to drive an outflow. It further demonstrates the power of the MUSE NFM instrument in resolving close-in features of stellar jets, particularly in high-radiation environments where more quiescent regions of the jet are illuminated. The principal conclusions of this study are summarized below.

1. A new complex of knots are discovered in the red-shifted lobe of the jet, two of which are shared between MUSE and HST observations (though were unreported in prior HST studies). The knots E1 and E3 are utilized to estimate a proper motion of 9.5 ± 1.1 mas yr^{-1} with a jet inclination angle $i_{\text{jet}} = 72.2° \pm 4.2°$, which appears contrary to previous interpretations of a nearly edge-on disk. Closer analysis suggests that the jet is not associated with the observed disk, and it is posited here that the jet is actually driven by a smaller companion.

2. We utilize a jet-wiggling model to explore for the first time the curvature in the jet, and find that in the absence of other forces (i.e. multiple strong side-winds) the curvature can be explained by orbital motion of the jet source. As recent evidence suggests this is a spectroscopic binary, this is not unreasonable. It is further reasoned that if this is due to a companion, we might expect the driving source to be ≤ 0.15 $M_\odot$ in orbit around an M0 or M1 type star ($M \sim 0.5$ $M_\odot$) at a separation of $\sim$ 30 au. This further suggests that companions can readily form within photoevaporating and photoionized disks, which speaks to the durability of nascent solar systems.

3. The [S II] doublet is examined and demonstrates that the proplyd is likely in the high-density limit ($n_e > 10^5$ cm^{-3}). Examination of the [Fe II] and [Ni II] emissions is found to agree with this density estimation. This is used in conjunction with

the [O I] and [S II] lines to estimate a lower limit on the mass-loss rate in the jet on the order of $10^{-10} - 10^{-11} M_{\odot}$ yr^{-1}. If we assume the jet is nearly completely photoionized we set an upper limit on the mass-loss rate of $< 10^{-9}\ M_{\odot}$ yr^{-1}. It is notable that similarly small values are observed in low-mass and sub-stellar objects such as brown dwarfs.

4. Finally, we look at the "proplyd lifetime problem" and estimate an evaporation time between $0.1 - 0.2$ Myr. The minimum dynamical age of the jet is found to be around 300 yr, indicating that the source is still quite active and that the jet may still be quite young. This additionally tells us that photoionization and photoevaporation of the proplyd had likely been occurring for some time before the jet was launched. This might indicate that the envelope has acted as a protective shell enclosing the jet and shielding it from a significant portion of Lyα radiation. This yields critical information about the durability of the accretion-outflow connection in the harshest of conditions. The possibility is also raised that the calculated dynamical age may drastically underestimate the true age, and we reason that if the jet has extended beyond the envelope it may have been completely destroyed.

Chapter 5

ESO-HA 1674

5.1 Introduction

This chapter focuses our attention upon the final object of study – the proto-brown dwarf (BD) candidate ESO-HA 1674, also known as Mayrit 1082188. As discussed in Chapter 1.1.2, jet launching is observed across the mass range, even as far down as sub-stellar objects like BDs. The importance of studying jets from BDs is perhaps most evidently seen in the consideration of their unique nature, straddling the divide between star and planet yet defying strict classification as either. As such they present a unique opportunity to probe the robustness and scalability of the jet launching model to the very lowest of masses we can (so far) directly image. Tentative evidence suggests that jets from BDs behave much like their higher-mass siblings (see Whelan et al., 2014; Whelan, 2014; Riaz et al., 2017), lending credence to the model's robustness. The most intriguing consequence of these observations is what this suggests about the very low-mass end of the mass spectrum. The accretion-ejection connection is well established, and it is known that strong Hα emission is associated with outflows. As Hα has been shown to be connected to planetary accretion (see e.g. Huélamo et al., 2018; Huélamo et al., 2022), it is possible that planets drive outflows as well. Thus BDs provide us with a fascinating laboratory to not only test to the launching model, but perhaps better understand planet formation as well.

Mayrit 1082188 (hereafter M1082188) is a particularly unique object as it is thus far the lowest luminosity jet ever observed (Riaz et al., 2015; Riaz and Whelan, 2015), and is externally irradiated by OB type stars within the σ-Orionis cluster as seen in Figure 5.1. The source itself is a very low luminosity ($L_{bol} = 0.16 \pm 0.03$ $L_{\odot}$) young source approximately 387 pc from the sun (α = 11:16:02.87 δ = −76:24:53.2; see Schaefer et al., 2016). Using sub-millimeter fluxes, Riaz and Whelan (2015) (see also Riaz et al., 2015) derived a total dust+gas mass for this system of $\sim$ 22 M_{Jup}. They reported a mean accretion rate $\dot{M}_{acc} = (3.0 \pm 1.0) \times 10^{-10}$ $M_{\odot}$ yr^{-1} and a mean mass-loss rate of $\dot{M}_{out} = (5.2 \pm 1.6) \times 10^{-10}$ $M_{\odot}$ yr^{-1}, both of which are consistent with other very low-mass sources. Additionally, Riaz et al. (2015) classify this as a Class Flat source (see also Chapter 1.1.2 and 1.1.2), indicating a tenuous envelope compared to Class I objects. Their modelling constrains the disk inclination angle to be between 45° and 60°.

Riaz and Whelan (2015) were the first to report the detection of a bipolar jet, utilizing spectro-astrometry (see Whelan et al., 2015, for a detailed explanation of this process) to estimate a jet PA of $\sim 102°$ and finding radial velocities < 50 km s^{-1}. Given an estimated disk inclination angle of 60° and assuming a jet roughly perpendicular to the disk, an upper limit of $v_j \sim 100$ km s^{-1} can be placed on the jet. Fluxes measured in their UVES data yield a mass-loss rate in the jet $\dot{M}_j$ of $\sim 3 \times 10^{-10}$ $M_\odot$ yr^{-1}. All these measurements support the classification of this source as a proto-BD.

The low luminosity of the jet and the low mass of the source make this an especially interesting candidate of study, as this situates the jet launching phenomena at one of the lowest mass limits thus far observed. Its external irradiation by stars in σ-Ori makes this of further interest as the quiescent, unshocked material in the jet can be rendered directly visible, allowing us to view regions in the jet that may otherwise have been unobservable. Additionally, complex shock models may not be necessary to understand the physical conditions in the jets, as the application of standard methods used to understand ionized nebulae can potentially be applied (Reipurth and Bally, 2001b; Bally and Reipurth, 2001).

In this Chapter I present the first direct images ever obtained of the outflow associated with M1082188. As can be seen from the whole of this thesis, the MUSE instrument is rich with information and observations obtained with it provide us with a wealth of information to explore. This Chapter is no exception. I will explore the morphology and kinematics of this outflow and derive $\dot{M}_{acc}$ and $\dot{M}_{out}$ rates for both the source and the jet for comparison with previous UVES data. This work will additionally place a strong emphasis on the feature we later interpret as a cavity present in the data, exploring its nature and discussing its importance in the context of the overall outflow mechanism. Together these things will shed light on the fascinating behaviors both of this source and of jets observed at the lowest of masses.

5.2 Observations

The data for this object was obtained with the MUSE instrument on 7 November, 2021, under Program ID 108.22MX.002 (P.I. A. Kirwan). The observations were in the adaptive-optics (AO) assisted Wide Field Mode (WFM) instrument configuration with an average seeing of $0\farcs56$ and photometric conditions. The data were reduced using standard procedures and calibration files with the `esoreflex` pipeline (see discussion in Chapter 2). The observations were obtained with a single observation block of exposure time $t_{exp} = 1800$ s.

The source itself presents very faint continuum emission, indicating its embedded nature and overall low luminosity. Due to this a simple background subtraction routine was chosen over the removal of the stellar continuum to avoid over-subtraction of key regions in the cube. This is further justified by comparison with UVES observations, where the continuum is present only faintly across the data. These methods are discussed in Chapter 2. Dereddening is performed assuming an extinction magnitude $A_{\rm V} = 2$.

The MUSE observations are compared with UVES data from 2014 (Program ID 094.C-0667(A); P.I. B. Riaz) reported by Riaz and Whelan (2015). To make these comparisons, a simulated slit was applied to the MUSE data at position angles (PA) of 0° and 90°. Riaz and Whelan (2015) used these PAs to infer the directions of the outflow axes, and the

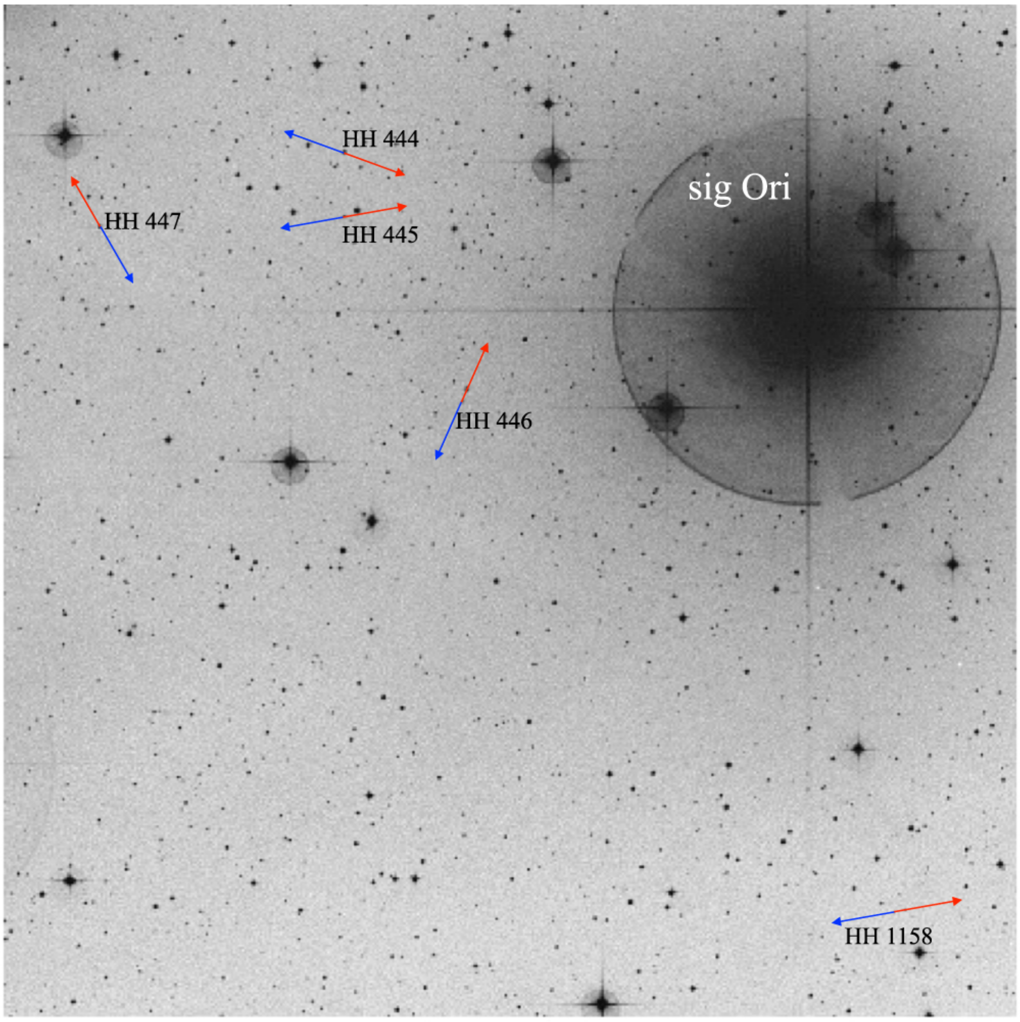

Figure 5.1: An image of multiple jet-launching sources around σ-Orionis, as observed with UKIDSS in the K_s band. M1082188 is shown in the bottom right as HH 1158, with arrows indicating the outflow orientation as estimated by Riaz and Whelan (2015). Image from Figure 1.1 of Riaz and Whelan (2015).

Figure 5.2: Three-color composite RGB image of the ESO-HA 1674 system. Red is Hα, blue is [S II]λ6716 Å, and green is [O I]λ6300 Å

fluxes they measured at these PAs were used to compute the accretion and outflow rate of the source.

5.3 Results

5.3.1 Morphology & Kinematics

Outflow & Cavity

The MUSE observations reported here constitute the first direct images captured of this outflow. The image quality delivered by the AO system additionally allows for a close-in look at the fascinating emission features not captured in the UVES data. In Figure 5.2, a three-color composite of the system is shown. The jet/counterjet system extends approximately 6000 au at high S/N (> 15), with fainter emission extending the total jet length as far as $\sim 13,000$ au (S/N ≤ 2). In Figure 5.3 it is seen that the red-shifted jet (PA $\approx 254°$) is fainter and apparently shorter than its blue-shifted counterpart, extending about $5''$ (~ 1900 au at 387 pc) from the source and featuring two distinct knots which we have named E and F. The blue-shifted jet has a PA $\approx 75°$, and has a bright section extending ~ 5000 au composed of four knots which we term A, B, C, and D. In smaller Hα velocity channels, a faint knot-like feature is seen in the red-shifted jet approximately $10''$

($\sim$ 3800 au) from the source and faint, diffuse blue-shifted emission is seen as far as 15″, to 20″ ($\sim$ 5800 – 7800 au) . The tenuous blue-shifted emission is faintly seen in Figure 5.2, while the red knot presents at too low a S/N to be detected in the full images. Smaller velocity channels of these are shown in Figures C.15 and C.16.

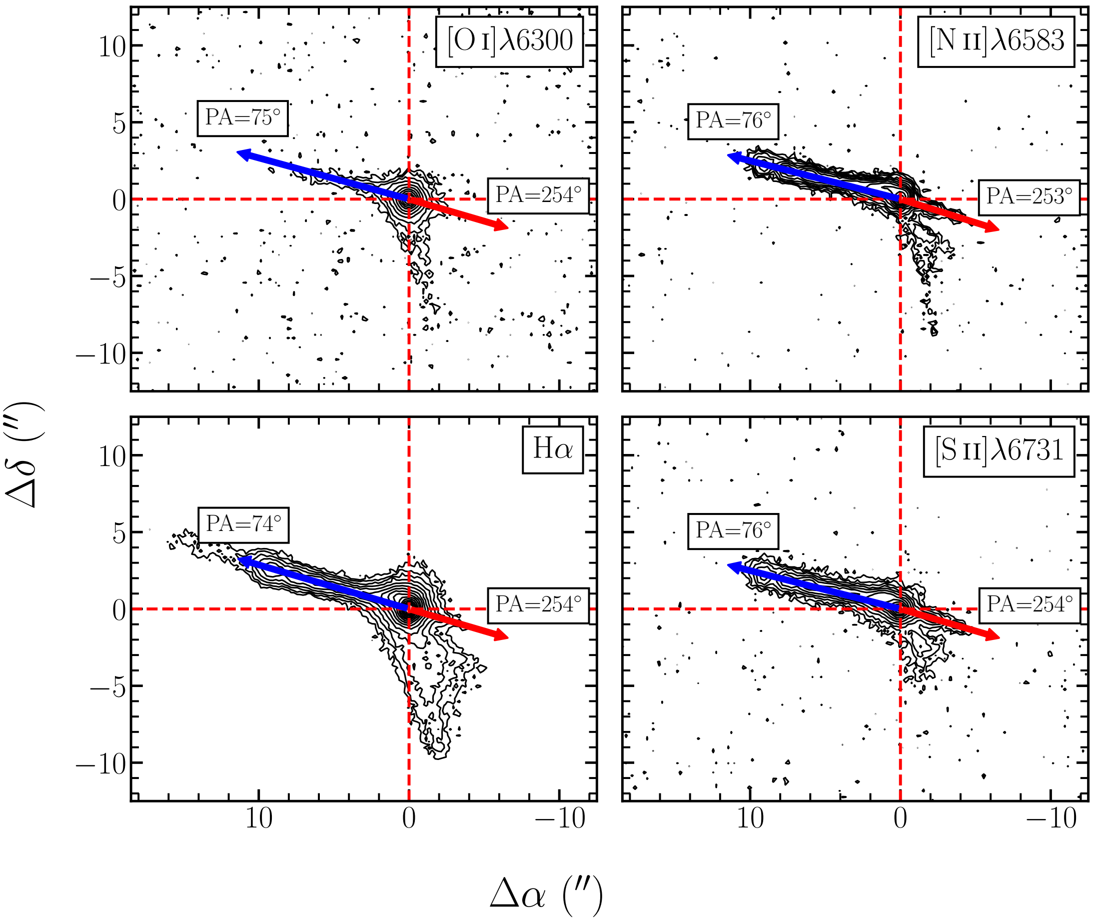

FIGURE 5.3: Contour maps of emission from the [O I], [S II], Hα, and [N II] lines. Position angles for the blue- and red-shifted jets are labeled in each figure. There is a small asymmetry in the PAs for the lines on the order of a few degrees.

The flux-integrated spectro-images shown in Figure 5.3 show that the forbidden emission lines (FELs) are offset slightly from the Hα emission. Further, in all images the blue- and red-shifted jet axes are slightly misaligned, and an interesting whistle-shaped feature is present where the blue jet emerges from the source position, and appears to curve away. This is most clearly observed in Figure 5.4.

One of the most striking features in the outflow is the presence of a feature that appears to be similar to a cavity or reflection nebula observed in CTTS and HAeBes below the west-pointing red-shifted emission. It is most prominent in Hα, as seen in Figure 5.3, and extends down to about 10″ ($\sim$ 3800 au), although it is evident in all FELs in that figure. Curiously, it is not present in any continuum images. The cavity is wide in Hα and has a rough PA of $\sim$ 195°. A smaller feature in the cavity is observed in the [N II] and [S II] lines with a PA of about 210°. The whistle feature discussed above has a PA $\sim$ 30° – 50°, making

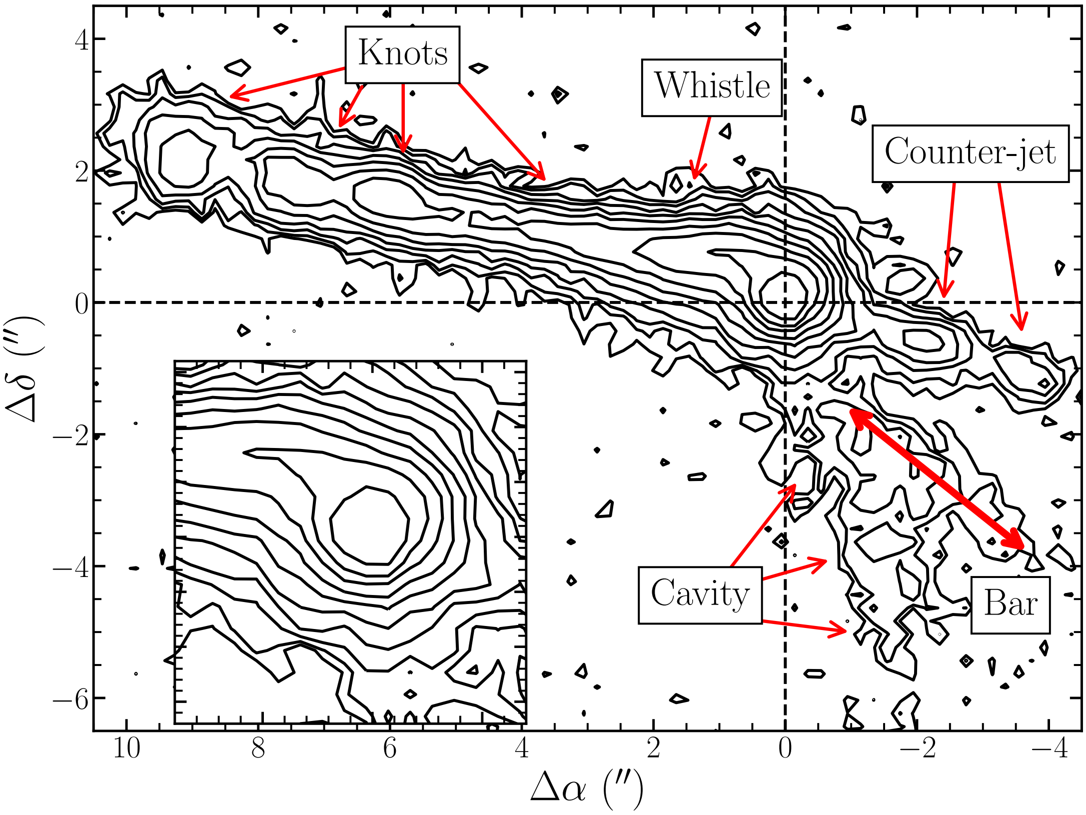

Figure 5.4: A spectro-image of the co-added [N II] doublet. The inset shows a zoomed-in view of the whistle-shaped feature present in the outflow. The prominent features are indicated by the red arrows.

it possible that this is also a feature of the cavity. More curious still is a sharp "bar" of emission that appears almost jet-like, extending about 4″ westward from the source and subtending a small angle with the red-shifted jet. The [N II] and [S II] doublets show this feature most clearly, and it appears to be red-shifted as well.

These PAs appear to contradict what is reported in Riaz and Whelan (2015), though in both cases the blue-shifted jet is pointing towards σ-Ori. An explanation for this is that spectro-astrometry may not be well-suited to complex outflow cases. The presence of the whistle north of the source and the outflow cavity towards the south would present as knot-like features in the 0° UVES data. The 90° cuts as well would capture only the lower parts of the blue-shifted lobe and upper portion of the red-shifted lobe. With the cavity/whistle features this would skew the derived jet PA away from its true position. In spite of this we observe in Figure 5.5 that the jet features identified in both epochs have shifted, allowing us to estimate a proper motion. In the right panel we see the red jet peak around 1″, and this same feature appears to peak around 1″.5 in the MUSE observations. This suggests a space proper motion of around 100 km s^{-1}. In both UVES and MUSE data the observed radial velocities are below 50 km s^{-1} (see Section 5.3.2) which indicates an average jet velocity between 100 − 120 km s^{-1}. The inclination angle of the jet with respect to the line of sight is found by $i_{\rm jet} = \tan^{-1} \langle v_{\rm tan} \rangle / \langle v_{\rm rad} \rangle$, yielding approximately 70° with a jet velocity around 110 km s^{-1} for the assumed proper motion. It is important to note however that this assumes the same features are being compared between epochs, and as such this represents a rough estimation.

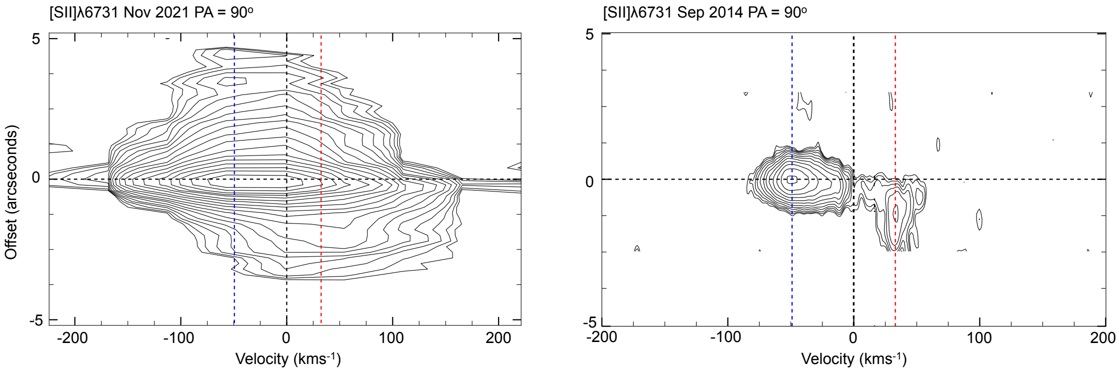

Figure 5.5: A comparison of the MUSE (left) and UVES (right) observations of M1082188 for the PA=90° PV arrays. The spectral resolution of MUSE is far lower so the structure is "compressed" with respect to the resolution UVES, but the same outflow trend is observed. Blue and red lines correspond with blue- and red-shifted emission identified in the UVES data.

Axis Asymmetry

This asymmetry is further seen in the jet centroid fits taken along the outflow axis. To explore this, the flux-integrated images were rotated by approximately 12.5° to align the jet axis roughly along the horizontal and analyzed with the method discussed in Chapter 2.3.3

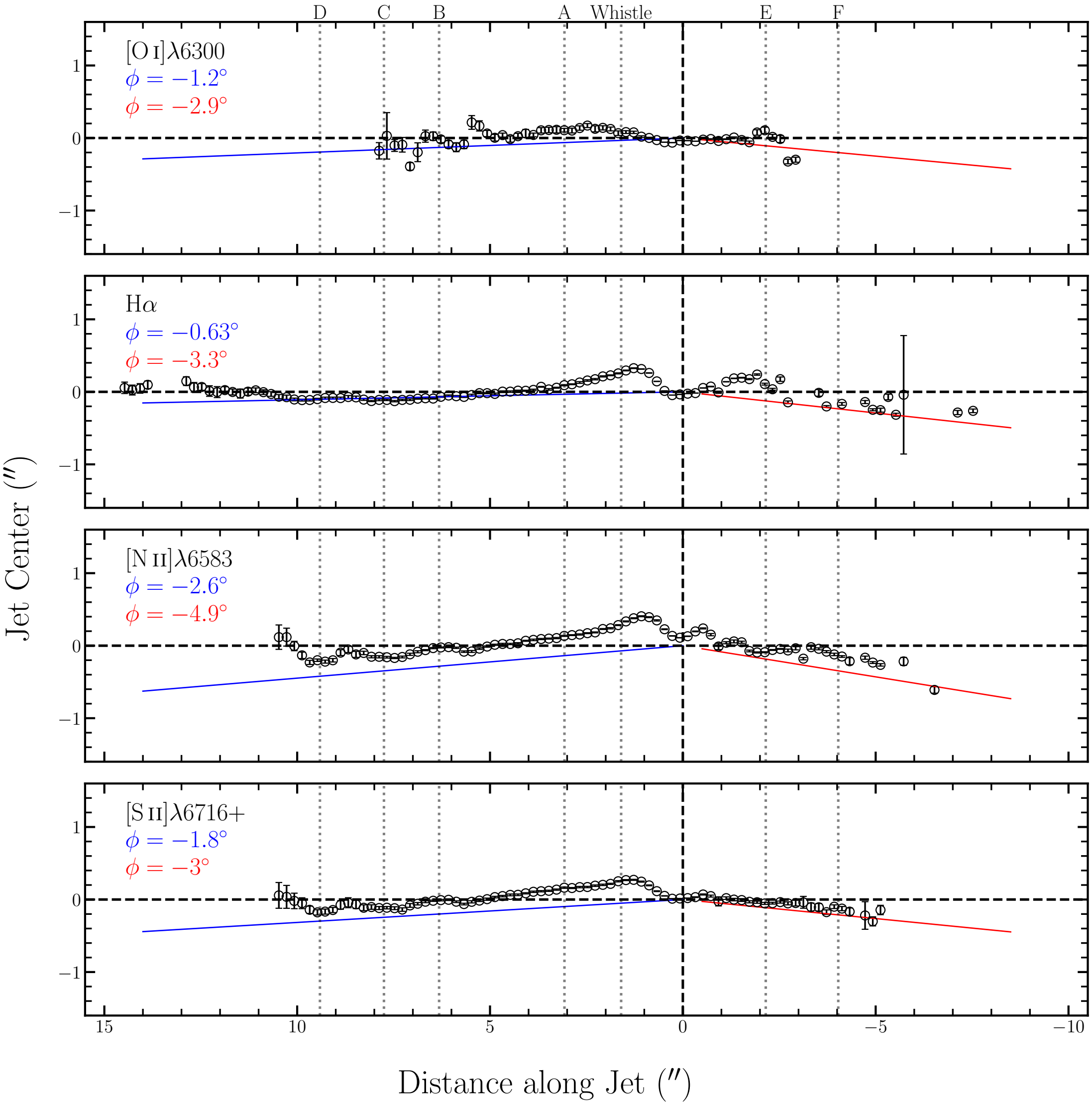

FIGURE 5.6: Jet centroid measurements taken along the M1082188 outflow axis.

(as well as Chapters 3 and 4). The centroids were further corrected for any rotational offsets by applying a linear fit and subtracting this from the data. The centroid errors were computed according to Equation 2.17. The result of this is shown in Figure 5.6. We observe a sharp bump along the trace of the centroids corresponding with the whistle feature, suggesting either an unresolved jet component or a significant offset of the intrinsic jet emission beginning around 200 au and persisting until approximately 1200 au.

Unfortunately this whistle feature complicates the jet opening angle estimation, resulting in a broad hump seen in the lines in Figure 5.7. As with the jet centroids, this sharp bump begins around $0\farcs5$ and reaches a maximum at $1''$ before slowly decreasing to a local minimum at $\sim 3''$. For both the centroids and FWHM measurements we observe that the fits to the red-shifted jet have considerably more noise than their blue-shifted counterpart. Combined with the presence of the source flux this contributed to further uncertainty in the opening angle estimation. Interestingly, the FWHM in the red lobe decreases in the

[N II] and [S II] lines, and the blue lobe is seen to increase steadily (∼ 4°) in all but the [O I] line, where it is nearly constant. In all cases the FWHM closest to the source is comparable to the image quality (∼ 0″.5). As we might anticipate from Chapter 3, we observe minima in the FWHM corresponding with maxima in the knot intensity profiles.

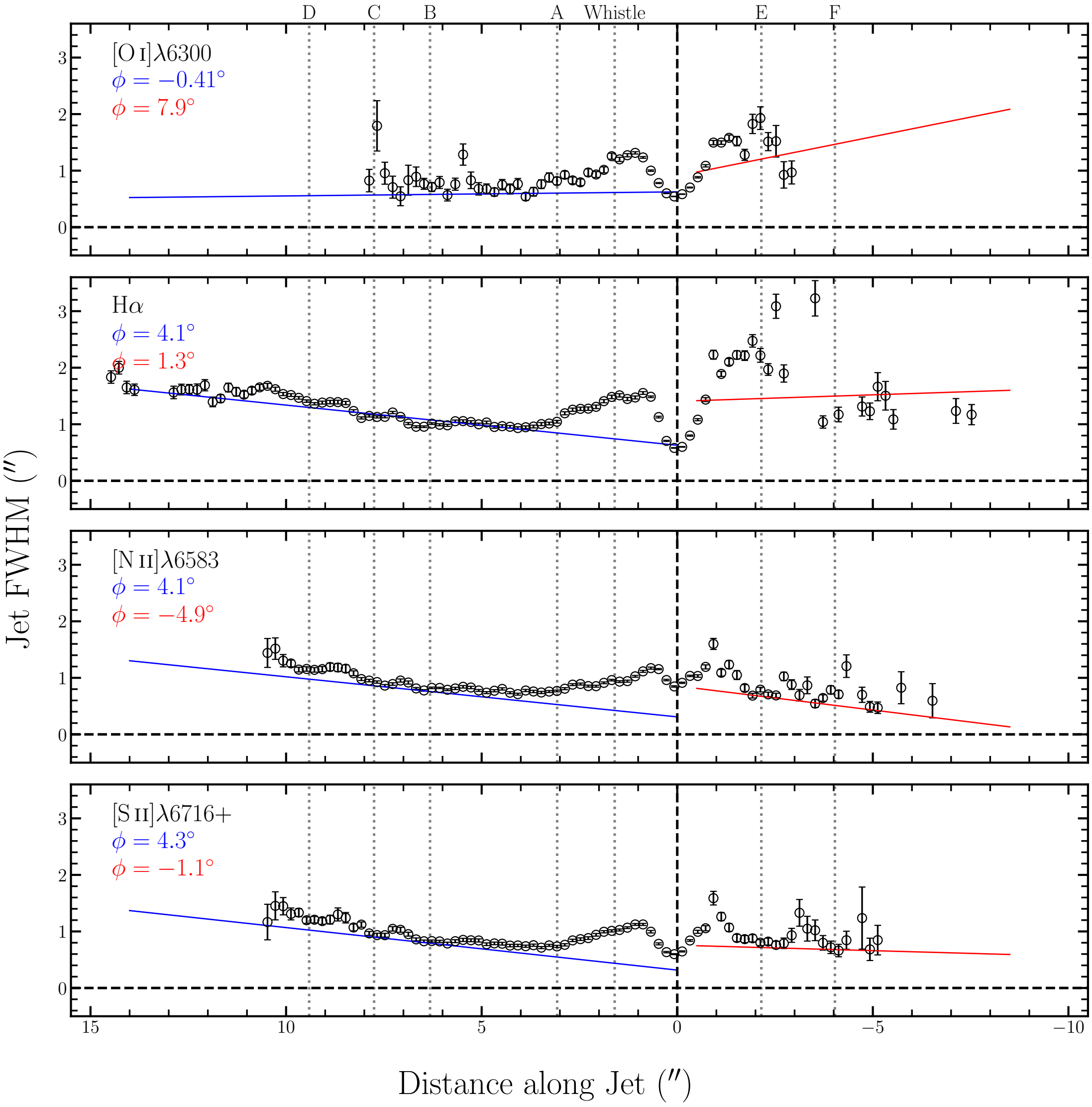

FIGURE 5.7: Jet FWHM measurements taken along the M1082188 outflow axis.

Velocity Structure

Examination of the velocity structure was undertaken using a combination of two methods. In the first method, PV diagrams were generated using simulated slits with a 1″ (5 pixel) width aligned along the blue and red lobes at the PAs shown in Figure 5.3. This allows for measurement of the knot offsets and their peak radial velocities using the methods discussed in Chapter 2.3, and highlights kinematic morphology in the outflow. A second method fits the line profiles at each pixel in the background-subtracted data cubes and generates a 2-D spatial map of the peak radial velocities. Combined, these methods provide a powerful tool for examining the spatio-kinematic structure of the outflow.

In addition to the PAs given in Figure 5.3, PV arrays were extracted at PA = 33° and 42° for [N II] and [S II], PA = 50° for [O I], and PA = 193° for Hα in order to examine the cavity and whistle features. In Figure 5.8, PV diagrams are shown for Hα and [S II]λ6716 Å at these PAs. Slight differences are observed between the PAs covering the red and blue lobes, but what is most striking is an apparent "knot"-like feature in the 33° cut in panel (b). This feature is additionally seen in the [N II]λ6583 Å data. Looking at the peak velocity as a function of spatial structure is further shown in Figure 5.9 and reveals interesting features in the jet and cavity. In Hα particularly, the bulk velocity of the cavity is slightly blue-shifted despite being oriented in the same direction as the red-shifted jet. Some redshifted emission is seen however, possibly suggesting this cavity is not an emitter but is rather reflecting scattered light. In the [S II] line the cavity features appear more strongly redshifted, peaking on the rim facing the jet.

Due to the lower velocity resolution of MUSE ($\sim$ 55 km s^{-1}) it is not possible to determine if there are any low velocity components in this data. The PV and $v_{\rm rad}$ maps both appear to indicate the cavity and whistle move with lower velocities than the rest of the flow, but this is more difficult to constrain with this instrument. An interpretation of these results will be discussed in Section 5.4.

5.3.2 Knot Identification

Now that the structure of the jet has been presented, we turn to a more formal identification of the features within it. This work is novel in that it is the first discovery of an extended knot-structure in the outflow, and we have named these knots (from red to blue) F, E, A, B, C, and D. Using the PV arrays shown above, spatial profiles were extracted from the 76° and 254° cuts of the [S II] doublet in order to calculate the knot positions. Despite the low luminosity of the source, emission at the source position dominates in the spatial profiles and can complicate the fits. Additionally, some of the features appear to be blended or have very broad profiles, again making accurate fitting more difficult.

In Figure 5.10, the result of this procedure is shown for the [S II]λ6716 line at two PAs. The 76° cut shows a broad swell at about 3″ which is interpreted as a knot, with a blended swell around 1″.6, which could not be fit. The 3″ feature could not be fit in the 254° cut but the 1″.6 feature is shown more clearly, and comparison with the other PAs and spectro-images identifies this as the whistle feature. To estimate the bulk velocities of each of these features, we extract a spectrum at each fitted knot peak and compute the radial velocity in both lines of the [S II] doublet. We co-added the resulting values for each PA and report these in Table 5.1. The centroid errors for individual fits were computed according to Equation 2.17, and the errors presented in the Table are the quadrature errors for the co-added fits. Uncertainties in the radial velocities are simply reported as the Gaussian σ due to the lower velocity resolution. All [S II] line profiles exhibit FWHM values below 100 km s^{-1}.

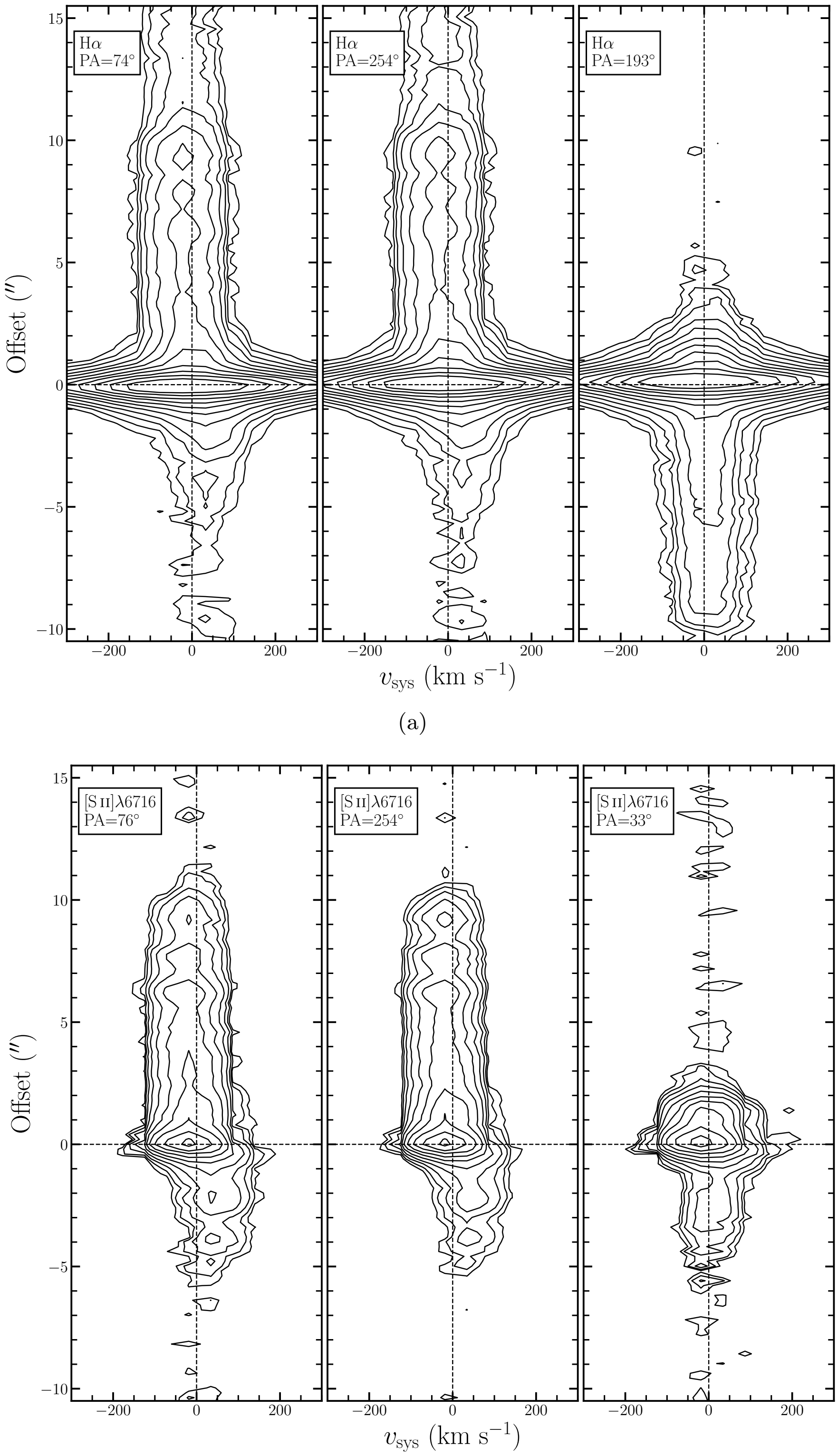

(a)

(b)

FIGURE 5.8: PVDs of the M1082188 outflow along multiple PAs. Figure (a) shows the Hα line with the slit oriented along the (left) blue lobe, (center) red lobe, and (right) cavity. Figure (b) shows the same but for the [S II]λ6716 Å line, with the final panel (right) oriented along the whistle feature. For each panel, contours begin at 3σ and scale logarithmically to about 75% of the peak value in that array.

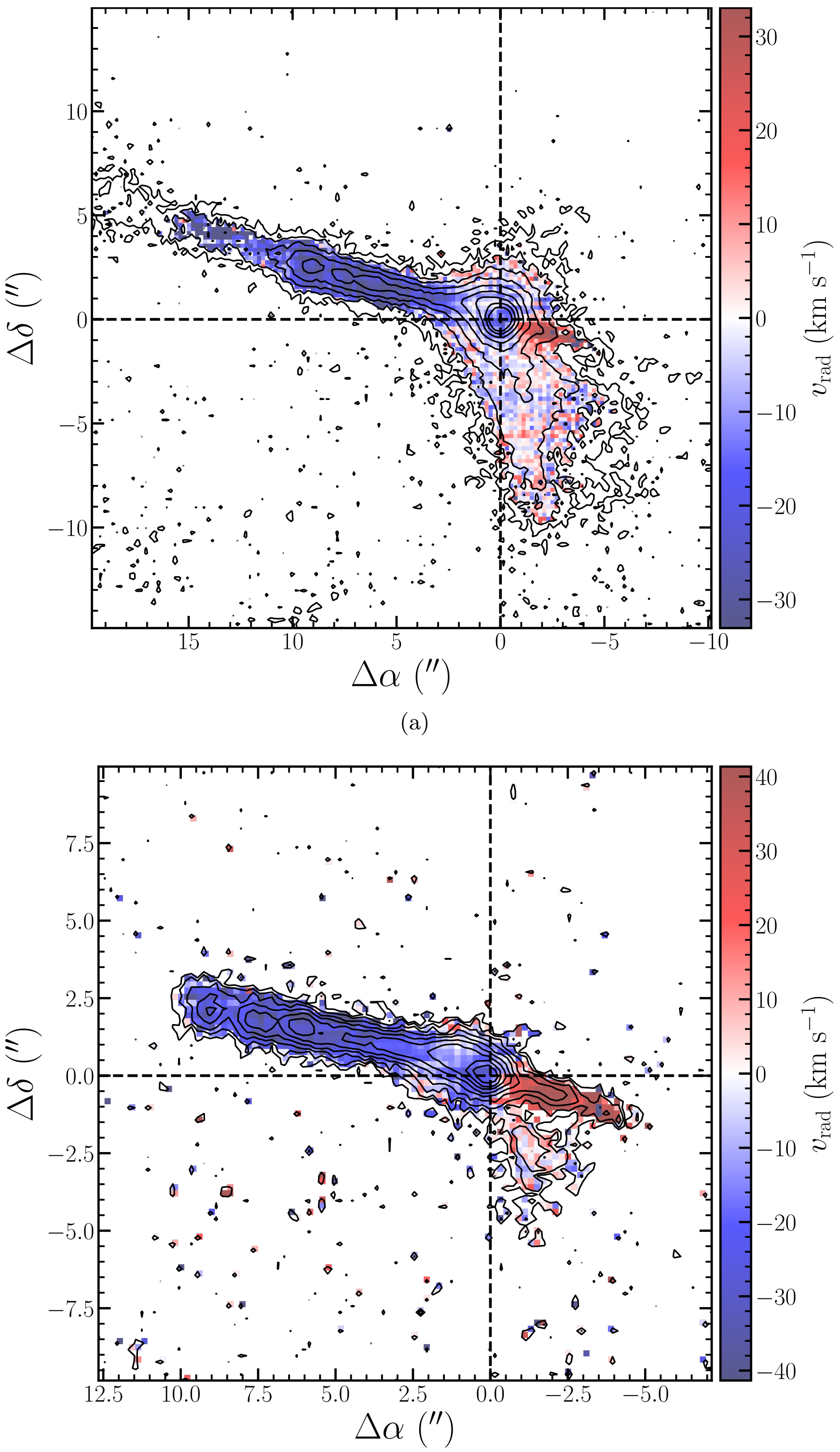

(a)

(b)

FIGURE 5.9: Radial velocity maps for the (a) Hα and (b) [S II]λ6716 emission lines. Each pixel corresponds to the peak radial velocity fit at that point. The black contours are the same as in Figure 5.3 in order to better correlate the velocity with spatial emission structure.

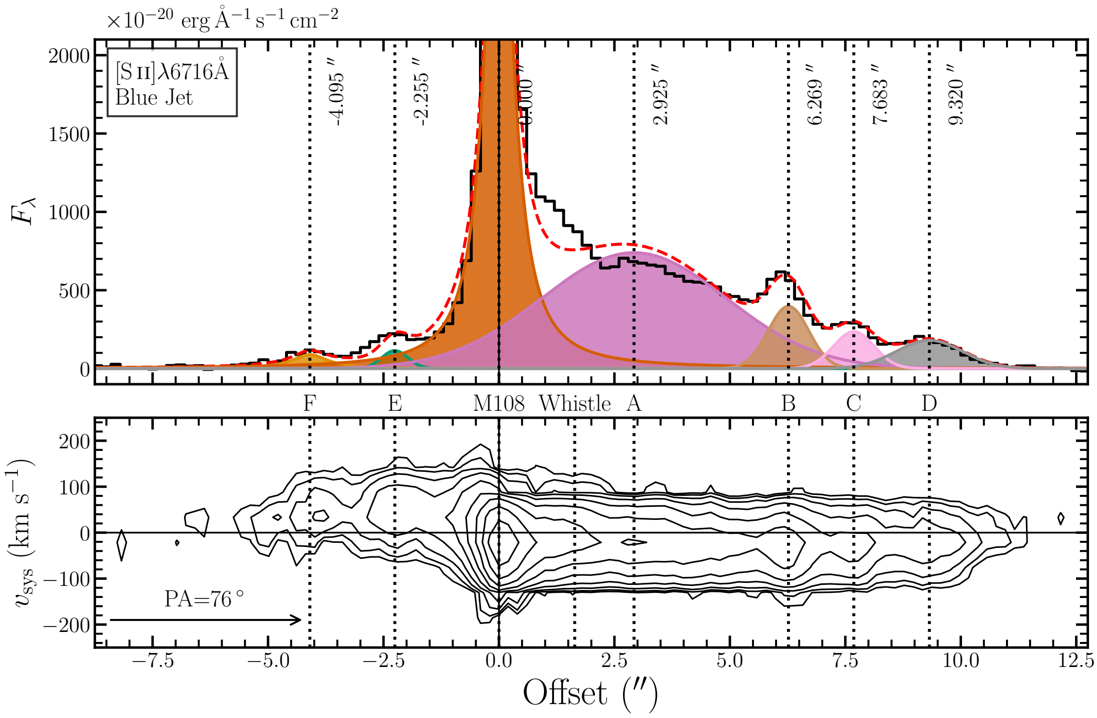

(a)

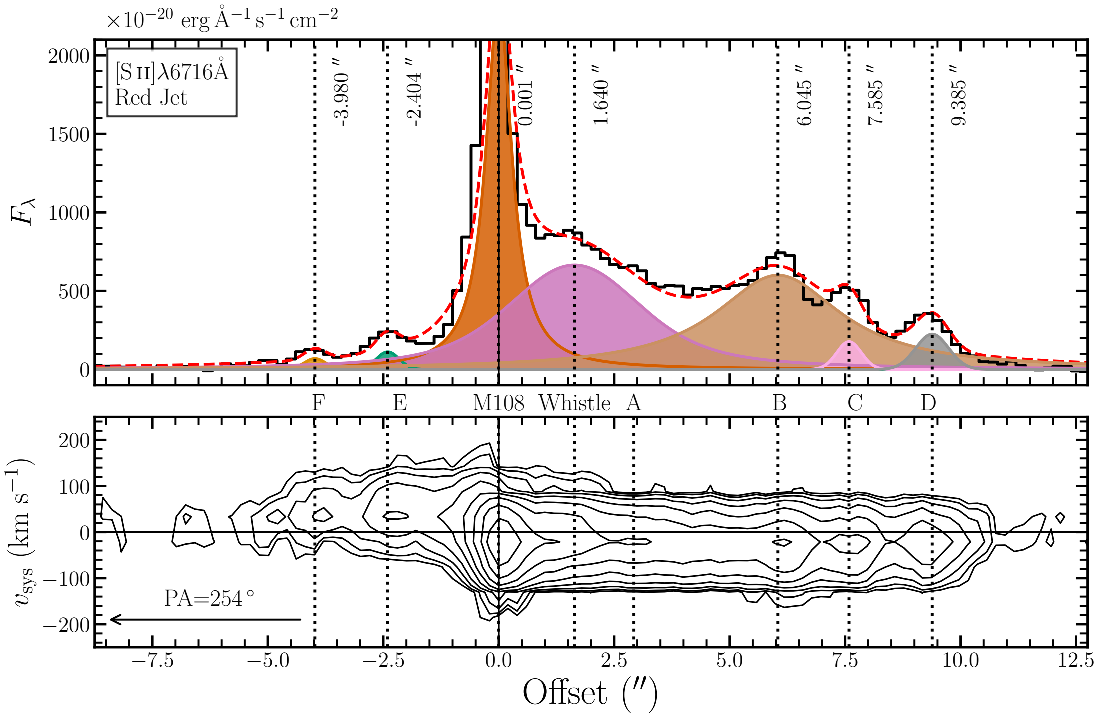

(b)

FIGURE 5.10: Spatial profiles of the M1082188 outflow in the [S II]λ6716 emission line for PA = 76° and PA = 254°. The top panels show the Gaussian fits to the profiles, and the bottom panels show the PV map of the line at their respective PAs.

Feature	PA = 76°		PA = 254°	
	x_t ($''$)	v_{rad} (km s^{-1})	x_t ($''$)	v_{rad} (km s^{-1})
F	-4.03 ± 0.24	46.0 ± 12.3	-3.99 ± 0.10	43.4 ± 14.8
E	-2.15 ± 0.11	47.6 ± 16.3	-2.28 ± 0.05	44.4 ± 17.6
Source	0.00 ± 0.01	-25.0 ± 10.0	0.00 ± 0.01	-24.2 ± 14.4
Whistle	...	...	1.64 ± 0.10	-12.2 ± 11.5
A	3.07 ± 0.33	-22.3 ± 16.2	3.41 ± 0.03	-24.4 ± 14.0
B	6.32 ± 0.05	-32.1 ± 10.3	6.21 ± 0.06	-32.1 ± 10.0
C	7.75 ± 0.09	-32.2 ± 13.3	7.67 ± 0.03	-31.5 ± 13.9
D	9.41 ± 0.17	-27.4 ± 11.4	9.41 ± 0.03	-28.2 ± 16.6

TABLE 5.1: Knot positions and radial velocities of the M1082188 outflow measured from the MUSE data. The values here are calculated using Gaussian fitting of the spatial profiles and line profiles, using the co-added [S II] doublet position-velocity arrays for position angles of 76° and 254°.

5.3.3 Mass Accretion & Outflow Rates

When comparing with the UVES data, it is evident that there are new structures observed that were not present in the 2014 observations. Riaz and Whelan (2015) additionally computed $\dot{M}_{out}$ and $\dot{M}_{acc}$ for the source, and a comparison with these values can help determine if there has been an outburst event since their study and better characterize the general activity of the source. In this section we have followed the method explained in Riaz et al. (2015) to compute the accretion and outflow rates for the source. We have additionally assumed the same stellar parameters and atomic data used in their study.

The width of the Hα line and strong presence of the Ca II IR triplet are indicators of heavy accretion. The [O I] is commonly used as well though it is a more indirect tracer as it forms above the disk (Riaz et al., 2015). Assuming magnetospheric accretion (see Chapter 1.2.1), the mass-accretion rate can be found utilizing the accretion luminosity L_{acc} by

$$\dot{M}_{acc} = \left(1 - \frac{R_*}{R_{in}}\right)^{-1} \frac{L_{\text{acc}} R_*}{G M_*} \approx 1.25 \frac{L_{\text{acc}} R_*}{G M_*}, \tag{5.1}$$

where R_* and M_* are the stellar radius and mass respectively, and R_{in} is the inner disk radius. The accretion luminosity L_{acc} can in turn be derived from the line luminosity L_{line} by

$$L_{\text{acc}} = a \log L_{\text{line}} + b, \tag{5.2}$$

where a and b are coefficients empirically determined from modeling the so-called "Balmer Jump", a process linked with UV excess and spectral veiling (Alcalá et al., 2011; Herczeg and Hillenbrand, 2008). To compute the line luminosity, we have de-reddened our measured fluxes assuming an extinction $A_{\text{V}} = 2$ and converted this to a luminosity by the relation $L_{\text{line}} = 4\pi d^2 F_\lambda$, where d is the distance to the emitter.

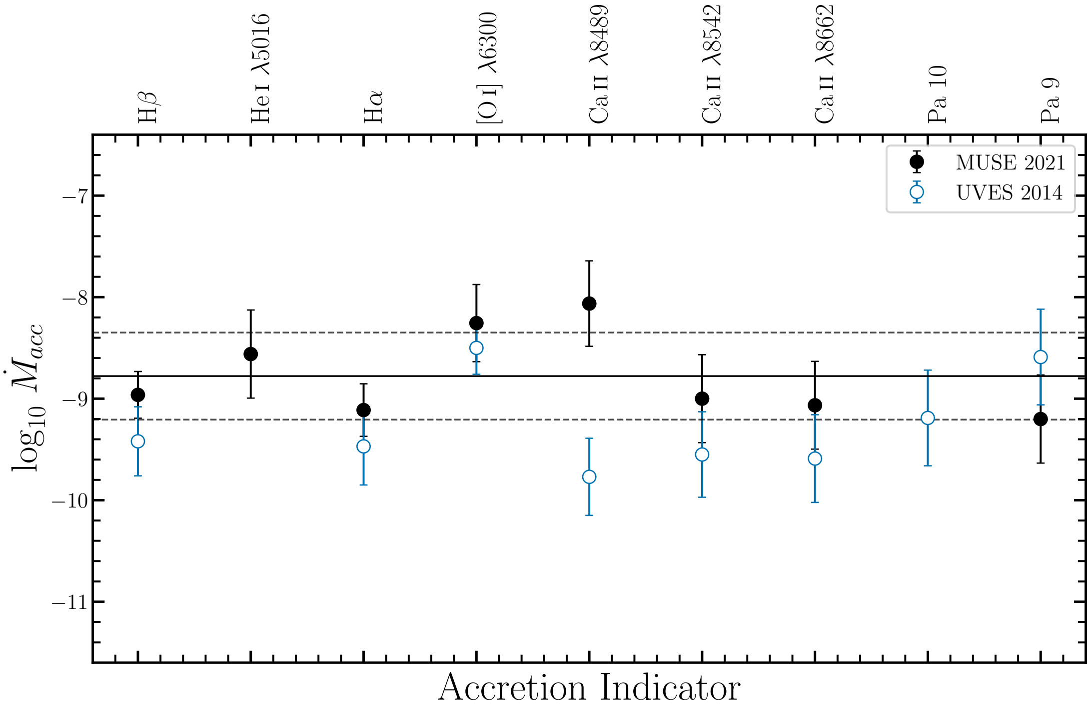

FIGURE 5.11: Comparison of $\dot{M}_{acc}$ rates (in units of log $M_\odot$ yr^{-1}) for selected indicators in the UVES and MUSE epochs.

In this section we have utilized the same distance ($d = 350$ pc) and stellar parameters as those assumed by Riaz et al. (2015), and have used the a and b terms found in Table 4 of Alcalá et al. (2014). While a more recent table has been published since then, as well as new distance measurements (see e.g. Schaefer et al., 2016), these are not used here in order to better compare with the UVES epoch. A comparison of the two epochs is shown in Figure 5.11, and the tabulated MUSE values are shown in Table 5.2. We do not observe the Pa 10 emission in the MUSE data, and we include the He I λ5016 line which is not reported in Riaz et al. (2015). Caution is advised for the Balmer lines and [O I], as these also feature jet emission and thus may not be entirely represented of the accretion of the source. The Ca II λ8489 line also appears to indicate anomalously strong accretion. If we exclude the Balmer lines, [O I], and the first of the Ca II triplet, the mean accretion rate is found to be $(1.3 \pm 0.8) \times 10^{-9}$ $M_\odot$ yr^{-1}, a factor of ∼ 4 higher than that measured from the UVES data.

Additionally, we can use Equation 4.3 compute the mass-loss from the [S II]λ6731 line for each of the features. For this, the PV arrays were integrated over each of the identified features for the [S II] doublet. The inferred electron densities peak at the source ($n_e = 8200 \pm 870$ cm^{-1}) and decrease with distance, as seen in Figure 5.12. Using these values and the fluxes measured over these integrations, the luminosity, mass, and mass-flux for each feature can be calculated. These values are given in Table 5.3. $\dot{M}_{out}$ at the source is found to be $(5.43 \pm 2.69) \times 10^{-10}$ $M_\odot$ yr^{-1}. Along the jet we find mean values of $\dot{M}_{out} = (1.87 \pm 0.68) \times 10^{-10}$ $M_\odot$ yr^{-1} for the red-shifted lobe and $\dot{M}_{out} = (5.25 \pm 1.28) \times 10^{-10}$ $M_\odot$

Indicator	λ Å	a	b	L_{acc} (log $L_\odot$)	$\dot{M}_{acc}$ (log $M_\odot$ yr^{-1})
Hβ	4861.325	1.11 ± 0.05	2.31 ± 0.23	-2.22 ± 0.23	-8.96 ± 0.23
He I	5016.678	0.09 ± 0.06	3.36 ± 0.39	-1.76 ± 0.38	-8.56 ± 0.43
Hα	6562.8	1.12 ± 0.07	1.50 ± 0.26	-2.37 ± 0.26	-9.11 ± 0.26
[O I]	6300.304	0.90 ± 0.01	2.49 ± 0.41	-1.52 ± 0.38	-8.26 ± 0.38
Ca II	8498.02	0.95 ± 0.07	2.18 ± 0.38	-1.32 ± 0.42	-8.06 ± 0.42
Ca II	8542.09	0.95 ± 0.08	2.13 ± 0.42	-2.33 ± 0.43	-9.00 ± 0.43
Ca II	8662.14	0.95 ± 0.09	2.20 ± 0.43	-2.46 ± 0.43	-9.06 ± 0.43
Pa 9	9229.014	1.13 ± 0.09	2.60 ± 0.47	-2.60 ± 0.47	-9.20 ± 0.43

TABLE 5.2: Mass-accretion rate of M1082188 using the accretion indicators visible in the MUSE data. The a and b terms given in Table 4 of Alcala are shown as well. The accretion luminosity and mass accretion rates are given in log form.

yr^{-1} in the blue lobe, in agreement with the asymmetry noted by Riaz and Whelan (2015). We observe a variation in the jet outflow rate as well, with the whistle presenting the highest values and the rate in general decreasing with distance from the source. From these we estimate launch efficiencies of approximately 0.14 in the red lobe, 0.40 in the blue lobe, and 0.42 at the source, with an overall launch efficiency of ~ 0.35. If the whistle feature is considered separately, this exhibits the highest ratio with a value of ~ 0.65. These values are high compared to low- and intermediate-mass stars ($\lesssim 0.1$), with the blue lobe and whistle being above the limit of ~ 0.3 set by magneto-centrifugal launch models (see Cabrit, 2009). This is not unexpected for BDs and may still be lower than what is observed in other similar objects (Whelan et al., 2009; Joergens et al., 2012).

5.3.4 An Unidentified Source

In examining the MUSE field images obtained from the full data cubes, we notice a faint source offset by about 1.″6 ($\sim$ 560 au) to the east of M1082188. This is shown in Figure 5.13. We very briefly address this here as its proximity raises the possibility of it being a potential companion. The point source is fainter by $\sim$ 4.5 mag and is not present in the background-subtracted cubes. It is close enough to the BD that the jet spectrum may "imprint" itself upon the smaller source, making its intrinsic spectrum impossible to disentangle from the jet in spectral regions where the jet presents strongly. This is primarily evident between 6000 Å and 7000 Å where the majority of jet emission is observed. This phenomenon is shown in Figure 5.14.

In Figure 5.15 we show spectra extracted from the BD and the point source in question over the range of the MUSE cubes. Overall the point source exhibits a relatively flat and unremarkable spectrum. We further compared this spectrum to the spectra of multiple sources in the in the FOV, which are marked in Figures C.2−C.4. We find a variety of spectral shapes in the field sources, and all comparisons further confirm the flat character of the point source in question. We finally compared this to the spectral templates obtained

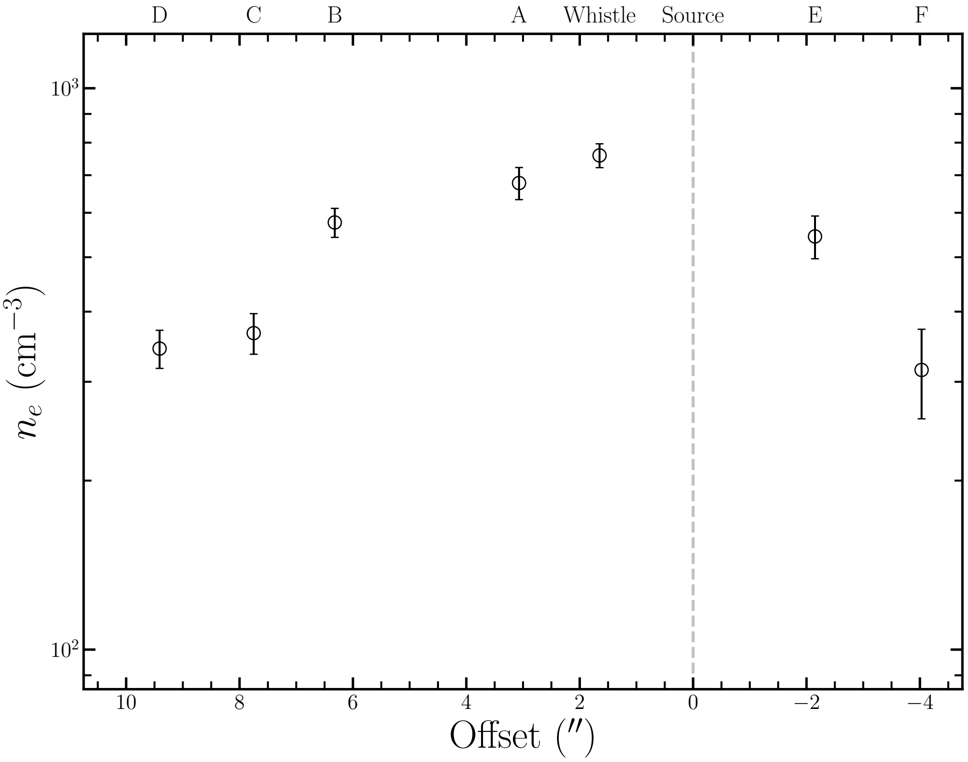

Figure 5.12: Electron densities inferred from the [S II] PV arrays. The density at the source is not shown in order to preserve a similar scale.

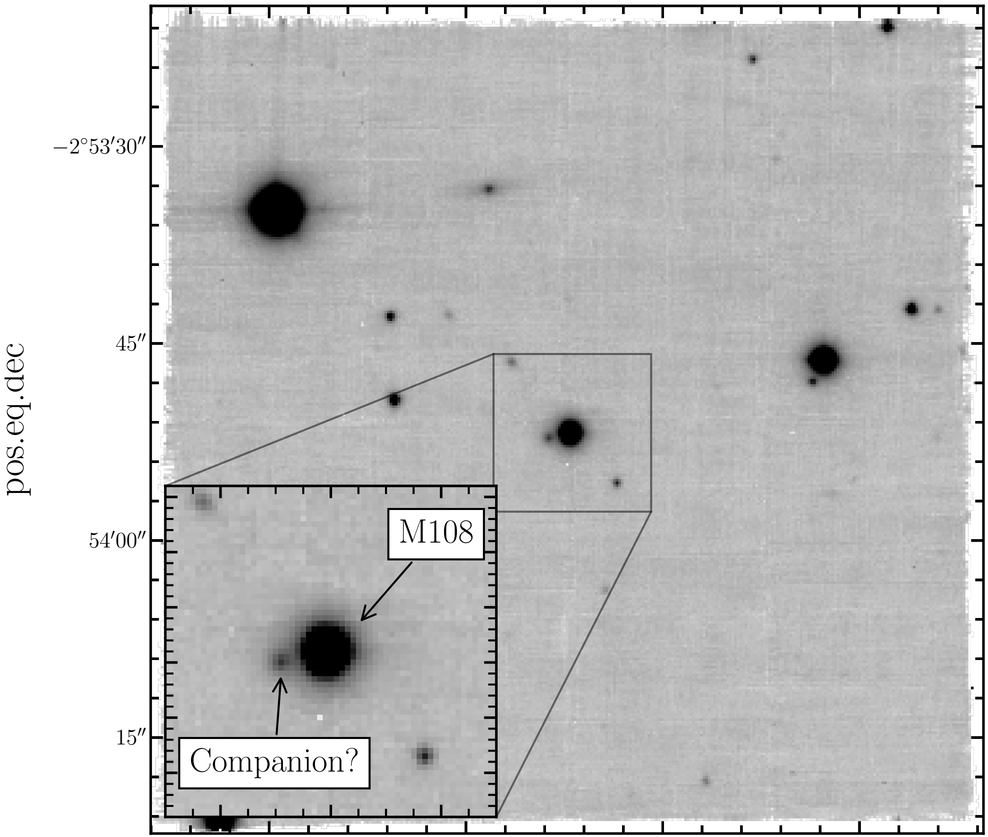

Figure 5.13: MUSE field image of M1082188. The inset shows a cutout centered on the BD with the unidentified source labeled.

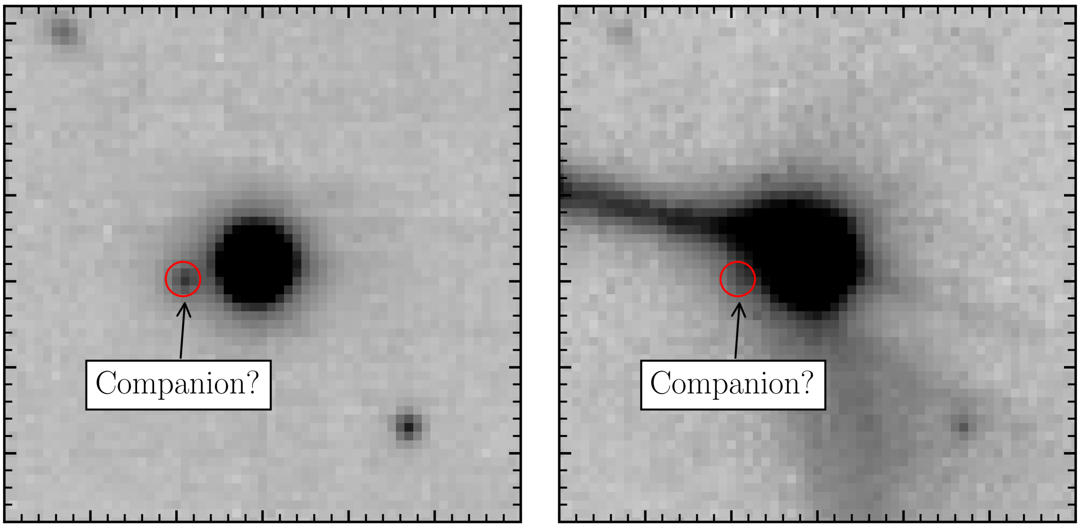

Figure 5.14: Similar to the insert seen in Figure 5.13, where the potential companion is circled in red and shown on the left in a continuum image and on the right in an Hα image. In the right panel it is seen that the Hα emission buries the fainter source and thus "imprints" the spectrum of that source with the spectrum of the jet.

with X-Shooter (see Figure B.1, as well as Chapter 4 and references there) and found no similarities with K- or M-type spectra. From this it seems unlikely that this is a companion as we would expect a spectral type indicative of a very low-mass object, and so it may be likely that this is only some background star or galaxy whose spectrum cannot be resolved with respect to the BD, and further observations would be required to better determine its nature.

Knot	L (10^{-7} $L_\odot$)	M (10^{-8} $M_\odot$)	$\dot{M}_{out}$ (10^{-10} $M_\odot$ yr^{-1})
F	0.9 ± 0.4	0.5 ± 0.2	1.58 ± 0.83
E	2.0 ± 0.8	0.7 ± 0.3	2.16 ± 1.08
Source	45.4 ± 18.4	17.9 ± 7.3	5.43 ± 2.69
Whistle	10.9 ± 0.4	2.8 ± 1.2	8.54 ± 4.25
A	6.1 ± 2.5	1.8 ± 0.7	5.36 ± 2.67
B	5.1 ± 2.1	1.7 ± 0.7	5.25 ± 2.63
C	2.9 ± 1.2	1.6 ± 0.7	4.82 ± 2.42
D	2.0 ± 0.8	1.1 ± 0.5	3.32 ± 1.76

Table 5.3: Luminosity, mass, and outflow rates for the M1082188 features in the [S II]λ6731 emission lines.

5.4 Discussion

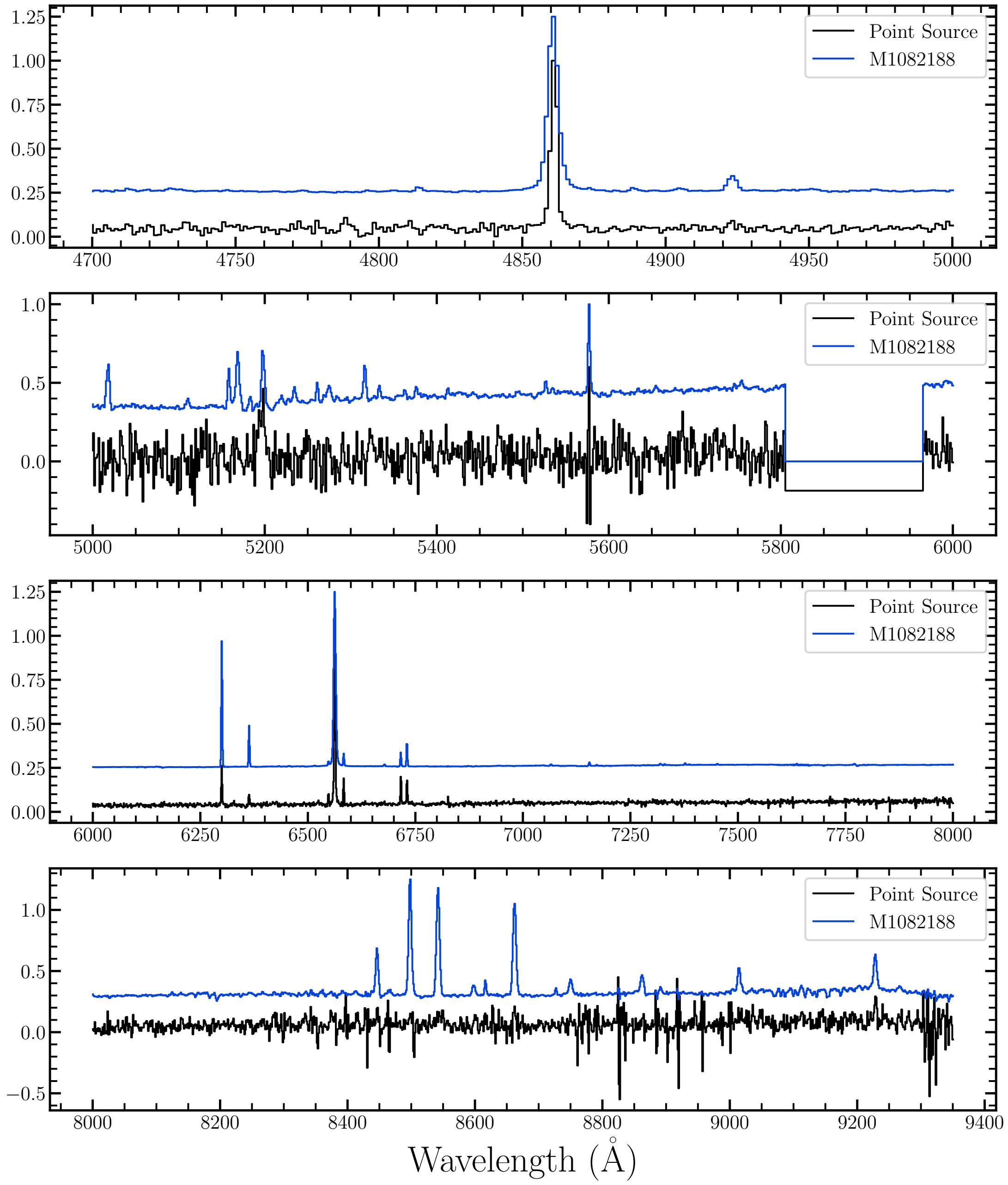

FIGURE 5.15: A comparison of the unidentified point source spectrum with M1082188. In the 6000 – 7000 Å range the imprint of jet emission on the point source is most evident, though it is also seen around Hβ as well.

5.4.1 Jet Curvature

Throughout Section 5.3.1 we have seen stark evidence of an asymmetric outflow, not only in its morphology but its density, accretion, and outflow rates as well. From Figure 5.3 we observe that the jet PA is different for each lobe, and this is further evidenced in Figure 5.6, where it is seen that the PA for both lobes is not only asymmetric, but features a general south-ward trend. While it does not appear as though there is any precession or orbital motion signatures within the jet, the fact that both PAs point below the horizontal supports a type of jet-deflection scenario. Whether this is due to a "rocket effect" or some form of radiation pressure (Bally, Youngblood, and Ginsburg, 2012) or a supersonic wind from σ-Ori (Masciadri and Raga, 2001) is uncertain with this data.

What we can say, however, is that the incident radiation from σ-Ori very likely plays a role in the bending of the jet. In addition to the asymmetric PAs, we can look at the Hα and [S II] lines to better glean this effect. For jets in which shock-driven excitation dominates we anticipate a Hα/[S II] ratio $\lesssim 1$, whereas ratios much greater than one are often observed in irradiated jet and therefore may be an indicator of irradiative processes (see e.g. Bally and Reipurth, 2001; Reipurth and Bally, 2001b). In Figure 5.16, we present the ratio map of the [S II] line relative to Hα, shown with contours computed from the forbidden S line. What is observed is that the Hα/[S II] ratio everywhere is significantly greater than unity, potentially indicating enhancement due to irradiation. This is seen most strongly around the source (> 14) and in the north-facing components of the blue-shifted jet. It is worth noting that both radiative and collisional processes can contribute to Hα emission. The collisional component can be quite strong following a shock which can also result in an Hα/[S II] ratio much greater than unity. The interpretation of irradiation is therefore given with caution as radiative and collisional contributions to Hα emission are strongly dependent on local conditions which we do not evaluate here.

The high ratio around the source is also curious as it presents an almost disk-like shape. A sketch of a disk inclined at about 60° from the plane of the sky is shown to highlight this feature. It exhibits a "flared" structure around the edges which, if interpreted as being related to the disk, could potentially indicate the strong irradiation of winds or a cavity swept up by the jet. An alternative interpretation of this is that the high densities close to the source result in more frequent collisions and de-excitation of the ion, as well as the line intensity being linearly proportional to n_e (rather than the n_e^2 proportionality in low density regimes). The effect of this is a quenching the [S II] lines which yields fainter [S II] emission in this region (Whelan et al., 2005). The nature of this feature is however ultimately uncertain.

The underside of the jet exhibits a ratio > 1 but is significantly lower than the other portions of the outflow. This is particularly interesting as the jet does not appear to have a high density (typically $< 10^3$ cm^{-1}), so shielding of the underside of the jet by the upper regions seems unlikely unless there is a dense, unseen neutral component not visible in the data. Such a scenario would appear to contraindicate irradiation as well, as external radiation is expected to reveal quiescent material. It could be that the low density of the jet is indicative of photoablation, in which case the observed bending of the jet could be due to the rocket effect (Bally, Youngblood, and Ginsburg, 2012).

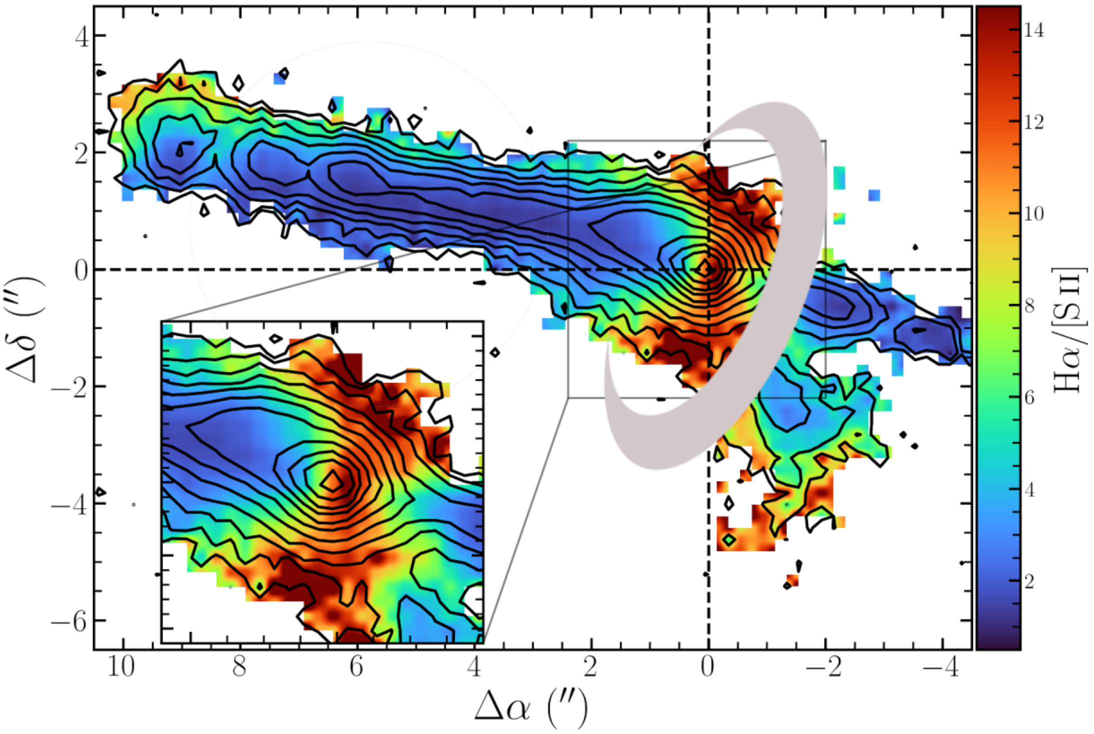

FIGURE 5.16: Ratio of the Hα and [S II] emission lines in M1082188, which is sensitive to ionization. The contours are computed from the co-added [S II] lines and are shown in a logarithmically increasing scale. A rough orientation of the disk is shown around the region with the highest ratio solely for purposes of visualization.

5.4.2 Launch Efficiency

In Section 5.3.3 the accretion and outflow rates for this object were presented and an estimate of the outflow efficiency was found to be above the limit implied by magneto-centrifugal launch models. An asymmetry is observed in the outflow rate between jet lobes with the red jet being significantly lower than its blue counterpart and is similar to that observed by Riaz and Whelan (2015). Due to the UVES data not being aligned along the PA of the jet, the current MUSE observations provide a better indication of the outflow rate along the jet axis as the jet is spatially resolved. The results in Table 5.3 show that the ratio of the blue to red jet features, excluding the whistle, ranges from $1.5 - 3.4$, which can be explained by the fact that the red jet is simply weaker and pointing away from the σ-Ori complex.

As the jet is expected to dissipate with distance from the source, the innermost features yield the most reliable estimate of the efficiency of the launch mechanism. Examining knots E and A indicates efficiencies of 0.17 ± 0.13 in the red jet and 0.41 ± 0.33 in the blue jet. If the whistle feature is considered separately it is seen that the outflow rate of of $8.54 \times 10^{-10}\ M_{\odot}\ \mathrm{yr}^{-1}$ is nearly comparable to the accretion rate of $1.3 \times 10^{-10}\ M_{\odot}\ \mathrm{yr}^{-1}$ ($\dot{M}_{out}/\dot{M}_{acc} \sim 0.65$). This is significant as a key prediction of D-wind models is that the mass-loss rate of the wind should be similar to the accretion rate Whelan et al. (2021); however this test relies upon discerning the narrow-component profile of the LVC, and the LVC is not observed in the MUSE data.

These ratios nonetheless reveal crucial information about the nature of the BD outflow, and indicate that even with the lower ratio in the red lobe the efficiency here is higher than that of CTTS and HAeBes. The ratios in the blue lobe and whistle both provide support for the argument that BDs may not be able to accrete enough material to fuse hydrogen due to a high ejection rate. Evidence for this is tentative, however. There are less than 20 known outflow-driving BD and very-low-mass object sources, and of these even fewer have well-constrained accretion and outflow measurements. Of the values reported however, approximately 60% of the $\dot{M}_{acc}/\dot{M}_{out}$ values are greater than 0.1 (Whelan et al., 2014; Riaz et al., 2015; Riaz and Whelan, 2015; Riaz and Bally, 2021). Further discussion on the nature of the whistle will be discussed below.

5.4.3 Dust-Scattering & the Nature of the Cavity

Below the bar: an inner cavity wall?

We turn our attention now to the feature below the red-shifted jet. In particular we are interested in the "bar" that runs roughly along the underside of the red lobe with an apparent knot-like feature observed in [S II] around $2''$ from the source (see Figure 5.2). Radial velocity maps reveal this feature to be red-shifted as well. It is not quite parallel to the jet, and subtends an angle of approximately 40° southward of the jet. To further explore this feature, we have simulated a slit parallel to the red jet at a PA of 254° and offset $\sim 1''$ in order to cover the emission. This is shown in Figure 5.17. For this analysis the two [S II] lines were co-added with a median clipping to boost the S/N while suppressing the propagation of background noise. Like the red jet, the bar feature appears to possess a low velocity red-shifted knot with a blue-shifted wing downstream of the emission.

We apply a line-fitting routine to the spatial profiles in the same manner as done with Figure 5.10 to better understand these features, which we show in Figure 5.18. A peak is observed along the cavity feature at $-1''.82$, which just precedes the position of knot E. A fit along the dispersion axis yields a velocity centroid between $5 - 10$ km s^{-1}. Interestingly, the ratio of these two offsets yields an angle $\sim 30° - 40°$, which appears to coincide with the angle between the bar and the true jet. This yields interesting information about the geometry and kinematics of the overall outflow system, which we shall see below.

That the "lag" of the knot feature behind knot E is consistent with the projection of knot E emission at an angle on the order of that between the jet and bar leads us to the conclusion that this feature is not itself an intrinsic emission. We interpret this instead as the reflection of the jet off the walls of a blue-shifted cavity. Solf and Böhm (1991) observed a similar occurrence with HH 1/2, where a strongly blue-shifted feature was seen extending

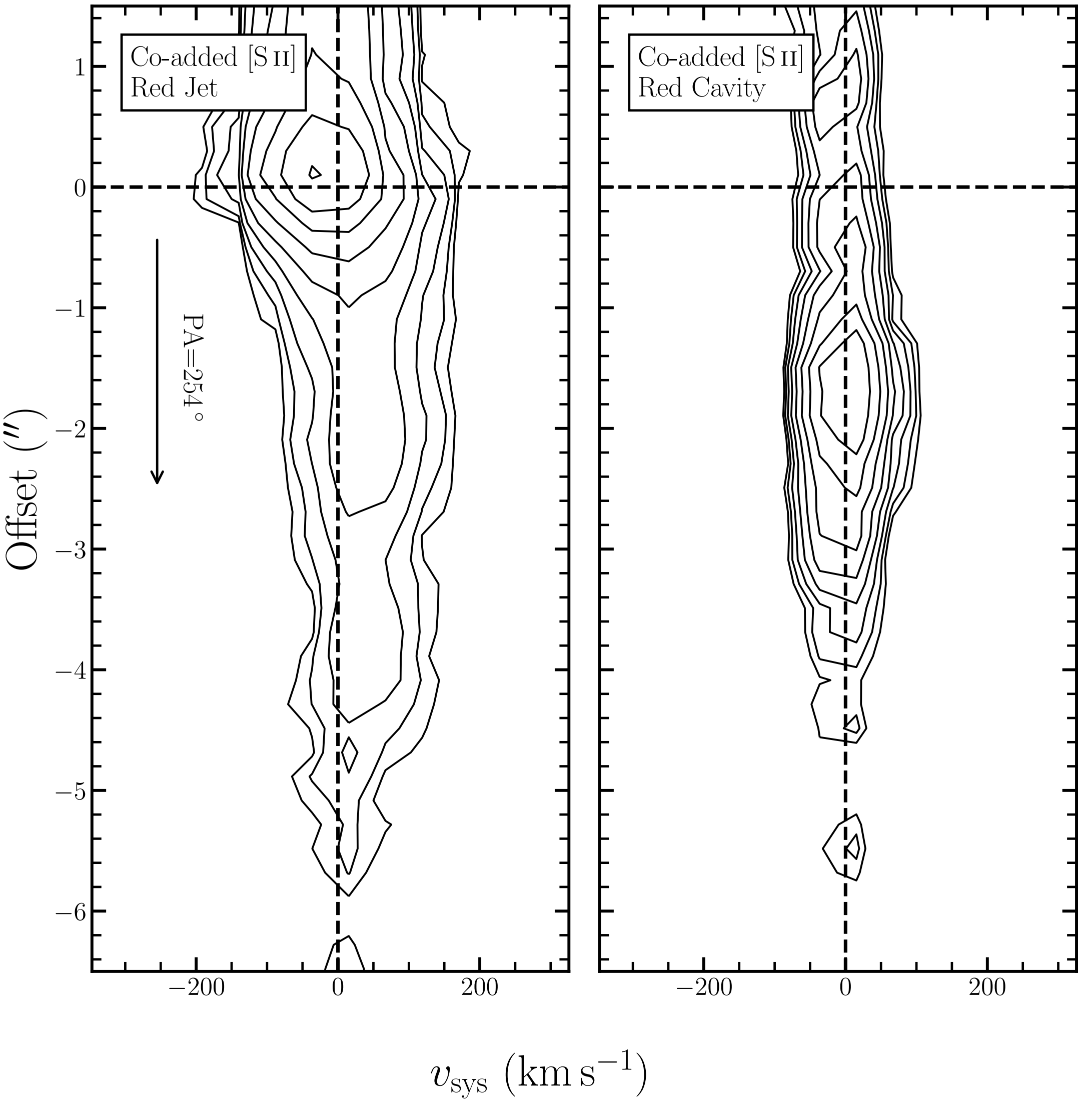

FIGURE 5.17: PV arrays showing the co-added [S II] jet and cavity emission.

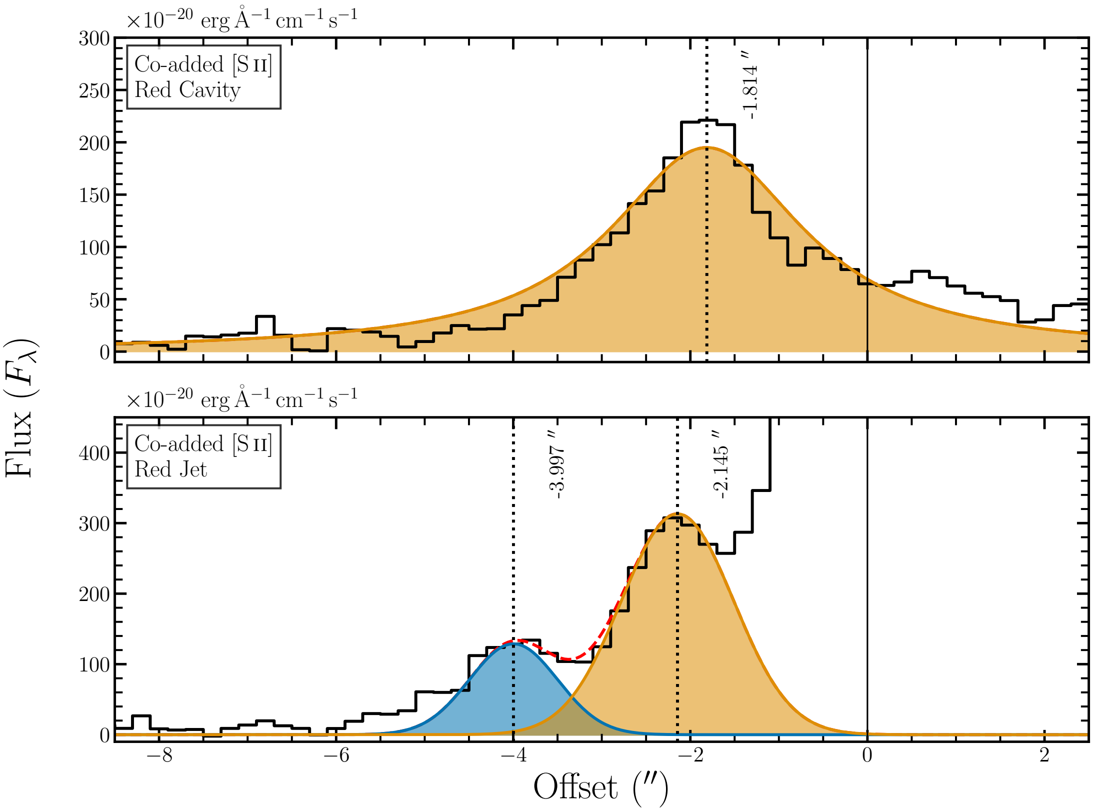

FIGURE 5.18: Spatial profiles of the cavity feature (top) and red-shifted jet (bottom) seen in the co-added [S II] lines. Each profile was computed from a PV-array taken at a PA of 254°. The cavity PV array was taken parallel to the jet feature.

beyond the known knots with wings that increased with distance from the source. They concluded that this was due to the light from the bow shock being scattered by a stationary mass of dust downstream of the jet which "sees" the light approaching as blue emission. In their analysis of density distributions they additionally found that the density in the strongly blue-shifted feature was roughly comparable to that of the bulk density of HH1, a result that would not be expected were the line emission to be formed locally by the extended feature. Following their observations Noriega-Crespo, Calvet, and Böhm (1991) worked to model this dust scattering with radiative transfer models and found that their results supported the conclusion of Solf and Böhm (1991).

In the case of M1082188, the radial velocity maps and PV diagrams both indicate that this feature is moving at a low velocity ranging between ±10 km s^{-1} with a line width of $\sim$ 100 km s^{-1}. If this feature is a local emitter, for example a second misaligned jet, then we would expect its density to vary significantly from that of the knot emission. In Figure 5.19, we show a trace of the electronic density computed at each spatial pixel in the PV arrays for the jet and cavity. In knot E we see a low density in the pre-shock region that corresponds to a density peak in the cavity feature, with the bulk densities being relatively comparable. This indicates that the shock in the jet and the dust within the cavity are co-moving features, and their directional vectors form a non-zero angle. This fact is evidenced by the offset peak in the cavity, as well as the peak in its electron density and broad swell downstream of its intensity profile. This cavity feature thus only appears to have a red-shifted knot because it is moving more slowly than the jet at an angle and "sees" the red-shifted jet emission as a blue-shifted source, scattering this bluer light towards the observer.

Evidence of a Wide-Angled Wind?

Let us consider now the structure of the cavity itself. In Section 5.4.3 we concluded that the feature observed southward of the red-shifted jet is actually a dust-scattered reflection of the red-shifted jet off the inner wall of a cavity, and in Section 5.3.1 we have interpreted the larger structure as a reflection nebula or cavity due to its similarity to features observed in low- and intermediate-mass stars. In this Section we will further explore the cavity itself and discuss some of the implications of our findings.

A first problem raised by the above conclusion is that the cavity is only observed in emission lines. Were we truly observing scattered light from the jet, why is this same scattering not present at all wavelengths? The most plausible explanation for this is the low luminosity of the source itself. In CTTSs and HAeBes it is often observed that the continuum emission dominates over jet emission (Whelan et al., 2009, see e.g.); however in M1082188 we observe the opposite, which is not uncommon for sub-stellar objects. While currently no U, B, or V magnitude measurements exist, we can make estimations using continuum images extracted from the MUSE data. Using the `mpdaf.sdetect` package, we have used the `muselet` routine to generate B, G, and R images from the entire MUSE data cube using 1/3 of the total wavelength range for each image. We then place an aperture centered on the source and extract the flux in each image, and convert this to

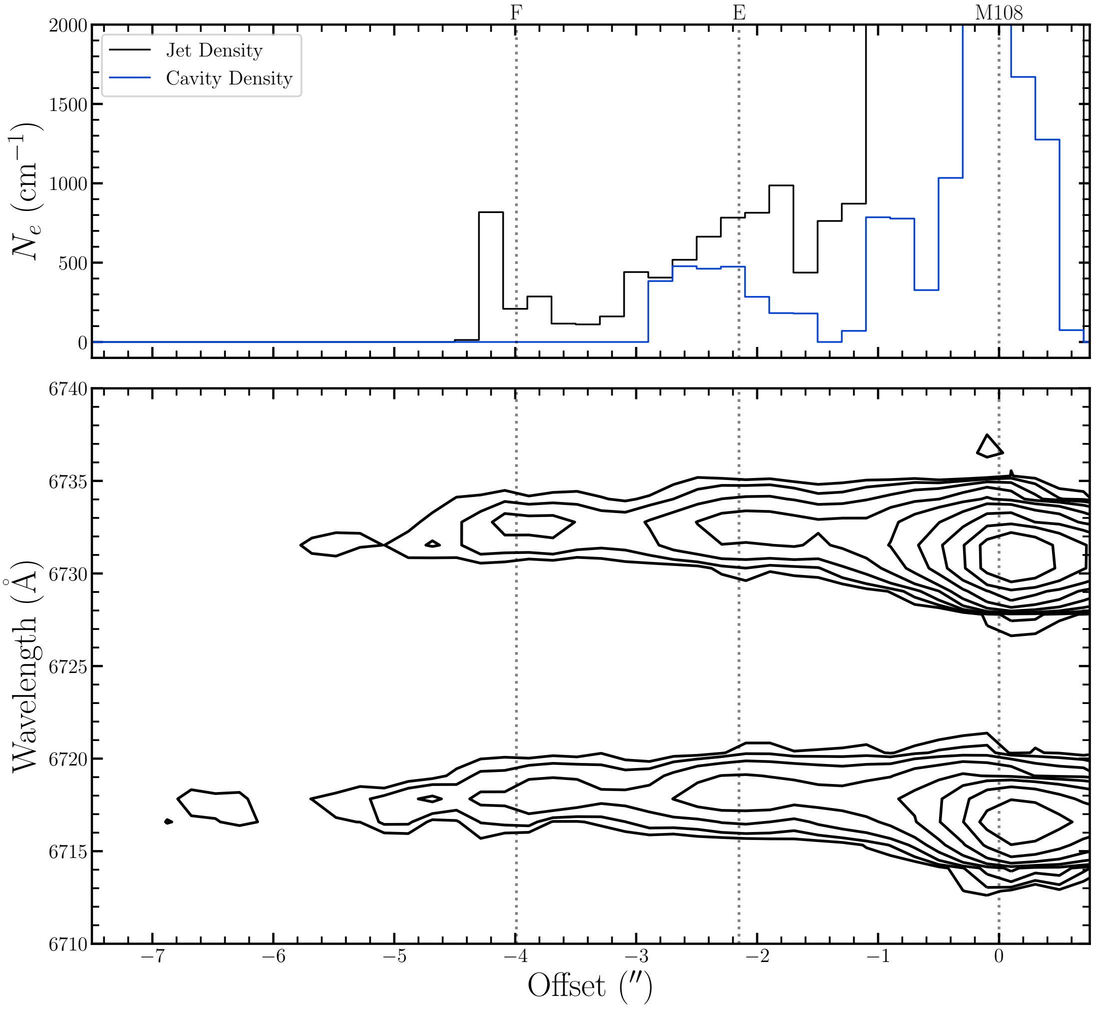

(a)

FIGURE 5.19: A comparison of the densities along the red-shifted jet and cavity feature in M1082188. The top panel shows the jet density in black, and the cavity density in blue. The bottom panel is a PV diagram of the [S II] doublet of the jet to demonstrate the how the densities compare with the emitting regions.

a magnitude based on the central wavelength for that image. This results in an average magnitude of ~ 18, which is consistent with very low luminosity objects. As the jet itself is much brighter, we conclude that the luminosity of the source is too low to be reflected above background level by the cavity, and so the cavity predominately reflects light only in emission lines.

Next we consider emission centroids along the cavity itself. For this we have followed the same jet-fitting routine discussed above in Section 5.3.1 but restricted the fitting to the region around the central source. The red-shifted jet was additionally masked to prevent biasing the fit towards the jet emission profile. This reveals an approximate trace of the potential inner cavity wall south of the red-shifted jet, as well as a trace of the broader and more extended feature below this. We also observe a similar trace in the whistle feature which increases sharply to about $1''$ before aligning with the centroids of the jet axis. In Figure 5.20 we have plotted these truncated centroids along with the contours computed from the co-added [S II] and [N II] lines. This plot additionally shows three parabolas placed roughly along the features traced by the centroids, though it is stressed that these curves are not fits to the actual emission profiles. In the red lobe two curves are shown, with one placed along the broader cavity and the other along the inner cavity wall. Interestingly, both red parabolic curves show wider opening angles (approximately 75° and 100° for the inner and outer walls, respectively) than the blue lobe ($\sim 35°$). A similar opening angle asymmetry was observed by Rodríguez-Kamenetzky et al. (2022) in their analysis of the jet associated with an intermediate-mass protostar, wherein they found evidence of two wind components that appeared to show evidence of both X-wind and D-wind like mechanisms. If the cavity is formed by material swept up along the disk or entrained by the jet, then this may hint at an asymmetric launch velocity between the two lobes.

This realization prompts a deeper look at the nature of the whistle, leading us to question whether this feature is fact a part of the jet, or if it is actually part of a cavity or potentially extended disk wind. This interpretation is strengthened somewhat by the low radial velocity (~ 12 km s^{-1}) of the feature and the high $\dot{M}_{out}/\dot{M}_{acc}$ value. In an X-wind model the initial wide-angled wind features a jet-like component that is collimated by field lines along the rotational axis (Shu et al., 1994a; Shu et al., 1994b). In such models we typically anticipate strong magnetic fields and jet velocities > 100 km s^{-1} to achieve this. While we do estimate a jet velocity on the order of 100 km s^{-1} we do not have magnetic field measurements, though evidence suggests that BDs may have fields as strong as their CTTS siblings (Berdyugina et al., 2017). The Disk-Wind model additionally predicts wide-angled winds, and the sharp increase in the FWHM along the trace of the feature suggests its flow is not as collimated as the jet. The scale of the feature however argues against this interpretation, as the collimation of the jet in either Disk- or X-Wind models is expected within the first 10 au from the source, and this feature extends to at least 500 au.

These observations lead us towards the conclusion that this is a feature of an unresolved cavity. We can further examine this by exploring smaller velocity channel maps of key emission lines, which reveals spatio-kinematic features in finer detail. Using the [S II] and [N II] lines, we construct velocity channel maps by integrating over the emission using two

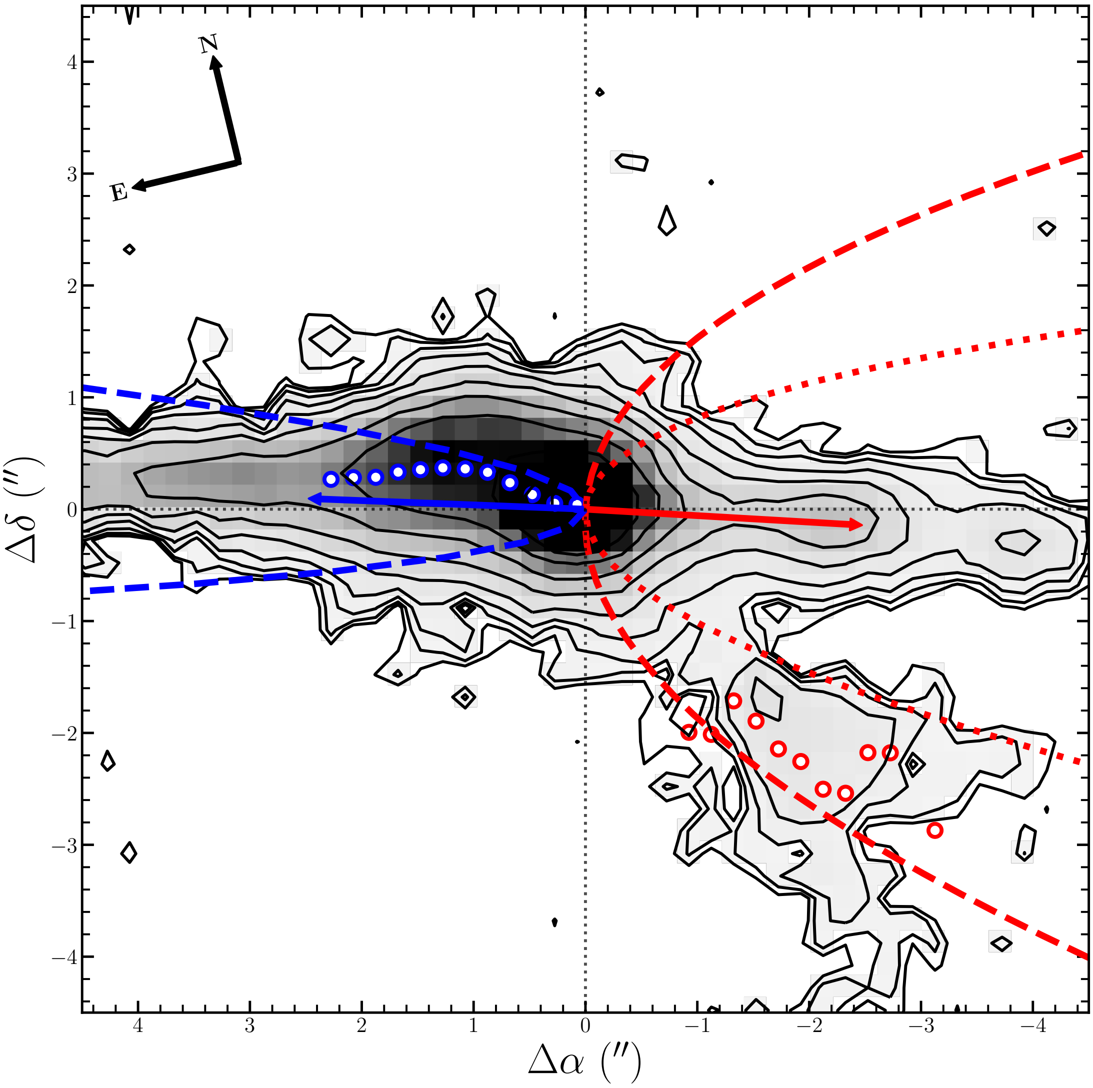

FIGURE 5.20: Spatial emission centroids fit along the cavity of M1082188. The jet axis directions for the blue and red lobes are indicated by colored arrows. The parabolas are shown for demonstrative purposes only and do not represent fits to the data.

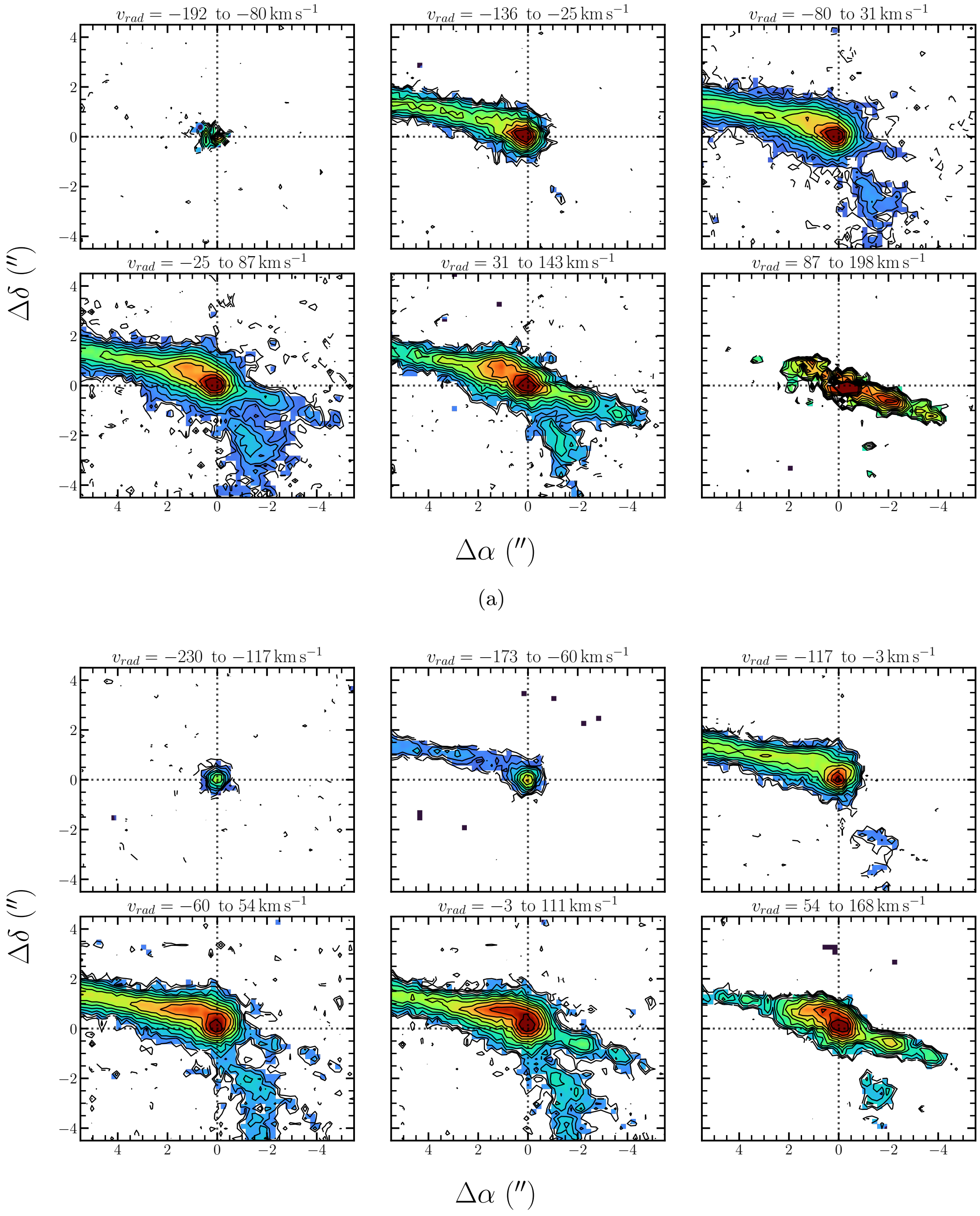

(a)

(b)

FIGURE 5.21: Velocity channel maps of the close-in whistle feature shown in (a) [S II]λ6716 Å and (b) [N II]λ6583 Å. Contours are computed beginning at a 3σ level and scaling logarithmically. The color maps show the intensity of the image using a square root stretch, again beginning at a 3σ level.

spectral planes for each integration step (2 × 1.25 Å). This is shown in Figure 5.21. This reveals interesting differences in the outflow structure between the two lines, with the red-shifted intensity being substantially greater in [S II] relative to [N II], while the whistle appears to persist into the red-shifted emission [N II] more prominently than [S II]. In both lines the structure presents a very broad line profile but peaks at fairly low velocities, indicative of a low-velocity outflow.

It is uncertain why this structure presents such a strong emission profile. As can be seen in Figure 5.21 the feature is substantially brighter than the knot emission. If it is a low-velocity flow associated with a cavity, we might at first expect fainter emission. Comparing with Figure 5.16(a) it does not appear to show excessively high indications of irradiation, and in panel (b) of the same image it does show signs stronger excitation, though this is weaker in comparison to the upper portions of the emission and may indicate quenching of the [S II] lines due to the higher density. If we consider this as a cavity, we are left with the puzzling questions as to why it appears to eventually realign itself with the jet emission and why it emits so strongly. Due to its proximity to the central source, it is likely that this brightness is actually due to dust-scattering of light from both an unresolved jet component and central source. The smaller opening angle compared to the red cavity may be due to radiation pressure from σ-Ori, as the blue-shifted jet is inclined at a greater angle towards the OB-complex than the red-shifted jet. If this is a slower, less dense wind-swept cavity then it would experience a greater pressure from σ-Ori than the denser jet and therefore presents a more “compact” opening angle than its red-shifted counterpart. This initially appears to be contraindicated by Figure 5.12, but if the assumption that its brightness is due to dust-scattered light then it should present a density profile similar to what it is reflecting, and from the same plot we do see that it is close both in space and inferred density to knot A, which would further suggest its nature as a reflective rather than intrinsically emitting structure.

5.5 Conclusions

In this Chapter we have explored the first direct images so far obtained of the outflow associated with M1082188 using the MUSE spectrograph in WFM+AO configuration. We have examined the accretion and outflow rate for the source and explored the physical conditions and outflow rate along the jet. The MUSE data additionally revealed a fascinating and complex cavity of scattered light which I have made the main focus of this Chapter. The cavity presents the most exciting results, as this appears to indicate that sub-stellar objects behave similarly to their low- and intermediate-mass counterparts, with either a disk-wind ejecting lower velocity material, the jet entraining dust in its wake, or perhaps a combination of the two processes. Below, I summarize the primary conclusions of this work.

1. For the first time, the knot complex of this proto-BD candidate was revealed in the optical regime. The outflow axis was found to have an asymmetric position angle that appears to be due to radiation pressure from the massive σ-Ori complex north of the source. A trace of the jet FWHM suggests an opening angle of the jet in the blue lobe of $\sim 4°$. We have additionally identified a feature we interpret to be a cavity of scattered light to the south-west of the source, as well as a curious "whistle" shaped feature close to the source in the blue-shifted lobe. The cavity is present only in emission line images, and we conclude that this is due the low luminosity of the source ($\sim$ 18 mag) It is important to note that, at the least, high resolution IR images are required to better understand the exact nature of this feature.

2. The accretion and mass-loss rates are measured for the source and compared with prior UVES measurements. Additionally, the [S II]λ6731 Å line is used to determine the mass-loss rate along the jet. We find an uncharacteristically large accretion rate in the Ca II λ8489 Å line, with the other accretion tracers being consistent with the UVES epoch. Excluding potentially anomalous lines, we derive a mean accretion rate of $(1.3 \pm 0.8) \times 10^{-9}\ M_{\odot}\ \mathrm{yr}^{-1}$, with an asymmetric mass loss rate in the jet of $(1.87 \pm 0.68) \times 10^{-10}\ M_{\odot}\ \mathrm{yr}^{-1}$ in the red lobe and $(5.25 \pm 1.28) \times 10^{-10}\ M_{\odot}\ \mathrm{yr}^{-1}$ in the blue lobe. This suggests a launch efficiency $\dot{M}_{out}/\dot{M}_{acc}$ between 0.16 and 0.42 in the red and blue lobes respectively, with the whistle feature being highest at ~ 0.65. These values are high in comparison with typical ratios in low- and intermediate-mass stars ($\lesssim 0.1$), but are similar to efficiencies observed in other BD objects. This high efficiency may be a contributing factor in the failure of BDs to accrete enough mass to fuse hydrogen.

3. We explore a curious feature above the cavity which presents a jet-like appearance with a seemingly red-shifted knot. This feature is part of a bar of emission that forms an angle of about 40° with the red jet. Using PV maps and spectro-images, we conclude that this is not an intrinsically emitting object, but is instead a slow-moving cavity approaching the observer. We interpret the red-shifted "knot" as dust-scattering of jet emission, which is evidenced by radial velocity maps and density

profiles. Additionally, the feature in question lags behind the red-shifted knot E, consistent with the projection of the light from knot E onto a cavity wall.

4. Finally, we examine the cavity feature and emission profile. A scenario is explored in which the "whistle" feature is interpreted as the blue-shifted companion to the red-shifted cavity, and we estimate cavity opening angles of $\sim 75°$ and 100° for the inner and outer walls of the red-shifted cavity, and 35° for the blue on this assumption. The low radial velocity of the whistle feature is additionally interpreted in context of a wide-angled wind, and we find it to be potentially in agreement with a general Disk-wind model. This is strengthened in part by the high inferred $\dot{M}_{out}/\dot{M}_{acc}$ ratio in this feature, as the D-Wind model predicts a wind outflow rate comparable to the accretion rate. Alternatively, this feature could indicate entrainment of ambient material by the jet. If this feature is a cavity, this suggests strong similarities between jet launching at the sub-stellar mass scale and jet launching in higher mass CTTS and HAeBes counterparts.

Chapter 6

Conclusions & Future Work

> The light that burns twice as bright burns half as long – and you have burned so very, very brightly, Roy.
>
> — Eldon Tyrell, *Blade Runner* (1982)

The connection between jets/outflows and accretion processes allows us a unique glimpse into the early life-cycle of young protostellar objects, as well as their impact on the overall star formation rate in the regions in which they form. In observations of young stars, their protoplanetary disks, the outflows they host, and the nature of their natal environments, we become increasingly aware of the complex nature of their interactions. To better understand the origins of our own host star it is necessary that we attempt to untangle the mysteries of these mechanisms. This necessitates a combination of observational and diagnostic techniques from X-ray to radio regimes in order to piece together the puzzle that is stellar evolution.

In this respect low- and intermediate-mass stars provide us with the best laboratories for this endeavor due to their long lives and general abundance. We may be particularly interested in Class I or Group I objects, as their fast, atomic outflows are readily visible at optical wavelengths and the source stars are evolved but still relatively young, allowing us to probe into early epochs of their evolution using well-understood physics. The development of IFS and AO-assisted instrumentation has given us access to a powerful set of tools that we can apply to these objects. Providing us with high angular resolution images over modest spectral ranges, IFS allows us to explore morphology and kinematics simultaneously on large and small scales, and utilize atomic physics to reveal important physical diagnostics within critical regions of emission.

In this thesis I have relied nearly exclusively upon the MUSE instrument, demonstrating its power and applicability to jets across a wide range of stellar masses, environmental conditions, and spatial scales. A principal aim of this project was to observe and compare the outflow mechanism in three unique objects: the Herbig Ae star HD 163296, an older intermediate-mass object and transitional-disk candidate; the giant proplyd 244-440, a spectroscopic binary in the Orion Nebula, just southeast of the Orion Bar; and the proto-BD candidate Mayrit 1082188, the lowest luminosity externally irradiated jet so far observed, located near the σ-Orionis cluster. With these considerations I have sought to explore the scalability and durability of the outflow model, and below I shall summarize the overall findings and conclusions of this work.

6.1 Summary of the Results

6.1.1 The Strange Case of HD 163296

In Chapter 3 we explored the outflow from an object that has recently found itself in the spotlight, particularly following the publication of the DSHARP survey and the proposed existence of multiple planets using several independent modeling methods. This object features a complex knotted jet with a known length of at least 6500 au, and shows evidence of continued activity. In addition to an asymmetric jet, HD 163296 also boasts two spectacular bow shocks HH 409 A and HH 409 C with diameters of about $6''$ and $4\farcs5$, respectively.

Our study compared the MUSE observations with X-Shooter observations from 2012 in order to study the proper motions of the knots. We found evidence of a new knot that appeared to contradict a previously proposed periodicity to launch events, as well as a blending of two additional knots which we interpreted as a collision. While this collision could indicate variable launch velocities, it could alternatively be explained by a slowing of one knot post-shock resulting in the second knot colliding with it.

The focus of our attention in this object however was a curious asymmetry in its emission profile. We found in Section 3.3.1 what appeared to be a tentative detection of a so-called wiggle along the ejection axis, which has been observed in various other sources and could be a signature of a close-in, unresolved companion (see e.g. Masciadri and Raga, 2002; Murphy et al., 2021; Erkal et al., 2021a, for other examples of this phenomenon). We used the masses and separations of the proposed planets to determine whether they could be inducing a deviation in the jet axis due to tidal or orbital forces, but found that the observed wiggling pattern could not be reproduced by this means. Through analysis of continuum images and the comparison of emission profiles with that of the effective PSF in the image, we concluded that the observed pattern was a consequence of an intrinsic asymmetry in the emission profile. While we could not ultimately diagnose its origin, this asymmetry appears to be related to shock processes within the jet which shift the emission peaks away from the axis. In Section 6.3 I will discuss future plans for exploring this phenomenon.

6.1.2 The Orion Proplyd 244-440

Leaving the isolation of the Herbig star, we set out on the path of the Hunter into the H II region of the Orion Nebula Complex in Chapter 4. Near and around the photodissociation region known as the Orion Bar is a wealth of photoevaporated objects, of which many are associated with HH objects. We presented the first in-depth exploration of the giant proplyd 244-440 using NFM+AO observations, and identified at least six knots in a highly curved, nearly S-shaped outflow connected to an unresolved inner source. The existence of proplyds poses a critical problem, however, as the observed mass-loss rates in the objects should have evaporated their disks quickly, yet NIR excess is still observed in the majority of the proplyds. While our study did not propose any solutions to this “lifetime problem”, our results were interpreted in this context.

The envelope surrounding the proplyd and the jet driven by an unresolved source are both present in numerous emission lines, and in Table B.1 we compile a list of the positively identified emission lines observed in the proplyd. Some lines feature only the jet, some only the envelope, and some a combination of the two. This provides us with a template for understanding the processes of ionization in the proplyd. For instance the presence of three ionization states of O can clearly delineate photoevaporating flows from the ionization front and further reveal the dense, neutral flows around the source (see Figures B.2 through B.4). That refractory species like Fe II and Ni II trace pure jet emission sheds further light on the physical conditions in the jet, as these typically indicate relatively high-density regions.

Examining archival HST observations, we discovered that two knots present in the MUSE data were faintly visible in two other epochs. This prompted a proper motions study, and we found very low tangential velocities on the order of 20 km s^{-1}. We reasoned that these were not uncharacteristic of tangential velocities in that region, and further noted that they were compatible with observed outflow speeds from very low-mass and sub-stellar objects. Perhaps the most salient consequence of this study was that it appeared to be incompatible with the orientation of the disk estimated from HST images. Even accounting for uncertainties and a jet-disk misalignment of up to 15°, we were unable to reconcile our inclination angle derived from our proper motions with these prior estimations.

We argued that these discrepancies were resolved under the assumption that the observed disk is not associated with the jet-driving source. To defend this we explore the curvature of the jet in light of wiggling jet models and find that the S-shaped morphology can potentially be explained by a jet driving source with $M_* < 0.15\ M_\odot$ in orbit around a $\sim 0.5\ M_\odot$ primary. We compare an on-source spectrum with a catalogue of K- and M-type spectral templates obtained with X-Shooter (Manara et al., 2013; Manara et al., 2017) and find a close match with an M0 or M1 type star, indicating a primary mass $\simeq 0.5\ M_\odot$.

6.1.3 The First Direct Images of HH 1158

Chapter 5 marks the final data chapter of this study, and here we present a fascinating look at the lowest luminosity irradiated jet yet observed. Prior to our MUSE observations no direct images of its outflow had been obtained, and its jet had only been inferred through spectro-astrometry by Riaz and Whelan (2015). We report the discovery of a chain of knots spanning a total length of $\sim$ 6000 au with tenuous emission as far as 7600 au in the blue lobe. Additionally there is evidence of a knot further out in the red lobe about 4300 au from the source. Below the red-shifted jet we find evidence of a large cavity extending southwards $\sim$ 3400 au. We focus our study on the morphology of the outflow, with a special attention paid to the cavity below the red-shifted jet.

Examination of the jet morphology reveals a noticeable asymmetry in the position angles of the red and blue lobes, possibly indicating deflection of the jet by the incident stellar winds from the nearby σ-Ori cluster to the north. Further evidence of this is seen in the Hα/[S II] ratio which shows strong signatures of irradiation along the upper portions of the jet. The peak values of this ratio are seen closest to the source in an almost disk-like distribution. The jet appears to be fairly low-density as inferred from the [S II] ratio with peak values around 800 cm^{-3} in the inner knots, decreasing to around 300 cm^{-3} in the outer regions.

In our exploration of the cavity features, we found a "bar" like extension that presents an emission profile similar to that of a jet. We explore this feature with PV diagrams and spatial profiles, and find that the apparently "knot" has a peak around $-1\overset{''}{.}8$, while the innermost red-shifted knot is observed at $-2\overset{''}{.}15$. Given the angle at which this bar feature extends relative to the known jet axis, the location of the knot in the feature is potentially a projection of knot E onto a dense wall of ambient material. This is supported by analysis of the velocity profiles of the jet knots and cavity, suggesting that this is actually the inner wall of a slow-moving cavity. This cavity is likely red-shifted and "sees" the higher velocity red-shifted jet moving away relative to its own motion. The jet emission is then blue-shifted and scattered back towards us at a lower velocity. Further support of this conclusion was observed in analysis of the jet densities along the bar feature and in the jet. In the jet, the observed densities are lower in the pre-shock region and peak post-shock. Conversely, the bar feature exhibits a peak density at the same position of the lower density pre-shocked emission in the jet. This indicates that the bar emission is reflecting the bright post-shock emission from the jet rather than being an intrinsic emitter.

On the blue-shifted side of the jet we also observe a "whistle" or claw-shaped feature most prominent in [S II] and [N II] emission, though it is observed in Hα and Hβ as well. This feature is shown in the spectro-images in Figures 5.3 and 5.4, and analysis of the jet centroids in Figure 5.6 reveals this to be significantly offset from the jet axis. Radial velocity measurements indicate that this feature is also slow-moving $\sim$ 12 km s^{-1}) relative to the rest of the knots. These results lead us to question whether this feature is part of the jet itself, or a component of a cavity or wide-angled, unresolved wind. If it is a cavity, a rough estimate of its curvature suggests an opening angle of $\sim 35°$. In contrast the red-shifted cavity appears to have an opening angle $\sim 70° - 100°$, potentially indicating asymmetric launch velocities between the two lobes. The nature of this whistle feature is possibly the most exciting open question in this data, and will be discussed in more detail below.

6.2 Understanding the Outflow Mechanism

As this thesis purportedly concerns itself with "edge cases" we finally must ask: what makes these objects unique, and with what thread do we tie them together? What fabric have we woven with these materials? While the implications are surely myriad, this study finds its greatest weight in what it implies about the nature of the outflow mechanism at the edges of its applicability. These three objects represent a substantial range of mass, age, and environment, and as such have much to tell us about the durability and scalability of the launching model.

6.2.1 An Aged Efficiency

As seen in Chapter 1.2.1, a factor that all jets appear to share in common is their connection to accretion. Without a reservoir of excess material and angular momentum, these wondrous spectacles would not exist. With the dissipation of the disk comes the dissipation of the jet, and the star comes into its adulthood. To observe jets and outflows at all stages in the early life-cycle of the protostar is comparable to a cartoon flip-book, which becomes only more rich the more animated pages we place into its bindings. In this respect we must find HD 163296 a truly exemplary object, as all evidence points towards its being near the end of its accretion phase and approaching the transitional disk phase. It is running out of the raw material required to launch a jet, and yet it persists in its outflow.

Its larger mass ($\sim 1.9\ M_{\odot}$) bears mention, as well. Evidence suggests that HAeBes lack the magnetic fields required to collimate matter by the magnetospheric accretion model, and more that the boundary-layer accretion model does not appear sufficient to explain their hunger. HD 163296 is below the “transition” mass discussed by Wichittanakom et al. (2020), but as its disk disperses so too will the magnetic field lines which thread throughout the disk, raising questions about the jet collimation process for these older objects. This provides us with a picture of a rather efficient engine capable of maximizing its use of the ever-dwindling reserves of dust and gas available to it.

The strong evidence of multiple planetary companions makes this all the more fascinating, as we are observing a solar system in the making whose central star is still actively erupting. The high frequency of binarity in YSOs and the detection of jets from many of these solar twins suggests that the disk-associated mechanism contributing to jet launching does not always hinder the formation of companions. In their study of the Th 28 system, Murphy et al. (2021) found that the morphology of the jet could be due to the presence of an unresolved BD companion within 0.3 au, a separation on a similar scale to the jet launching radius predicted by both X-wind and D-wind models (~ 0.5 au). Other studies of jet precession bear out similar results, strengthening our conclusion that companions of all sorts may form in a disk that is actively feeding a jet-launching source. This possibility leads us to consideration of the durability of the launch engine.

6.2.2 A Rugged Durability

Following in the footsteps of the latter discussion on the efficiency of the launch mechanism, we look now at the case of the Orion proplyd. The Orion proplyds are fascinating enough, and studies of their behavior reveal critical information regarding outflows in H II regions. Despite the intense photoevaporation by massive OB-stars, these resilient objects stubbornly trod onwards towards the main sequence phase. The fossil record they leave in their wake is one of supreme interest as it sheds light on the durability of the outflow mechanism.

The proplyd 244-440 is therefore an excellent case study. Not only does it feature a spectacular jet, but this jet appears to be driven by a smaller companion. The picture this provides of the launching engine is one of a durable and rugged capability. It tells us that processes that would cut short the life of the star by stripping away its disk are nevertheless insufficient to stop the accretion/outflow process. If it is the case that this jet is driven by a smaller companion, then we must recognize that this companion is within the photoevaporating disk and is at a marked disadvantage in the evolutionary game.

It is interesting to consider whether the source is accreting from the disk of its host star. As more and more of the host disk is stripped away, the companion will have less raw material to utilize in its growth. The photoevaporating winds as well must bombard this companion and complicate its growth process. If the source accretes from its own disk, then this is perhaps more impactful as the ionized winds of the host would add incredible turbulence to the smaller disk. From this we observe that the mechanism of jet launching is quite rugged, and as with HD 163296 this proplyd testifies to its efficiency as well.

6.2.3 A Scalable Model

Our final discussion leads us to consider the behavior of jets at the very lowest of masses. As noted in Chapter 1.1.2 the formation of brown dwarfs is still a mystery and it is unclear whether they form like stars or like planets, likening them perhaps to a "missing link" in the fossil record. At all stages of the analysis undertaken in Chapter 5 we observe that M1082188 exhibits behaviors quite similar to proper stars. A very exciting implication of this is the possibility that planets may drive jets in the early stages of their formation. They must accrete matter, after all: must they likewise eject some portion of what they consume?

Such a question is ultimately beyond this work, but our study of M1082188 nevertheless presents us with exciting implications regarding the nature of jet launching. The evidence shows that M1082188 is externally irradiated by σ-Ori, and the behavior of its outflow is similar to other irradiated objects. This speaks to the durability mentioned above, particularly as this outflow system is less powerful that systems seen in higher mass stellar objects. Perhaps most enlightening is that we observe a large cavity associated with this outflow system, potentially indicative of the presence of winds. This profound discovery speaks to a universality in the outflow mechanism as these winds are anticipated from MHD models developed to explain jets low- and intermediate-mass driving sources.

The whistle feature in Chapter 5.4.3 was seen to be a comparatively dense, bright, low-velocity structure close to the source. Its orientation and morphology led us to question whether this is part of a cavity connected to an extended disk wind. If this is a cavity swept out by disk winds then we are left with the conclusion that the same mechanism driving jets in other YSOs is at play in BDs. This is, perhaps, the most profound consequence of this study, as it suggests that not only is there a universality to the launch mechanism but that it scales with the source mass. This argument is further strengthened by other observations of this jet. The velocity, density, luminosity, and outflow rates all exhibit low value, and all appear to be "scaled down" with respect to higher mass driving sources. Two critical questions are raised by this discovery. If the cavity is swept out by winds or is formed by entrainment of material in the wake of the jet, to what degree is it responsible for the removal of angular momentum from the system? What is the nature of the outflow component responsible for opening up the cavities? To answer these will require further study and observation, which I will discuss in Section 6.3.

6.3 Future Endeavors

A single thesis is not enough to fully explore the monumental amount of information that can be gleaned from MUSE observations. Each of the objects I have presented argue on their own merit for deeper examination, and here I provide brief plans for future research.

A crucial component of jet studies is that of the energetics of the outflow and the turbulence injected into the surrounding environment by shocks. HD 163296 features two prominent bow shocks with remarkable clarity in the MUSE data sets, and these alone could provide the foundation for a substantial body of work. The ionization front in the Orion proplyd 244-440 displays similar behavior, and although the dynamics of IFs are substantially different from standard bow shocks they nonetheless reveal valuable information about outflow energetics. Finally, the observing block which provided the M1082188 data additionally contained another BD object called Mayrit 1701117 (hereafter M1701117) with a large scale (~ 1 pc) curved jet feature several prominent bow shocks.

The next goal of my research will first be an in-depth examination of the bow shocks seen in HD 163296 and M1701117. This will involve utilizing state-of-the-art shock models and diagnostic code to untangle the physical parameters along the shocks. MUSE is well-suited to this endeavor as evidenced by the spatial maps shown throughout this thesis. The large angular size of the bow shocks and high S/N will allow for pre- and post-shock regions in the shocks to be clearly resolved with high contrast. Differentiating between these regions is important for creating parameter maps of density, temperature, and ionization fraction. Additionally, the massive scale of the M1701117 jet required a mosaic of exposures and were all AO-corrected, making possible a shock study at near-diffraction limited resolution.

With the new Enhanced Resolution Imager and Spectrograph (ERIS) onboard the VLT recently completing its science verification phase, we will soon have a next generation successor of the older SINFONI instrument. The Orion proplyd was observed as part of the science verification phase (though the data has not been reduced) of this instrument, and these will be the first NIR IFU images of this object. Importantly the ERIS observations will constitute a third epoch of monitoring of this source, and is anticipated to yield rich information about the dynamics of the photoevaporating flow. If the jet is present in this new epoch we would expect an important complement to the study provided in Chapter 4. It is noted however that even without the ERIS observations, the MUSE data set still possesses secrets that the next phase of my research will seek to uncover.

A second goal in my future work will be the continued exploration of the physical conditions in externally irradiated jets. With 244-440 this was complicated by a few facts. The jet appeared to be shielded to a large degree from EUV radiation, and so radiation models will likely not be applicable. We also do not observe the jet in temperature-sensitive lines like [N II], and the flux in Hα is impossible to disentangle from the envelope emission so ultimately we cannot produce (n_e, T_e) maps for this jet. The BDs are much better candidates in this regard, and an examination of the effects of radiation will not only inform the diagnostic study but also allow us to better characterize the curvature of the jets.

A third goal will be the expansion of the sample of jet-driving BDs and proto-BDs with a focus on the nature of winds and cavities. To accomplish this goal my most immediate plan is to continue the kinematic study of the cavity in M1082188 and begin the same study for M1701117. The primary challenge in this is that BD jets typically exhibit low velocities, and for IFU instruments like MUSE it can be difficult to resolve these smaller velocity features. The detection of cavities is nonetheless an important step in this regard, as we can compare them directly to CTTS and HAeBes. Even with moderate velocity resolution it is possible to seek for rotation signatures through kinematic study which will indicate whether or not there is a wind origin to these cavities.

6.4 MUSE-ing Upon the Strange

Throughout this study we have seen the power of the MUSE instrument in its application to protostellar jets. Its modest spectral range, high angular resolution, and large FOV allow for the simultaneous examination of spatial and kinematic features. With it we can explore jet morphology as a function of wavelength, revealing key information about ionization and physical parameters within the flow. When operated in NFM we achieve near-diffraction limited spatial resolution and realize unparalleled views of microjets and outflows close-in to the source. The ability to produce ratio maps in the spatial domain permits us to further quantify the morphological structure of key physical parameters, such as density, temperature, and ionization. The high angular resolution further allows us to isolate critical structures in bow shocks and irradiated outflows.

The value of this work is most strongly argued in the way that it informs us about the overall nature of the outflow mechanism. Our focus has been on “edge cases” as it is at the boundaries of our understanding that we often find the most beautiful physics. Comparison of our findings at these boundaries with better understood cases is a necessary test of the robustness of the outflow model. IFS has aided our endeavors here, and we have found evidence of the universality of the launch mechanism with similarities shared across the mass range. With each generation of technology we make small steps towards a better understanding of this fascinating phenomenon, and we may certainly anticipate that instruments like MUSE will only increase in their importance as we develop more sophisticated tools to decipher what these observations present to us.

Appendix A

Supplemental HD 163296 Data

This Appendix features additional information to provide further context to the discussions set forth in Chapter 3. Specifically, it will endeavor to better understand the nature of the intrinsic emission asymmetry discussed in Chapter 3.4.2. Additionally, it was noted that future work is planned which will focus exclusively upon the bow shock and the physical conditions in the jet. The physical conditions were not a concern of this work as a quite recent publication by Xie et al. (2021) focused upon just this question, and the interest of the current work was more upon the morphology of the jet anything else. However those authors were interested solely in the knots seen in the MUSE NFM data and did not involve the bow shocks in HH 409 A and HH 409 C.

A.1 Intrinsic Emission Asymmetry

In Chapter 3.4.2 a representative plot was shown of the spatial profiles across the knot and inter-knot regions to demonstrate the possibility of an intrinsic emission asymmetry in the jet and rule out the “wiggling jet” scenario. This process was done for three FELs and the Hα line. Figures A.1−A.4 show spatial profiles taken transverse to the selected knots labeled in each panel, along with the inter-knot profile and the effective PSF profile. Figures A.5−A.8 show the residuals of the PSF-subtracted knot and inter-knot profiles, which are normalized to highlight the relative contribution of the profiles. In all residuals with the exception of Hα, a marked asymmetry is observed in the presence of the peaks shifted preferentially in the negative direction. When combined with the centroid plots in Chapter 3 (Figures 3.7 and 3.8) it is seen that these appear to be due to an emission asymmetry rather than true jet axis wandering.

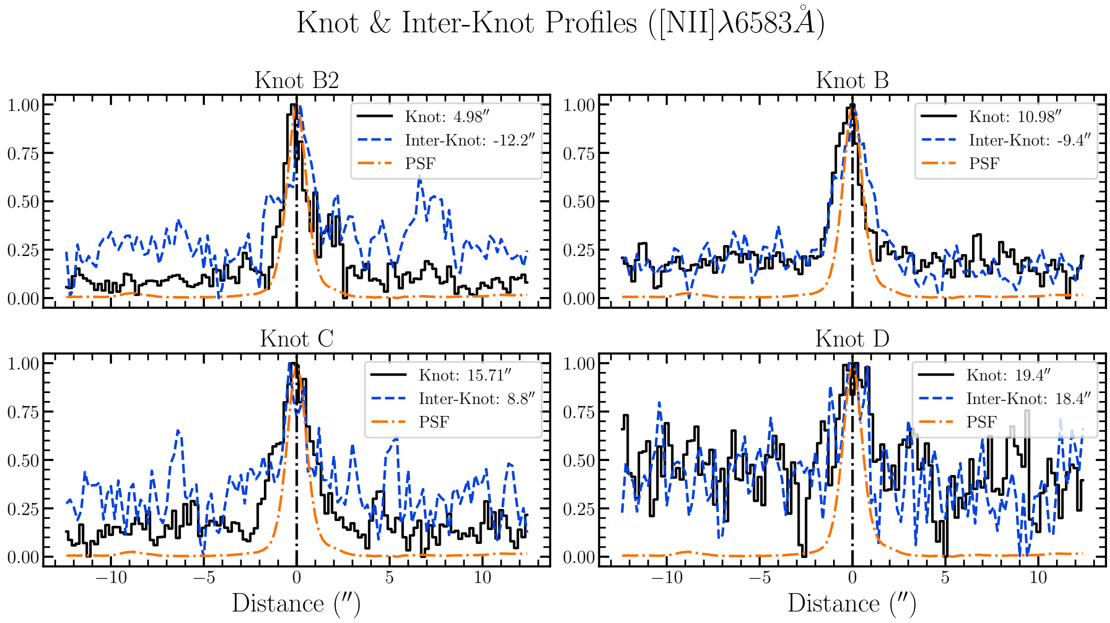

FIGURE A.1: Knot and inter-knot spatial profiles taken transverse to the knots listed at the top of the panels for the [N II]λ6853 Å emission line. The profiles are all normalized to unity. The effective PSF (dashed orange line) is constructed by the method discussed in Chapter 3.4.2.

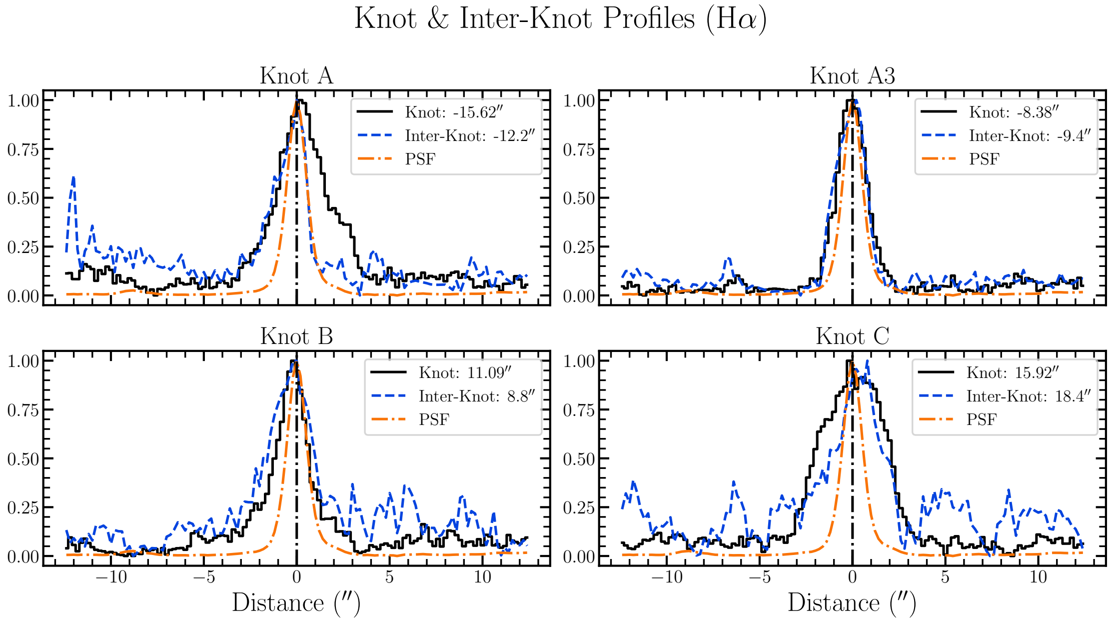

FIGURE A.2: Same as for Figure A.1, but for the Hα emission line.

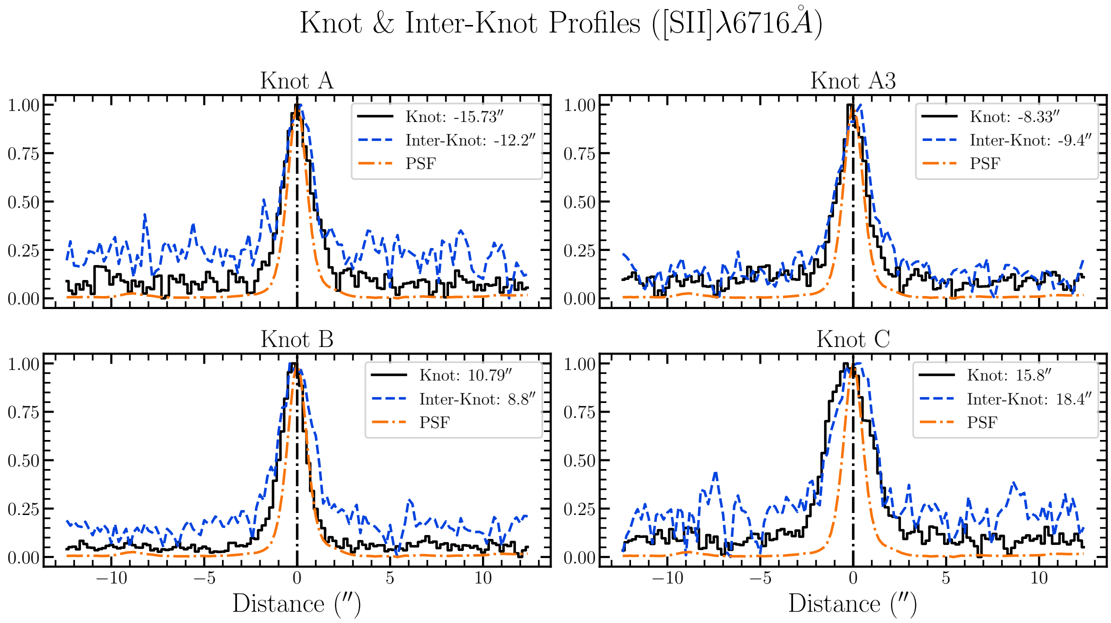

FIGURE A.3: Same as for Figure A.1, but for the [S II]λ6716 Å emission line.

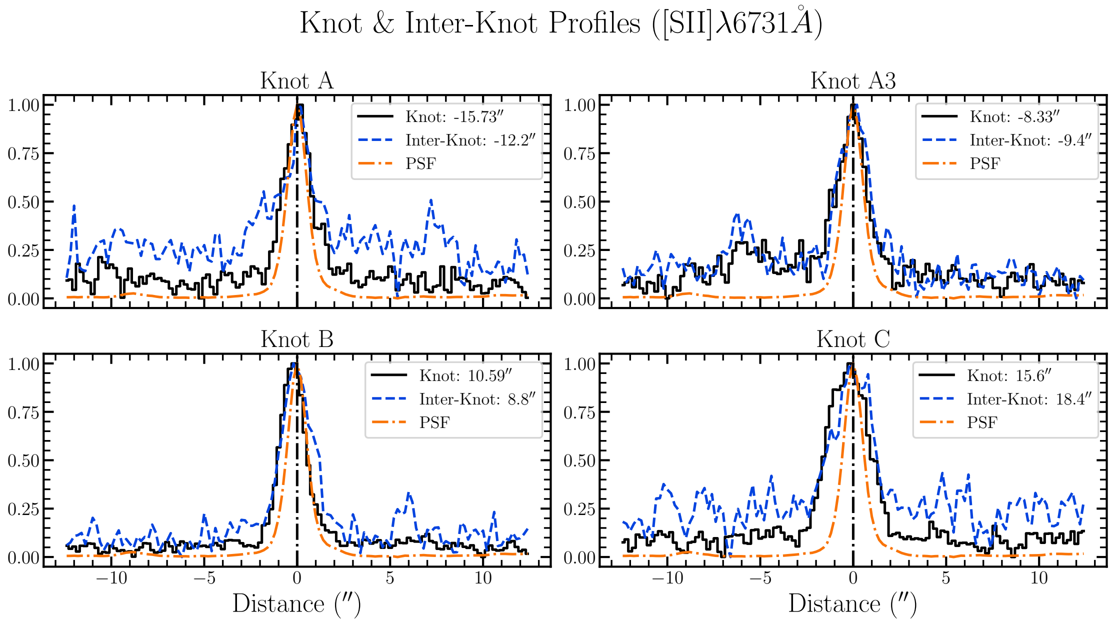

FIGURE A.4: Same as for Figure A.1, but for the [S II]λ6731 Å emission line.

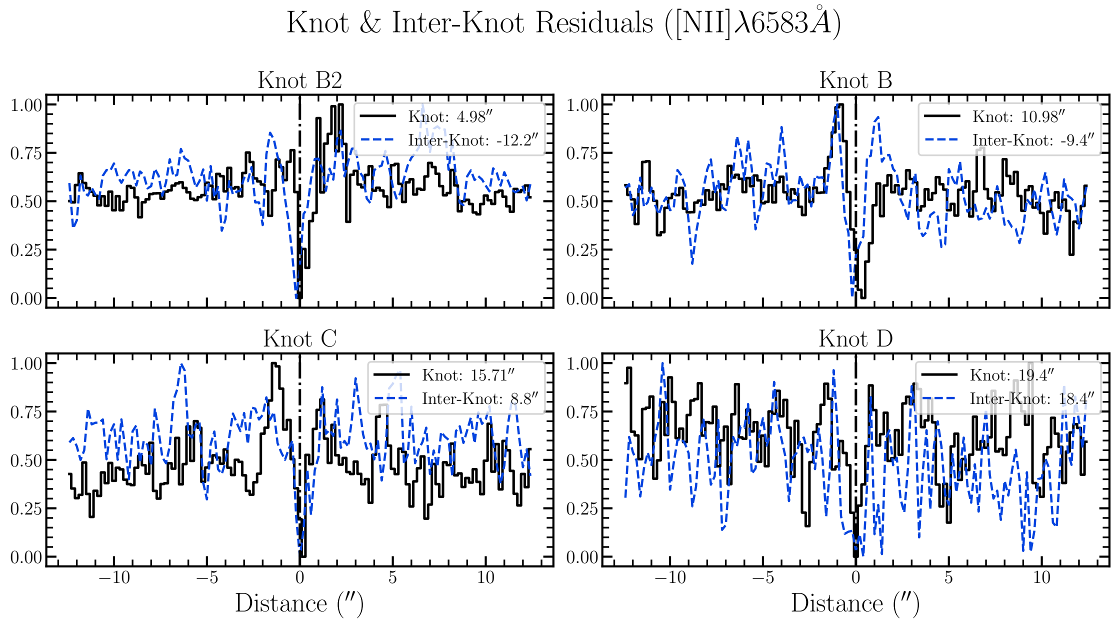

FIGURE A.5: PSF-subtracted residuals of the knot and inter-knot profiles for the [N II]λ6853 Å emission line. The residuals are normalized to unity.

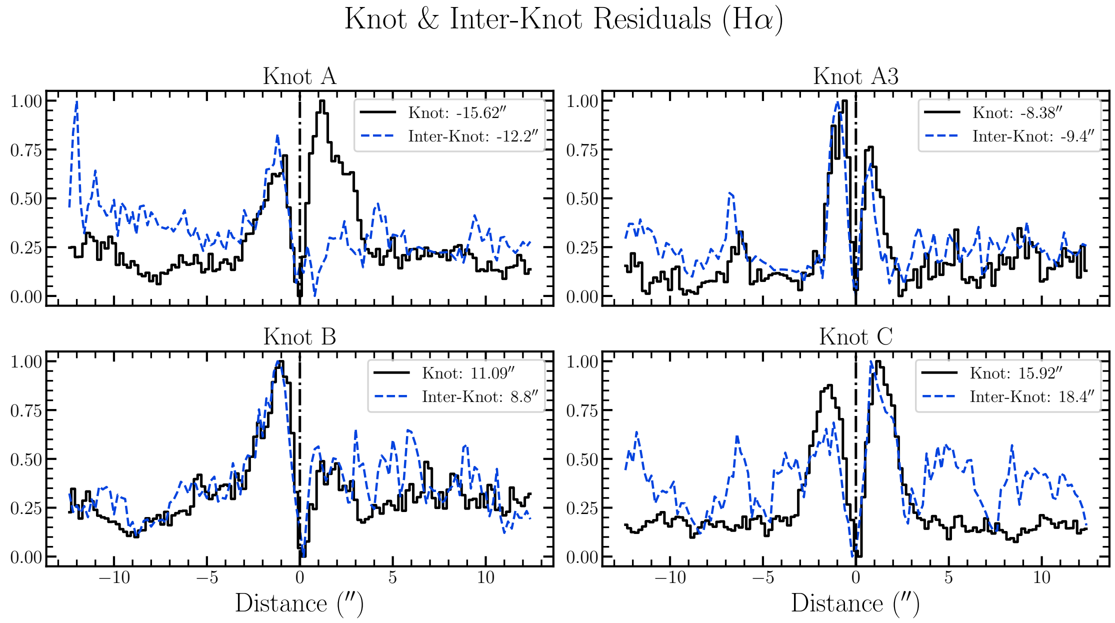

FIGURE A.6: Same as Figure A.5 but for the Hα emission line.

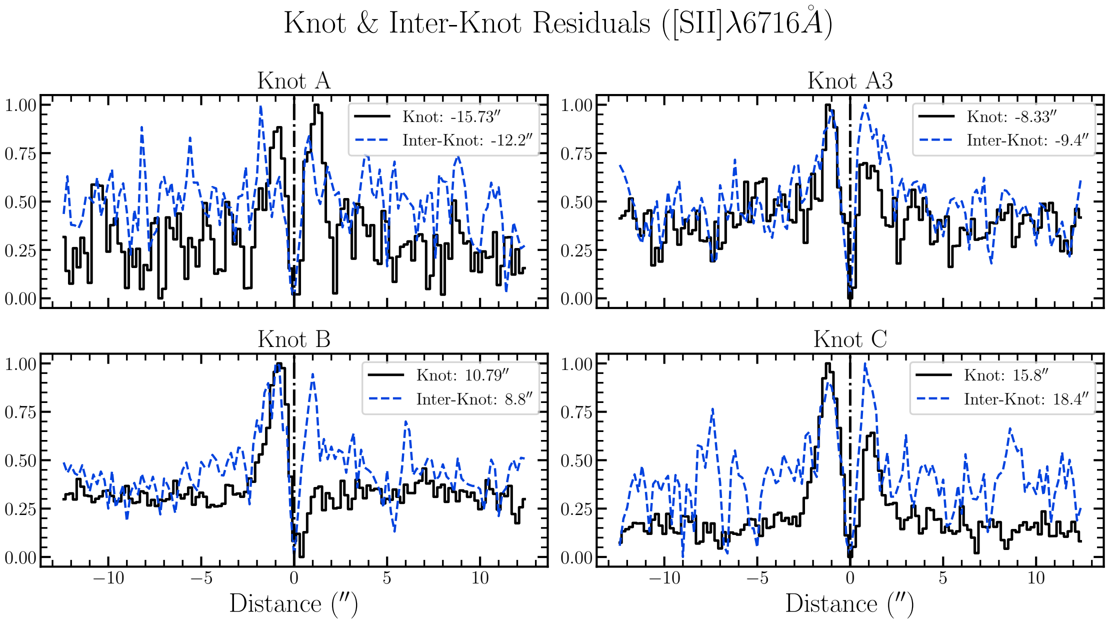

Figure A.7: Same as for Figure A.5, but for the [S II]λ6716 Å emission line.

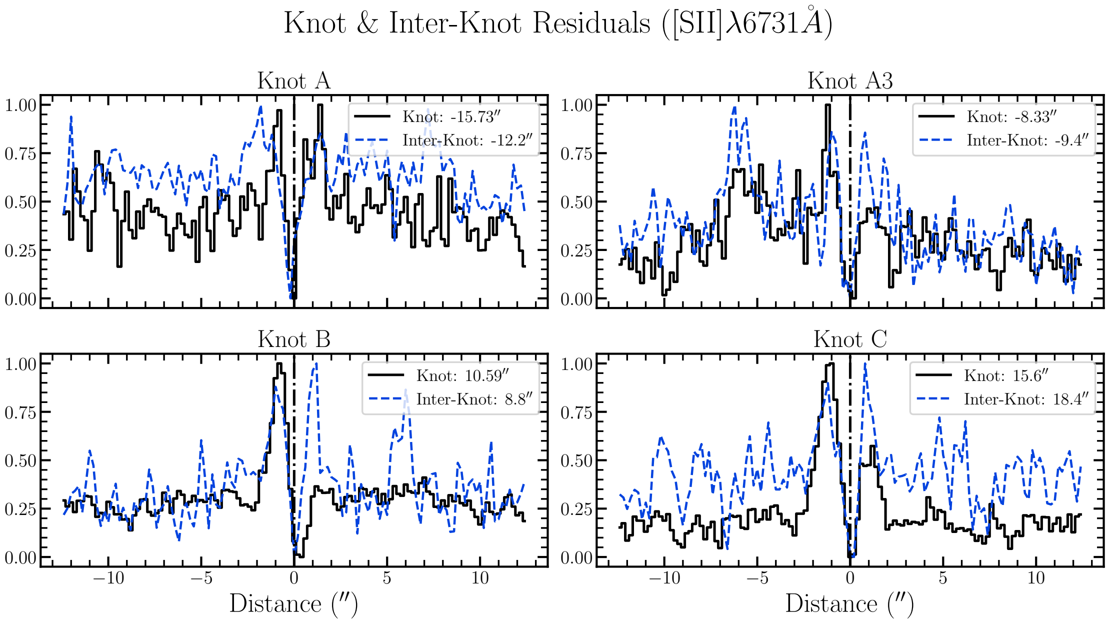

Figure A.8: Same as for Figure A.5, but for the [S II]λ6731 Å emission line.

Appendix B

Supplemental Proplyd Data

In this Appendix, the complexity of the Orion proplyd 244-440 discussed in Chapter 4 is displayed. As seen in Table B.1 the proplyd emission is identified in multiple lines over the MUSE spectral range, revealing both the envelope and jet structure throughout a range of ionization potentials. This section thus functions as a catalogue for spatial and kinematic emission features in the proplyd, as well as other supplemental data not immediately relevant to the central thesis of this work.

B.1 Spectral Type

Many of the results discussed in Chapter 4 require us to have at least a broad estimate of the source mass. If we are to utilize a jet wiggling model, for example, a key assumption is that the source contains a binary as a critical parameters is the ratio of the companion mass to the primary. Similarly, any jet proper motion study or computation of mass-outflow rates must be compared against some mass if we are to determine how reasonable our values are. To accomplish this, we extracted an on-source spectrum, corrected for extinction, and compared it with several spectra of known stellar types to find which is most similar as shown in Figure B.1.

The spectral templates shown were all observed on the X-Shooter instrument and their spectral types reported in Manara et al. (2013) and Manara et al. (2017). Based on this, we argue that proplyd 244-440 is most likely an M0 or M1 spectral type star, placing it on the very low-mass end. We believe this to be reasonable as well, as the proper motions and radial velocities are both quite low, indicative of a low-power outflow. Additionally, the estimated mass-outflow rate is comparable with those seen in brown dwarfs, strengthening this argument (Whelan et al., 2014; Riaz and Whelan, 2015; Riaz et al., 2017).

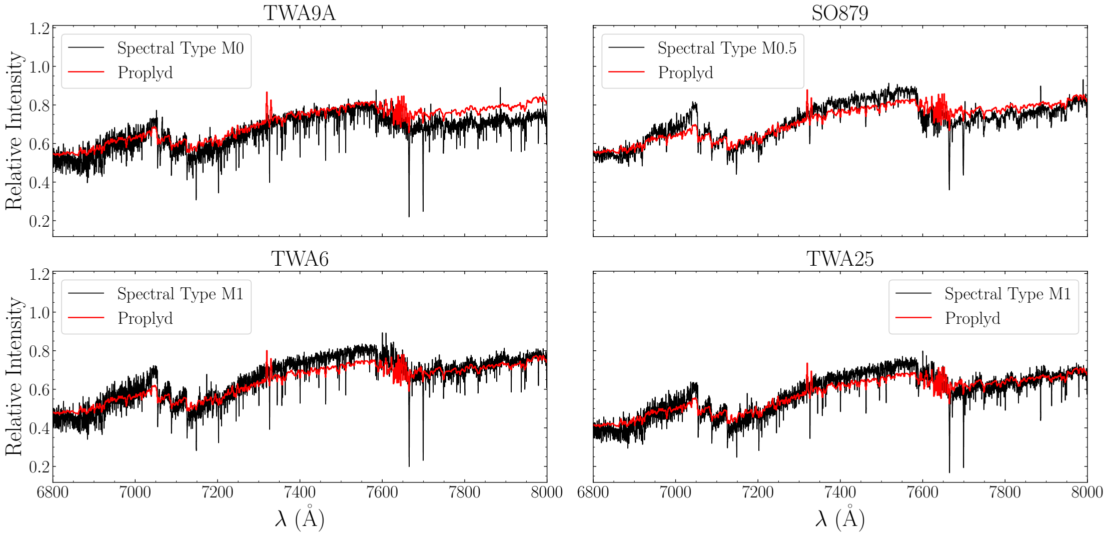

FIGURE B.1: On-source spectrum of 244-440 (red) over-plotted with spectra from a sample of M-type YSOs. The spectral type of each YSO is given in the legend of each panel.

B.2 Line Identification

Presented in this table is a catalogue of identified emission lines associated with the proplyd as observed in the MUSE NFM cubes. While other lines are observed, only lines that could be positively identified are reported.

λ_{air} (Å)	Ion	Type	Jet	λ_{obs} (Å)
4861.30	H I	$4-2$	E	4861.5
4921.93	He I	${}^{1}\mathrm{D}_{2} - {}^{1}\mathrm{P}_{0}$	E	4922.8
4958.91	[O III]	${}^{1}\mathrm{D}_{2} - {}^{3}\mathrm{P}_{1}$	E	4959.1
4881.07	[Fe III]	${}^{3}\mathrm{H}_{4} - {}^{5}\mathrm{D}_{4}$	B	4880.4
5006.80	[O III]	${}^{1}\mathrm{D}_{2} - {}^{3}\mathrm{P}_{2}$	E	5007.8
5015.70	He I	${}^{1}\mathrm{D}_{2} - {}^{3}\mathrm{P}_{2}$	E	5016.6
5056.89	[Ni IV]	${}^{4}\mathrm{F}_{7/2} - {}^{4}\mathrm{D}_{5/2}$	B	5055.3
5158.80	[Fe II]	$a^{4}\mathrm{H}_{13/2} - a^{4}\mathrm{F}_{9/2}$	B, R	5159.1
5197.90	[N I]	${}^{2}\mathrm{D}_{3/2} - {}^{4}\mathrm{S}_{3/2}$	E	5199.1
5261.60	[Fe II]	$b^{4}\mathrm{H}_{13/2} - a^{4}\mathrm{F}_{7/2}$	B	5261.3
5271.60	[Ni VI]?	$b^{4}\mathrm{H}_{9/2} - a^{4}\mathrm{F}_{9/2}$	B	5171.4
5754.60	[N II]	${}^{1}\mathrm{S}_{2} - {}^{1}\mathrm{D}_{0}$	E	5755.3
6300.30	[O I]	${}^{1}\mathrm{D}_{1} - {}^{3}\mathrm{P}_{2}$	B, R, E	6301.1
6312.00	[S III]	${}^{1}\mathrm{S}_{0} - {}^{1}\mathrm{D}_{2}$	E	6314.1
6363.70	[O I]	${}^{1}\mathrm{D}_{2} - {}^{3}\mathrm{P}_{1}$	B, R, E	6363.2
6548.00	[N II]	${}^{1}\mathrm{D}_{2} - {}^{3}\mathrm{P}_{1}$	R, E	6551.6
6562.80	H I	$3-2$	R, E	6562.8
6583.50	[N II]	${}^{1}\mathrm{D}_{2} - {}^{3}\mathrm{P}_{2}$	R, E	6584.1
6678.71	He I	${}^{1}\mathrm{D}_{2} - {}^{1}\mathrm{P}_{1}$	E	6678.1
6716.40	[S II]	${}^{2}\mathrm{D}_{5/2} - {}^{4}\mathrm{S}_{3/2}$	B, R, E	6715.3
6731.80	[S II]	${}^{2}\mathrm{D}_{3/2} - {}^{4}\mathrm{S}_{3/2}$	B, R, E	6729.1
7065.70	He I	${}^{3}\mathrm{D}_{1} - {}^{3}\mathrm{P}_{0}$	E	7066.6
7135.80	[Ar III]	${}^{1}\mathrm{D}_{2} - {}^{3}\mathrm{P}_{2}$	E	7136.6
7155.20	[Fe II]	$a^{2}\mathrm{G}_{9/2} - a^{4}\mathrm{F}_{9/2}$	B, R	7155.3
7172.00	[Fe II]	$a^{2}\mathrm{G}_{7/2} - a^{4}\mathrm{F}_{7/2}$	B, R	7175.3
7281.35	He I	${}^{1}\mathrm{S}_{0} - {}^{1}\mathrm{Po}_{1}$	E	7280.5
7319.90	[O II]	${}^{2}\mathrm{P}_{5/2} - {}^{2}\mathrm{D}_{3/2}$	R, E	7322.8
7330.70	[O II]	${}^{2}\mathrm{P}_{5/2} - {}^{2}\mathrm{D}_{3/2}$	R, E	7332.8
7377.80	[Ni II]	${}^{2}\mathrm{F}_{7/2} - {}^{2}\mathrm{D}_{5/2}$	B, R	7380.3
7388.20	[Fe II]	$a^{2}\mathrm{G}_{7/2} - a^{4}\mathrm{F}_{5/2}$	B, R	7387.8
7411.61	[Ni II]	${}^{2}\mathrm{F}_{5/2} - {}^{2}\mathrm{D}_{3/2}$	B	7410.2
7452.50	[Fe II]	$a^{2}\mathrm{G}_{7/2} - a^{4}\mathrm{F}_{5/2}$	B, R	7452.8
7751.10	[Ar III]	${}^{1}\mathrm{D}_{2} - {}^{3}\mathrm{P}_{1}$	E	7751.6
8125.30	[Cr II]	$a^{6}\mathrm{D}_{7/2} - a^{6}\mathrm{S}_{5/2}$	B	8125.0
8243.83	Ca I?	${}^{1}\mathrm{S}_{0} - {}^{1}\mathrm{P}^{\mathrm{o}}{}_{1}$	E	8242.9

Continued on next page

Table B.1 – continued from previous page

λ_{air} (Å)	Ion	Type	Jet	λ_{obs} (Å)
8393.44	He I?	${}^1\mathrm{D}_2 - {}^1\mathrm{P^o}_1$	E	8392.99
8446.13^a	[Fe II]?	$a^2\mathrm{D}^2{}_{5/2} - a^4\mathrm{D}_{3/2}$	B	8445.0
8446.36^a	O I	${}^3\mathrm{P}_2 - {}^3\mathrm{So}_1$	E	8447.1
8578.70	[Cl II]	${}^1\mathrm{D}_2 - {}^3\mathrm{P}_2$	E	8579.0
8617.00	[Fe II]	$a^4\mathrm{P}_{5/2} - a^4\mathrm{F}_{9/2}$	B, R	8616.0
8750.47	H I	$12 - 3$	E	8751.0
8861.96	O II	${}^4\mathrm{G^o}_{9/2} - {}^4\mathrm{F}_{7/2}$	E	8872.9
8891.90	[Fe II]	$a^4\mathrm{P}_{3/2} - a^4\mathrm{F}_{7/2}$	B, R	8892.8
9014.93	H I	$10 - 3$	E	9015.2
9033.49	[Fe II]	$a^4\mathrm{P}_{1/2} - a^4\mathrm{F}_{5/2}$	B	9032.9
9051.20	[Fe II]	$a^4\mathrm{P}_{5/2} - a^4\mathrm{F}_{7/2}$	B, R	9051.2
9068.60	[S III]	${}^1\mathrm{D}_2 - {}^3\mathrm{P}_1$	B, E	9069.3
9226.63^a	[Fe II]	$a^4\mathrm{P}_{3/2} - a^4\mathrm{F}_{5/2}$	B	9225.3
9227.80^a	He I	${}^3\mathrm{P} - {}^3\mathrm{D}$	E	9228.9

Table B.1: Observed emission lines in the proplyd 244-440. **B** and **R** refer to blue- and red-shifted emission respectively, while **E** denotes envelope emission. Uncertain identifications are labeled with a question mark. The approximate central emission is shown in the λ_{obs} column, as it was not possible to fit a Gaussian to all emission lines due to contributions from the proplyd envelope. $^{(a)}$ Blended emission.

B.3 Tri-Color Composites

This section contains a selection of tri-color composite images, which were produced using both background subtracted and non-background subtracted cubes as labeled. This allows for the discrimination between emitting features in the proplyd. For example, Figure B.4 shows three ionization states of forbidden oxygen emission, demarcating the dense, neutral emission ([O I] and jet features) from the ionization front ([O II]) and photoevaporating flows ([O III]). Background-subtracted and unsubtracted images are shown side-by-side to demonstrate the differences between the corrected and uncorrected cubes.

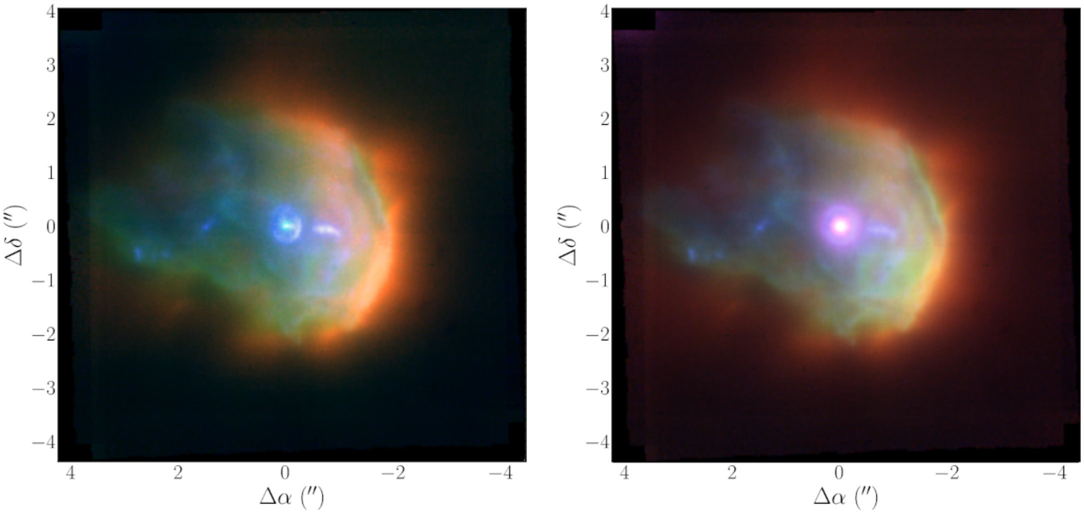

Figure B.2: Three-color flux-integrated image composites of the proplyd 244-440 for the background-subtracted (left) and unsubtracted (right) data. Red is [Ar III]λ7136, green is Hα, and blue is [O I]λ6300.

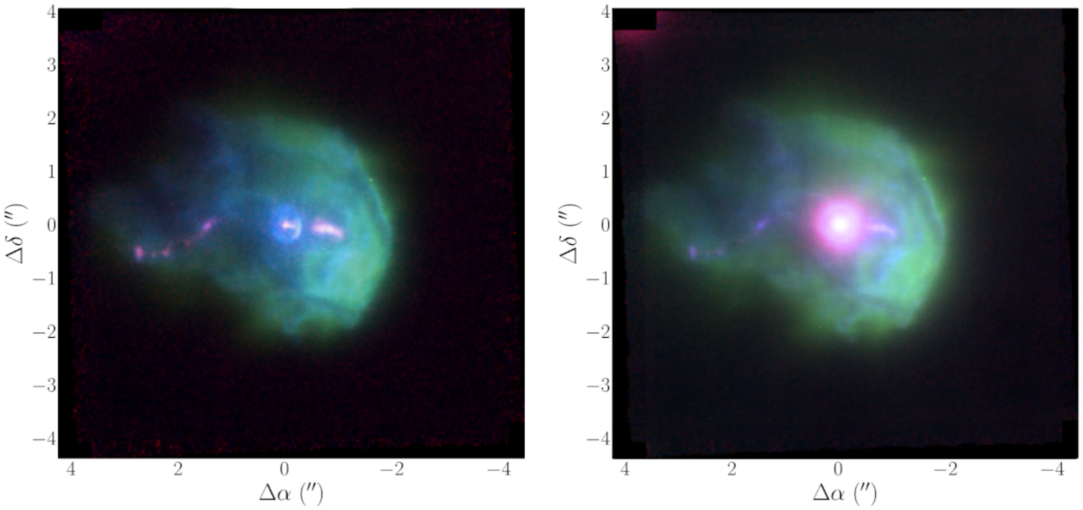

Figure B.3: Same as Figure B.2. Red is [Fe II]λ7155, green is [N II]λ6548, and blue is [O I]λ6300.

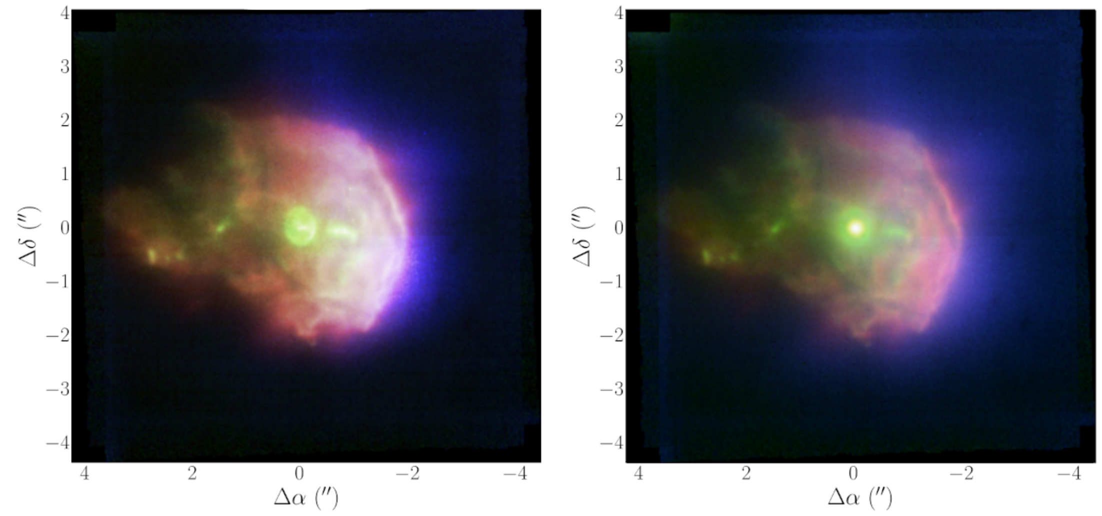

Figure B.4: Same as Figure B.2. Red is [O ii]λ7320, green is [O i]λ6300, and blue is [O iii]λ5007.

B.4 Brightness Distribution

In Chapter 4 a short discussion was given regarding the brightness distribution of the [S II] ratio and its implications on the effectiveness of this line in density determination. In Figure B.5, two cumulative distribution functions are shown for the partitioned [S II] images, showing the background partitions and the emission feature partitions.

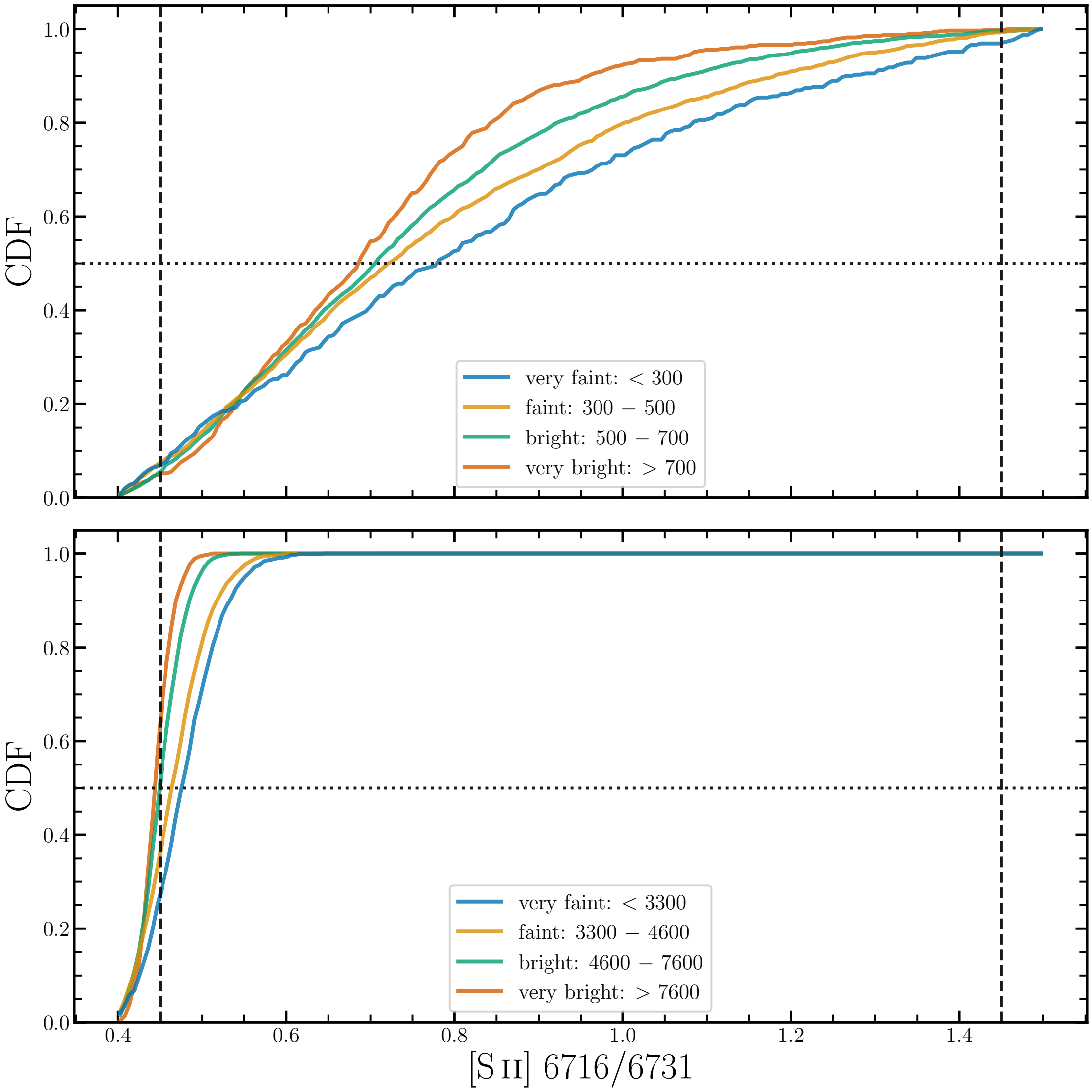

FIGURE B.5: Cumulative distribution of the partitioned [S II] brightness as a function of electronic density n_e for selected background regions (top) and envelope+jet emissions (bottom).

B.5 Position-Velocity Maps

A nebular removal technique was mentioned in Chapter 2, but ultimately eschewed in favor of a simpler analysis. In this section I present various position-velocity diagrams (PVDs) to demonstrate the effects of the nebular removal technique on the PV-arrays. Due to the asymmetry of the proplyd jet, two “cuts” were taken at different position angles (PA) in order to fully capture the extent of the emission. For a PA of 263°, the western/blue-shifted emission is contained, as well as knot E3 in the eastern/red-shifted lobe. The eastern/red-shifted emission is captured by a cut with a PA of 101°. In each case the simulated slit width is $0\farcs5$ (20 pixels). Contours are computed by applying a sigma-clipping routine to the data to establish the RMS noise in the array and increasing in logarithmic increments from this baseline. For the [Fe II] and [Ni II] lines, a spatial profile across the knot emissions is also shown, with the knots fitted and labeled accordingly. In all figures, the direction of the simulated slit is shown.

A few interesting revelations come from this. First, as the nebular subtraction removes some of the envelope emission, peaks form in the envelope due to shocks as the photoevaporated flow interacts with impinging extreme-UV radiation. Second, strong evidence that shock processes dominate within the jet itself are seen in the [Fe II] and [Ni II] lines, particularly in knots E1 and E1. Knot E3 is observed in both PAs and displays a morphology similar to bow shocks in other jets. A peak velocity is seen around 100 km s^{-1} at $\sim 2\farcs2$ and sharply decreasing over a $0\farcs3$ interval. The blue-shifted jet shows peaks which are separated by widths comparable to the image quality. The W1-W3 knot complex is strongly blended, which may be indicative of collisions or an asymmetric launch velocity (as was suggested in Chapter 3 for the HD 163296 knots), or perhaps may be the consequence of the jet interacting with the envelope or ionization front – a possibility raised in Chapter 4.4.1.

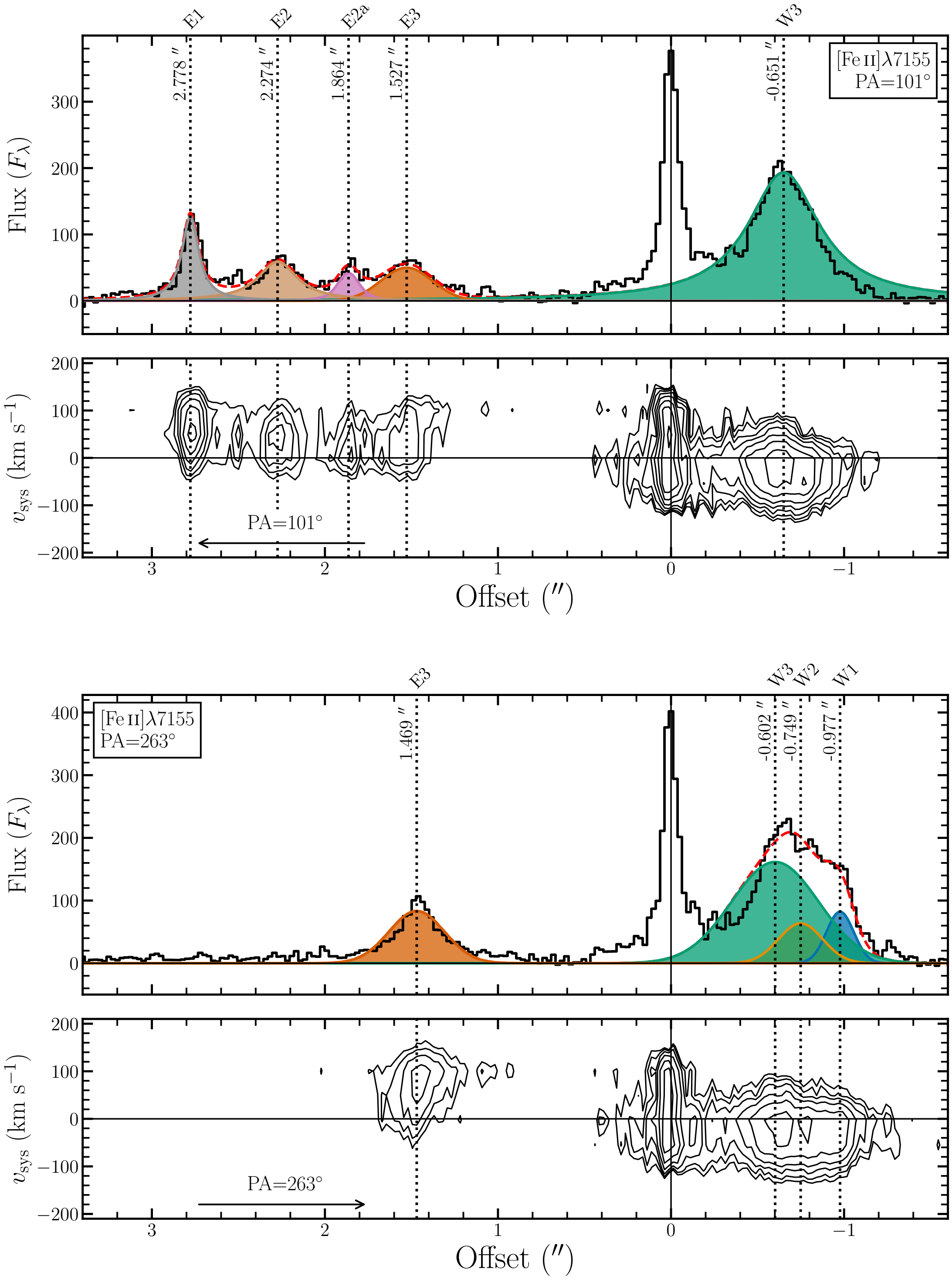

FIGURE B.6: PV diagram and spatial profile of the [Fe II]λ7155 line

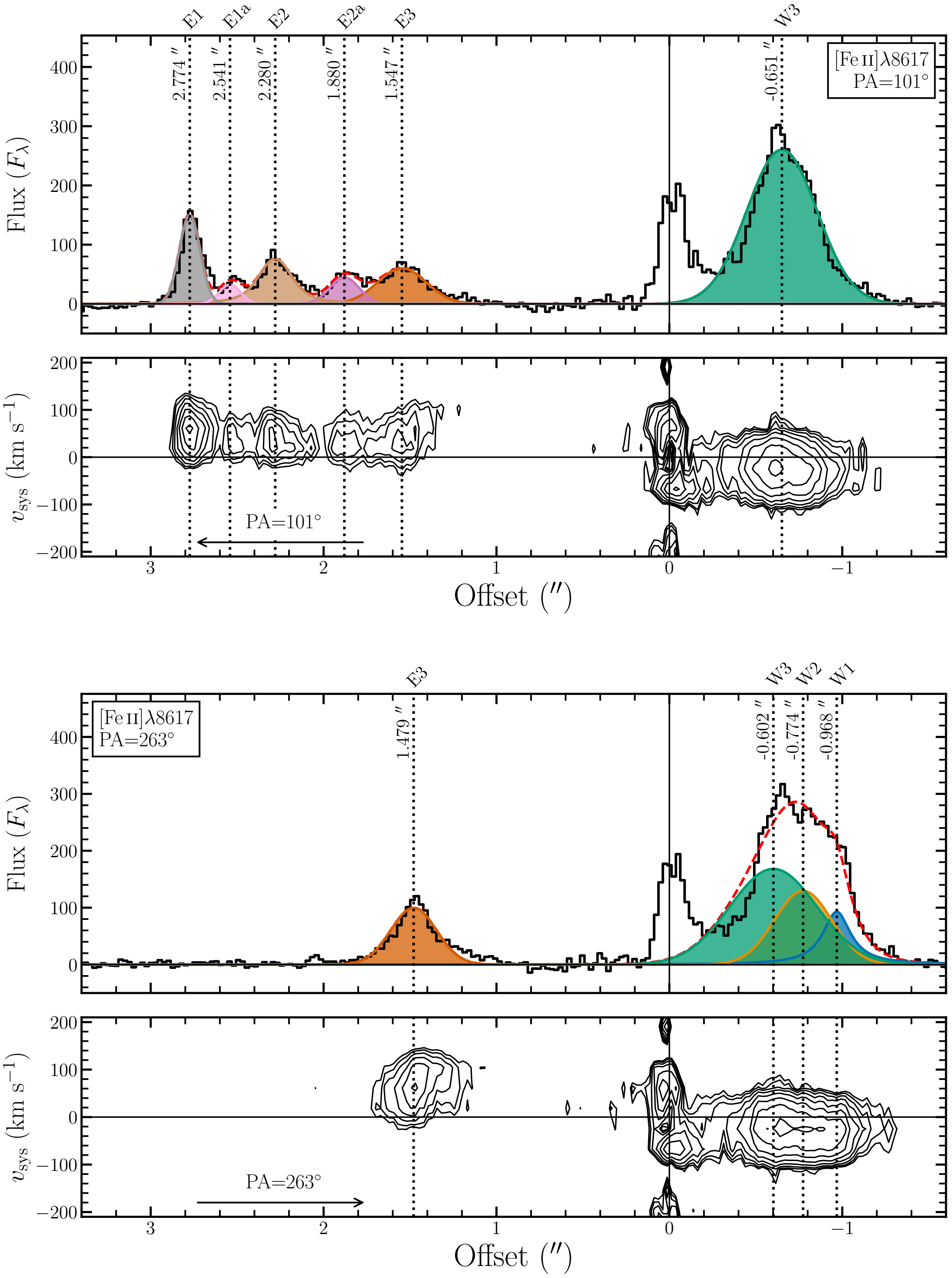

FIGURE B.7: PV diagram and spatial profile of the [Fe II]λ8617 line

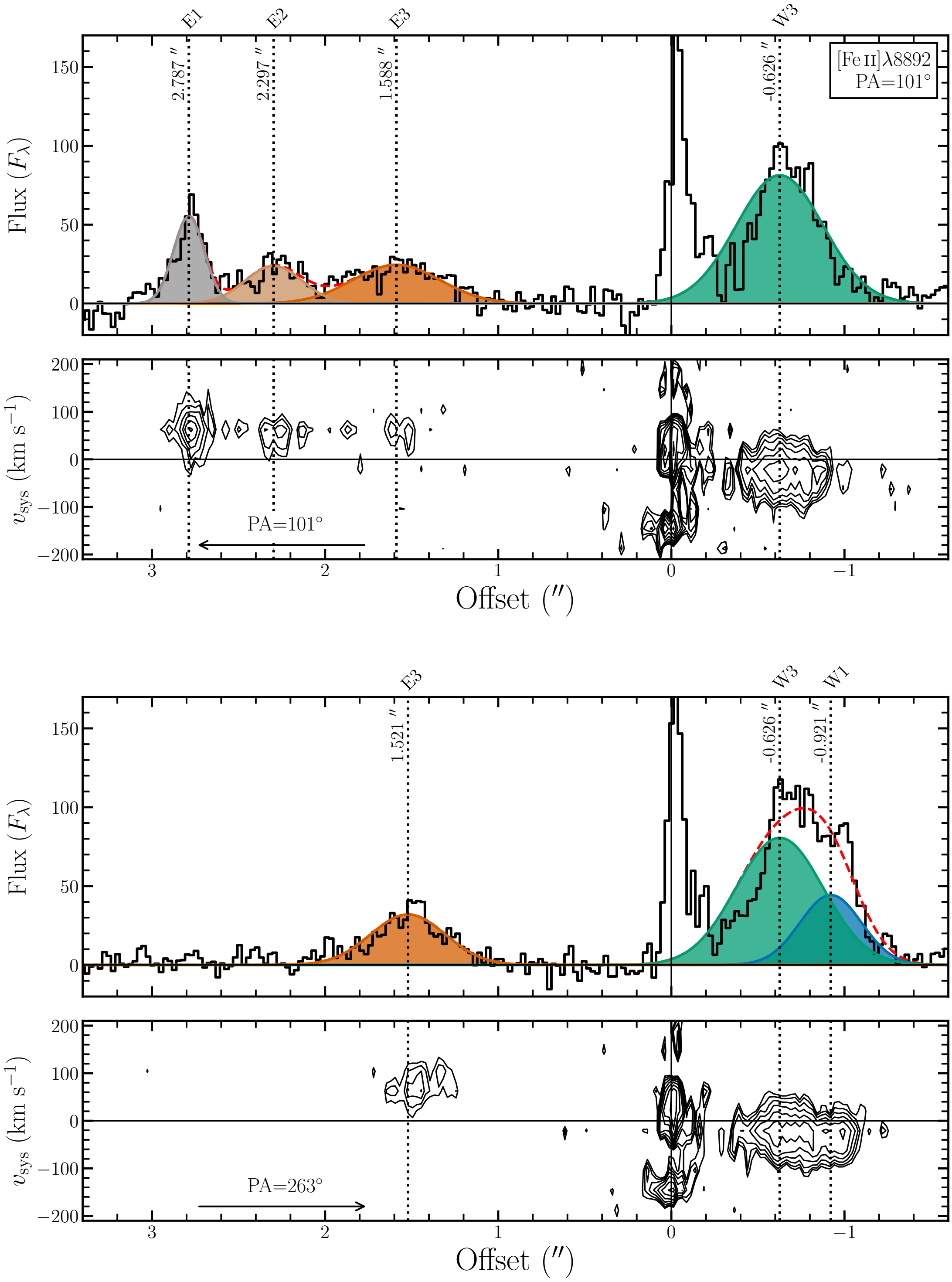

FIGURE B.8: PV diagram and spatial profile of the [Fe II]λ8892 line.

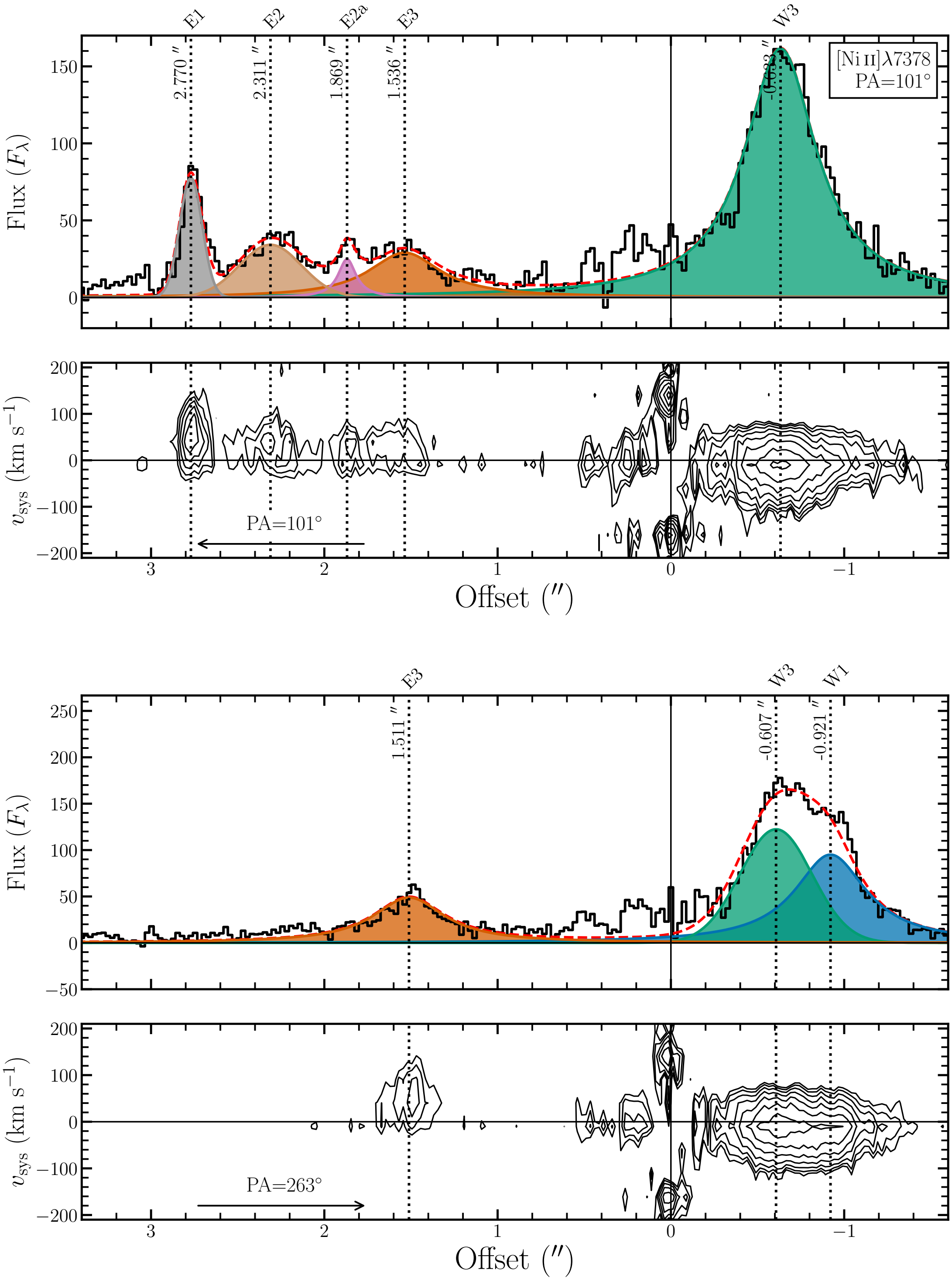

FIGURE B.9: PV diagram and spatial profile of the [Ni II]λ7378 line.

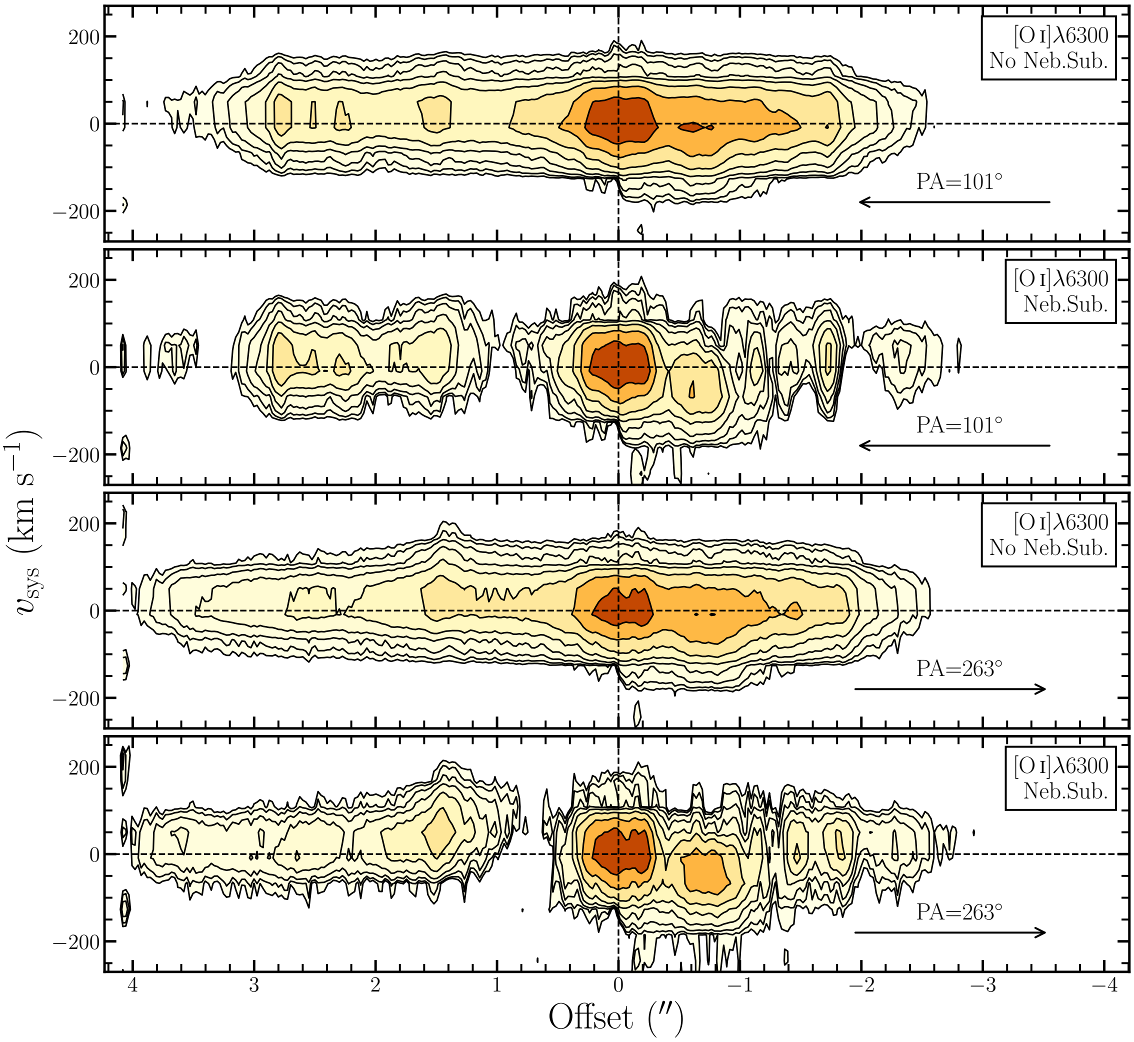

Figure B.10: PV diagrams of the [O I]λ6300 line. The first and third rows are shown without the nebular subtraction method, while the second and fourth rows feature the nebular subtraction. It is important to note that the blue-shifted jet emission does not extend beyond ~ 1.″5. Emission beyond that distance is purely envelope emission.

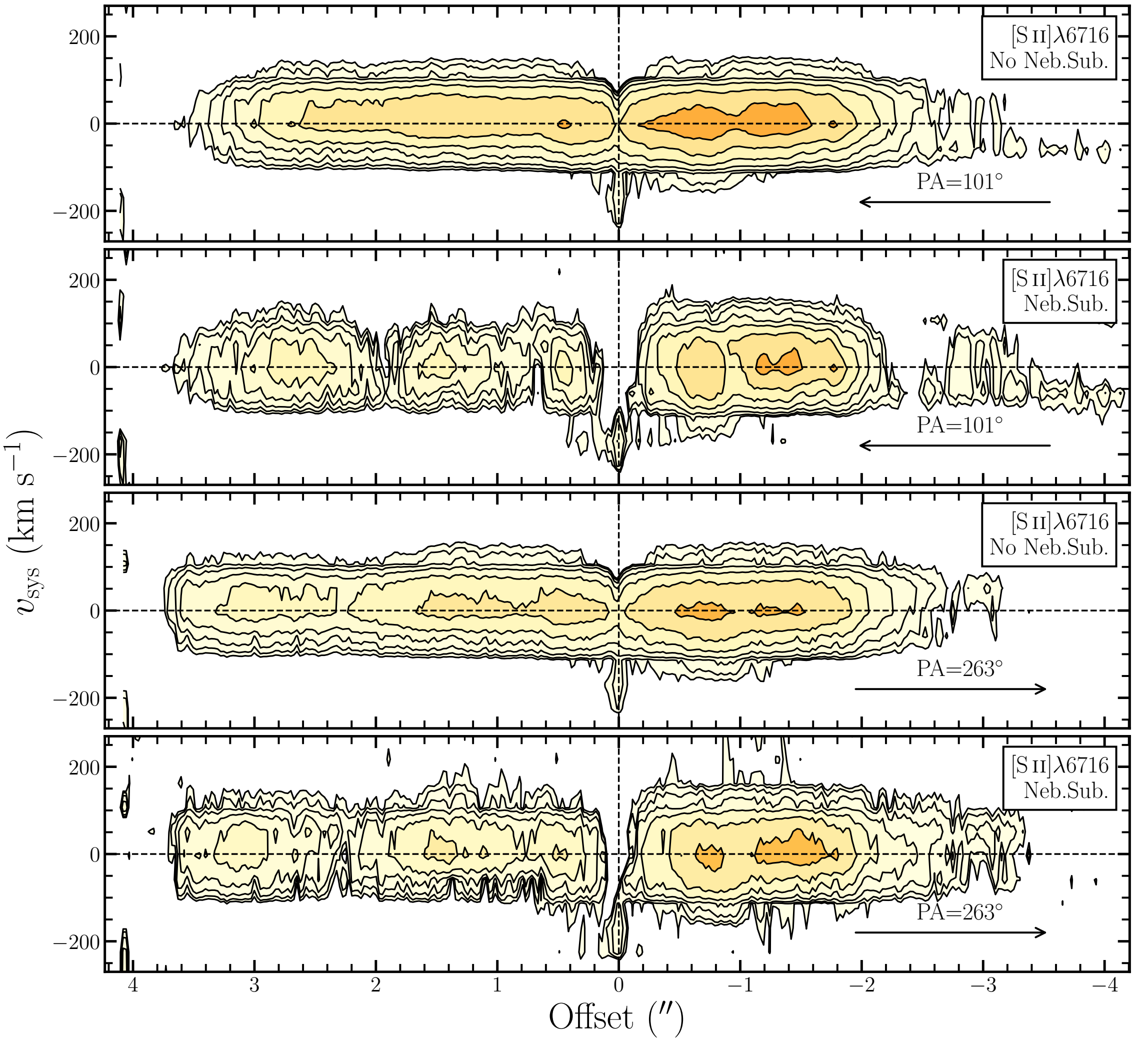

Figure B.11: Same as Figure B.10, but for the [S II]λ6716 line. As with the above figure, emission beyond 1″.5 in the blue-shifted line is envelope emission. In this instance, apparent shocked structures in the envelope are visible as peaks in the contours beyond 1″.5.

Appendix C

Supplemental ESO-HA 1674 Data

In this Appendix is presented supplementary data to the study of the proto-BD ESO-HA 1674, which was discussed in Chapter 5. A catalogue of spatial and kinematic emission features is shown in addition to spectral analysis of point sources in the MUSE FOV.

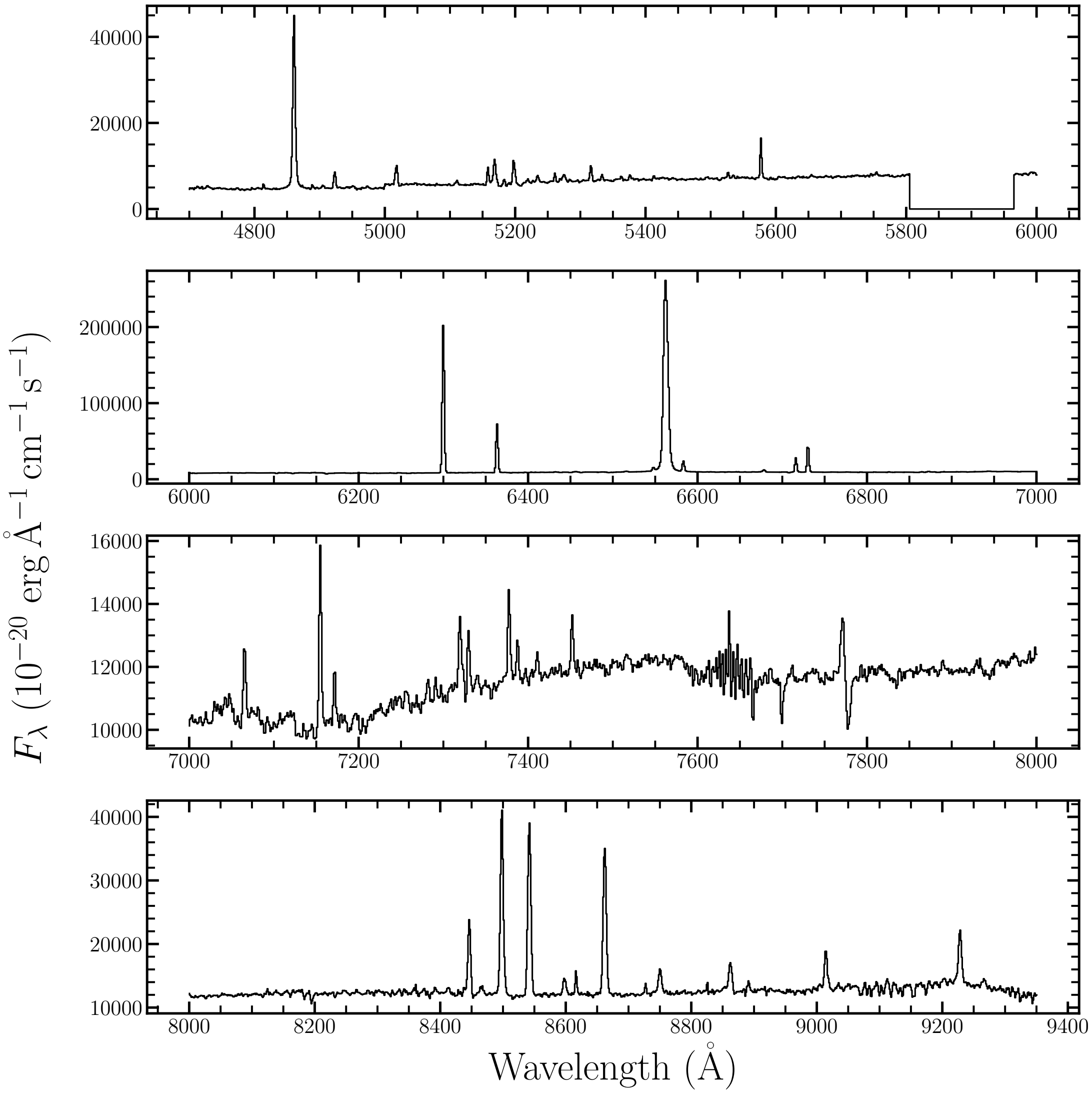

FIGURE C.1: On-source spectrum of M1082188 shown over the entire MUSE spectral range.

C.1 Spectral Analysis

We present plots of spectra from M1082188, and explore the unidentified point source discussed in Chapter 5.3.4

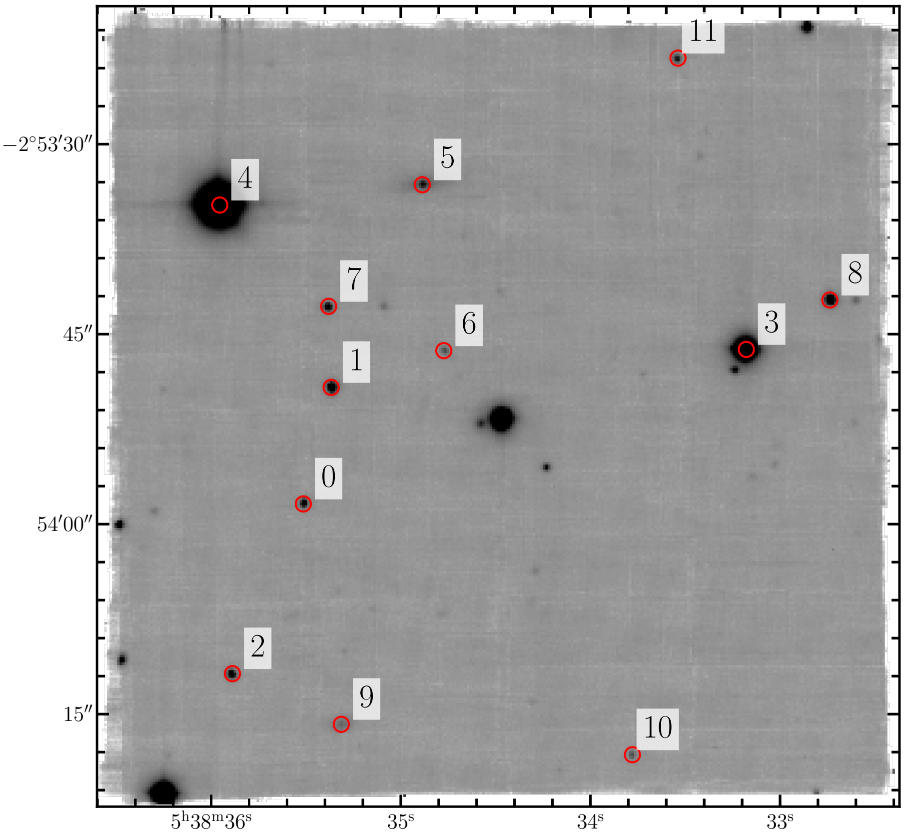

FIGURE C.2: Point sources in the M1082188 data cubes. Spectra were extracted at each location and compared with the point source of interest to determine if the source in question is a background source or companion to M1082188.

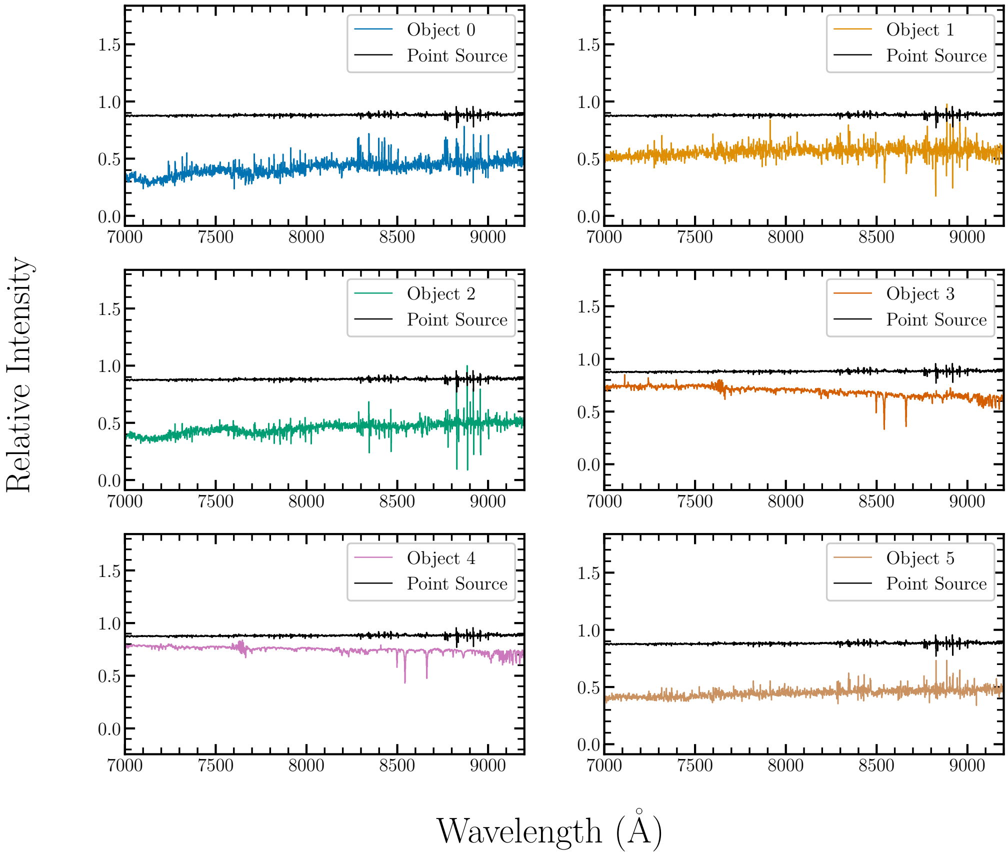

FIGURE C.3: Normalized spectra of the first six point sources labeled in Figure C.2 compared with the point source in question.

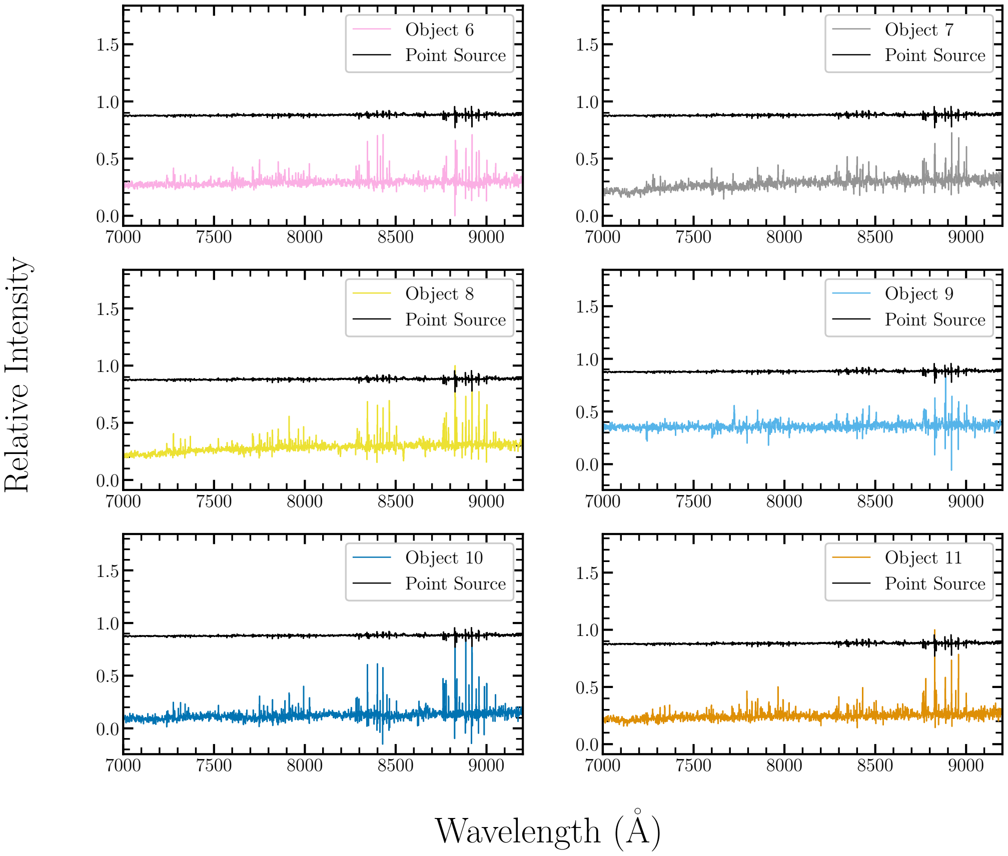

FIGURE C.4: Same as Figure C.3 but for the remaining sources.

C.2 Kinematics

In this Section we present kinematic maps of the emission lines discussed in Chapter 5. Figures C.5−C.8 show radial velocity and FWHM maps with superimposed contours in order to correlate emission features. Each contour map was computed in the same way in the manner discussed in Chapter 5.3.1. Position-velocity maps are given in Figures C.9 for varying PAs in order to capture the jet, cavity, and whistle features.

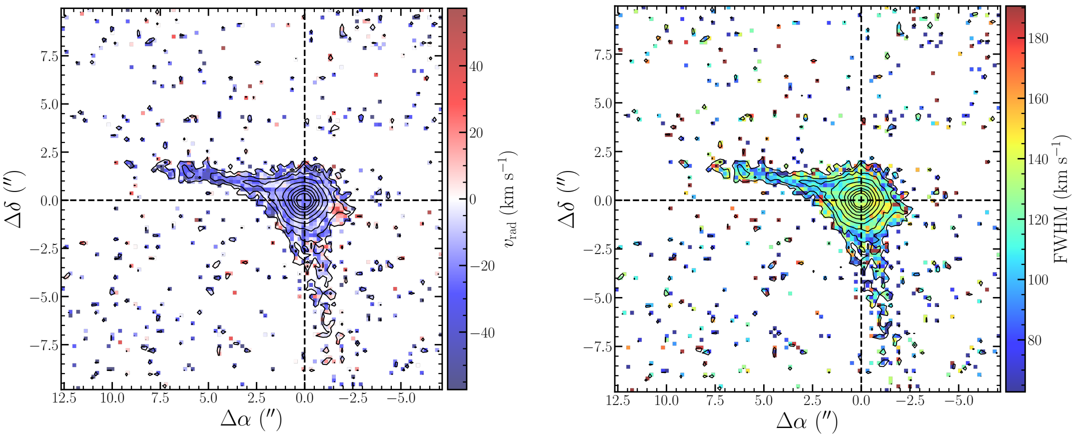

(a)

(b)

FIGURE C.5: Radial velocity map (a) and FWHM map (b) of the [O I]λ6300 Å emission line.

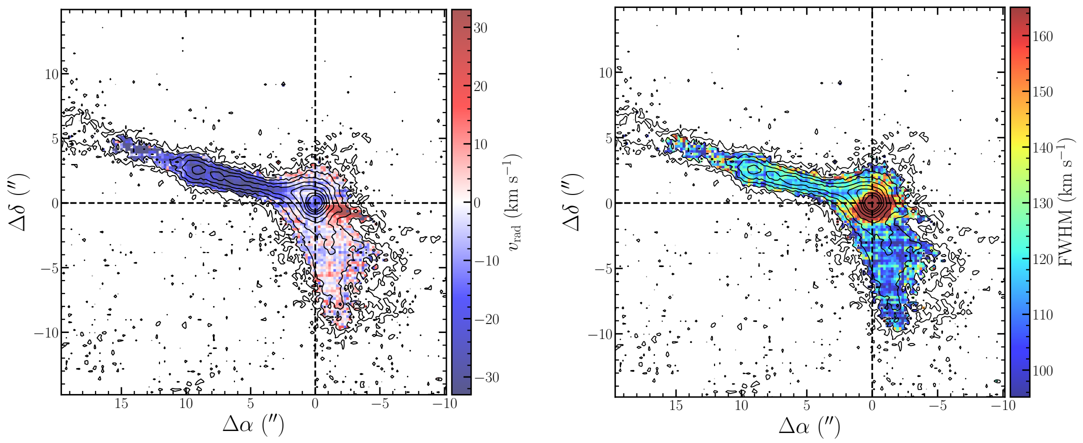

(a) (b)

Figure C.6: Same as Figure C.5, but for the Hα line.

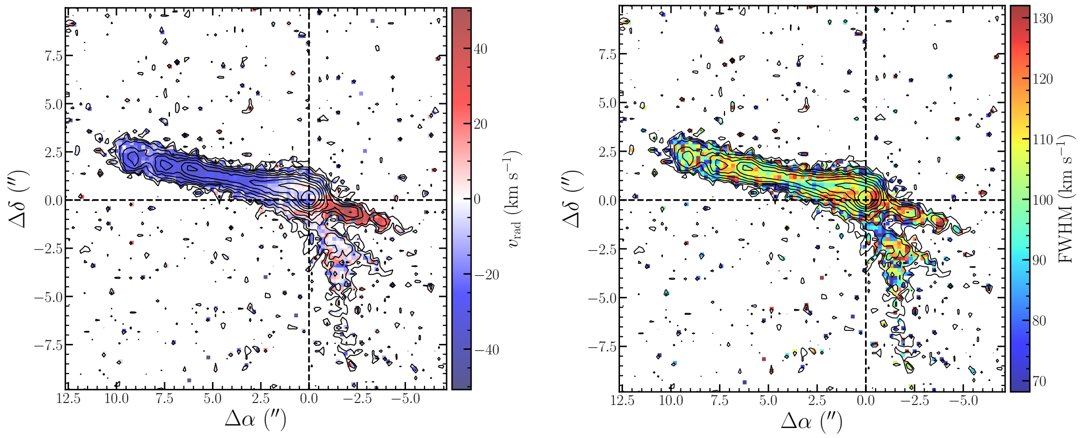

(a) (b)

Figure C.7: Same as Figure C.5 but for the [N II]λ6583 Å line.

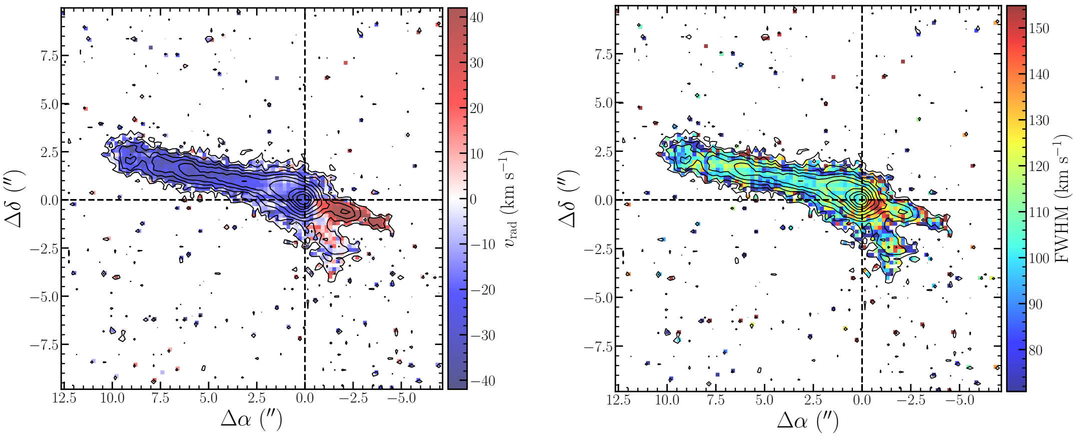

(a) (b)

Figure C.8: Same as Figure C.5 but for the [S ii]λ6731 Å emission line.

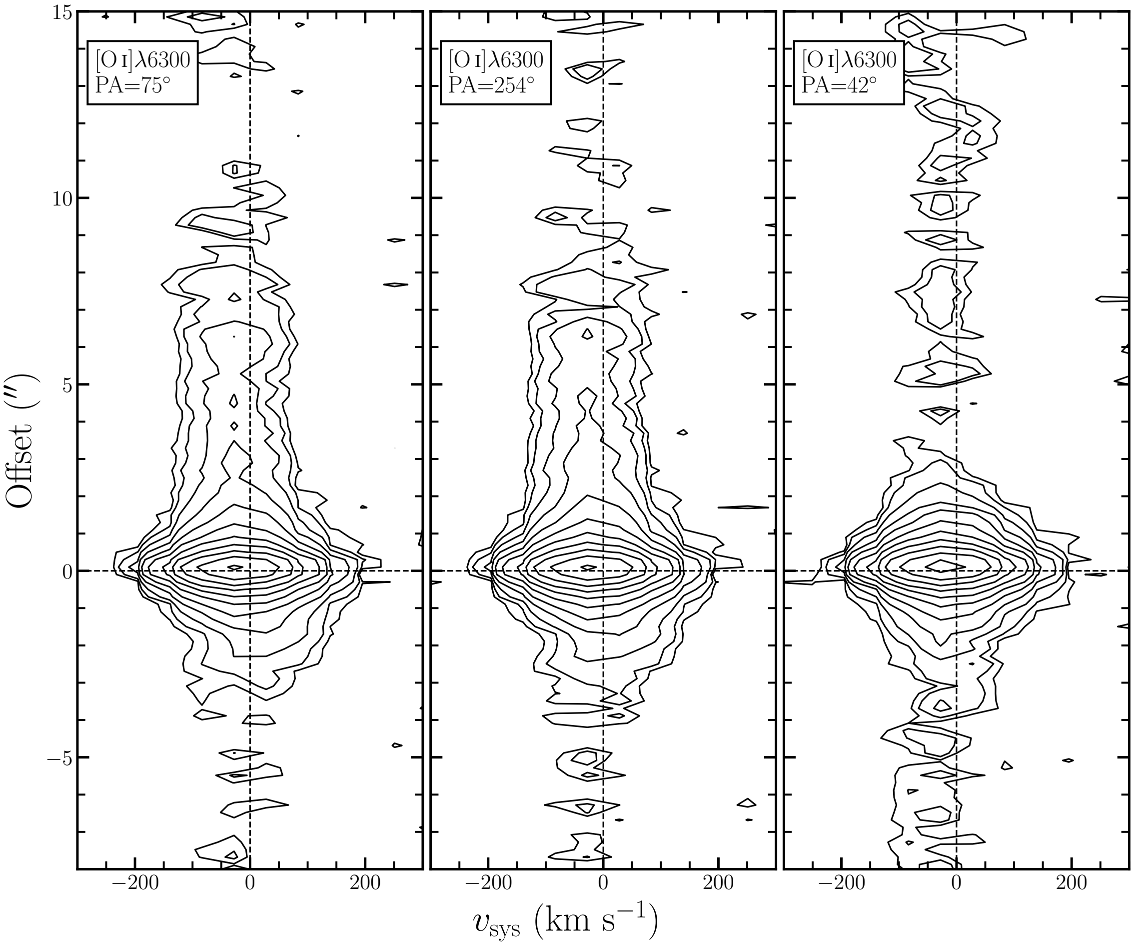

Figure C.9: Position-velocity maps for the [O i]λ6300 Å line with PAs of 76° for the blue jet (left), 254° for the red jet (center), and 33° for the cavity feature.

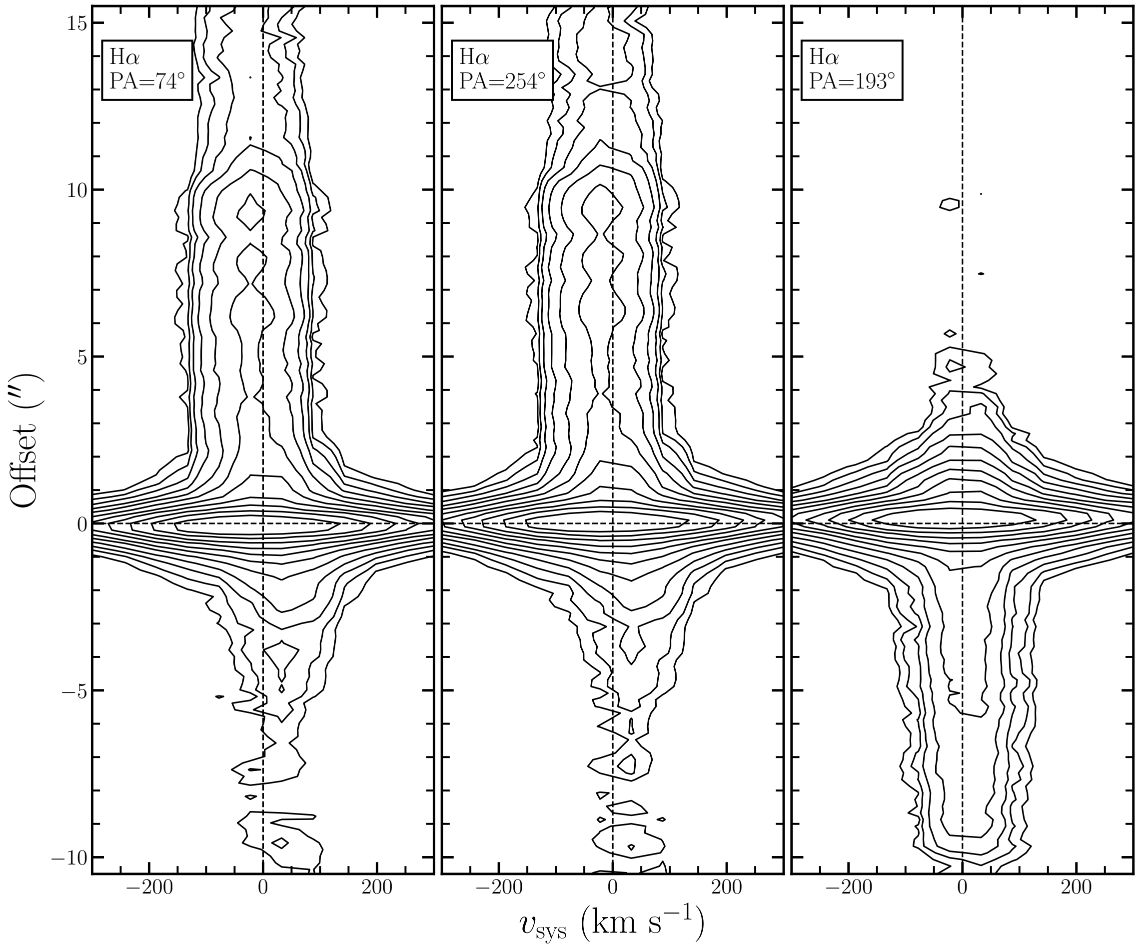

Figure C.10: Same as Figure C.9 but for the Hα line. PAs of 74° correspond to the blue jet (left), 254° to the red jet (center), and 193° to the cavity feature.

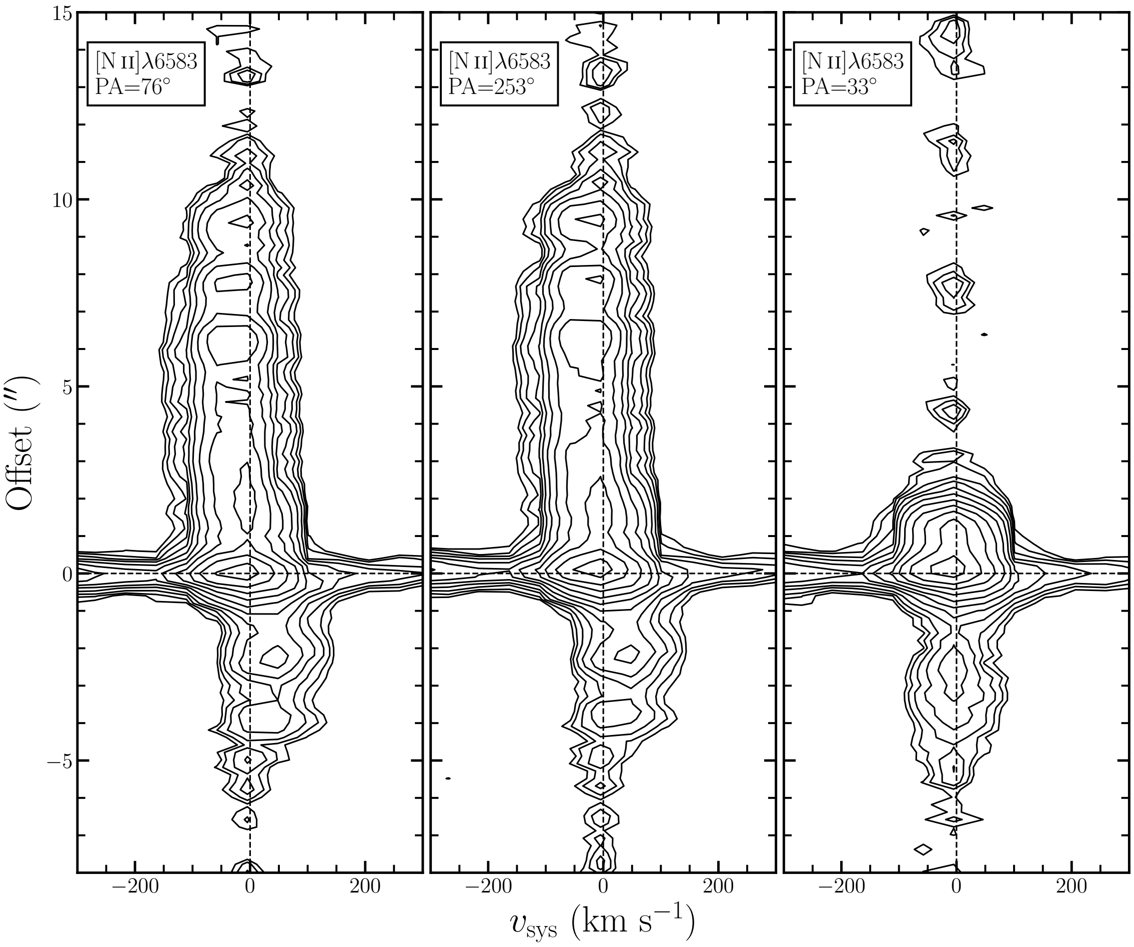

Figure C.11: Same as Figure C.9 but for the [N II]λ6583 Å line. PAs of 76° correspond to the blue jet (left), 254° to the red jet (center), and 33° to the cavity feature.

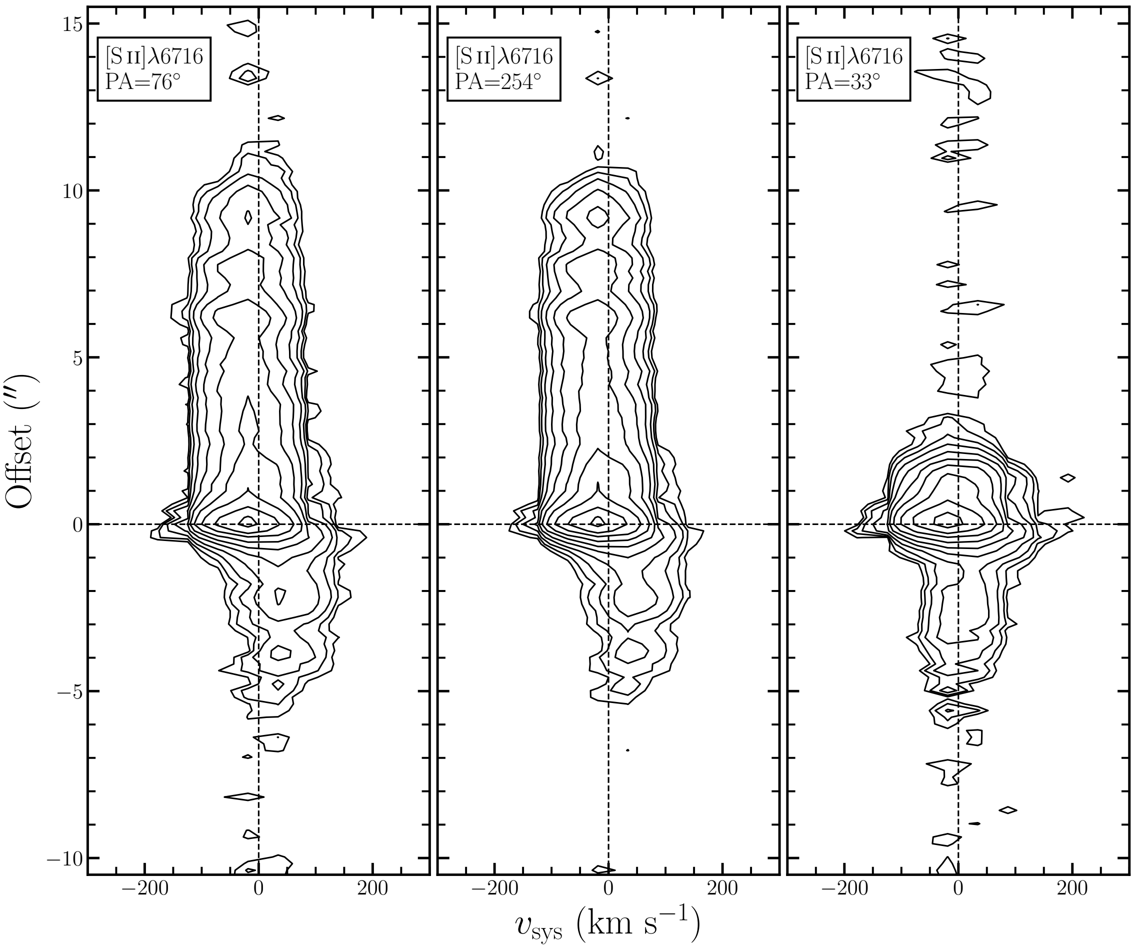

FIGURE C.12: Same as Figure C.9 but for the [S II]λ6716 Å line. PAs of 76° correspond to the blue jet (left), 254° to the red jet (center), and 33° to the cavity feature.

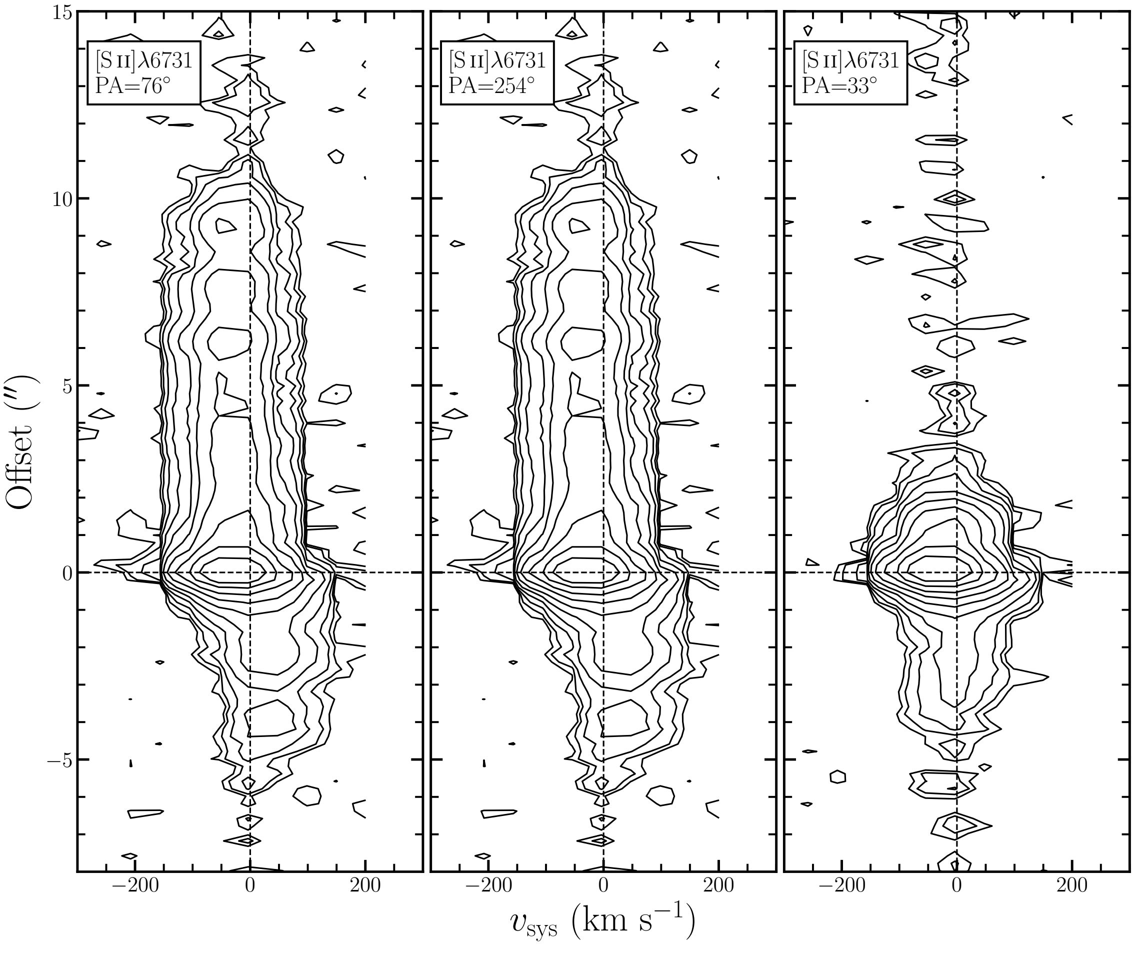

FIGURE C.13: Same as Figure C.9 but for the [S II]λ6731 Å line. PAs of 76° correspond to the blue jet (left), 254° to the red jet (center), and 33° to the cavity feature.

C.3 Velocity Channel Maps

Integration over the full emission range to produce an image can result in fainter features being excluded from the final image. Additionally, a flux-integrated image does not always reveal how spatial information varies with velocity. To explore this, smaller channel maps are produced and reported in this section to highlight the velocity-dependent spatial structure of the outflow in important emission lines. Contours in each image are computed beginning at a 3σ level and scaling logarithmically. The color maps show the intensity of the channel image using a square-root stretch beginning at a 3σ level. The channel maps are constructed in the same way as discussed in Chapter 5.4.3 using two spectral planes for each integration step. The exception to this is the Hα which uses a single spectral plane for each step in order to isolate red and blue features separately.

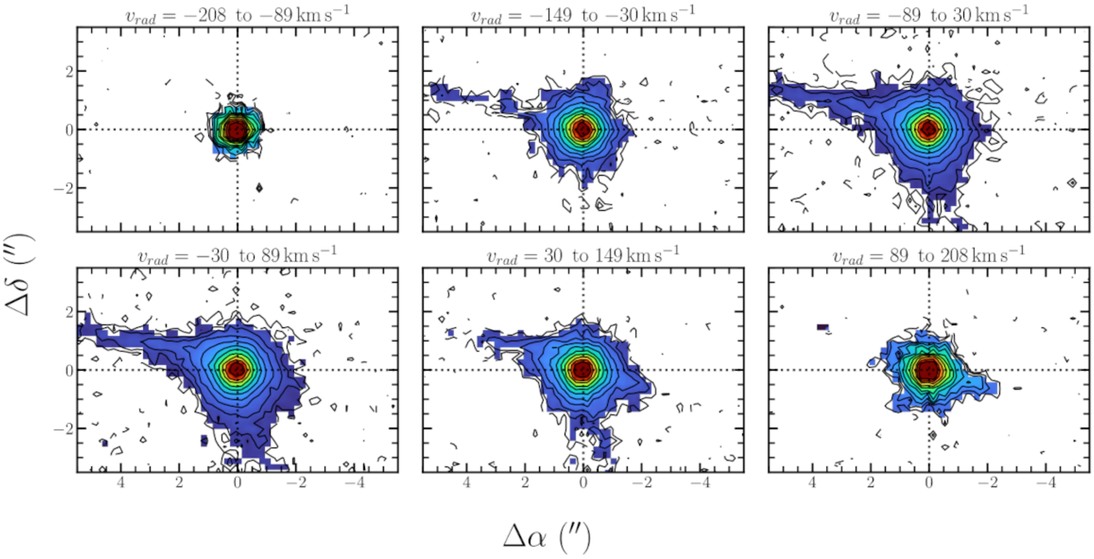

FIGURE C.14: Velocity channel maps of the [O I]λ6300 Å emission line.

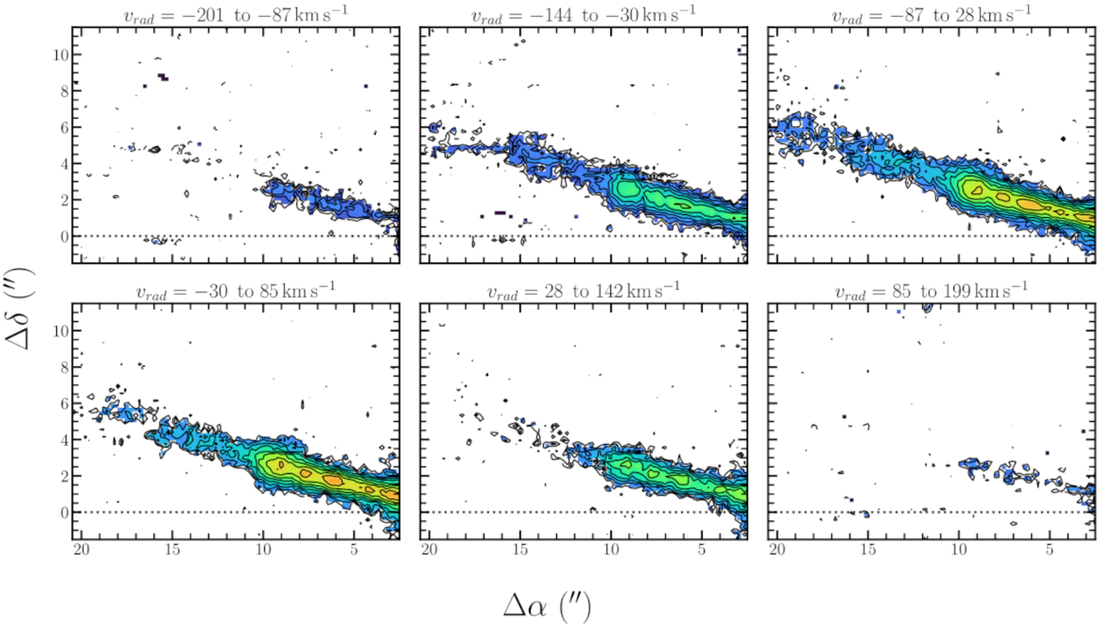

FIGURE C.15: Same as Figure C.14 but for the Hα blue-shifted emission. Diffuse emission is seen out to 20″ in the mid-range velocity channels (−144 to −30 km s^{-1}).

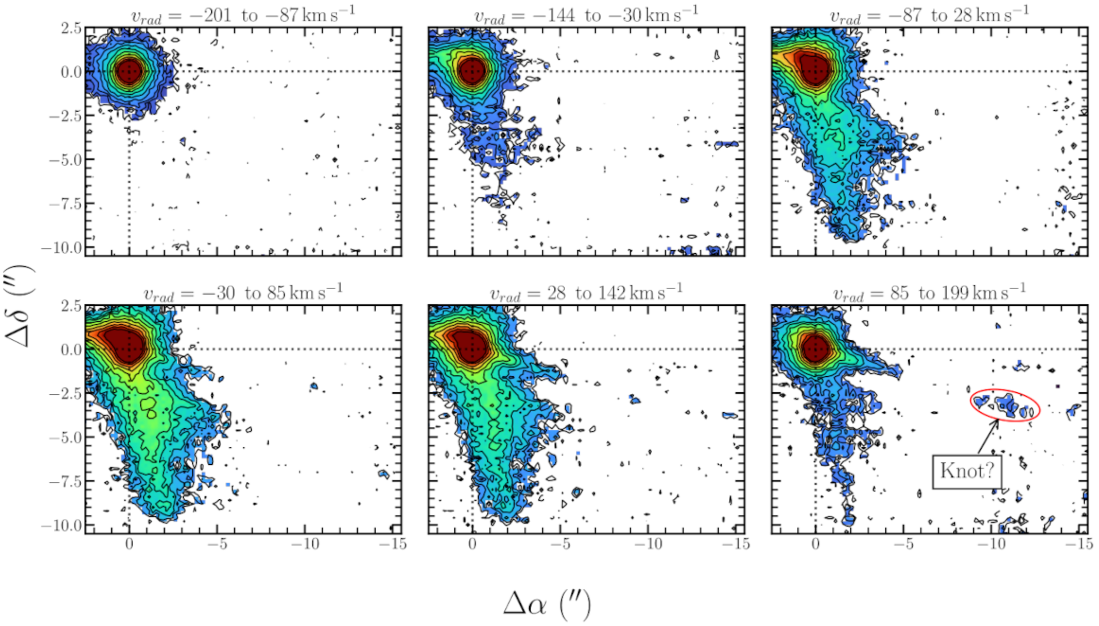

FIGURE C.16: Same as Figure C.15 but for the Hα red-shifted emission. The cavity begins to appear at blue-shifted velocities but is predominately centered around lower velocities. A potential knot is seen at the highest velocity and is labeled in the bottom right panel.

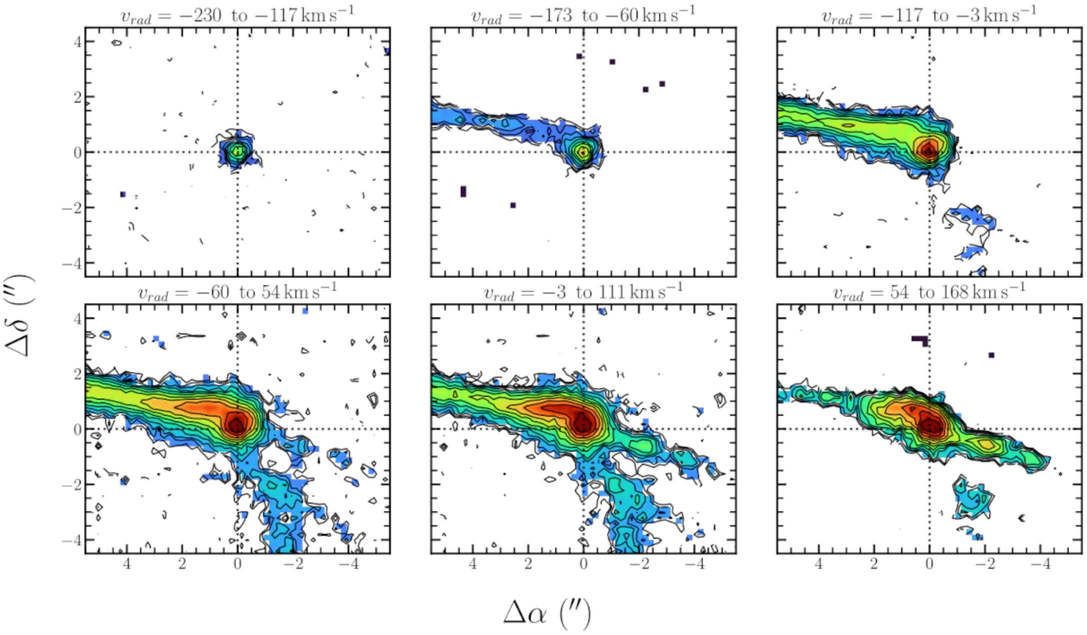

Figure C.17: Same as Figure C.14 but for the [N II]λ6583 Å line. The whistle feature is seen in blue- and red-shifted channels though its velocity centroid is slightly blue-shifted (see Table 5.1). In the bottom right panel the claw feature is more compact and red-shifted, strengthening the conclusion that this is a wide wind or cavity.

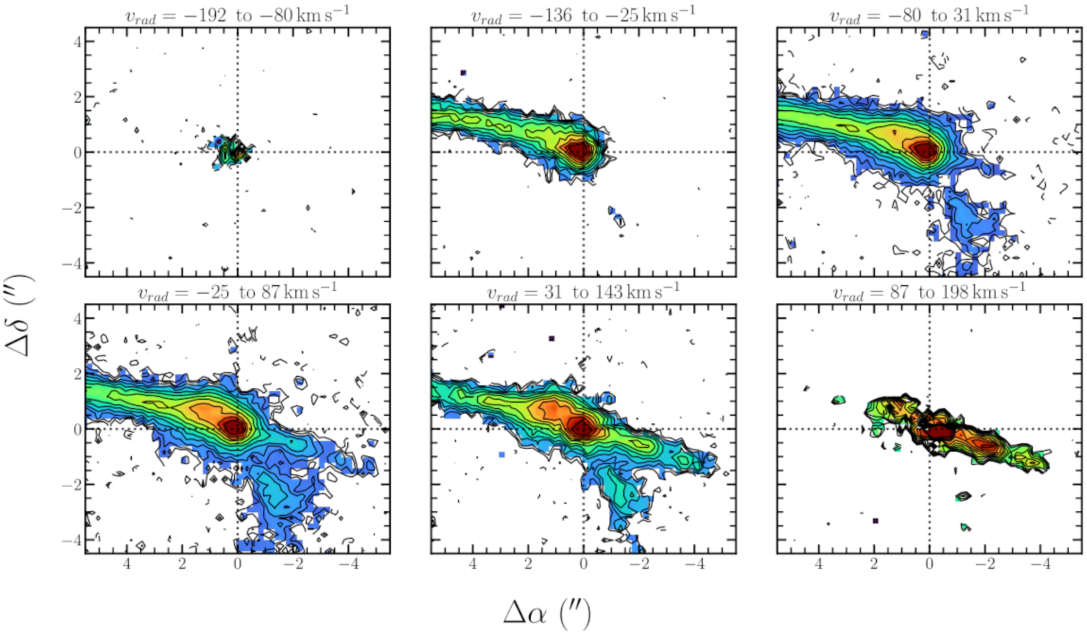

Figure C.18: Same as Figure C.14 but for the [S II]λ6716 Å line. As with the [N II] line, the whistle is broad with a slightly blue-shifted velocity centroid, and has more compact red-shifted features appearing to indicate a low velocity wind or cavity.

Bibliography

Alcalá, J. M. et al. (Mar. 2011). “An X-shooter survey of star forming regions: Low-mass stars and sub-stellar objects”. In: *Astronomische Nachrichten* 332.3, p. 242. DOI: `10.1002/asna.201111526`.

Alcalá, J. M. et al. (Jan. 2014). “X-shooter spectroscopy of young stellar objects. IV. Accretion in low-mass stars and substellar objects in Lupus”. In: Astron. Astrophys. 561, A2, A2. DOI: `10.1051/0004-6361/201322254`. arXiv: `1310.2069 [astro-ph.SR]`.

Andre, P., D. Ward-Thompson, and M. Barsony (May 2000). “From Prestellar Cores to Protostars: the Initial Conditions of Star Formation”. In: *Protostars and Planets IV*. Ed. by V. Mannings, A. P. Boss, and S. S. Russell, p. 59. arXiv: `astro-ph/9903284 [astro-ph]`.

André, Ph. (Jan. 2002). “The Initial Conditions for Protostellar Collapse: Observational Constraints”. In: *EAS Publications Series*. Ed. by Jerome Bouvier and Jean-Paul Zahn. Vol. 3. EAS Publications Series, pp. 1–38. DOI: `10.1051/eas:2002043`.

Andre, Philippe, Derek Ward-Thompson, and Mary Barsony (Mar. 1993). “Submillimeter Continuum Observations of rho Ophiuchi A: The Candidate Protostar VLA 1623 and Prestellar Clumps”. In: Astrophys. J. 406, p. 122. DOI: `10.1086/172425`.

André, Philippe et al. (2004). “Submillimeter studies of prestellar cores and protostars: Probing the initial conditions for protostellar collapse”. In: *Astrophysics and Space Scince* 292.1-4, pp. 325–337.

Andrews, Sean M. et al. (Dec. 2018). “The Disk Substructures at High Angular Resolution Project (DSHARP). I. Motivation, Sample, Calibration, and Overview”. In: Astrophys. J. Lett. 869.2, L41, p. L41. DOI: `10.3847/2041-8213/aaf741`. arXiv: `1812.04040 [astro-ph.SR]`.

Anglada, Guillem et al. (June 2007). “Proper Motions of the Jets in the Region of HH 30 and HL/XZ Tau: Evidence for a Binary Exciting Source of the HH 30 Jet”. In: Astron. J. 133.6, pp. 2799–2814. DOI: `10.1086/517493`. arXiv: `astro-ph/0703155 [astro-ph]`.

Bacciotti, Francesca and Jochen Eislöffel (Feb. 1999). “Ionization and density along the beams of Herbig-Haro jets”. In: Astron. Astrophys. 342, pp. 717–735.

Bacciotti, Francesca et al. (July 2000). “Hubble Space Telescope STIS Spectroscopy of the Optical Outflow from DG Tauri: Structure and Kinematics on Subarcsecond Scales”. In: Astrophys. J. Lett. 537.1, pp. L49–L52. DOI: `10.1086/312745`. arXiv: `astro-ph/0005463 [astro-ph]`.

Bacciotti, Francesca et al. (Sept. 2002). “Hubble Space Telescope/STIS Spectroscopy of the Optical Outflow from DG Tauri: Indications for Rotation in the Initial Jet Channel”.

In: Astrophys. J. 576.1, pp. 222–231. DOI: `10.1086/341725`. arXiv: `astro-ph/0206175 [astro-ph]`.

Baines, Deborah et al. (Apr. 2006). “On the binarity of Herbig Ae/Be stars”. In: *Monthly Notices of the Royal Astronomical Society* 367.2, pp. 737–753. ISSN: 0035-8711. DOI: `10.1111/j.1365-2966.2006.10006.x`. eprint: `https://academic.oup.com/mnras/article-pdf/367/2/737/3308993/367-2-737.pdf`. URL: `https://doi.org/10.1111/j.1365-2966.2006.10006.x`.

Bally, John, C. R. O’Dell, and Mark J. McCaughrean (June 2000). “Disks, Microjets, Windblown Bubbles, and Outflows in the Orion Nebula”. In: Astron. J. 119.6, pp. 2919–2959. DOI: `10.1086/301385`.

Bally, John and Bo Reipurth (Jan. 2001). “Irradiated Herbig-Haro Jets in the Orion Nebula and near NGC 1333”. In: Astrophys. J. 546.1, pp. 299–323. DOI: `10.1086/318258`. arXiv: `astro-ph/0009376 [astro-ph]`.

Bally, John, Allison Youngblood, and Adam Ginsburg (Sept. 2012). “The Spindle: An Irradiated Disk and Bent Protostellar Jet in Orion”. In: Astrophys. J. 756.2, 137, p. 137. DOI: `10.1088/0004-637X/756/2/137`.

Bally, John et al. (Aug. 1998). “Disk Mass Limits and Lifetimes of Externally Irradiated Young Stellar Objects Embedded in the Orion Nebula”. In: Astron. J. 116.2, pp. 854–859. DOI: `10.1086/300469`.

Bally, John et al. (Feb. 2011). “Explosive Outflows Powered by the Decay of Non-hierarchical Multiple Systems of Massive Stars: Orion BN/KL”. In: Astrophys. J. 727.2, 113, p. 113. DOI: `10.1088/0004-637X/727/2/113`. arXiv: `1011.5512 [astro-ph.GA]`.

Bautista, Manuel A., Jianfang Peng, and Anil K. Pradhan (Mar. 1996). “Excitation of [Ni II] and [Fe II] Lines in Gaseous Nebulae”. In: Astrophys. J. 460, p. 372. DOI: `10.1086/176976`.

Beall, J. H. (Jan. 2015). “A Review of Astrophysical Jets”. In: *XI Multifrequency Behaviour of High Energy Cosmic Sources Workshop (MULTIF15)*, 58, p. 58.

Beccari, G. et al. (July 2017). “A tale of three cities. OmegaCAM discovers multiple sequences in the color-magnitude diagram of the Orion Nebula Cluster”. In: Astron. Astrophys. 604, A22, A22. DOI: `10.1051/0004-6361/201730432`. arXiv: `1705.09496 [astro-ph.SR]`.

Berdyugina, S. V. et al. (Sept. 2017). “First Detection of a Strong Magnetic Field on a Bursty Brown Dwarf: Puzzle Solved”. In: Astrophys. J. 847.1, 61, p. 61. DOI: `10.3847/1538-4357/aa866b`. arXiv: `1709.02861 [astro-ph.SR]`.

Bjerkeli, Per et al. (Dec. 2016). “Resolved images of a protostellar outflow driven by an extended disk wind”. In: Nature 540.7633, pp. 406–409. DOI: `10.1038/nature20600`. arXiv: `1612.05148 [astro-ph.SR]`.

Blagrave, K. P. M. et al. (Jan. 2007). “Deviations from He I Case B Recombination Theory and Extinction Corrections in the Orion Nebula”. In: Astrophys. J. 655.1, pp. 299–315. DOI: `10.1086/510151`. arXiv: `astro-ph/0610621 [astro-ph]`.

Blandford, Roger, David Meier, and Anthony Readhead (Aug. 2019). "Relativistic Jets from Active Galactic Nuclei". In: Annu. Rev. Astron. Astrophys. 57, pp. 467–509. DOI: `10.1146/annurev-astro-081817-051948`. arXiv: `1812.06025 [astro-ph.HE]`.

Bradt, Hale (2014). *Astrophysics Processes.*

Bretscher, Otto (1997). *Linear algebra with applications.* Prentice Hall Eaglewood Cliffs, NJ.

Brugel, E. W., E. Olmsted, and K. H. Boehm (Sept. 1983). "Spectrophotometry of low excitation Herbig-Haro objects." In: Astron. Astrophys. 125, pp. 23–28.

Cabrit, Sylvie (Jan. 2009). "Observational Constraints to Steady Jet Models in Young Stars". In: *Protostellar Jets in Context.* Vol. 13. Astrophysics and Space Science Proceedings, pp. 247–257. DOI: `10.1007/978-3-642-00576-3_30`.

Cabrit, Sylvie, J. Ferreira, and C. Dougados (Feb. 2011). "Molecular and atomic jets in young low-mass stars: Properties and origin". In: *Jets at All Scales.* Ed. by Gustavo E. Romero, Rashid A. Sunyaev, and Tomaso Belloni. Vol. 275, pp. 374–382. DOI: `10.1017/S1743921310016431`.

Cardelli, Jason A., Geoffrey C. Clayton, and John S. Mathis (Oct. 1989). "The Relationship between Infrared, Optical, and Ultraviolet Extinction". In: Astrophys. J. 345, p. 245. DOI: `10.1086/167900`.

Carroll, Bradley W and Dale A Ostlie (2017). *An introduction to modern astrophysics.* Cambridge University Press.

Cauley, P. Wilson and Christopher M. Johns-Krull (Dec. 2014). "Diagnosing Mass Flows around Herbig Ae/Be Stars Using the He I λ10830 Line". In: Astrophys. J. 797.2, 112, p. 112. DOI: `10.1088/0004-637X/797/2/112`. arXiv: `1410.6964 [astro-ph.SR]`.

Chevance, Mélanie et al. (Mar. 2022). "The Life and Times of Giant Molecular Clouds". In: *arXiv e-prints*, arXiv:2203.09570, arXiv:2203.09570. arXiv: `2203.09570 [astro-ph.GA]`.

Clarke, C. J. (Apr. 2007). "The photoevaporation of discs around young stars in massive clusters". In: Mon. Not. R. Astron. Soc. 376.3, pp. 1350–1356. DOI: `10.1111/j.1365-2966.2007.11547.x`. arXiv: `astro-ph/0702112 [astro-ph]`.

Clarke, S. D., A. P. Whitworth, and D. A. Hubber (May 2016). "Perturbation growth in accreting filaments". In: Mon. Not. R. Astron. Soc. 458.1, pp. 319–324. DOI: `10.1093/mnras/stw407`. arXiv: `1602.07651 [astro-ph.GA]`.

Clarke, S. D. et al. (June 2017). "Filamentary fragmentation in a turbulent medium". In: Mon. Not. R. Astron. Soc. 468.2, pp. 2489–2505. DOI: `10.1093/mnras/stx637`. arXiv: `1703.04473 [astro-ph.GA]`.

Coffey, Deirdre et al. (Apr. 2004). "Rotation of Jets from Young Stars: New Clues from the Hubble Space Telescope Imaging Spectrograph". In: Astrophys. J. 604.2, pp. 758–765. DOI: `10.1086/382019`. arXiv: `astro-ph/0312300 [astro-ph]`.

Coffey, Deirdre et al. (July 2007). "Further Indications of Jet Rotation in New Ultraviolet and Optical Hubble Space Telescope STIS Spectra". In: Astrophys. J. 663.1, pp. 350–364. DOI: `10.1086/518100`. arXiv: `astro-ph/0703271 [astro-ph]`.

Coffey, Deirdre et al. (Apr. 2012). "Jet Rotation Investigated in the Near-ultraviolet with the Hubble Space Telescope Imaging Spectrograph". In: Astrophys. J. 749.2, 139, p. 139. DOI: `10.1088/0004-637X/749/2/139`. arXiv: `1202.3250 [astro-ph.GA]`.

de Valon, A. et al. (Feb. 2020). "ALMA reveals a large structured disk and nested rotating outflows in DG Tauri B". In: Astron. Astrophys. 634, L12, p. L12. DOI: `10.1051/0004-6361/201936950`. arXiv: `2001.09776 [astro-ph.SR]`.

Devine, David et al. (Oct. 2000). "A Lyα Bright Jet from a Herbig AE Star". In: Astrophys. J. Lett. 542.2, pp. L115–L118. DOI: `10.1086/312939`.

Dobbs, C. L. et al. (Jan. 2014). "Formation of Molecular Clouds and Global Conditions for Star Formation". In: *Protostars and Planets VI*. Ed. by Henrik Beuther et al., p. 3. DOI: `10.2458/azu_uapress_9780816531240-ch001`. arXiv: `1312.3223 [astro-ph.GA]`.

Doppmann, G. W. et al. (Sept. 2005). "The Physical Natures of Class I and Flat-Spectrum Protostellar Photospheres: A Near-Infrared Spectroscopic Study". In: Astron. J. 130.3, pp. 1145–1170. DOI: `10.1086/431954`. arXiv: `astro-ph/0505295 [astro-ph]`.

Draine, B. T. (Dec. 2003). "Scattering by Interstellar Dust Grains. I. Optical and Ultraviolet". In: Astrophys. J. 598.2, pp. 1017–1025. DOI: `10.1086/379118`. arXiv: `astro-ph/0304060 [astro-ph]`.

Draine, Bruce T. and Christopher F. McKee (Jan. 1993). "Theory of interstellar shocks." In: Annu. Rev. Astron. Astrophys. 31, pp. 373–432. DOI: `10.1146/annurev.aa.31.090193.002105`.

Dunham, M. M. et al. (Jan. 2014). "The Evolution of Protostars: Insights from Ten Years of Infrared Surveys with Spitzer and Herschel". In: *Protostars and Planets VI*. Ed. by Henrik Beuther et al., p. 195. DOI: `10.2458/azu_uapress_9780816531240-ch009`. arXiv: `1401.1809 [astro-ph.GA]`.

Eislöffel, J., M. D. Smith, and C. J. Davis (July 2000). "Spectroscopy of molecular hydrogen in outflows from young stars". In: Astron. Astrophys. 359, pp. 1147–1161.

Eisner, J. A. et al. (June 2018). "Protoplanetary Disk Properties in the Orion Nebula Cluster: Initial Results from Deep, High-resolution ALMA Observations". In: Astrophys. J. 860.1, 77, p. 77. DOI: `10.3847/1538-4357/aac3e2`. arXiv: `1805.03669 [astro-ph.SR]`.

Ellerbroek, L. E. et al. (Mar. 2014). "Relating jet structure to photometric variability: the Herbig Ae star HD 163296". In: Astron. Astrophys. 563, A87, A87. DOI: `10.1051/0004-6361/201323092`. arXiv: `1401.3744 [astro-ph.SR]`.

Erkal, J. et al. (June 2021a). "Launching the asymmetric bipolar jet of DO Tau". In: Astron. Astrophys. 650, A46, A46. DOI: `10.1051/0004-6361/202038977`. arXiv: `2104.07484 [astro-ph.SR]`.

Erkal, Jessica et al. (Sept. 2021b). "Probing Jets from Young Embedded Sources: Clues from HST Near-IR [Fe II] Images". In: Astrophys. J. 919.1, 23, p. 23. DOI: `10.3847/1538-4357/ac06c5`. arXiv: `2106.04414 [astro-ph.SR]`.

Estalella, Robert et al. (Aug. 2012). "The Counterjet of HH 30: New Light on Its Binary Driving Source". In: Astron. J. 144.2, 61, p. 61. DOI: `10.1088/0004-6256/144/2/61`. arXiv: `1206.3391 [astro-ph.GA]`.

Fitzpatrick, Edward L. (Jan. 1999). "Correcting for the Effects of Interstellar Extinction". In: Publ. Astron. Soc. Pac. 111.755, pp. 63–75. DOI: `10.1086/316293`. arXiv: `astro-ph/9809387 [astro-ph]`.

Flaherty, Kevin M. et al. (Nov. 2015). "Weak Turbulence in the HD 163296 Protoplanetary Disk Revealed by ALMA CO Observations". In: Astrophys. J. 813.2, 99, p. 99. DOI: `10.1088/0004-637X/813/2/99`. arXiv: `1510.01375 [astro-ph.SR]`.

Frank, A. et al. (Jan. 2014). "Jets and Outflows from Star to Cloud: Observations Confront Theory". In: *Protostars and Planets VI*. Ed. by Henrik Beuther et al., p. 451. DOI: `10.2458/azu\_uapress\_9780816531240-ch020`. arXiv: `1402.3553 [astro-ph.SR]`.

Gaia Collaboration et al. (May 2021). "Gaia Early Data Release 3. Summary of the contents and survey properties". In: Astron. Astrophys. 649, A1, A1. DOI: `10.1051/0004-6361/202039657`. arXiv: `2012.01533 [astro-ph.GA]`.

Garufi, A. et al. (Aug. 2019). "SPHERE view of the jet and the envelope of RY Tauri". In: Astron. Astrophys. 628, A68, A68. DOI: `10.1051/0004-6361/201935546`. arXiv: `1906.06910 [astro-ph.SR]`.

Giannini, T. et al. (Nov. 2015). "Solving the Excitation and Chemical Abundances in Shocks: The Case of HH 1". In: Astrophys. J. 814.1, 52, p. 52. DOI: `10.1088/0004-637X/814/1/52`. arXiv: `1510.06880 [astro-ph.SR]`.

Grady, C. A. et al. (Dec. 2000). "STIS Coronagraphic Imaging of the Herbig AE Star: HD 163296". In: Astrophys. J. 544.2, pp. 895–902. DOI: `10.1086/317222`.

Grieves, Nolan et al. (Aug. 2021). "Populating the brown dwarf and stellar boundary: Five stars with transiting companions near the hydrogen-burning mass limit". In: Astron. Astrophys. 652, A127, A127. DOI: `10.1051/0004-6361/202141145`. arXiv: `2107.03480 [astro-ph.SR]`.

Guidi, G. et al. (Sept. 2018). "High-contrast imaging of HD 163296 with the Keck/NIRC2 L'-band vortex coronograph". In: Mon. Not. R. Astron. Soc. 479.2, pp. 1505–1513. DOI: `10.1093/mnras/sty1642`. arXiv: `1806.08263 [astro-ph.EP]`.

Hacar, A. et al. (Mar. 2018). "An ALMA study of the Orion Integral Filament. I. Evidence for narrow fibers in a massive cloud". In: Astron. Astrophys. 610, A77, A77. DOI: `10.1051/0004-6361/201731894`. arXiv: `1801.01500 [astro-ph.GA]`.

Hartigan, P. (2008). "Measurement of Physical Conditions in Stellar Jets". In: *Jets from Young Stars II*. Ed. by Francesca Bacciotti, Leonardo Testi, and Emma Whelan. Vol. 742, p. 15.

Hartigan, P., R. Holcomb, and A. Frank (May 2019). "Proper Motions and Shock Wave Dynamics in the HH 7-11 Stellar Jet". In: Astrophys. J. 876.2, 147, p. 147. DOI: `10.3847/1538-4357/ab18fa`. arXiv: `1904.05983 [astro-ph.SR]`.

Hartigan, Patrick, Suzan Edwards, and Louma Ghandour (Oct. 1995). "Disk Accretion and Mass Loss from Young Stars". In: Astrophys. J. 452, p. 736. DOI: `10.1086/176344`.

Hartigan, Patrick, Jon A. Morse, and John Raymond (Nov. 1994). "Mass-Loss Rates, Ionization Fractions, Shock Velocities, and Magnetic Fields of Stellar Jets". In: Astrophys. J. 436, p. 125. DOI: `10.1086/174887`.

Hartigan, Patrick et al. (Feb. 1999). “Hubble Space Telescope Faint Object Spectrograph Optical and Ultraviolet Spectroscopy of the Bow Shock HH 47A”. In: Astrophys. J. 512.2, pp. 901–915. DOI: `10.1086/306792`.

Hartmann, Lee, Gregory Herczeg, and Nuria Calvet (Sept. 2016). “Accretion onto Pre-Main-Sequence Stars”. In: Annu. Rev. Astron. Astrophys. 54, pp. 135–180. DOI: `10.1146/annurev-astro-081915-023347`.

Henney, W. J. and S. J. Arthur (July 1998). “Modeling the Brightness Profiles of the Orion Proplyds”. In: Astron. J. 116.1, pp. 322–335. DOI: `10.1086/300433`.

Henney, W. J. and C. R. O’Dell (Nov. 1999). “A Keck High-Resolution Spectroscopic Study of the Orion Nebula Proplyds”. In: Astron. J. 118.5, pp. 2350–2368. DOI: `10.1086/301087`. arXiv: `astro-ph/9908018 [astro-ph]`.

Herbig, George H. (Mar. 1960). “The Spectra of Be- and Ae-Type Stars Associated with Nebulosity”. In: Astrophys. J. Suppl. Ser. 4, p. 337. DOI: `10.1086/190050`.

Herczeg, Gregory J. and Lynne A. Hillenbrand (July 2008). “UV Excess Measures of Accretion onto Young Very Low Mass Stars and Brown Dwarfs”. In: Astrophys. J. 681.1, pp. 594–625. DOI: `10.1086/586728`. arXiv: `0801.3525 [astro-ph]`.

Hillenbrand, Lynne A. et al. (Oct. 1992). “Herbig Ae/Be Stars: Intermediate-Mass Stars Surrounded by Massive Circumstellar Accretion Disks”. In: Astrophys. J. 397, p. 613. DOI: `10.1086/171819`.

Huang, Jane et al. (Dec. 2018). “The Disk Substructures at High Angular Resolution Project (DSHARP). II. Characteristics of Annular Substructures”. In: Astrophys. J. Lett. 869.2, L42, p. L42. DOI: `10.3847/2041-8213/aaf740`. arXiv: `1812.04041 [astro-ph.EP]`.

Hubrig, S. et al. (Jan. 2014). “Magnetic fields of Herbig Ae/Be stars”. In: *European Physical Journal Web of Conferences*. Vol. 64. European Physical Journal Web of Conferences, 08006, p. 08006. DOI: `10.1051/epjconf/20136408006`. arXiv: `1308.6777 [astro-ph.SR]`.

Huélamo, N. et al. (May 2018). “Searching for H_α emitting sources around MWC 758. SPHERE/ZIMPOL high-contrast imaging”. In: Astron. Astrophys. 613, L5, p. L5. DOI: `10.1051/0004-6361/201832874`. arXiv: `1803.09264 [astro-ph.SR]`.

Huélamo, N. et al. (Dec. 2022). “Searching for H_α-emitting sources in the gaps of five transitional disks. SPHERE/ZIMPOL high-contrast imaging”. In: Astron. Astrophys. 668, A138, A138. DOI: `10.1051/0004-6361/202243918`. arXiv: `2210.02212 [astro-ph.EP]`.

Hummer, D. G. and P. J. Storey (Feb. 1987). “Recombination-line intensities for hydrogenic ions - I. Case B calculations for H I and He II.” In: Mon. Not. R. Astron. Soc. 224, pp. 801–820. DOI: `10.1093/mnras/224.3.801`.

Isella, Andrea et al. (Dec. 2016). “Ringed Structures of the HD 163296 Protoplanetary Disk Revealed by ALMA”. In: Phys. Rev. Lett. 117.25, 251101, p. 251101. DOI: `10.1103/PhysRevLett.117.251101`.

Isella, Andrea et al. (Dec. 2018). “The Disk Substructures at High Angular Resolution Project (DSHARP). IX. A High-definition Study of the HD 163296 Planet-forming

Disk". In: Astrophys. J. Lett. 869.2, L49, p. L49. DOI: `10.3847/2041-8213/aaf747`. arXiv: `1812.04047 [astro-ph.SR]`.

Joergens, V. et al. (July 2012). "The bipolar outflow and disk of the brown dwarf ISO 217". In: Astron. Astrophys. 543, A151, A151. DOI: `10.1051/0004-6361/201219206`. arXiv: `1205.3166 [astro-ph.SR]`.

Johns-Krull, Christopher M., Jeff A. Valenti, and Christopher Koresko (May 1999). "Measuring the Magnetic Field on the Classical T Tauri Star BP Tauri". In: Astrophys. J. 516.2, pp. 900–915. DOI: `10.1086/307128`.

Kogure, Tomokazu and Kam-Ching Leung (2010). *The Astrophysics of Emission-Line Stars*. Vol. 342. Springer Science & Business Media.

Königl, A. and R. E. Pudritz (May 2000). "Disk Winds and the Accretion-Outflow Connection". In: *Protostars and Planets IV*. Ed. by V. Mannings, A. P. Boss, and S. S. Russell, p. 759. arXiv: `astro-ph/9903168 [astro-ph]`.

Kounkel, Marina et al. (May 2019). "Close Companions around Young Stars". In: Astron. J. 157.5, 196, p. 196. DOI: `10.3847/1538-3881/ab13b1`. arXiv: `1903.10523 [astro-ph.SR]`.

Lai, Dong (July 2003). "Warping of Accretion Disks with Magnetically Driven Outflows: A Possible Origin for Jet Precession". In: Astrophys. J. Lett. 591.2, pp. L119–L122. DOI: `10.1086/377163`. arXiv: `astro-ph/0306012 [astro-ph]`.

Lee, Chin-Fei et al. (Feb. 2021). "First Detection of Interaction between a Magnetic Disk Wind and an Episodic Jet in a Protostellar System". In: Astrophys. J. Lett. 907.2, L41, p. L41. DOI: `10.3847/2041-8213/abda38`. arXiv: `2101.03293 [astro-ph.GA]`.

Lee, Chin-Fei et al. (Mar. 2022). "Magnetocentrifugal Origin for Protostellar Jets Validated through Detection of Radial Flow at the Jet Base". In: Astrophys. J. Lett. 927.2, L27, p. L27. DOI: `10.3847/2041-8213/ac59c0`. arXiv: `2203.00961 [astro-ph.GA]`.

Li, Z. Y. et al. (Jan. 2014). "The Earliest Stages of Star and Planet Formation: Core Collapse, and the Formation of Disks and Outflows". In: *Protostars and Planets VI*. Ed. by Henrik Beuther et al., p. 173. DOI: `10.2458/azu_uapress_9780816531240-ch008`. arXiv: `1401.2219 [astro-ph.SR]`.

Lucy, L. B. (Feb. 1995). "Fluorescent excitation of [Ni II] lines in the spectra of gaseous nebulae." In: Astron. Astrophys. 294, pp. 555–567.

Manara, C. F. et al. (Mar. 2013). "X-shooter spectroscopy of young stellar objects. II. Impact of chromospheric emission on accretion rate estimates". In: Astron. Astrophys. 551, A107, A107. DOI: `10.1051/0004-6361/201220921`. arXiv: `1301.3058 [astro-ph.GA]`.

Manara, C. F. et al. (Sept. 2017). "An extensive VLT/X-shooter library of photospheric templates of pre-main sequence stars". In: Astron. Astrophys. 605, A86, A86. DOI: `10.1051/0004-6361/201730807`. arXiv: `1705.10075 [astro-ph.SR]`.

Mao, S. Alwin, Eve C. Ostriker, and Chang-Goo Kim (July 2020). "Cloud Properties and Correlations with Star Formation in Self-consistent Simulations of the Multiphase ISM". In: Astrophys. J. 898.1, 52, p. 52. DOI: `10.3847/1538-4357/ab989c`. arXiv: `1911.05078 [astro-ph.GA]`.

Marti, J., L. F. Rodriguez, and B. Reipurth (Oct. 1993). "HH 80-81: A Highly Collimated Herbig-Haro Complex Powered by a Massive Young Star". In: Astrophys. J. 416, p. 208. DOI: `10.1086/173227`.

Masciadri, E. and A. C. Raga (Jan. 2001). "A Jet-Side Wind Interaction Model for the Curved Jets in the Orion Nebula". In: Astron. J. 121.1, pp. 408–412. DOI: `10.1086/318049`.

— (Apr. 2002). "Herbig-Haro Jets from Orbiting Sources". In: Astrophys. J. 568.2, pp. 733–742. DOI: `10.1086/338767`.

Maucó, Karina et al. (May 2018). "Herschel PACS Observations of 4-10 Myr Old Classical T Tauri Stars in Orion OB1". In: Astrophys. J. 859.1, 1, p. 1. DOI: `10.3847/1538-4357/aabf40`. arXiv: `1804.06377 [astro-ph.SR]`.

Maurri, L. et al. (May 2014). "Physical properties of the jet from DG Tauri on sub-arcsecond scales with HST/STIS". In: Astron. Astrophys. 565, A110, A110. DOI: `10.1051/0004-6361/201117510`. arXiv: `1401.0483 [astro-ph.SR]`.

McCall, Marshall L. (Nov. 2004). "On Determining Extinction from Reddening". In: Astron. J. 128.5, pp. 2144–2169. DOI: `10.1086/424933`.

McLeod, Anna F. et al. (Feb. 2018). "A parsec-scale optical jet from a massive young star in the Large Magellanic Cloud". In: Nature 554.7692, pp. 334–336. DOI: `10.1038/nature25189`. arXiv: `1801.08147 [astro-ph.SR]`.

Méndez-Delgado, J. E. et al. (Sept. 2021). "Photoionized Herbig-Haro Objects in the Orion Nebula through Deep High Spectral Resolution Spectroscopy. II. HH 204". In: Astrophys. J. 918.1, 27, p. 27. DOI: `10.3847/1538-4357/ac0cf5`. arXiv: `2106.08667 [astro-ph.GA]`.

Mendigutía, Ignacio (May 2020). "On the Mass Accretion Rates of Herbig Ae/Be Stars. Magnetospheric Accretion or Boundary Layer?" In: *Galaxies* 8.2, p. 39. DOI: `10.3390/galaxies8020039`. arXiv: `2005.01745 [astro-ph.SR]`.

Mesa-Delgado, A. et al. (Oct. 2012). "Ionized gas diagnostics from protoplanetary discs in the Orion nebula and the abundance discrepancy problem". In: Mon. Not. R. Astron. Soc. 426.1, pp. 614–634. DOI: `10.1111/j.1365-2966.2012.21230.x`. arXiv: `1205.0509 [astro-ph.GA]`.

Muro-Arena, G. A. et al. (June 2018). "Dust modeling of the combined ALMA and SPHERE datasets of HD 163296. Is HD 163296 really a Meeus group II disk?" In: Astron. Astrophys. 614, A24, A24. DOI: `10.1051/0004-6361/201732299`. arXiv: `1802.03328 [astro-ph.EP]`.

Murphy, A. et al. (Aug. 2021). "A MUSE spectro-imaging study of the Th 28 jet: Precession in the inner jet". In: Astron. Astrophys. 652, A119, A119. DOI: `10.1051/0004-6361/202141315`. arXiv: `2107.08065 [astro-ph.SR]`.

Nisini, B. et al. (Jan. 2018). "Connection between jets, winds and accretion in T Tauri stars. The X-shooter view". In: Astron. Astrophys. 609, A87, A87. DOI: `10.1051/0004-6361/201730834`. arXiv: `1710.05587 [astro-ph.SR]`.

Noriega-Crespo, Alberto, Nuria Calvet, and Karl-Heinz Böhm (Oct. 1991). “Models for Light Scattering by Dust around Herbig-Haro Objects”. In: Astrophys. J. 379, p. 676. DOI: `10.1086/170541`.

O’Dell, C. R., W. Kollatschny, and G. J. Ferland (Mar. 2017). “Which Stars Are Ionizing the Orion Nebula?” In: Astrophys. J. 837.2, 151, p. 151. DOI: `10.3847/1538-4357/aa6198`.

O’Dell, C. R. et al. (Aug. 1997). “Herbig Haro Objects in the Orion Nebula.” In: Astron. J. 114, pp. 730–743. DOI: `10.1086/118507`.

O’Donnell, James E. (Feb. 1994). “R v-dependent Optical and Near-Ultraviolet Extinction”. In: Astrophys. J. 422, p. 158. DOI: `10.1086/173713`.

Osterbrock, D.E. and G.J. Ferland (2006). *Astrophysics Of Gas Nebulae and Active Galactic Nuclei.* University Science Books. ISBN: 9781891389344.

Pagnini, G. and R. K. Saxena (May 2008). “A note on the Voigt profile function”. In: *arXiv e-prints*, arXiv:0805.2274, arXiv:0805.2274. arXiv: `0805.2274 [math-ph]`.

Pascual, N. et al. (Feb. 2016). “The far-infrared behaviour of Herbig Ae/Be discs: Herschel PACS photometry”. In: Astron. Astrophys. 586, A6, A6. DOI: `10.1051/0004-6361/201526605`. arXiv: `1511.08356 [astro-ph.SR]`.

Pinte, C. et al. (June 2018). “Kinematic Evidence for an Embedded Protoplanet in a Circumstellar Disk”. In: Astrophys. J. Lett. 860.1, L13, p. L13. DOI: `10.3847/2041-8213/aac6dc`. arXiv: `1805.10293 [astro-ph.SR]`.

Pinte, C. et al. (Feb. 2020). “Nine Localized Deviations from Keplerian Rotation in the DSHARP Circumstellar Disks: Kinematic Evidence for Protoplanets Carving the Gaps”. In: Astrophys. J. Lett. 890.1, L9, p. L9. DOI: `10.3847/2041-8213/ab6dda`. arXiv: `2001.07720 [astro-ph.SR]`.

Podio, L. et al. (Sept. 2006). “Recipes for stellar jets: results of combined optical/infrared diagnostics”. In: Astron. Astrophys. 456.1, pp. 189–204. DOI: `10.1051/0004-6361:20054156`. arXiv: `astro-ph/0606280 [astro-ph]`.

Pollack, James B. et al. (Nov. 1996). “Formation of the Giant Planets by Concurrent Accretion of Solids and Gas”. In: Icarus 124.1, pp. 62–85. DOI: `10.1006/icar.1996.0190`.

Porter, John M., R. D. Oudmaijer, and D. Baines (Dec. 2004). “On the spectroastrometric separation of binary point-source fluxes”. In: Astron. Astrophys. 428, pp. 327–337. DOI: `10.1051/0004-6361:20035686`. arXiv: `astro-ph/0408284 [astro-ph]`.

Pudritz, R. E. et al. (Jan. 2007). “Disk Winds, Jets, and Outflows: Theoretical and Computational Foundations”. In: *Protostars and Planets V*. Ed. by Bo Reipurth, David Jewitt, and Klaus Keil, p. 277. arXiv: `astro-ph/0603592 [astro-ph]`.

Raga, A. C., R. Mundt, and T. P. Ray (Dec. 1991). “Collimation of stellar jets - constraints from the observed spatial structure. I. Data analysis methods.” In: Astron. Astrophys. 252, pp. 733–739.

Raga, A. C. et al. (Jan. 2009). “Curved Herbig-Haro jets immersed in a stellar wind”. In: Astron. Astrophys. 493.1, pp. 115–118. DOI: `10.1051/0004-6361:200810900`.

Ray, T. P. (June 1994). “Herbig Ae/Be Stars”. In: Astrophys. Space Sci. 216.1-2, pp. 71–86. DOI: `10.1007/BF00982471`.

Ray, T. P. and J. Ferreira (Dec. 2021). “Jets from young stars”. In: New Astron. Rev. 93, 101615, p. 101615. DOI: `10.1016/j.newar.2021.101615`. arXiv: `2009.00547 [astro-ph.SR]`.

Reipurth, Bo and John Bally (Jan. 2001a). “Herbig-Haro Flows: Probes of Early Stellar Evolution”. In: Annu. Rev. Astron. Astrophys. 39, pp. 403–455. DOI: `10.1146/annurev.astro.39.1.403`.

— (Jan. 2001b). “Herbig-Haro Flows: Probes of Early Stellar Evolution”. In: Annu. Rev. Astron. Astrophys. 39, pp. 403–455. DOI: `10.1146/annurev.astro.39.1.403`.

Reipurth, Bo and Cathie Clarke (July 2001). “The Formation of Brown Dwarfs as Ejected Stellar Embryos”. In: Astron. J. 122.1, pp. 432–439. DOI: `10.1086/321121`. arXiv: `astro-ph/0103019 [astro-ph]`.

Reiter, Megan, Nathan Smith, and John Bally (Dec. 2016). “[Fe II] jets from intermediate-mass protostars in Carina”. In: Mon. Not. R. Astron. Soc. 463.4, pp. 4344–4365. DOI: `10.1093/mnras/stw2296`. arXiv: `1609.02607 [astro-ph.SR]`.

Riaz, B. and J. Bally (Mar. 2021). “Accretion and outflow activity in proto-brown dwarfs”. In: Mon. Not. R. Astron. Soc. 501.3, pp. 3781–3805. DOI: `10.1093/mnras/staa3905`. arXiv: `2012.08612 [astro-ph.SR]`.

Riaz, B. and E. T. Whelan (Dec. 2015). “HH 1158: The Lowest Luminosity Externally Irradiated Herbig-Haro Jet”. In: Astrophys. J. Lett. 815.2, L31, p. L31. DOI: `10.1088/2041-8205/815/2/L31`. arXiv: `1512.00016 [astro-ph.SR]`.

Riaz, B. et al. (Jan. 2015). “Very low-luminosity Class I/flat outflow sources in σ Orionis”. In: Mon. Not. R. Astron. Soc. 446.3, pp. 2550–2559. DOI: `10.1093/mnras/stu2139`. arXiv: `1410.3377 [astro-ph.SR]`.

Riaz, B. et al. (July 2017). “First Large-scale Herbig-Haro Jet Driven by a Proto-brown Dwarf”. In: Astrophys. J. 844.1, 47, p. 47. DOI: `10.3847/1538-4357/aa70e8`. arXiv: `1705.01170 [astro-ph.SR]`.

Ricci, L., M. Robberto, and D. R. Soderblom (Nov. 2008). “The Hubble Space Telescope/Advanced Camera for Surveys Atlas of Protoplanetary Disks in the Great Orion Nebula”. In: Astron. J. 136.5, pp. 2136–2151. DOI: `10.1088/0004-6256/136/5/2136`.

Rich, Evan A. et al. (Apr. 2019). “Multi-epoch Direct Imaging and Time-variable Scattered Light Morphology of the HD 163296 Protoplanetary Disk”. In: Astrophys. J. 875.1, 38, p. 38. DOI: `10.3847/1538-4357/ab0f3b`. arXiv: `1811.07785 [astro-ph.SR]`.

Rich, Evan A. et al. (Oct. 2020). “Disk Illumination and Jet Variability of the Herbig Ae Star HD 163296 Using Multi-epoch HST/STIS Optical, Near-IR, and Radio Imagery and Spectroscopy”. In: Astrophys. J. 902.1, 4, p. 4. DOI: `10.3847/1538-4357/abb2a3`. arXiv: `2008.11606 [astro-ph.SR]`.

Robberto, M. et al. (Dec. 1993). “High-resolution imaging of NGC 7027.” In: Astron. Astrophys. 280, pp. 241–254.

Rodenkirch, P. J. et al. (Mar. 2021). “Modeling the nonaxisymmetric structure in the HD 163296 disk with planet-disk interaction”. In: Astron. Astrophys. 647, A174, A174. DOI: `10.1051/0004-6361/202038484`. arXiv: `2012.09217 [astro-ph.EP]`.

Rodríguez-Kamenetzky, Adriana R. et al. (June 2022). “Resolving the Collimation Zone of an Intermediate-mass Protostellar Jet”. In: Astrophys. J. Lett. 931.2, L26, p. L26. DOI: `10.3847/2041-8213/ac6fd1`. arXiv: `2205.10422 [astro-ph.SR]`.

Rubinstein, A. E. et al. (June 2018). “A Cavity of Large Grains in the Disk around the Group II Herbig Ae/Be Star HD 142666”. In: Astrophys. J. 860.1, 7, p. 7. DOI: `10.3847/1538-4357/aabfba`. arXiv: `1804.07343 [astro-ph.SR]`.

Schaefer, G. H. et al. (Dec. 2016). “Orbits, Distance, and Stellar Masses of the Massive Triple Star σ Orionis”. In: Astron. J. 152.6, 213, p. 213. DOI: `10.3847/0004-6256/152/6/213`. arXiv: `1610.01984 [astro-ph.SR]`.

Schlaufman, Kevin C. (Jan. 2018). “Evidence of an Upper Bound on the Masses of Planets and Its Implications for Giant Planet Formation”. In: Astrophys. J. 853.1, 37, p. 37. DOI: `10.3847/1538-4357/aa961c`. arXiv: `1801.06185 [astro-ph.EP]`.

Schutte, Maria C. et al. (Oct. 2020). “Discovery of a Nearby Young Brown Dwarf Disk”. In: Astron. J. 160.4, 156, p. 156. DOI: `10.3847/1538-3881/abaccd`. arXiv: `2007.15735 [astro-ph.SR]`.

Sheehan, Patrick D. et al. (Nov. 2016). “A VLA Survey for Faint Compact Radio Sources in the Orion Nebula Cluster”. In: Astrophys. J. 831.2, 155, p. 155. DOI: `10.3847/0004-637X/831/2/155`. arXiv: `1609.00025 [astro-ph.GA]`.

Shu, F. H. et al. (May 2000). “X-Winds Theory and Observations”. In: *Protostars and Planets IV*. Ed. by V. Mannings, A. P. Boss, and S. S. Russell, pp. 789–814.

Shu, Frank et al. (July 1994a). “Magnetocentrifugally Driven Flows from Young Stars and Disks. I. A Generalized Model”. In: Astrophys. J. 429, p. 781. DOI: `10.1086/174363`.

Shu, Frank H. et al. (July 1994b). “Magnetocentrifugally Driven Flows from Young Stars and Disks. II. Formulation of the Dynamical Problem”. In: Astrophys. J. 429, p. 797. DOI: `10.1086/174364`.

Solf, J. and K. H. Böhm (July 1991). “Spectroscopic Study of Direct and Dust-scattered Line Emission in the HH 1–HH 2 System”. In: Astrophys. J. 375, p. 618. DOI: `10.1086/170224`.

Stoehr, F. et al. (Aug. 2008). “DER_SNR: A Simple & General Spectroscopic Signal-to-Noise Measurement Algorithm”. In: *Astronomical Data Analysis Software and Systems XVII*. Ed. by R. W. Argyle, P. S. Bunclark, and J. R. Lewis. Vol. 394. Astronomical Society of the Pacific Conference Series, p. 505.

Teague, Richard et al. (June 2018). “A Kinematical Detection of Two Embedded Jupiter-mass Planets in HD 163296”. In: Astrophys. J. Lett. 860.1, L12, p. L12. DOI: `10.3847/2041-8213/aac6d7`. arXiv: `1805.10290 [astro-ph.EP]`.

Terquem, C. et al. (Feb. 1999). “Precession of Collimated Outflows from Young Stellar Objects”. In: Astrophys. J. Lett. 512.2, pp. L131–L134. DOI: `10.1086/311880`. arXiv: `astro-ph/9812155 [astro-ph]`.

Tobin, John J. et al. (June 2009). "Kinematics of the Orion Nebula Cluster: Velocity Substructure and Spectroscopic Binaries". In: Astrophys. J. 697.2, pp. 1103–1118. DOI: `10.1088/0004-637X/697/2/1103`. arXiv: `0903.2775 [astro-ph.SR]`.

Vázquez-Semadeni, Enrique et al. (Dec. 2019). "Global hierarchical collapse in molecular clouds. Towards a comprehensive scenario". In: Mon. Not. R. Astron. Soc. 490.3, pp. 3061–3097. DOI: `10.1093/mnras/stz2736`. arXiv: `1903.11247 [astro-ph.GA]`.

Wassell, E. J. et al. (Oct. 2006). "An Asymmetric Outflow from the Herbig Ae Star HD 163296". In: Astrophys. J. 650.2, pp. 985–997. DOI: `10.1086/507268`.

Waters, L. B. F. M. and C. Waelkens (Jan. 1998). "Herbig Ae/Be Stars". In: Annu. Rev. Astron. Astrophys. 36, pp. 233–266. DOI: `10.1146/annurev.astro.36.1.233`.

Weilbacher, Peter M. et al. (Oct. 2015). "A MUSE map of the central Orion Nebula (M 42)". In: Astron. Astrophys. 582, A114, A114. DOI: `10.1051/0004-6361/201526529`. arXiv: `1507.00006 [astro-ph.GA]`.

Weilbacher, Peter M. et al. (Sept. 2020). "The data processing pipeline for the MUSE instrument". In: Astron. Astrophys. 641, A28, A28. DOI: `10.1051/0004-6361/202037855`. arXiv: `2006.08638 [astro-ph.IM]`.

Whelan, E. T. (Jan. 2014). "Jets from young stars and brown dwarfs". In: *Astronomische Nachrichten* 335.5, p. 537. DOI: `10.1002/asna.201412062`. arXiv: `1406.7627 [astro-ph.SR]`.

Whelan, E. T. et al. (Dec. 2009). "Classical T Tauri-like Outflow Activity in the Brown Dwarf Mass Regime". In: Astrophys. J. 706.2, pp. 1054–1068. DOI: `10.1088/0004-637X/706/2/1054`. arXiv: `0910.2665 [astro-ph.SR]`.

Whelan, E. T. et al. (Oct. 2014). "Accretion-ejection connection in the young brown dwarf candidate ISO-ChaI 217". In: Astron. Astrophys. 570, A59, A59. DOI: `10.1051/0004-6361/201424067`. arXiv: `1408.5011 [astro-ph.SR]`.

Whelan, E. T. et al. (July 2015). "Spectro-astrometry of LkCa 15 with X-Shooter: Searching for emission from LkCa 15b". In: Astron. Astrophys. 579, A48, A48. DOI: `10.1051/0004-6361/201425578`. arXiv: `1504.04824 [astro-ph.SR]`.

Whelan, E. T. et al. (May 2021). "Evidence for an MHD Disk Wind via Optical Forbidden Line Spectroastrometry". In: Astrophys. J. 913.1, 43, p. 43. DOI: `10.3847/1538-4357/abf55e`. arXiv: `2104.05561 [astro-ph.SR]`.

Whelan, Emma T. et al. (June 2005). "A resolved outflow of matter from a brown dwarf". In: Nature 435.7042, pp. 652–654. DOI: `10.1038/nature03598`. arXiv: `astro-ph/0506485 [astro-ph]`.

Whitworth, Anthony P. (2018). "Brown Dwarf Formation: Theory". In: *Handbook of Exoplanets*. Ed. by Hans J. Deeg and Juan Antonio Belmonte, 95, p. 95. DOI: `10.1007/978-3-319-55333-7_95`.

Wichittanakom, C. et al. (Mar. 2020). "The accretion rates and mechanisms of Herbig Ae/Be stars". In: Mon. Not. R. Astron. Soc. 493.1, pp. 234–249. DOI: `10.1093/mnras/staa169`. arXiv: `2001.05971 [astro-ph.SR]`.

Winter, Andrew J. et al. (Dec. 2019). "A solution to the proplyd lifetime problem". In: Mon. Not. R. Astron. Soc. 490.4, pp. 5478–5493. DOI: `10.1093/mnras/stz2545`. arXiv: `1909.04093 [astro-ph.SR]`.

Woitke, P. et al. (Oct. 2018). "Modelling mid-infrared molecular emission lines from T Tauri stars". In: Astron. Astrophys. 618, A57, A57. DOI: `10.1051/0004-6361/201731460`. arXiv: `1807.05784 [astro-ph.SR]`.

Xie, C. et al. (Dec. 2020). "Searching for proto-planets with MUSE". In: Astron. Astrophys. 644, A149, A149. DOI: `10.1051/0004-6361/202038242`. arXiv: `2011.08043 [astro-ph.EP]`.

— (June 2021). "A MUSE view of the asymmetric jet from HD 163296". In: Astron. Astrophys. 650, L6, p. L6. DOI: `10.1051/0004-6361/202140602`. arXiv: `2106.01661 [astro-ph.SR]`.

Zhang, Shangjia et al. (Dec. 2018). "The Disk Substructures at High Angular Resolution Project (DSHARP). VII. The Planet-Disk Interactions Interpretation". In: Astrophys. J. Lett. 869.2, L47, p. L47. DOI: `10.3847/2041-8213/aaf744`. arXiv: `1812.04045 [astro-ph.EP]`.

Zhu, Zhaohuan (Mar. 2019). "Inclined massive planets in a protoplanetary disc: gap opening, disc breaking, and observational signatures". In: Mon. Not. R. Astron. Soc. 483.3, pp. 4221–4241. DOI: `10.1093/mnras/sty3358`. arXiv: `1812.01262 [astro-ph.EP]`.